UNIVERSITY OF SOUTHAMPTON
SCHOOL OF CHEMISTRY

Computational methods for first-principles molecular dynamics with linear-scaling density functional theory

by
Valerio Vitale

Thesis for the degree of Doctor of Philosophy

April 2017

University of Southampton
school of chemistry

Doctor of Philosophy Computational methods for first-principles molecular dynamics with linear-scaling density functional theory
by Valerio Vitale

Abstract

Nowadays, Kohm-Sham density functional theory (KS-DFT) calculations are routinely employed in several research fields, due to the ability of KS-DFT to provide great accuracy for a wide class of molecular systems and materials. Unfortunately, conventional KS-DFT calculations, although very powerful, require a computational cost that goes with the cube of the system size N, also known as $O\left(N^3\right)$ scaling, undermining in practice the study of large systems. The advent of linear-scaling, or $O\left(N\right)$, DFT (LS-DFT) methods, relying on the locality of the electronic matter, has enabled calculations on increasingly large systems, up to tens of thousands of atoms. The central tenet of linear-scaling methods is the exponential decay in real space of the single-particle reduced density matrix. This property allows to enforce localisation constraints on the electronic structure, significantly reducing the size of the matrices, such as the Hamiltonian matrix, and increasing their sparsity. The single-particle density matrix in the LS-DFT formalism is expanded in terms of a set of atom-centred, strictly localised functions. Employing periodic boundary conditions (PBCs), the energy is minimised with respect to all the degrees of freedom in the density matrix, which allows to attain chemical accuracy using a high-resolution minimal basis set. The combination of localisation constraints and sparse algebra form the substrate for $O\left(N\right)$ calculations. In this thesis, we used Onetep, a linear-scaling DFT program, to carry out our calculations. The aim of our research is to combine molecular dynamics simulations, within the Born-Oppenheimer approximation (BOMD), with linear-scaling DFT methods. In particular, our main goal is to advance current methodology by developing new algorithms to better exploit locality in BOMD and to reduce the computational load while maintaining DFT accuracy.

Dipole moment autocorrelation functions can directly be employed to obtain the IR spectrum of a given molecular system. DFT-MD simulations offer the perfect tool to generate accurate autocorrelation functions which automatically take into account the anharmonicity of the potential energy surface and temperature effects. Computational IR spectroscopy plays a pivotal role in the understanding of conformational changes of biomolecules, which tend to show several almost-degenerate conformers at room temperatures (floppy molecules). It is particularly valuable when interpreting their fingerprint in solution in combination with experimental spectra. We have implemented two algorithms for the computation of the local electronic dipole moments of molecules in solution. Both methods demand a strategy to partition the density. These methods enable the computation of IR spectra of large molecules, such as polypeptide, in explicit

solvent. In the resulting IR spectrum the effect of the solvent on the target molecule is automatically captured, whereas its IR signature is removed. We expect these new functionalities to be very helpful in the understanding of how bio-molecules interact with the solvent at room temperature and the effect of these interactions on conformational changes.

Computationally, the most demanding step in molecular dynamics simulations is the evaluation of energies and forces. This has particular severe consequences on BOMD-based approaches. In fact, a self-consistent field (SCF) step is required at each MD step, which in turn requires multiple energy evaluations. As a consequence, the SCF loop has a major effect on the computational load and overall wall-time. MD Schemes that are capable to by-pass the SCF loop altogether, e.g. Car-Parrinello MD or fixed charge force fields in classical MD, are inherently faster in terms of wall-time per MD step, although they usually demand a much smaller time-step. Moreover, the quality of the converged density matrix is crucial for energy conservation and forces in the LS-DFT BOMD approaches. In theory, the self-consistent solution does not depend on the initial guess. In practice, the SCF optimisation is always incomplete, leading to memory effects and the breaking of time-reversal symmetry, which gives rise to systematic errors in energy gradients that manifest as a drift in microcanonical energy. To ameliorate this problem, we present two integration schemes based on an extended-Lagrangian (XL) approach which introduces extended or auxiliary electronic degrees of freedom to generate good quality time-reversible initial guesses in the SCF loop. Both schemes are improvements over the original XL formulation, which suffered from numerical noise accumulation. The first approach, known as dissipative XL (dXL), introduces a dissipative-like term in the Verlet integration (modified Verlet) of the auxiliary degrees of freedom; the second approach, known as inertial XL (iXL), introduces a thermostat, hence requiring a velocity Verlet integrator. We have implemented both schemes in ONETEP and studied their performance using liquid water as test case. In collaboration with the authors of the schemes, we have analysed the energy drift in both classical polarisable force field MD calculations and LS-DFT BOMD. We have found that both schemes are very efficient in reducing the number of SCF iterations while maintaining good energy drifts and have similar performance. We believe that our implementation and analysis will be very beneficial for future applications both with LS-DFT BOMD and classical polarisable force field MD since both schemes constitute important algorithmic improvements that markedly extend the timescales accessible to classical and LS-DFT MD simulations alike.

Contents

List of Figures

List of Tables

Declaration of authorship

I, Valerio Vitale, declare that the thesis entitled "Computational methods for first-principles molecular dynamics with linear-scaling density functional theory" and the work presented in the thesis are both my own, and have been generated by me as the result of my own original research. I confirm that:

- this work was done wholly or mainly while in candidature for a research degree at this University;
- where any part of this thesis has previously been submitted for a degree or any other qualification at this University or any other institution, this has been clearly stated;
- where I have consulted the published work of others, this is always clearly attributed;
- where I have quoted from the work of others, the source is always given. With the exception of such quotations, this thesis is entirely my own work;
- I have acknowledged all main sources of help;
- where the thesis is based on work done by myself jointly with others, I have made clear exactly what was done by others and what I have contributed myself;
- parts of this work have been published as papers:
  - Anharmonic Infrared Spectroscopy through the Fourier Transform of Time Correlation Function Formalism in ONETEP. Vitale, Valerio and Dziedzic, Jacek and Dubois, Simon M.-M. and Fangohr, Hans and Skylaris, Chris-Kriton. *Journal of Chemical Theory and Computation* **11**(7), 2015.
  - Performance of extended Lagrangian schemes for molecular dynamics simulations with classical polarizable force fields and density functional theory. Vitale, Valerio and Dziedzic, Jacek and Albaugh, Alex and Niklasson, Anders M. N. and Head-Gordon, Teresa and Skylaris, Chris-Kriton. *J. Chem. Phys.* **146**(12), 2017.

Signed: . . . . . .
Date: . . . . . .

Acknowledgements

The last three and half years of research have been very exciting, intense and also hard sometimes. I feel I have been able to grow both professionally and as a person. I am delighted to finally be able to see most of our scientific findings gathered into a single document, to form this Ph. D. dissertation. I am very grateful to all the people that in a way or another have contributed to make it possible:

- To my first supervisor, Prof. Chris-Kriton Skylaris, for his participation in all our projects, for his much-appreciated scientific advice, and for his support.
- To my second supervisor, Prof. Hans Fangohr especially for his support during my first year of Ph. D. and for his scientific contribution to the work on the anharmonic vibrational spectra.
- To the Doctoral Training Centre (DTC) of the Institute of Complex Systems Simulation (ICSS) for funding my research via an integrated four-years studentship jointly with the Engineering and Physical Sciences Research Council (EPSRC) (EPRSC Grant No EP/G03690X/1).
- To Dr. Jacek Dziedzic for his active involvement in the works concerning the calculation of anharmonic vibrational spectra and the extended Lagrangian schemes, as well as for helping me improving my computing programming skills and for always be helpful when I needed. But especially for being a good friend.
- To the people I had the opportunity to collaborate with: Prof. Hans Fangohr and Dr. Simon Dubois for the work on the anharmonic vibrational spectra. Alex Albaugh, Dr. Anders Niklasson and Prof. Teresa Head-Gordon for the work on the performance of extended Lagrangian schemes.
- To the members of the Skylaris group, past and present, for creating a friendly environment within and outside the office. Alvaro Ruiz-Serrano, Ben Lowe, Chris Sampson, Frank Longford, Gabriele Boschetto, Jacek Dziedzic, James Womack, Karl Wilkinson, Lucas Verga, Max Phipps, Stephen Fox, Tom Ellaby. It has been lot of fun sharing this experience with you. I would especially like to thank Jolyon Aarons, for allowing me to officiate his wedding ceremony, for the countless conversations we had on disparate topics and for being always a source of enlightenment and joy.
- To the friends in Southampton: Olga Dziedzic, Jindi Li, Hairul Hisham Hamzah, Joe Reed, Chris Crispin, Jack Weatheritt and Kostantinos Kouvaris.

This Ph. D. dissertation is dedicated to my better half Martina. She has been a constant source of inspiration since the first time we met, almost fifteen years ago. I would also like to thank my parents and my brothers, whose support has ultimately made this thesis possible.

Introduction

> *Nature isn't classical, dammit, and if you want to make a simulation of nature, you'd better make it quantum mechanical, and by golly it's a wonderful problem, because it doesn't look so easy.*

Richard Feynman, *International Journal of Theoretical Physics, volume 21, p. 467-488*, 1982

All the processes occurring at the microscopic scale in the low-energy spectrum, of which chemical processes are a subset, can in principle be described by quantum mechanics (QM). The equation governing the motion of electrons and nuclei, which make up the atoms, were proposed by Schrödinger, Dirac and others, between 1926 and 1930[4–8]. Therefore, at least in principle, we can make sense of the wide range of phenomena arising in real materials by solving the equations of QM. It is well known that these equations are very complicated and for all but few simple systems only approximate solutions exist[9]. This is the reason why, over the last sixty years, physicists and chemists alike, have made a tremendous effort in conceiving theoretical and numerical methods to find approximate but accurate solutions to these equations. This process has led to a plethora of approaches that have greatly improved our understanding of chemical processes. Nowadays, we have at our disposal a hierarchy of *ab initio*[1] models providing several levels of approximations and accuracy, see Refs. 10 and 11 for a review of the most common computational methods.

However, the complexity of approximate models remains enormous, even for systems containing only a handful of atoms. The role of atomistic simulations is precisely to translate these theoretical models into computer programs in order to perform such a stupendous number of calculations and provide accurate predictions. Among the *ab initio* computational methods, density functional theory (DFT) is the most popular. DFT is an exact reformulation of QM principles, based on the electron density function, rather

[1] *Ab initio* is Latin for "from the beginning" or "from first principles". These models are entirely based on QM and basic physical constants, e.g. the mass and charge of electrons.

than on the much more complex Schrödinger wave-function, developed by Hohenberg and Kohn in the 1964[12] and rearranged into an operational form by Kohn and Sham in the 1965[13], cf. Chapter 2, Sections 2.1-2.3. Efficient and robust algorithms based on DFT have been developed during the last three decades[14]. These are extensively used by the scientific community to calculate electronic, optical, and structural properties of crystals, amorphous systems, surfaces and molecules[15–17]. For large systems, from tens to thousands of atoms, DFT simulations represent, *de facto*, the *ab initio* method of choice. For such (relatively) large systems, the computational cost of all the other *ab initio* methods, with a similar or higher accuracy, is prohibitive and preclude any kind of calculation, even today in the era of high performance computing systems.

Conventional, plane-waves based, Kohn-Sham DFT (KS-DFT) simulations, although very powerful, still require a computational cost that asymptotically scales cubically with the number N of atoms in the system, sometimes referred to $O\left(N^3\right)$ methods[2]. Although the $O\left(N^3\right)$ scaling law seems favorable compared to other *ab initio* methods, it still poses some bounds for large systems, e.g. biological molecules and nano-devices, where thousands of atoms are involved. Consequently, in the last twenty years, there has been a growing interest in developing new methods able to reduce the computational overload while maintaining a good level of accuracy[18–21]. In particular, this has led to linear-scaling methods, also known as order-N or $O\left(N\right)$ methods. This has made possible the study of very large systems, such as proteins, electronic and optic nano-devices, and nano-catalysts[22–26]. In order to achieve a linear-scaling method, one needs to exploit the locality or *nearsightedness*, as coined by W. Kohn [27, 28], of the electronic matter. This property will be discussed in depth in Sec. 2.4.

Molecular dynamics (MD) simulations can be combined with *ab initio* methods (AIMD). The basic idea underlying every AIMD scheme is to compute the forces on the nuclei from electronic structure calculations that are performed "on-the-fly" as the molecular dynamics trajectory is generated[29]. Usually nuclei are treated classically, i.e. solving Hamilton's equations. In particular, two major class of DFT molecular dynamics (DFT-MD) exist: Car-Parrinello MD[30] (CPMD) and Born-Oppenheimer MD[31, 32] (BOMD). Both have extensively been used, in recent years, to study either systems that are inherently dynamical, e.g. conformational analysis of (bio)molecules at non-zero temperatures[33, 34], chemical reaction paths in gas and condensed phase[35], surface processes[36], solvation phenomena[37, 38] and so forth or as an alternative method to find the equilibrium structures of molecules, clusters, and surfaces at both low and high P, T conditions[39, 40], the latter being typically found in geology and astrophysics[16]. DFT-MD is also used to compute different kinds of spectra, e.g. I.R. and Raman spectra.

[2] More precisely $O\left(N^3\right)$ scaling law for computational time and $O\left(N^2\right)$ for the memory storage.

DFT-MD approaches have a greater flexibility compared to classical molecular dynamics ones, where the interactions between nuclei are described by parametrized potentials. This is a serious drawback for classical MD, especially when treating complex materials, where the electronic structure changes qualitatively during the course of the simulation. Moreover, a quantum description of chemical reactions can only be obtained with AIMD methods. Notably, unforeseen phenomena can simply emerge during the simulation, giving to DFT-MD methods a truly predictive power. Despite its advantages, putting molecular dynamics on *ab initio* grounds poses some obstacles. Correlation lengths and relaxation times achievable with DFT-MD are shortened (from microseconds to tens of picoseconds). Nonetheless, nowadays this drawback can be ameliorated in part by the ever increasing power of computing resources.

Our research focused mainly on the development of new approaches for DFT-MD simulations in the framework of linear-scaling DFT. Strictly localised orbitals were used to expand the the Kohn-Sham molecular orbitals. These orbitals are atom-centred functions localised within spheres, cf. Sec. 2.4. The ground state is found via a direct minimisation of an energy functional, with no diagonalisation of the Kohn-Sham Hamiltonian, hence avoiding the costly $O\left(N^3\right)$ step. The procedure consists of a self-consistent, variational search to optimise the set of degrees of freedom that describe the system subject to some constraints, cf. Sec. 2.4. All our developments were implemented in the ONETEP (Order-N Electronic Total Energy Package) code [18, 41]. ONETEP is a linear-scaling DFT (LS-DFT) program which has the unique property of keeping the level of accuracy tunable through a single parameter as in conventional plane-waves DFT. During our investigations we were able to advance our understanding of the theory for AIMD methods that use strict localisation constraints to reduce the computational cost. Within this framework, we developed new algorithms to study the vibrational spectra of large molecules in solutions through DFT-MD. Furthermore, in collaboration with two research groups at University of Berkeley (California,US) and at Los Alamos National Laboratory (New Mexico,US), we have studied the performance of novel integration schemes designed to accelerate both classical polarisable force field MD and LS-DFT MD. All the algorithms resulted from our research are available as part of the ONETEP distribution and are accessible to the scientific community.

THESIS OUTLINE

In Chapter 1 we introduce the basic ideas of quantum mechanics and some of the approximations to solve the quantum many-body problem. The most popular approach for this purpose is the density functional theory approach, to which Chapter 2 is dedicated. Moreover, in this chapter we also introduce the general concepts behind

linear-scaling DFT (LS-DFT) methods and their implementation in the ONETEP program. Born-Oppenheimer molecular dynamics is the subject of Chapter 3. LS-DFT methods can be combined with BOMD to compute the IR spectra of molecules through the Fourier transform of the dipole moment autocorrelation function. Two new schemes to compute the dipole moment of selected atoms, such as single molecules, in a larger environment, such as the solvent are presented in Chapter 4. Our schemes are capable of computing fully anharmonic infrared spectra of molecules in the gas phase and in solution at finite temperature. Finally, schemes for speeding-up BOMD in ONETEP, such as extended-Lagrangian schemes [42], are the topic of the Chapter 5. Additionally, Appendices show extra results that could potentially be used in future developments, which were obtained during the course of the main research projects.

Chapter 1

Theoretical background

> *The machinery of the world is far too complex for the simplicity of men.*
>
> Jorge Luis Borges, *Dreamtigers*

Since these earliest works by the pioneers of quantum mechanics, several interpretations of the fundamental principles have been proposed: from the Copenhagen interpretation ("orthodox interpretation") of Bohr and Heisenberg[43], to the path-integral interpretation of Dirac and Feynman[44, 45], to the more exotic "many-worlds" interpretation of Everett III[46]. However interesting the ontological problems of QM might be, they rather belong to the realm of philosophy of science, and they are outside of the scope of this thesis. In this thesis I will adopt a more operational approach: I will introduce the formalism of QM and make use of its mathematical framework, which is necessary to understand our methodology, but I will not attempt to disentangle the intricacy of the many interpretations and their consequences on the underlying structure of Nature[47].

1.1 The principles of quantum mechanics

The flaws of classical mechanics started to be unveiled during the last part of the nineteenth century[1]. They clearly demonstrated the inadequacy of the classical theory to explain the processes at the microscopic scale. A new form of mechanics was required, which emerged during the first quarter of the twentieth century, called quantum mechanics[2]

[1] The most prominent being the ultraviolet catastrophe, the photoelectric effect and the instability of atomic structure, see 48 for an excellent review on the subject.

[2] Incidentally, also the special theory of relativity and the general theory of relativity were invented in the first quarter of the twentieth century. This is why we refer to those 25 years as one of the golden age of

Historically, the first attempts for a new mechanics can be found in Planck's works on black-body radiation and the $I - \nu$ dispersion relation[49]. After came Einstein, de Broglie and Bohr with new ideas for the behaviour of microscopic particles, which were able to explain the lines in the hydrogen spectrum[50, 51], but were still incomplete. In 1925 Heisenberg[6], Born and Jordan[52] developed a more coherent theory based on physical observables and their non-commutative algebra, called matrix mechanics. Few months later Schrödinger proposed his famous approach based on differential equations and wave-functions, called wave mechanics[4, 5]. He also showed that the two formulations were mathematically equivalent. In 1926, Dirac and Jordan working independently formulated quantum mechanics in a more abstract formalism called transformation mechanics[44], which is the formalism I will follow in this thesis. In 1948, Feynman devised the path integral formulation[45], which is at the core of modern quantum field theories.

Quantum mechanics provides the laws of motion for microscopic particles. Quantum chemistry (QC) deals with the application of these laws to problems in chemistry. In non-relativistic QM the state of a system at any given time, is represented by an abstract vector-state Ψ in a complex Hilbert space $\mathcal{H}$[3], usually denoted by the symbol $|\Psi\rangle$ in Dirac's notation[44, 53, 54], known as a *ket*. The fact that a dynamical state can be represented by a vector in a linear space is at the heart of the so-called *superposition principle of states*[44]. The space $\mathcal{H}$ can be either finite-dimensional or infinite-dimensional depending on the number of states in which the system can be observed. For each vector $|\Psi\rangle$ in $\mathcal{H}$ we can define a dual vector $\langle\Psi|$, called *bra*, belonging to the dual space $\mathcal{H}^* \equiv L(\mathcal{H}, \mathbb{C})$-the space of linear operators on $\mathcal{H}$ -via the product

$$\langle\Psi|\Psi\rangle : \mathcal{H}^* \times \mathcal{H} \to \mathbb{C}.$$

We assume a *one-to-one* correspondence between bras and kets[44]. In virtue of this correspondence, the abstract state vector can be described by a either a ket or a bra, and the theory is symmetric with respect to the change $|\rangle \to \langle|$. The inner product has the following properties:

1. Positive definiteness:

$$\langle a|a\rangle \geq 0, \quad \text{where} \quad \langle a|a\rangle = 0 \iff |a\rangle = 0.$$

physics.

[3]To be more precise, a QM state is represented by a ray in $\mathcal{H}$, hence by a point in the projective Hilbert space $\mathcal{P}(\mathcal{H})$. For relativistic systems the state is represented by a spinor Ψ_σ.

2. Conjugate symmetry:

$$\langle a|b\rangle = \overline{\langle b|a\rangle}.$$

3. Antilinearity in the first argument:

$$\langle a + ca'|b\rangle = \langle a|b\rangle + \bar{c}\,\langle a'|b\rangle\,.$$

4. Linearity in the second argument:

$$\langle a|b + cb'\rangle = \langle a|b\rangle + c\,\langle a|b'\rangle\,,$$

for any $|a\rangle, |b\rangle, |a'\rangle, |b'\rangle \in \mathcal{H}$ and $c \in \mathbb{C}$. In point 3, $\bar{c}$ represents the complex conjugate of the complex number c. For any observable in classical mechanics, say A, there exists a self-adjoint linear operator $\hat{A}$ acting on $\mathcal{H}$[4]. The adjoint operator $\hat{A}^\dagger$ is defined via the inner product

$$\langle a|\hat{A}b\rangle = \langle a\hat{A}^\dagger|b\rangle\,, \quad \forall\, |a\rangle, |b\rangle \in \mathcal{H}\,.$$

We can always define the adjoint of a linear operator in finite-dimensional Hilbert spaces. However, care must be taken when considering infinite-dimensional spaces where continuous and unbounded operators can arise[5]. In computational chemistry, in order to perform real calculations on a computer, we always deal with finite basis sets to describe a state vector in $\mathcal{H}$, since we only have access to finite-memory machines. Therefore, we will mostly adopt finite-dimensional Hilbert spaces for our derivations and we will only mention the results for the infinite-dimensional cases where relevant. The spectrum of $\hat{A}$, $\boldsymbol{\sigma}(\hat{A})$, represents all the possible outcomes of a measurement. Hence, the only values that will ever be observed in any measurement are those satisfying the eigenvalue equation

$$\hat{A}\,|n\rangle = \alpha_n\,|n\rangle\,, \tag{1.1}$$

where α_n is the nth-eigenvalue corresponding to the nth-eigenstate $|n\rangle$. Self-adjointness, $\hat{A} = \hat{A}^\dagger$, forces all the eigenvalues $\{\alpha_n\}$ to be real. Also, eigenstates associated with different eigenvalues are mutually orthogonal by construction, but they are not normalised

[4]There exists particular cases where an observable can not be cast as the expectation value of *any* operator. Instead it arises from the gauge-invariant property of the phase of the wave-function. A typical example, is the polarisation of dielectrics in bulk[55–57]

[5]In this case, one has to find a dense subset $\mathcal{D} \subset \mathcal{H}$ such as the linear operator is bounded. This implies that the domain of an unbounded operator is smaller than the full Hilbert space and "generalised eigenvectors", defined in the vector space of distributions, must be invoked. In practice, in the infinite-dimensional case the vector space is described by a function space, so that the abstract states are represented by single-valued, square-integrable functions and distributions; the L^2-space is usually adopted in this situation.

in general. From these, an orthonormal basis $B(\mathcal{H})$ can always be found, even in the degenerate case. Assuming orthonormality, and with a slight abuse of notation, any state $|\Psi\rangle$ can be expanded in this basis:

$$|\Psi\rangle = \sum_n c_n |n\rangle ,$$

where $\langle m|\Psi\rangle = c_m \in \mathbb{C}$, since $\langle m|n\rangle = \delta_{mn}$. If a basis is complete, one has the closure relation: $\sum_n |n\rangle \langle n| = \hat{I}$. In the infinite-dimensional case, we need an "infinite basis" into which $|\Psi\rangle$ can be expanded. For example, we can use the eigenstates of the position operator as a basis $|\mathbf{r}\rangle$:

$$|\Psi\rangle = \int \mathrm{d}\mathbf{r}\, \Psi(\mathbf{r}) |\mathbf{r}\rangle ,$$

where $\Psi(\mathbf{r}) = \langle \mathbf{r}|\Psi\rangle$. This is exactly what one usually refers to as Schrödinger wave-function[58, 59] in the position representation. One could use a different representation, e.g. the momentum representation $\Psi(\mathbf{p})$. The two representations are mathematically different but physically equivalent. In fact, they are related by a unitary transformation (Fourier transform). If we want to describe the behaviour of electrons, we need a mixed basis $|\mathbf{x}\rangle = |s\mathbf{r}\rangle$ in order to take into account the spin states too. In non-relativistic QM, electronic spin has to be introduced *a posteriori*. However, in the full-relativistic Dirac equation[44], the electronic spin emerges naturally from the algebra of the so-called 2×2 Pauli matrices $\sigma_i, i = 1, 2, 3$. For a N-particle system of electrons, we would have $\Psi(\mathbf{x}_1, \mathbf{x}_2, \ldots, \mathbf{x}_N) = \langle \mathbf{x}_1, \mathbf{x}_2, \ldots, \mathbf{x}_N|\Psi\rangle$. The orthonormality condition becomes

$$\langle \mathbf{x}|\mathbf{x}'\rangle = \langle s\mathbf{r}|s'\mathbf{r}'\rangle = \delta_{s,s'}\delta(\mathbf{r} - \mathbf{r}'),$$

where $\delta_{a,b}$ is the Kronecker delta and $\delta(x)$ is the Dirac delta function. The completeness of the basis is expressed as

$$\int \mathrm{d}\mathbf{x}\, |\mathbf{x}\rangle \langle \mathbf{x}| = \sum_s \int \mathrm{d}\mathbf{r}\, |s\mathbf{r}\rangle \langle \mathbf{r}s| = \hat{I}.$$

Upon measurement of the observable A, the probability of finding the system in a given state $|s\rangle$ at a given time t with corresponding eigenvalue α_s, is provided by $P_s = \bar{c}_s c_s = |c_s|^2$. Only if the system is in the exact eigenstate $|s\rangle$ of $\hat{A}$ then $P_s = 1$ and $P_r = 0, \forall\, |r\rangle$ orthogonal to $|s\rangle$. Clearly, the sum over all the possibilities has to give a probability equal to 1, i.e.

$$\sum_n P_n = \sum_n |c_n|^2 = 1.$$

After the measurement, the system is said to collapse[6] in one of the eigenstates of $\hat{A}$ and subsequent measurements of the observable A will always produce the same result. The expectation value $\langle A \rangle$ of the observable A, i.e. the average value over all the possible outcomes is computed as

$$\langle A \rangle = \langle \Psi | \hat{A} | \Psi \rangle = \sum_s |c_s|^2 \alpha_s.$$

This is exactly what we would expect the average over infinitely many trials to yield.

Linear operators in Hilbert spaces form a non-commutative algebra. If we consider two distinct operators $\hat{A}$ and $\hat{B}$ their commutator is defined as

$$\left[\hat{A}, \hat{B}\right] = \hat{A}\hat{B} - \hat{B}\hat{A},$$

which in general is different from zero, meaning that the two operators do not share the same eigenstates[44]. Physically, this can be explain by considering the effect of a measurement on a quantum system. Any measurement performed on a quantum system introduces a perturbation on the state (cf. collapse of the state). If we perform two measurements, e.g. first we measure the observable A and then B, we are performing the following operation on the state vector: $\hat{B}\hat{A}\,|\Psi\rangle$. Measuring B first and then A, i.e. $\hat{A}\hat{B}\,|\Psi\rangle$, yields in general a different outcome, since the way $\hat{A}$ affects the state is in general different from the perturbation introduced by $\hat{B}$. Given this, it follows that no experiment can be designed that can measure two observables simultaneously, since the state can not collapse on two different eigenstates, cf. *Heisenberg's uncertainty principle*[44]. However, if the two operators commute, a measurement of A brings the system in one of the eigenstates of $\hat{B}$ and *vice versa* and their commutator is zero. The two observables are said to be *compatible* and can be measured simultaneously.

QC is mainly involved with studying the behaviour of electrons in matter. All the particles found in Nature so far, fall in one of two categories: fermions or bosons. Fermions follow the so-called Fermi-Dirac statistics[60, 61]. The fermionic wave-function $\Psi(\mathbf{x}_1, \mathbf{x}_2, \ldots, \mathbf{x}_N)$ is antisymmetric with respect to the exchange of any two of coordinates $\mathbf{x}_i \rightarrow \mathbf{x}_j$:

$$\Psi(\mathbf{x}_1, \ldots, \mathbf{x}_i, \ldots, \mathbf{x}_j, \ldots, \mathbf{x}_N) = -\Psi(\mathbf{x}_1, \ldots, \mathbf{x}_j, \ldots, \mathbf{x}_i, \ldots, \mathbf{x}_N). \tag{1.2}$$

Hence, the general state-vector belongs to a subspace of $\mathcal{H}$, called the antisymmetric space $\mathcal{H}^{\mathrm{A}}$. This implies that two fermions can not have the same set of coordinates, which is also known as the Pauli exclusion principle. Bosons on the other hand follow the

[6] See the Copenhagen interpretation.

so-called Bose-Einstein statistics. The bosonic wave-function is symmetric with respect to the exchange of any two coordinates. Consequently, no Pauli exclusion principle applies to bosons. This property of the wave-function has its roots in a very fundamental property of QM particles: indistinguishablity. In fact, in QM, the trajectories of particles of the same class, e.g. electrons, cannot be uniquely identified. If we start with an initial configuration of two particles A and B in two different positions, $\mathbf{r}_1$ and $\mathbf{r}_2$ respectively, and at a later time we found the the two particles in the positions $\mathbf{r}_3$ and $\mathbf{r}_4$, one cannot say if particle A followed the path from $\mathbf{r}_1$ to $\mathbf{r}_3$ or from $\mathbf{r}_1$ to $\mathbf{r}_4$ (similarly for particle B). Therefore the wave-function for the two cases needs not to differ by more than a constant factor. If we introduce an exchange operator $\hat{P}_{34}$, we can write

$$\hat{P}_{34}\Psi(\mathbf{r}_3, \mathbf{r}_4) = \Psi(\mathbf{r}_4, \mathbf{r}_3) = c\Psi(\mathbf{r}_3, \mathbf{r}_4). \tag{1.3}$$

Clearly, if one applies the exchange operator twice the result is the identity operator, i.e. $\hat{P}_{34}^2 = \hat{I}$. So we find the following relation

$$\hat{P}_{34}^2\Psi(\mathbf{r}_3, \mathbf{r}_4) = c^2\Psi(\mathbf{r}_3, \mathbf{r}_4) \Rightarrow c = \pm 1. \tag{1.4}$$

This result is readily extended to N particles. Therefore from the indistinguishability, i.e. (1.4), we recover the symmetries of the wave-function for bosons and fermions.

1.2 Time evolution

In the Schrödinger picture the state vector $|\Psi\rangle$ is a dynamical object. As a consequence, one needs to postulate a rule for determining the time evolution of $|\Psi(t)\rangle$ in absence of a measurement. This rule, for non-relativistic systems, is the time-dependent Schrödinger equation[4, 5, 44] (TDSE)

$$\partial_t |\Psi(t)\rangle = -\frac{i}{\hbar}\hat{H}|\Psi(t)\rangle, \tag{1.5}$$

where $\hat{H}$ is the Hamiltonian operator, $i = \sqrt{-1}$ and $\hbar = h/2\pi$, with h being referred to as Planck's constant. Although, we can find a line of reasoning to make (1.5) physically plausible, it must be considered as a postulate. Interestingly, (1.5) is a first-order differential equation, which implies that only one initial condition $|\Psi(0)\rangle$ has to be specified in order to predict the future states. Moreover, it is also linear, as we would expect from the superposition principle, so that any linear combination of two solutions is still a solution. Remarkably, in classical mechanics a mathematically similar equation exists, which involve the Liouvillian $L = i\{\cdot, H\}$ and the phase space vector $\mathbf{x}$ to give: $\dot{\mathbf{x}} = iL\mathbf{x}$. For a time-independent Hamiltonian the Liouville equation has the formal solution

$\mathbf{x}(t) = \exp[iLt]\mathbf{x}(0)$. By analogy, the TDSE-with time-independent Hamiltonian operators-has the formal solution

$$|\Psi(t)\rangle = e^{-i\hat{H}t/\hbar}\,|\Psi(0)\rangle\,. \tag{1.6}$$

In QM the Hamiltonian operator plays the role of generator of time evolution. The unitary operator $\hat{U}(t) = e^{-i\hat{H}t/\hbar}$, is called the time evolution operator. The unitary condition, $\hat{U}^{\dagger}(t)\hat{U}(t) = \hat{I}$, is a physically necessary condition that guarantees for an initially normalised state-vector to remain normalised throughout the evolution, and therefore generate proper probabilities. The eigenvalues of the Hamiltonian operator give the allowed energy levels of the system and if the Hamiltonian is time-independent so are its eigenvalues. In this case, the expectation value $\langle\hat{H}\rangle$ is a constant of motion and the system is conservative. The eigenvalues E_n and eigenstates $|E_n\rangle$ of the time-independent Hamiltonian can be found by solving the time-independent Schrödinger equation (TISE):

$$\hat{H}\,|E_n\rangle = E_n\,|E_n\rangle\,. \tag{1.7}$$

We can expand $|\Psi(0)\rangle$ in terms of the energy eigenstates

$$|\Psi(0)\rangle = \sum_n c_n\,|E_n\rangle\,, \tag{1.8}$$

and since $\hat{U}$ (t) commutes with $\hat{H}$, we find the following relation

$$\hat{U}(t)\,|E_n\rangle = e^{-i\hat{H}t/\hbar}\,|E_n\rangle = e^{-iE_nt/\hbar}\,|E_n\rangle\,. \tag{1.9}$$

Substituting (1.8) and (1.9) in (1.6) yields

$$|\Psi(t)\rangle = \sum_n c_n e^{-iE_nt/\hbar}\,|E_n\rangle\,, \tag{1.10}$$

where $c_n = \langle E_n|\Psi(0)\rangle$.

If an operator $\hat{A}$ commute with the Hamiltonian, from (1.9) and (1.1) it is straightforward to show that

$$|\langle\alpha_n|\Psi(t)\rangle|^2 = |\langle\alpha_n|\Psi(0)\rangle|^2\,, \tag{1.11}$$

which implies that the probabilities of finding the system in a given state do not change with time. In the Heisenberg picture, it is the operator representing a given observable to function as a dynamical object. Therefore, the rule for the time evolution of a given

operator $\hat{A}(t)$ is the Heisenberg equation of motion:

$$\frac{\mathrm{d}\hat{A}(t)}{\mathrm{d}t} = -\frac{i}{\hbar}\left[\hat{A}(t), \hat{H}(t)\right]. \tag{1.12}$$

Also in this case, there is a remarkable similarity of (1.12) with the classical equation for the evolution of phase space functions. The formal solution of (1.12) is

$$\hat{A}(t) = e^{i\hat{H}t/\hbar}\hat{A}(0)e^{-i\hat{H}t/\hbar} = \hat{U}^{\dagger}(t)\hat{A}(0)\hat{U}(t). \tag{1.13}$$

The operator $\hat{A}(0)$ at the initial time is the corresponding operator in the Schrödinger picture. If $\hat{A}$ commutes with the Hamiltonian, then it does not depend on time and is a constant of motion. In this case, (1.11) is a natural consequence of the Heisenberg picture.

1.3 Density matrix, pure and mixed states

So far, we have assumed that a quantum system is described by a state-vector $|\Psi\rangle$ in a Hilbert space. This is by definition a *pure* state. In particular, if we have N particles in our system we denote the state-vector as $|\Psi_N\rangle$ and the associated N-particle Hilbert space as $\mathcal{H}_N$. However, there exist many situations whereby such description breaks down, e.g. in the case of a subsystem interacting with a larger closed system, or a system in thermal equilibrium with an external bath. We refer to these states as "less than maximum information" states[62], since we are not including in this description all the information of the "system + surroundings". In these situations, the system is said to be in a *mixed* state, and a density matrix operator approach becomes necessary[62–65]. Mixed states represent statistical ensembles of quantum states, which can be properly described through the *ensemble* density operator[10, 62]

$$\hat{\Gamma} = \sum_i p_i \left|\Psi_i\right\rangle\left\langle\Psi_i\right|, \quad \sum_i p_i = 1, \tag{1.14}$$

where p_i represents the probability of the system to be in the pure state $|\Psi_i\rangle$, so that $0 \leq p_i < 1, \quad p_i \in \mathbb{R}\,\forall i$. The index i runs over the set of all accessible pure states. In (1.14), the $|\Psi_i\rangle$ are not bound to have the same number of particles and in general they belong to a larger Hilbert space, known as the Fock space $\mathcal{F}$, which is the direct sum of N-particle Hilbert spaces for $N = 0, 1, \ldots$, cf. second-quantization [44]. Notably, the density operator approach enables to describe both pure states and mixed states with the same formalism. Using an arbitrary complete basis $\{|s\rangle\}$ of $\mathcal{F}$, one can show the following properties for $\hat{\Gamma}$:

1. Positive semi-definiteness:

$$\langle s|\hat{\Gamma}|s\rangle = \sum_{i}^{N} p_i \left|\langle s|\Psi_i\rangle\right|^2 \geq 0.$$

   Hence, p_i are the eigenvalues of $\hat{\Gamma}$ and they are always ≥ 0;

2. Hermitian symmetry:

$$\overline{\langle s|\hat{\Gamma}|s\rangle} = \sum_{i} \bar{p}_i \overline{\langle s|\Psi_i\rangle \langle \Psi_i|s\rangle} = \sum_{i} p_i \langle s|\Psi_i\rangle \langle \Psi_i|s\rangle = \langle s|\hat{\Gamma}|s\rangle\,;$$

3. Unit trace:

$$\mathrm{Tr}(\hat{\Gamma}) = \sum_{s}\sum_{i} p_i \langle s|\Psi_i\rangle \langle \Psi_i|s\rangle = \sum_{i}\sum_{s} p_i \langle \Psi_i|s\rangle \langle s|\Psi_i\rangle = \sum_{i} p_i = 1;$$

When the system is in the i-th pure state, $p_i = 1$ and $p_j = 0, \forall j \neq i$. We denote the density operator for pure states $\hat{\rho_{\mathrm{N}}} = |\Psi_{\mathrm{N}}\rangle \langle \Psi_{\mathrm{N}}|$, to distinguish it from the more general *ensemble* operator. Hence, for pure states, the density operator is a (rank one) projection, therefore idempotent

$$\hat{\rho}_{\mathrm{N}}^2 = \hat{\rho}_{\mathrm{N}}\hat{\rho}_{\mathrm{N}} = |\Psi_{\mathrm{N}}\rangle \langle \Psi_{\mathrm{N}}|\Psi_{\mathrm{N}}\rangle \langle \Psi_{\mathrm{N}}| = |\Psi_{\mathrm{N}}\rangle \langle \Psi_{\mathrm{N}}| = \hat{\rho}_{\mathrm{N}}. \tag{1.15}$$

This automatically enforces the eigenvalues to be either 1 or 0. We have stressed the fact that $\hat{\rho_N}$ and $|\Psi_N\rangle$ belong to the same N-particle Hilbert space, while $\hat{\Gamma}$ in general does not. The $\hat{\rho_N}$ holds the same amount of information of $|\Psi_N\rangle$. The more general *ensemble* density operator lacks the idempotency requirement, i.e. $\hat{\Gamma} \neq \hat{\Gamma}^2$.

The expectation value of an observable, for a system in a mixed state, is the statistical average of all the possible pure-state expectation values belonging to the ensemble

$$\begin{aligned}
\langle \hat{A} \rangle \equiv \sum_{i} p_i \langle \hat{A} \rangle_i &= \sum_{i} p_i \langle \Psi_i|\hat{A}|\Psi_i\rangle = \sum_{s}\sum_{i} p_i \langle \Psi_i|\hat{A}|s\rangle \langle s|\Psi_i\rangle \\
&= \sum_{s}\sum_{i} p_i \langle s|\Psi_i\rangle \langle \Psi_i|\hat{A}|s\rangle = \sum_{s} \langle s|\hat{\Gamma}\hat{A}|s\rangle \\
&= \mathrm{Tr}(\hat{\Gamma}\hat{A}).
\end{aligned} \tag{1.16}$$

A similar equation can be written for the density operator $\hat{\rho}_{\mathrm{N}}$

$$\langle \hat{A} \rangle = \langle \Psi_{\mathrm{N}}|\hat{A}|\Psi_{\mathrm{N}}\rangle = \mathrm{tr}(\hat{\rho}_{\mathrm{N}}\hat{A}), \tag{1.17}$$

We have adopt the convention for the trace of operators belonging to different spaces

given in Ref. 59. From the time-dependent Schrödinger equation for the state function, we can derive the equation for the time evolution of the N-particle density operator

$$\partial_t \hat{\rho}_{\mathrm{N}} = -\frac{i}{\hbar}\left[\hat{H}_{\mathrm{N}}, \hat{\rho}_{\mathrm{N}}\right], \tag{1.18}$$

For a stationary state, $\hat{\rho}_{\mathrm{N}}$ is independent of time and it commutes with the Hamiltonian.

1.4 The variational principle

In Sec. (1.2), we have shown that the energy eigenstates of a time-independent system can be found by solving the TISE (1.7). The expectation value E of an arbitrary normalised state $|\Psi\rangle$ with Hamiltonian $\hat{H}$ is given by

$$E = \langle \hat{H} \rangle = \langle \Psi | \hat{H} | \Psi \rangle = \sum_n |c_n|^2 E_n, \tag{1.19}$$

where we have used the completeness property of the energy eigenstates. The variational principle states that the Hamiltonian is bounded from below, with the lowest energy value E_0 known as the ground state energy and the associated state vector, the ground state vector $|\Psi_0\rangle = |E_0\rangle$. Any other state $|\Phi\rangle$ which is not the ground state will result in a higher expectation energy

$$E = \langle \Phi | \hat{H} | \Phi \rangle = \sum_n |c_n|^2 E_n \geq \sum_n |c_n|^2 E_0 = \langle \Psi_0 | \hat{H} | \Psi_0 \rangle = E_0. \tag{1.20}$$

Interestingly, the TISE can be cast as a variational problem[66]. To do that, we need to consider the expectation value of the Hamiltonian $E = \langle \hat{H} \rangle = \langle \Psi | \hat{H} | \Psi \rangle$, which is a functional of the state vector $|\Psi\rangle$, i.e. $E[|\Psi\rangle]$. The first variation of E reads

$$\delta E[|\Psi\rangle] = E[|\Psi + \delta\Psi\rangle] - E[|\Psi\rangle] = \langle \Psi + \delta\Psi | \hat{H} | \Psi + \delta\Psi \rangle - \langle \Psi | \hat{H} | \Psi \rangle, \tag{1.21}$$

where $|\delta\Psi\rangle$ represents a variation of the state-vector and we have assumed normalised states. Expanding (1.21) and neglecting terms that are second-order or higher in $|\delta\Psi\rangle$ we find

$$\langle \delta\Psi | \hat{H} - E | \Psi \rangle + c.c., \tag{1.22}$$

where $c.c.$ stays for complex conjugate. From (1.22) we can see that $E[|\Psi\rangle]$ is stationary, i.e. $\delta[E] = 0$, if $|\Psi\rangle$ is an auto-state of the Hamiltonian

$$\delta E[|\Psi\rangle] = 0 \iff (\hat{H} - E)|\Psi\rangle = 0. \tag{1.23}$$

This shows that the TISE and the variational principle are essentially equivalent.

1.5 The Hellmann-Feynman theorem

If the system depends on a parameter, say λ, we can compute the effect of an infinitesimal change in λ on the energy, i.e. the conjugate force, as

$$\frac{\mathrm{d}E[|\Psi_\lambda\rangle]}{\mathrm{d}\lambda} = \frac{\partial E[|\Psi_\lambda\rangle]}{\partial\lambda} + \frac{\delta E[|\Psi_\lambda\rangle]}{|\delta\Psi\rangle}\Big|_{|\Psi\rangle=|\Psi_\lambda\rangle} \frac{\mathrm{d}\,|\Psi_\lambda\rangle}{\mathrm{d}\lambda}. \tag{1.24}$$

At the ground state, the energy E is extremal with respect to all possible variations of the state vector $|\delta\Psi\rangle$, hence also to $\frac{\mathrm{d}|\Psi_\lambda\rangle}{\mathrm{d}\lambda}\delta\lambda$, cf. Sec. 1.4. Consequently, the second term on the r.h.s. of (1.24) vanishes. The only non-zero term arises from the explicit dependence of the energy functional on λ:

$$\begin{aligned}
\frac{\partial E}{\partial\lambda} &= \left\langle \frac{\partial\Psi_\lambda}{\partial\lambda}\middle|\hat{H}_\lambda\middle|\Psi_\lambda\right\rangle + \left\langle\Psi_\lambda\middle|\frac{\partial\hat{H}_\lambda}{\partial\lambda}\middle|\Psi_\lambda\right\rangle + \left\langle\Psi_\lambda\middle|\hat{H}_\lambda\middle|\frac{\partial\Psi_\lambda}{\partial\lambda}\right\rangle \\
&= E\left(\left\langle\frac{\partial\Psi_\lambda}{\partial\lambda}\middle|\Psi_\lambda\right\rangle + \left\langle\Psi_\lambda\middle|\frac{\partial\Psi_\lambda}{\partial\lambda}\right\rangle\right) + \left\langle\Psi_\lambda\middle|\frac{\partial\hat{H}_\lambda}{\partial\lambda}\middle|\Psi_\lambda\right\rangle \\
&= E\frac{\partial}{\partial\lambda}\langle\Psi_\lambda\,|\,\Psi_\lambda\rangle + \left\langle\Psi_\lambda\middle|\frac{\partial\hat{H}_\lambda}{\partial\lambda}\middle|\Psi_\lambda\right\rangle \\
&= \left\langle\Psi_\lambda\middle|\frac{\partial\hat{H}_\lambda}{\partial\lambda}\middle|\Psi_\lambda\right\rangle,
\end{aligned} \tag{1.25}$$

where on the second line we have made use of the fact that $|\Psi_\lambda\rangle$ is a solution of the Schrödinger equation. The relation in (1.25) is known as the "Hellmann-Feynman" theorem[67, 68], although previous versions of (1.25), from Pauli, Schrödinger, Born & Fock and Güttinger had appeared in the literature. It states that in order to compute the derivative of the energy with respect to a parameter, the derivative of the wave-function is not required. If the parameter is one of the atomic positions, $\mathbf{R}_I$ say, we find the force $\mathbf{F}_I$ on the Ith atom to be

$$\mathbf{F}_I = -\frac{\mathrm{d}E}{\mathrm{d}\mathbf{R}_I} = -\left\langle\Psi\middle|\frac{\partial\hat{H}}{\partial\mathbf{R}_I}\middle|\Psi\right\rangle. \tag{1.26}$$

Care has to be taken when dealing with derivatives of operators with respect to a parameter, since the validity of the theorem relies on the way derivatives are defined and whether the domain[69] of the operator depends on the parameter itself[7]. In general, the

[7] In particular one needs to specify the topology to adopt on the space of linear operator on $\mathcal{H}$.

theorem is valid not only for the exact wave-function but also for variationally obtained wave-functions. However, if the $|\Psi_\lambda\rangle$ is not a perfect eigenstate of the Hamiltonian or it is expanded in a basis set whose functions depends on the parameter, other terms must be considered on the r.h.s. of (1.24) in order for the equation to hold. In particular, in the case of a finite basis set $\{\psi_i(\mathbf{r};\mathbf{R}_I)\}$ with functions centred on nuclei, a change in the nuclear positions, e.g. $\mathbf{R}_I + \mathrm{d}\mathbf{R}_I$ causes the corresponding basis functions also to be shifted, $\psi_i(\mathbf{r};\mathbf{R}_I + \mathrm{d}\mathbf{R}_I) = \psi_i(\mathbf{r};\mathbf{R}_I) + \delta\psi_i \mathrm{d}\mathbf{R}_I$. In general, it is not guaranteed that the variation $\delta\psi_i$ in the basis function caused by such shift in the nuclear position could be expanded in the original finite basis set.

1.6 The molecular Hamiltonian

Evidently, the Hamiltonian operator plays a fundamental role in QC. For a molecular system, with non-relativistic interactions, the Hamiltonian in the position representation takes on the form

$$\hat{H} = -\frac{1}{2}\sum_i \nabla_i^2 - \sum_I \frac{1}{2M_I}\nabla_I^2 - \sum_i \sum_I \frac{Z_I}{|\mathbf{r}_i - \mathbf{R}_I|} + \frac{1}{2}\sum_{I\neq J}\frac{Z_I Z_J}{R_{IJ}} + \frac{1}{2}\sum_{i\neq j}\frac{1}{r_{ij}}, \tag{1.27}$$

where the index i runs over all the electrons and the index I over all the nuclei, M_I and Z_I are the mass and the charge of nucleus I, $R_{IJ} = |\mathbf{R}_I - \mathbf{R}_J|$ and $r_{ij} = |\mathbf{r}_i - \mathbf{r}_j|$. The first two terms on the r.h.s. of (1.27) are the kinetic energy operators for the electrons and nuclei, respectively. The remaining three terms are the Coulomb potential operators describing the attractive electron-nucleus interaction and the repulsive nucleus-nucleus interaction and electron-electron interaction, respectively. Here, we are tacitly assuming that pair potentials are sufficient to describe the interactions (no N-body potential). In (1.27) we have used the so-called atomic units (a.u.). According to the a.u. convention, the elementary charge, the reduced Planck's constant, the mass of electrons and Coulomb constant are all set equal to 1, i.e. $e = \hbar = m_e = (4\pi\epsilon_0)^{-1} = 1$. Distances are measured in bohr $a_0 = 5.29177249 \times 10^{-11}$ m , energies in hartrees $E_h = 4.35974417 \times 10^{-18}$ J and times in atomic units of time (aut) = $\hbar/\ E_h$= $2.418884326 \times 10^{-17}$ s . The Hamiltonian in (1.27) does not contain any spin-dependent term (weak spin-spin and spin-orbit interactions are neglected), thereby it commutes with the total spin operator. Relativistic terms can be introduced as corrections in an *ad hoc* fashion.

1.7 The Born-Oppenheimer approximation

As aforementioned, many studies in QC deal with the non-relativistic TISE. In particular, one is primarily concerned with the behaviour of electrons, since the majority of chemical phenomena involves changes in the electron cloud only, whereas the inner structure of nuclei is unaffected. In QC nuclei are usually seen as the source of electric (and magnetic for NMR) fields, but play virtually no other role. Hence a very good approximation is to neglect their quantum nature and instead treat them as classical point-charge particles[8]. The Born-Oppenheimer (BO) approximation[31] is a method to partially separate the electronic degrees of freedom from the nuclear ones. By applying the BO approximation to the TISE two coupled equations are obtained: the electronic TISE and the nuclear TISE. In practice, after the BO approximation one takes the classical limit for the nuclear TISE. Pictorially, the BO separation can be understood in terms of relative masses and momenta of electrons and nuclei. In fact, on average the mass of an atomic nucleus is $10^3 - 10^4$ times larger than the mass of an electron. The forces acting on electrons and nuclei are of the same magnitude. Consequently, the change in their momenta can be assumed to be of the same magnitude. Accordingly, since nuclei are much heavier than electrons their velocities are smaller. One often says that electrons react instantaneously to the motion of the nuclear field or that at a given instant, electrons *see* the instantaneous positions of the nuclei, whereas the nuclei only *see* an averaged electron distribution. The BO ansatz for the total wave-function $\Psi(\{\mathbf{r}_i\},\{\mathbf{R}_I\}) = \langle\{\mathbf{r}_i\},\{\mathbf{R}_I\}|\Psi\rangle$ is

$$\Psi(\{\mathbf{r}_i\},\{\mathbf{R}_I\}) \approx \sum_{s=0}^{\infty} \Phi_s(\{\mathbf{r}_i\};\{\mathbf{R}_I\})\chi_s(\{\mathbf{R}_I\}), \tag{1.28}$$

where $\Phi_s(\{\mathbf{r}_i\};\{\mathbf{R}_I\})$, called the electronic wave-function, depends directly on the positions of the all electrons and parametrically on the positions of all nuclei, whereas $\chi_s(\{\mathbf{R}_I\})$ is called the nuclear wave-function, and is a function of the latter only. BO separation dictates that the two wave-functions individually satisfy Schrödinger-like equations:

$$\hat{H}_{\text{elec}}\Phi_s(\{\mathbf{r}_i\};\{\mathbf{R}_I\}) = \epsilon_s(\{\mathbf{R}_I\})\Phi_s(\{\mathbf{r}_i\};\{\mathbf{R}_I\}); \tag{1.29}$$

$$\hat{H}_{\text{nuc}}\chi_s(\{\mathbf{R}_I\}) = E_s\chi_s(\{\mathbf{R}_I\}), \tag{1.30}$$

[8] A notable exception are proton transfers, which need a full quantum description of electrons and nuclei.

where

$$\hat{H}_{\text{elec}} = -\frac{1}{2}\sum_i \nabla_i^2 - \sum_i \sum_I \frac{Z_I}{|\mathbf{r}_i - \mathbf{R}_I|} + \frac{1}{2}\sum_{I\neq J}\frac{Z_I Z_J}{R_{IJ}} + \frac{1}{2}\sum_{i\neq j}\frac{1}{r_{ij}}, \tag{1.31}$$

is the electronic Hamiltonian and (1.29) is called the electronic TISE, whereas

$$\hat{H}_{\text{nuc}} = -\sum_I \frac{1}{2M_I}\nabla_I^2 + \epsilon(\{\mathbf{R}_I\}), \tag{1.32}$$

is the nuclear Hamiltonian and (1.30) is called the nuclear TISE. The function $\epsilon(\{\mathbf{R}\})$ is the BO potential energy surface (PES) generated by the electrons for a fixed array of nuclei and plays the role of the potential in which the nuclei move. The energy E is the eigenvalue of the molecular Hamiltonian (1.27). It is straightforward to see that the BO approximation is equivalent to considering the ansatz in (1.28) and neglect terms in the Hamiltonian containing derivatives of the electronic wave-function with respect to the nuclear positions. In fact, applying the molecular Hamiltonian (1.27) to (1.28), yields

$$\begin{aligned} - & \frac{1}{2}\chi_s \sum_i \nabla_i^2 \Phi_s - \sum_I \frac{1}{2M_I}\nabla_I^2 \Phi_s \chi_s - \sum_i \sum_I Z_I \frac{\Phi_s \chi_s}{|\mathbf{r}_i - \mathbf{R}_I|} \\ + & \chi_s \frac{1}{2}\sum_{i\neq j}\frac{\Phi_s}{r_{ij}} + \frac{1}{2}\sum_{I\neq J} Z_I Z_J \frac{\Phi_s \chi_s}{R_{IJ}}, \end{aligned} \tag{1.33}$$

where for the sake of clarity we have dropped the explicit dependence of the wave-functions on the electron and nuclear positions. The second term on the r.h.s. of (1.34) involves derivatives of the the electronic wave-function with respect to nuclear positions. By expanding this term we find

$$\sum_I \frac{1}{2M_I}\nabla_I^2 \Phi_s \chi_s = \sum_I \frac{1}{2M_I}\left[\chi_s \nabla_I^2 \Phi_s + \Phi_s \nabla_I^2 \chi_s + 2\nabla_I \Phi_s \nabla_I \chi_s\right], \tag{1.34}$$

neglecting the terms involving derivatives of Φ_s with respect to nuclear positions, i.e. $\nabla_I \Phi_s / 2M_I$ and $\nabla_I^2 \Phi_s / 2M_I$, the only term surviving is $\Phi_s \nabla_I^2 \chi_s / 2M_I$. The (1.34) becomes

$$\hat{H}\Phi_s\chi_s \approx \Phi_s\left(-\sum_I \frac{1}{2M_I}\nabla_I^2 \chi_s\right) + \chi_s \hat{H}_{\text{elec}}\Phi_s = E\Phi_s\chi_s, \tag{1.35}$$

which is equivalent to (1.29)-(1.30), assuming the electronic wave-function to be normalised

$$\int d\mathbf{r}_1 \ldots d\mathbf{r}_N \, \Phi_s^* \Phi_{s'} = \delta_{s,s'} \quad \text{and} \quad \epsilon_s(\{\mathbf{R}_I\}) = \int d\mathbf{r}_1 \ldots d\mathbf{r}_N \, \Phi_s^* \hat{H}_{\text{elec}} \Phi_s, \tag{1.36}$$

and the coupling terms to be zero

$$\begin{aligned} C_{ss'} &= -\sum_I \frac{1}{2M_I} \int \mathrm{d}\mathbf{r}_1 \ldots \mathrm{d}\mathbf{r}_N \, \Phi_s^* \nabla_I^2 \Phi_{s'} \\ &\quad - \sum_I \frac{1}{M_I} \left(\int \mathrm{d}\mathbf{r}_1 \ldots \mathrm{d}\mathbf{r}_N \, \Phi_s^* \nabla_I \Phi_{s'} \right) \nabla_I = 0. \end{aligned} \tag{1.37}$$

The rationale for neglecting the coupling terms is the following: we admit the electronic wave-function to strongly depend on the nuclear positions, so that the derivatives $\nabla_I \Phi$ have magnitudes comparable to $\nabla_i \Phi$. However, as mentioned above, the mass of the nuclei is much larger than the mass of the electrons, which makes these terms negligible in most cases. A more accurate approximation is to retain the diagonal part of the coupling terms:

$$C_{ss} = -\sum_I \frac{1}{2M_I} \left[\int \mathrm{d}\mathbf{r}_1 \ldots \mathrm{d}\mathbf{r}_N \, \Phi_s^* \nabla_I^2 \Phi_s + \left(\int \mathrm{d}\mathbf{r}_1 \ldots \mathrm{d}\mathbf{r}_N \, \Phi_s^* \nabla_I \Phi_s \right) \nabla_I \right], \tag{1.38}$$

where the second term can be shown to be zero from the requirement that Φ_s are normalised. This is sometimes called the "adiabatic" approximation. Both approximations are useful to describe systems that undergo an adiabatic processes, i.e. systems whose electrons remain in a given s state (usually the ground state) of the corresponding evolving Hamiltonian. The wave-function Ψ and the energy may change during the process, but the electrons do not change state. This approximation works quite well, as long as no degeneracy or near degeneracy between electronic states is encountered, i.e. when the energy of the electronic state in which the electrons are and any other state is well separated and higher than the average energy of thermal fluctuations. We can therefore approximate the total wave-function by a simple direct product as

$$\Psi(\{\mathbf{r}_i\}, \{\mathbf{R}_I\}) \approx \Phi_s(\{\mathbf{r}_i\}; \{\mathbf{R}_I\}) \chi_s(\{\mathbf{R}_I\}), \tag{1.39}$$

The off-diagonal states, that couple different electronic states, need to be explicitly computed in "diabatic" processes and for electron-phonon interactions. In these cases, the electrons can transit from one state to another, the latter being a different eigenstates of the evolving Hamiltonian, e.g. vertical transitions.

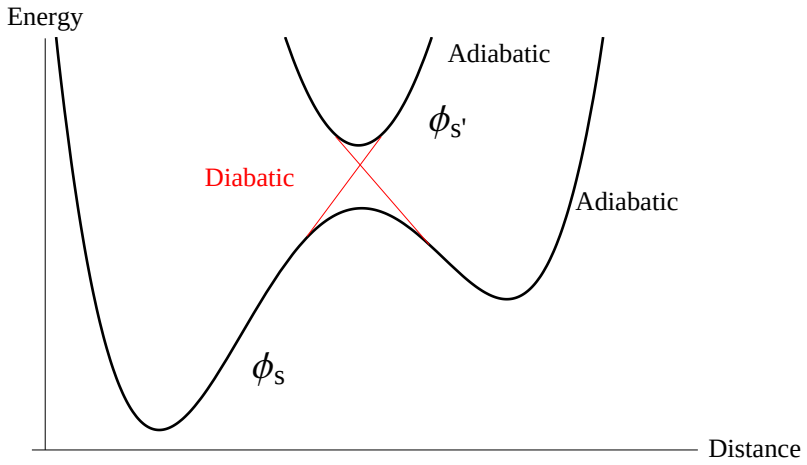

Figure 1.1: Sketch of the difference between an adiabatic process (black surfaces) and a non-adiabatic process (red surface).

1.8 Overview of wave-function methods

One of the first effort to reduce the complexity of the many-electron problem was put forward by Hartree, Fock, Brillouin and Slater, readily after the renowned Schrödinger 1926 paper. Nowadays, this method is knwon as Hartree-Fock method[70–73], which introduces the concept of single-electron molecular orbitals $\psi_i(\mathbf{x})$ in a mean-field, where $\mathbf{x} = \{s, \mathbf{r}\}$ is a vector containing both spin and spatial coordinates. The *ansatz* for the antisymmetric N-electron wave-function is constructed from a Slater determinant of the single-electron orbitals[72] $\psi_i(\mathbf{x}_j)$

$$\Psi(\mathbf{x}_1, \cdots, \mathbf{x}_N) = \frac{1}{\sqrt{N!}} \det \begin{pmatrix} \psi_1(\mathbf{x}_1) & \cdots & \psi_1(\mathbf{x}_N) \\ \vdots & \ddots & \vdots \\ \psi_N(\mathbf{x}_1) & \cdots & \psi_N(\mathbf{x}_N) \end{pmatrix} \tag{1.40}$$

where $\frac{1}{\sqrt{N!}}$ is a normalisation factor. The antisymmetry of the wave-function is guaranteed by the properties of determinants. The expectation value of the total electronic energy, i.e. $\langle \Psi | \hat{H}_{\text{elec}} | \Psi \rangle$, is then minimised with respect to all the degrees of freedom in the ψ's subject to the orthonormalisation constraints, i.e. $\langle \psi_i(\mathbf{x}) | \psi_j(\mathbf{x}') \rangle = \delta_{ss'}\delta_{ij}$. From this minimisation

process the Hartree-Fock (HF) equations are found[58]

$$\begin{aligned}\hat{f}(\mathbf{r})\psi_i(\mathbf{r}) &= \left[-\frac{1}{2}\nabla^2 - \sum_I \frac{Z_I}{|\mathbf{R}_I - \mathbf{r}|} + 2\sum_j^{N/2}\int d\mathbf{r}' \frac{|\psi_j(\mathbf{r}')|^2}{|\mathbf{r}-\mathbf{r}'|}\right]\psi_i(\mathbf{r}) \\ &\quad - \sum_j^{N/2}\int d\mathbf{r}' \frac{\psi_j^*(\mathbf{r}')\psi_i(\mathbf{r}')}{|\mathbf{r}-\mathbf{r}'|}\psi_j(\mathbf{r}) \\ &= \varepsilon_i\psi_i(\mathbf{r}),\end{aligned} \tag{1.41}$$

where $\hat{f}(\mathbf{r})$ is the so-called Fock operator and we have have assumed a closed-shell system[9]. The closed-shell Fock operator in (1.41) thus take the form

$$\hat{f}(\mathbf{r}) = \hat{h}(\mathbf{r}) + \sum_j \left[2\hat{J}_j(\mathbf{r}) - \hat{K}_j(\mathbf{r})\right], \tag{1.42}$$

where $\hat{h}(\mathbf{r}) = -\frac{1}{2}\nabla^2 - \sum_I \frac{Z_I}{|\mathbf{R}_I-\mathbf{r}|}$ is called the single particle core Hamiltonian and is orbital-independent. The operator $\hat{J}_j(\mathbf{r})$, whose action on an orbital $\psi_i(\mathbf{r})$ is given by

$$\hat{J}_j(\mathbf{r})\psi_i(\mathbf{r}) = \int d\mathbf{r}' \frac{|\psi_j(\mathbf{r}')|^2}{|\mathbf{r}-\mathbf{r}'|}\psi_i(\mathbf{r}), \tag{1.43}$$

is knwon as the Coulomb operator. The expectation value $\left\langle \hat{J} \right\rangle$ returns the classical electrostatic energy of two charge densities. Finally, the operator $\hat{K}_j(\mathbf{r})$, whose action on an orbital $\psi_i(\mathbf{r})$ is given by

$$\hat{K}_j(\mathbf{r})\psi_i(\mathbf{r}) = \int d\mathbf{r}' \frac{\psi_j^*(\mathbf{r}')\psi_i(\mathbf{r}')}{|\mathbf{r}-\mathbf{r}'|}\psi_j(\mathbf{r}) = \int d\mathbf{r}' \frac{\psi_j^*(\mathbf{r}')\hat{\Pi}_{ij}\psi_j(\mathbf{r}')\psi_i(\mathbf{r})}{|\mathbf{r}-\mathbf{r}'|}, \tag{1.44}$$

is a purely quantum mechanical operator that has no classical counterpart. The operator $\hat{\Pi}_{ij}$ is a permutation operator. It arises as a consequence of the antisymmetry of the electron wave-function. The major drawback of the HF method is that only correlation between parallel spin orbitals is taken into account[58], while other kind of correlations (static or dynamic) are ignored.

Post-Hartree-Fock methods refine the description of the quantum system by including an explicit treatment of the electron correlation, which in general is achieved by adding more determinants to the HF wave-function. Successful approaches include Møller-Plesset (MP) perturbation theory[74], coupled cluster [75], configuration interaction (CI)[76], and multi-configurational self-consistent field (MCSCF) approaches such as

[9] Extension to open-shell systems is straightforward[58]

CASSCF [77, 78].

Chapter 2

Density functional theory

Density Functional Theory (DFT) is an alternative, yet equivalent, *ab initio* method, which describes the state of a system of fully interacting electrons through the electronic charge density function $n(\mathbf{r})$, which is a much simpler function compared to the complex many-body wave function Ψ encountered in the previous chapter. Hence, for a system of N electrons the resulting complexity of the problem is, in principle, greatly reduced as one needs to deal with a function of only 3 spatial coordinates. The first model adopting the electron density function to describe the properties of molecules and materials was the so-called Thomas-Fermi model[79–81]. However, in this model severe approximations were introduced which made it unfit to describe the quantum nature of materials. Notably, the major drawback of the model was its incapability of producing the electronic shell structure of an atom[82]. A rigorous derivation showing the importance of the electronic charge density to describe the properties of the electronic ground state came much later thanks to Hohenberg and Kohn (HK) in 1964[12], today known as density functional theory. The popularity of this new theory, is mainly due to the approach proposed by Kohn and Sham (KS) in the 1965[13], although different approaches exist, notably orbital free DFT[83]. In their epoch-making article, Kohn and Sham designed an operational scheme for making real calculations feasible from the theory developed the year before. Subsequent theoretical developments, improvements in numerical methods and the advent of modern computers have made DFT-based programs the most used tool in computational chemistry and computational material science. Plane-waves DFT is the conventional implemented route, as the level of accuracy, i.e. the number of plane waves used to describe the electronic density, can be tuned by a single parameter (the kinetic energy cut-off). Moreover, plane-waves provide a natural basis in which to expand electronic states subject to periodic boundary conditions. Thanks to highly optimised algorithms, in conventional DFT programs the number of computations asymptotically

increase as the third power of the number of atoms in the system[1] [84], giving one of the best accuracy *vs.* computational cost trade-off amongst *ab initio* methods. However, this still represents a bottle-neck for the study of very large systems ($N_{\text{at}} > 500$). As mentioned in the introduction section, this is the main reason that led to the development of new methods showing a more favourable scaling while maintaining the same level of accuracy. Linear-scaling DFT (LS-DFT) programs[18–21] are a clear result of this effort.

The core ideas of conventional DFT and linear scaling DFT and their implementation in actual computer codes, are the subject of this chapter. In Sec. 2.1 the original HK theorems are presented. Sec. 2.2 deals with the Kohn-Sham mapping and its implementation using plane-waves as basis set. A general discussion on periodic boundary conditions, Bloch states and Wannier functions is the subject of Sec. 2.3. Finally, in Sec. 2.4 the fundamental ideas behind linear-scaling methods are presented, e.g. nearsightedness of electronic matter, localised orbitals and sparse algebra. An overview of the ONETEP implementation is also given.

2.1 The Hohenberg and Kohn theorems

Hohenberg and Kohn key idea is that any physical observables, such as the total energy, may be defined as a *functional*[2] of the ground state electronic density[3]: $F[n_0(\mathbf{r})]$. The density is a scalar function of position (and spin for spin-polarised systems), and it contains the same information enclosed in the many-body electronic wave functions for the ground state and all the excited states[4]. This is true regardless of the system's size. Congruently, we are not describing the system through a function Ψ of $(3+1)N$ coordinates, but through a scalar function n of only $3+1$ co-ordinates.

As a consequence of the BO approximation, the TISE may be rewritten as:

$$\hat{H}\,|\Psi\rangle = (\hat{F} + \hat{V}_{\text{ext}})\,|\Psi\rangle = E\,|\Psi\rangle\,, \tag{2.1}$$

where $\hat{F}$ is a universal operator, equal for all systems consisting of interacting electrons and given by

$$\hat{F} = -\frac{1}{2}\sum_i \nabla_i^2 + \frac{1}{2}\sum_{i\neq j}\frac{1}{r_{ij}}.$$

[1] The $O\left(N^3\right)$ law is largely due to the diagonalisation of the Hamiltonian matrix, performed during SCF procedure for solving the Kohn-Sham equations.

[2] A functional is a map (or a function) from an arbitrary complex space to the real numbers: $F(\cdot) : \mathbb{C}^n \mapsto \mathbb{R}$. The notion of functional then, naturally extends the notion of a function.

[3] The state with the lowest energy.

[4] However, theoretical developments to extract excited state properties from the ground state density are still ongoing, with time-dependent density functional theory (TDDFT) as a possible route.

The $\hat{V}_{\text{ext}}$ represents the external potential operator, where in the case of no external fields, reduces simply to the Coulomb potential operator due to the static array of nuclei. This partition of the electronic Hamiltonian shows that, once the number of electrons N and the external potential $V_{\text{ext}}(\mathbf{r})$ are known, the problem is completely specified. Formally, the ground state electronic density can be written as

$$\begin{aligned} n_0(\mathbf{r}) &= \langle \Psi_0 | \hat{n} | \Psi_0 \rangle \\ &= N \int \dots \int \mathrm{d}\mathbf{r}_2 \mathrm{d}\mathbf{r}_3 \dots \mathrm{d}\mathbf{r}_N \, \Psi_0^*(\mathbf{r}, \mathbf{r}_2, \dots, \mathbf{r}_N) \Psi_0(\mathbf{r}, \mathbf{r}_2, \dots, \mathbf{r}_N), \end{aligned} \tag{2.2}$$

where N is the number of electrons, and $\Psi_0(\mathbf{r}, \mathbf{r}_2, \dots, \mathbf{r}_N)$ is the ground state wave-function in the position representation. Hereafter, the dependence on spin is omitted for sake of simplicity. In (2.2) we have exploited the antisymmetry property of the fermionic wave-functions. The density operator $\hat{n}(\mathbf{r})$ is defined as

$$\hat{n}(\mathbf{r}) = \sum_i^{N_{\text{el}}} \delta(\mathbf{r} - \mathbf{r}_i), \tag{2.3}$$

$n_0(\mathbf{r})$ is a positive semi-definite function, satisfying the normalisation condition

$$\int \mathrm{d}\mathbf{r} \, n_0(\mathbf{r}) = N. \tag{2.4}$$

The first HK theorem states that for any system of interacting electrons, in a given external potential $V_{\text{ext}}(\mathbf{r})$, there exists a one-to-one mapping between the ground state electronic density $n_0(\mathbf{r})$ and the given external potential. More precisely, for the non-degenerate case, the ground state density uniquely determines the external potential, i.e. $V_{\text{ext}}(\mathbf{r})$ is a unique functional of the density.

Once the external potential is defined, the Hamiltonian is also uniquely determined. To see this, it sufficient to show that a unique functional $F[n(\mathbf{r})]$ exists. Given $V_{\text{ext}}(\mathbf{r})$ we solve the TISE to find the ground state wave-function Ψ_0, from which a ground state density function is generated through (2.2). Density functions generated with this procedure belong to the class of $v-$representable densities. For all these densities, we may define the functional $F[n(\mathbf{r})] = \langle \Psi | \hat{F} | \Psi \rangle$. Since $n(\mathbf{r})$ determines the number of electrons N, which in turn determines the $\hat{F}$ and the external potential, which in turn determines $|\Psi\rangle$ through (1.7), it follows that $F[n(\mathbf{r})]$ is unique. When the ground state is degenerate, the theorem is no longer valid.

The proof of the theorem is given by contradiction (*reductio ad absurdum*). We assume

there exist two potentials $V_{\text{ext}}^{(1)}(\mathbf{r})$ and $V_{\text{ext}}^{(2)}(\mathbf{r})$, that differ by more than a constant, leading to two different Hamiltonians $\hat{H}^{(1)}$ and $\hat{H}^{(2)}$, with different ground state wave-functions $|\Psi_0^{(1)}\rangle$ e $|\Psi_0^{(2)}\rangle$. We are also assuming that both wave-functions generate the same density $n(\mathbf{r})$. According to the variational principle of Sec. 1.4 we have

$$E^{(1)} = \langle \Psi_0^{(1)} | \hat{H}^{(1)} | \Psi_0^{(1)} \rangle < \langle \Psi_0^{(2)} | \hat{H}^{(1)} | \Psi_0^{(2)} \rangle \,, \tag{2.5}$$

where the inequality strictly holds as long as the states are non-degenerate, which is what it is assumed here. The second term in (2.5) may be rearranged as

$$\begin{aligned} \langle \Psi_0^{(2)} | \hat{H}^{(1)} | \Psi_0^{(2)} \rangle &= \langle \Psi_0^{(2)} | \hat{H}^{(2)} | \Psi_0^{(2)} \rangle + \langle \Psi_0^{(2)} | \hat{H}^{(1)} - \hat{H}^{(2)} | \Psi_0^{(2)} \rangle \\ &= E^{(2)} + \int \mathrm{d}\mathbf{r} \, \left[V_{\text{ext}}^{(1)}(\mathbf{r}) - V_{\text{ext}}^{(2)}(\mathbf{r}) \right] n_0(\mathbf{r}), \end{aligned} \tag{2.6}$$

so that

$$E^{(1)} = E^{(2)} + \int \mathrm{d}\mathbf{r} \, \left[V_{\text{ext}}^{(1)}(\mathbf{r}) - V_{\text{ext}}^{(2)}(\mathbf{r}) \right] n_0(\mathbf{r}). \tag{2.7}$$

Analogously, we may consider $E^{(2)}$ instead of $E^{(1)}$ and find an equivalent equation to (2.7) but with the indices (1) and (2) interchanged

$$E^{(2)} = E^{(1)} + \int \mathrm{d}\mathbf{r} \, \left[V_{\text{ext}}^{(2)}(\mathbf{r}) - V_{\text{ext}}^{(1)}(\mathbf{r}) \right] n_0(\mathbf{r}). \tag{2.8}$$

Adding up (2.7) and (2.8) yields

$$E^{(1)} + E^{(2)} < E^{(1)} + E^{(2)}, \tag{2.9}$$

which is clearly a contradiction, hence proving the theorem. Consequently, the density function uniquely determines the external potential up to a constant. This theorem however does not give us any information on how to solve the full-interacting many-body problem.

The second HK theorem addresses the problem of how to find the ground state density. In particular, it states that given an external potential, $E[n]$ is a universal functional of the density. For each $V_{\text{ext}}(\mathbf{r})$ the exact ground state energy is the absolute minimum of the energy functional and the density that minimises $E[n]$ is the ground state density $n_0(\mathbf{r})$, i.e.

$$\arg\min_{n(\mathbf{r})} E[n(\mathbf{r})] = n_0(\mathbf{r}).$$

$$\hat{V}_{\text{ext}} \in \mathcal{V} \mapsto |\Psi_0\rangle \in \mathcal{H}^{\text{A}} \mapsto n(\mathbf{r}_0) \in \mathcal{N}_{\mathcal{V}}.$$

The proof of the second HK theorem starts with defining the following energy functional for a given external potential

$$\begin{aligned} E_{\mathrm{HK}}[n] &= T[n] + E_{\mathrm{int}}[n] + \int \mathrm{d}\mathbf{r}\, V_{\mathrm{ext}}(\mathbf{r}) n(\mathbf{r}) \\ &\equiv F_{\mathrm{HK}}[n] + \int \mathrm{d}\mathbf{r}\, V_{\mathrm{ext}}(\mathbf{r}) n(\mathbf{r}). \end{aligned} \tag{2.10}$$

The functional $F_{\mathrm{HK}}[n]$ will be universal by construction as the kinetic energy and the electron-electron interaction do not depend on the specifics of the system. From the first theorem one can readily find

$$\langle \Psi | \hat{H} | \Psi \rangle = \langle \Psi | \hat{F} + \hat{V}_{\mathrm{ext}} | \Psi \rangle = F_{\mathrm{HK}}[n] + \int \mathrm{d}\mathbf{r}\, V_{\mathrm{ext}}(\mathbf{r}) n(\mathbf{r}) = E_{\mathrm{HK}}[n], \tag{2.11}$$

since $n(\mathbf{r})$ determines $V_{\mathrm{ext}}(\mathbf{r})$, which in turn determines $|\Psi\rangle$. Notably, $E_{\mathrm{HK}}[n] = E_0$ if $|\Psi\rangle = |\Psi_0\rangle$ and correspondingly n is the ground state density for the given potential. If we now consider a different $|\Psi_1\rangle \neq |\Psi_0\rangle$, it follows from the variational principle that

$$E_0 = E_{\mathrm{HK}}[n_0] = \langle \Psi_0 | \hat{H} | \Psi_0 \rangle < \langle \Psi_1 | \hat{H} | \Psi_1 \rangle = E_{\mathrm{HK}}[n_1]. \tag{2.12}$$

Hence, there exists a density, corresponding to the ground state density, for which $E_{\mathrm{HK}}[n]$ is minimum. Unfortunately, the $F_{\mathrm{HK}}[n]$ is not known *a priori* and the theorem only guarantees that such a functional exists, but no indication on its functional form is given. No exact functional is known for any system with more than one electron. This is a direct consequence of the complexity of the interactions of a quantum many-body problem. Furthermore, this theorem only provides information on the ground state density without specifying how an excited state density might be determined.

Mermin[85] has shown that for system in thermal equilibrium an analogue theory may be developed with the grand potential energy functional replacing the HK energy functional and with the density matrix in place of the density function. From this alternative energy functional, equilibrium properties of electrons may be obtained, such as the entropy, the specific heat, etc.

2.1.1 Levy and Lieb derivation

Levy and Lieb[86–88] (LL) followed a different route to obtain the ground state density, which removes the constraint of the HK formulation on the non-degenerate states and also allows for a larger space of possible densities to be considered. The main idea is to take into account all the wave-functions that produce the same density function and to

perform a two-step minimisation procedure. Given a wave-function Ψ, we can write the total energy as

$$E = \langle \Psi | \hat{F} | \Psi \rangle + \int \mathrm{d}\mathbf{r}\, V_{\mathrm{ext}}(\mathbf{r}) n(\mathbf{r}). \tag{2.13}$$

In the first step, the first term on r.h.s. of (2.13) is minimised with respect to all the wave-functions having the same density $n(\mathbf{r})$:

$$F_{\mathrm{LL}}[n] = \min_{\int \mathrm{d}\mathbf{r}_2 \cdots \mathrm{d}\mathbf{r}_N \, |\Psi(\mathbf{r}, \mathbf{r}_2, \cdots, \mathbf{r}_N)|^2 = n(\mathbf{r})} \left[\langle \Psi | \hat{F} | \Psi \rangle \right] = \langle \Psi_{\mathrm{min}} | \hat{F} | \Psi_{\mathrm{min}} \rangle \,. \tag{2.14}$$

Hence, we obtain a unique minimum energy functional for a given density

$$E_{\mathrm{LL}}[n] = F_{\mathrm{LL}}[n] + \int \mathrm{d}\mathbf{r}\, V_{\mathrm{ext}}(\mathbf{r}) n(\mathbf{r}). \tag{2.15}$$

In the second step one minimises the energy functional $E_{\mathrm{LL}}[n]$ in (2.15) with respect to the degrees of freedom in the density and it can be shown that $E_{\mathrm{LL}}[n_0] = E_0$, with n_0 being the ground state density. The LL functional is formally different from the HK functional in (2.10) inasmuch as it is defined for any density function obtainable from an antisymmetric N-body wave-function. This different constraint is known as $N-$representability of the density function and is a much weaker constraint than the $v-$representability. In fact, any "well-behaved" density can be shown to belong to the class of $N-$representable densities[89] while this is not true for $v-$representable densities.

Notably, also the LL formulation does not provide the functional form of $F[n]$ for the N-body problem. Up to date, no exact functional is known and only approximated versions have been developed. For these approximated functionals to be accurate, the major obstacle lies in the description of the electron correlation, which is at the heart of the wide range of quantum phenomena in matter.

2.2 The Kohn and Sham mapping

Soon after the first HK paper, Kohn and Sham (KS) developed a strategy[13] to overcome the difficulties encountered in making the theory useful for calculating properties of real materials. The KS *ansatz* consists in mapping the fully-interacting N-body problem to an auxiliary non-interacting N single-particle problem subject to an effective potential $V_{\mathrm{KS}}(\mathbf{r})$, such as it reproduces the same density of the fully-interacting system. With this approach, we may calculate the properties of many-body systems exactly using independent-particle methods; in practice, this approach has opened the doors to approximate formulations for the functional $F[n]$ that have proved to be very successful in

describing ground state properties of real materials.

In the KS framework, the density is given by

$$n(\mathbf{r}) = \sum_{i=1}^{N_{\text{occ}}} \left|\psi_i^{\text{KS}}(\mathbf{r})\right|^2, \tag{2.16}$$

where the index i runs over the occupied states, and ψ_i^{KS} are the single-particle KS states, solution of the KS equations that we will derived below. For a fully-interacting N-body system we may write

$$F[n] = T[n] + E_{\text{int}}[n], \tag{2.17}$$

where $T[n]$ and $E_{\text{int}}[n]$ are the true kinetic energy and the electron-electron electrostatic interaction energy of the fully-interacting many-body system, respectively. As we mentioned above, these functionals must account for the correlation and exchange effects, but the exact functionality in terms of the density remains largely unknown. Moreover, it can be shown that these functionals are inherently non-local and the functional derivative $\frac{\delta}{\delta n}$ of both $T[n]$ and $E_{\text{int}}[n]$ show discontinuities as the number of electrons takes on integer increments. In the KS approach, $F[n]$ is decomposed into three components

$$F_{\text{KS}}[n] = T_{\text{ind}} + E_H[n] + E_{\text{XC}}[n], \tag{2.18}$$

where T_{ind} and $E_H[n]$ are the kinetic energy and the classical electrostatic interaction energy (Hartree energy) for non-interacting particles, respectively

$$T_{\text{ind}} = -\frac{1}{2}\sum_{i}^{N_{occ}} \int \mathrm{d}\mathbf{r}\, \psi_i^*(\mathbf{r})\nabla^2\psi_i(\mathbf{r}) \tag{2.19}$$

$$E_H[n] = \frac{1}{2}\int \mathrm{d}\mathbf{r}\mathrm{d}\mathbf{r}'\, \frac{n(\mathbf{r})n(\mathbf{r}')}{|\mathbf{r}-\mathbf{r}'|}, \tag{2.20}$$

while $E_{\text{XC}}[n]$ represents the so-called exchange-correlation functional, which in principle contains all the non classical electron-electron interaction, and the difference between the kinetic energy of the fully-interacting system and non-interacting system: $E_{\text{XC}}[n] = (T[n] - T_{\text{ind}}) + (E_{\text{int}}[n] - E_H[n])$. Of course, the exact nature of this functional remains unknown, hindering the capability of performing exact calculations. Conversely, the external potential can always be cast in a simple form

$$V_{\text{ext}}[n] = \int \mathrm{d}\mathbf{r}\, V_{\text{ext}}(\mathbf{r})n(\mathbf{r}). \tag{2.21}$$

Combining (2.19), (2.20) and (2.21) gives the KS energy functional

$$E_{\mathrm{KS}}[n] = T_{\mathrm{ind}} + E_H[n] + E_{\mathrm{XC}}[n] + \int \mathrm{d}\mathbf{r}\, V_{\mathrm{ext}}(\mathbf{r}) n(\mathbf{r}). \tag{2.22}$$

Minimising (2.22) with respect to the degrees of freedom in the density, with the normalisation constraint $\int \mathrm{d}\mathbf{r}\, n(\mathbf{r}) = N$, is equivalent to find the stationary solution to the variational problem

$$\delta \left[E_{\mathrm{KS}}[n] - \mu \left(\int \mathrm{d}\mathbf{r}\, n(\mathbf{r}) - N \right) \right] = 0, \tag{2.23}$$

where μ is a Lagrange multiplier. The corresponding Euler-Lagrange equations are

$$\frac{\delta T_{\mathrm{ind}}}{\delta n} + V_{\mathrm{KS}}[n] - \mu = 0. \tag{2.24}$$

Formally, since T_{ind} is explicitly a functional of the KS orbitals, rather than the density, one should use functional derivatives with respect to $\psi_i^*(\mathbf{r})$ (and $\psi_i(\mathbf{r})$ for the c.c. equations) as

$$\frac{\delta T_{\mathrm{ind}}}{\delta \psi_i^*(\mathbf{r})} = -\frac{1}{2}\nabla^2 \psi_i(\mathbf{r}), \qquad \frac{\delta n(\mathbf{r})}{\delta \psi_i^*(\mathbf{r})} = \psi_i(\mathbf{r}). \tag{2.25}$$

Hence, for $\delta E_{\mathrm{KS}} = \frac{\delta E_{\mathrm{KS}}[n]}{\delta \psi_i^*(\mathbf{r})} \delta \psi_i^* + c.c = 0$, we obtain

$$\left[-\frac{1}{2}\nabla^2 \psi_i(\mathbf{r}) + \int \mathrm{d}\mathbf{r}' \frac{n(\mathbf{r}')\psi_i(\mathbf{r})}{|\mathbf{r}-\mathbf{r}'|} + V_{\mathrm{ext}}(\mathbf{r})\psi_i(\mathbf{r}) + \frac{\delta E_{\mathrm{XC}}[n]}{\delta n}\psi_i(\mathbf{r}) - \varepsilon_i \psi_i(\mathbf{r}) \right] \delta \psi_i^*(\mathbf{r}) + c.c. = 0. \tag{2.26}$$

Since complex conjugate terms in (2.26) are independent they must individually be set to zero. Moreover, $\delta\psi_i^*$ is an arbitrary variation so that the expression within the brackets must vanish. This gives the following set of Schrödinger-like eigenvalues equations, known as *Kohn-Sham* equations

$$\hat{H}_{\mathrm{KS}} \psi_i(\mathbf{r}) = \varepsilon_i \psi_i(\mathbf{r}), \tag{2.27}$$

where

$$\hat{H}_{\mathrm{KS}} = \Bigg[\underbrace{-\frac{1}{2}\nabla^2}_{\text{Kinetic energy}} + \underbrace{\int \mathrm{d}\mathbf{r}' \frac{n(\mathbf{r}')}{|\mathbf{r}-\mathbf{r}'|}}_{\text{Hartree potential}} + \underbrace{V_{\mathrm{ext}}(\mathbf{r})}_{\text{External potential}} + \underbrace{\frac{\delta E_{\mathrm{XC}}[n]}{\delta n}}_{\mathrm{V_{XC}\ potential}} \Bigg]. \tag{2.28}$$

The explicit form of the Hamiltonian in (2.28) clearly shows that the KS equations must be solved self-consistently. In fact, to build the KS Hamiltonian operator, we need to know the KS orbitals to compute the density, thence the Hartree potential and the

exchange correlation potential. The resulting electron field gives rise to the so-called self-consistent field (SCF). In principle, were the exact form of the exchange-correlation potential $V_{\mathrm{XC}}(\mathbf{r}) = \frac{\delta E_{\mathrm{XC}}[n]}{\delta n}$ known, the ground state density for the non-interacting system would match that of the fully-interacting system with the external potential $V_{\mathrm{ext}}(\mathbf{r})$. The total energy of the non-interacting system, often referred to as the band-structure energy E_{BS}, is given by the sum of the single-particle energies

$$E_{\mathrm{BS}}[n] = \sum_{i}^{N_{\mathrm{occ}}} \varepsilon_i = T_{\mathrm{ind}} + 2E_{\mathrm{H}}[n] + \int \mathrm{d}\mathbf{r}\, V_{\mathrm{XC}}(\mathbf{r})n(\mathbf{r}) + \int \mathrm{d}\mathbf{r}\, V_{\mathrm{ext}}(\mathbf{r})n(\mathbf{r}), \tag{2.29}$$

whereas the total energy of the fully-interacting system is

$$E[n] = F[n] + \int \mathrm{d}\mathbf{r}\, V_{\mathrm{ext}}(\mathbf{r})n(\mathbf{r}) = E_{\mathrm{BS}}[n] - E_{\mathrm{H}}[n] + E_{\mathrm{XC}}[n] - \int \mathrm{d}\mathbf{r}\, V_{\mathrm{XC}}(\mathbf{r})n(\mathbf{r}) = E_{\mathrm{BS}}[n] - E_{\mathrm{DC}}[n], \tag{2.30}$$

where the DC subscript stays for "double counting". The above equation may be readily extended to the case[90] of fractional occupancies f_i, with the constraint that $f_i \in [0, 1]\, \forall i$. The constraint of a fixed number of electrons implies

$$\sum_i f_i = N \quad \text{or} \quad 2\sum_i^{N/2} f_i = N, \tag{2.31}$$

where the second equations refers to spin-degenerate systems. For the free-electron model the occupation numbers f_i are drawn from the Fermi-Dirac (FD) distribution

$$f_i(\varepsilon_i) = \left[1 + \exp\left(\frac{\varepsilon_i - \mu}{\kappa_{\mathrm{B}} T}\right)\right]^{-1}, \tag{2.32}$$

where κ_{B} is the Boltzmann constatn and T is the temperature. At $T = 0$ K, the FD distribution collapses onto the Heaviside distribution. In this case, μ represents the chemical potential. It is worth noting that the KS orbitals, generated from the auxiliary system, do not physically represent the electron states as in HF, same is true for the KS eigenvalues which do not represent the energies of the electronic states. Consequently, the Koopman's theorem for the first ionisation energy[91] is in general not valid in KS DFT.

2.2.1 Local density approximation for exchange-correlation functional

As shown in the previous section, in order to make the KS equations operational, one needs to have an adequate expression for the exchange-correlation functional, since the exact expression is unknown. During the last three decades, a plethora of ever more sophisticated functionals has emerged. This is still a very active field of research, with many new functionals been produced every year. Different strategies can be pursued to build new classes of functionals, ranging from simple physical intuition to machine learning and genetic algorithms techniques[92]. The correction to the kinetic energy term and the removal of the self-interaction in the Hartree term, represent two major challenges encountered in developing new functionals. The simplest approximation, known as local density approximation (LDA), or its slightly more refined version known as local spin density approximation (LSDA), states that a system of interacting electrons locally behaves as an homogeneous electron gas. This means that the density is uniform (or slowly changing) within an infinitesimal volume d$\mathbf{r}$. We can therefore write

$$E_{\mathrm{XC}}^{\mathrm{LDA}}[n] = \int \mathrm{d}\mathbf{r}\, n(\mathbf{r}) \varepsilon_{\mathrm{XC}}^{\mathrm{homo}}([n], \mathbf{r}), \tag{2.33}$$

where $\varepsilon_{\mathrm{XC}}^{\mathrm{homo}}$ represents the exchange-correlation energy for an electron in a homogeneous gas, with density $n(\mathbf{r}) = n^{\mathrm{homo}}$. This formulation has had an incredible success, for two major reasons: 1) The exchange part of the functional $\varepsilon_{\mathrm{X}}^{\mathrm{homo}}$ is known analytically since 1930 Dirac's paper[93]

$$E_{\mathrm{X}}[n] = \frac{3}{4}\left(\frac{3}{\pi}\right)^{\frac{1}{3}} \int \mathrm{d}\mathbf{r}\, n^{\frac{4}{3}}(\mathbf{r}), \tag{2.34}$$

while the correlation term was obtained by Perdew and Zunger via a parametrisation[94] of numerical Monte Carlo results[95] and analytic results at high density limit[96]; 2) The accuracy of the results on a number of materials, mainly simple metals (due also to a fortuitous cancellation of errors). Obviously, we expect that such approximation would show its limit when used to describe systems where the electron density changes rapidly, e.g. atoms and molecules, but also in systems where the electron correlation plays an important role. However, astonishingly, accurate results for inhomogeneous systems have been reported[97], allegedly attributed to the so-called adiabatic connection between the fully-interacting system and the non-interacting system[98].

2.2.2 Generalised gradient approximation and beyond

A generally more accurate description may be obtained by introducing information on how quickly the density changes in a volume $\mathrm{d}\mathbf{r}$, i.e. considering $\varepsilon_{\mathrm{XC}}$ as a function of the gradient of the density as well. This formulation is known as gradient expansion approximation (GEA) and is a semi-local approximation. However, some physical constraints must be satisfied to generate meaningful exchange-correlation functionals, such as the sum rule for the true *exchange-correlation hole* $n_{\mathrm{xc}}(\mathbf{r}, \mathbf{r}')$

$$\int \mathrm{d}\mathbf{r}' \, n_{\mathrm{xc}}(\mathbf{r}, \mathbf{r}') = -1, \tag{2.35}$$

which is not satisfied by this approximation. Moreover, the absolute value of the gradients of the density can be large, effectively preventing the GEA expansion to be performed. The functionals that satisfies the sum rule for $n_{\mathrm{xc}}(\mathbf{r}, \mathbf{r}')$ and introduce information on the gradients are known as *generalized gradient approximation* (GGA) functionals. In general, we have

$$E_{\mathrm{XC}}^{\mathrm{GGA}} = \int \mathrm{d}\mathbf{r} \, n(\mathbf{r}) \varepsilon_{\mathrm{XC}}(n(\mathbf{r}), |\nabla n(\mathbf{r})|) \tag{2.36}$$

$$= \int \mathrm{d}\mathbf{r} \, n(\mathbf{r}) \varepsilon_{\mathrm{X}}^{\mathrm{homo}}(n(\mathbf{r})) F_{\mathrm{XC}}(n(\mathbf{r}), |\nabla n(\mathbf{r})|). \tag{2.37}$$

The integral in (2.36) does not uniquely define the function F_{XC} so that different GGA functionals may be generated that also satisfy the physical constraints (hence, they form a class). Notably, the most widely used GGA functionals for solids are Perdew-Wang[99] (PW91) and Perdew-Burke-Ernzerhof[100] (PBE). In chemistry, one popular GGA functional is the Becke-Lee-Yang-Parr[101, 102] (BLYP) functional, which is used in this thesis. Other strategies to improve the description of the exchange and the correlation are:

- Meta-GGA (analytic and semi-empirical), are semi-local functionals[101, 103–105] of the density and the occupied orbitals, where a dependence on the kinetic energy density (τ) is introduced in $\varepsilon_{\mathrm{XC}}$:

$$\varepsilon_{\mathrm{XC}} = \varepsilon_{\mathrm{XC}}(\mathbf{r}, |\nabla n(\mathbf{r})|, \tau(\mathbf{r})), \quad \text{with} \quad \tau(\mathbf{r}) = \frac{1}{2} \sum_{i}^{N_{\mathrm{occ}}} |\nabla \psi(\mathbf{r})|^2 .$$

- Semiempirical Hyper-GGA or Hybrid functionals, where a percentage of the exact

HF exchange is introduced:

$$E_{\mathrm{X}}^{\mathrm{HF}} = -\frac{1}{2}\sum_{i,j}\iint \mathrm{d}\mathbf{r}\mathrm{d}\mathbf{r}'\,\psi_i^*(\mathbf{r})\psi_j^*(\mathbf{r})\frac{1}{|\mathbf{r}-\mathbf{r}'|}\psi_i(\mathbf{r}')\psi_j(\mathbf{r}'),$$

for instance, the B3LYP functional[106]:

$$\begin{aligned} E_{\mathrm{XC}}^{\mathrm{BLYP}}[n] &= E_{\mathrm{X}}^{\mathrm{LDA}}[n] + 0.20(E_{\mathrm{X}}^{\mathrm{HF}}[\{\psi_i\}] - E_{\mathrm{X}}^{\mathrm{LDA}}) + \\ &\quad 0.72(E_{\mathrm{X}}^{\mathrm{B88}} - E_{\mathrm{X}}^{\mathrm{LDA}}) + E_{\mathrm{C}}^{\mathrm{VWN}} + 0.81(E_{\mathrm{C}}^{\mathrm{LYP}} - E_{\mathrm{C}}^{\mathrm{VWN}}), \end{aligned}$$

where $E_{\mathrm{X}}^{\mathrm{B88}}$ is the exchange part of the Becke 88 GGA functional[101], $E_{\mathrm{C}}^{\mathrm{LYP}}$ is the correlation part of the Lee-Yang-Parr GGA functional[102] and $E_{\mathrm{C}}^{\mathrm{VWN}}$ is the correlation part of the Vosko-Nilk-Nusair LDA functional[107].

The sophistication of these functionals is much higher than LDA. However, although the accuracy often increases in going from LDA to Hyper-GGA, the computational time goes up enormously[108], which poses limits on the actual systems' size that can be studied. In the DFT community, all these approximations are metaphorically assigned to rugs of a ladder, known as Jacob's ladder of density functional approximations[105, 109, 110], such as one may ascend from the "Hartree world" to the "Heaven of chemical accuracy" (beyond Hybrid functionals).

2.2.3 Pseudopotentials

We have shown that the electronic problem may be cast as the problem of solving a set of single-particle Schrödinger-like equations, with the following Hamiltonian

$$\hat{H}_{\mathrm{KS}} = -\frac{1}{2}\nabla^2 + \hat{V}_{\mathrm{KS}}(\mathbf{r}). \tag{2.38}$$

Without any further approximation, we should solve (2.38) to self-consistency for all the occupied eigenstates. However, it is experimentally observed[5] that the core electrons, the ones in the proximity of the nucleus, are nearly unaffected by the chemical environment, i.e. the distributions of the other electrons in the system.

Strictly speaking, the only electrons taking part in chemical bonds and contributing to the bonding energy are the valence electrons. As a result, if the core electron energies[6], could be removed from the calculation, the energy changes, which determine the physical properties of a system, would be easier to calculate accurately. As a consequence of the

[5] For example through X-ray diffraction experiments
[6] Which compose a large fraction of the total energy

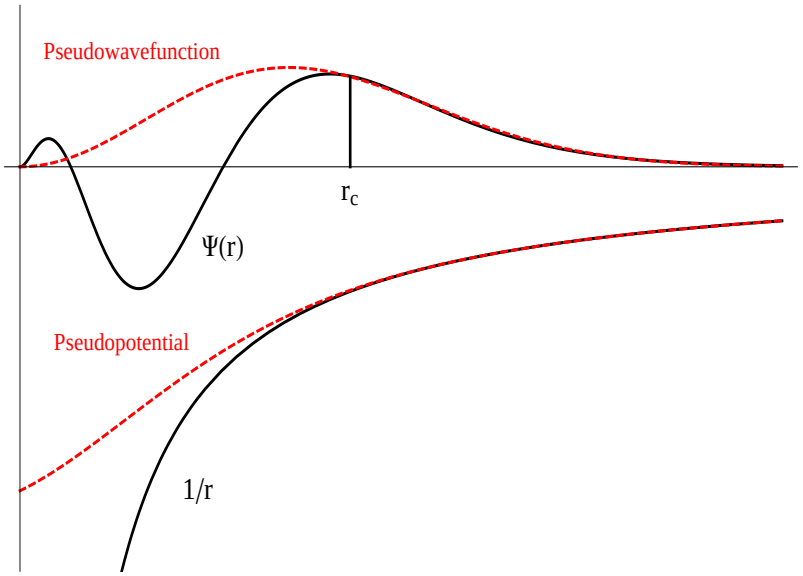

Figure 2.1: Exact potential and exact wave-function in solid black; pseudopotential and pseudowave-function in dashed red.

orthogonality constraints, the valence states must exhibit rapid oscillations in the core region. From the computational point of view, the representation of these oscillations can be onerous, as one needs a large number of basis functions for a faithful representation. Hence, larger matrices are demanded with a severe increase in both memory space and computation times.

Luckily, a strategy to by-pass the computation of core states exists, which return smoother valence states with exact eigenvalues generated via a smoother ionic pseudopotential[111] in (2.38). In fact, it can be proven that for the valence states, the Coulomb potential, that shows a singularity for $r \mapsto \mathrm{R}_{\mathrm{nucleus}}$, can be replaced by a much smoother pseudopotential[112]. The nuclear attraction is largely screened by a repulsive term, confined in the core region.

In order to see how the core states may be integrated out, let consider an atomic Hamiltonian, with the following separation between the core states $|\psi_c\rangle$ and the valence states $|\psi_v\rangle$:

$$\hat{H}\,|\psi_c\rangle = \varepsilon_c\,|\psi_c\rangle \tag{2.39}$$

$$\hat{H}\,|\psi_v\rangle = \varepsilon_v\,|\psi_v\rangle\,. \tag{2.40}$$

Orthogonality, $\langle\psi_c|\psi_v\rangle = 0$, is a natural consequence of the Hamiltonian being a self-

adjoint operator. We may define a new set of valence states $\{|\tilde{\psi}_v\rangle\}$ as

$$|\psi_v\rangle = |\tilde{\psi}_v\rangle + \sum_c B_c |\psi_c\rangle , \tag{2.41}$$

where the $|\tilde{\psi}_v\rangle$ change be made to slowly vary, while the second term on the r.h.s. of (2.41) takes care of the oscillations. From the orthogonality condition it readily follows

$$B_c = -\left\langle \psi_c | \tilde{\psi}_v \right\rangle . \tag{2.42}$$

Substituting (2.42) and (2.41) into (2.40), yields

$$\hat{H}\left(|\tilde{\psi}_v\rangle - \sum_c |\psi_c\rangle \langle \psi_c|\tilde{\psi}_v\rangle\right) = \varepsilon_v \left(|\tilde{\psi}_v\rangle - \sum_c |\psi_c\rangle \langle \psi_c|\tilde{\psi}_v\rangle\right), \tag{2.43}$$

which we can rearrange as

$$\hat{H}|\tilde{\psi}_v\rangle + \sum_c (\varepsilon_v - \varepsilon_c) |\psi_c\rangle \langle \psi_c|\tilde{\psi}_v\rangle = \varepsilon_v |\tilde{\psi}_v\rangle . \tag{2.44}$$

Thus, the pseudo-valence states obeys Schrödinger-like equations, with the Hamiltonian $\hat{H}_{\mathrm{PS}} = \hat{H} + \sum_c (\varepsilon_v - \varepsilon_c) |\psi_c\rangle \langle \psi_c|$, and eigenvalues ε_v. The extra term in the Hamiltonian is an energy-dependent repulsive potential, localised in the core, whose effect is to cancel part of the Coulomb potential of the nuclei. We can define a pseudopotential as the sum of the bare nuclear potential and the non-local repulsive potential

$$V^{\mathrm{PS}}(\mathbf{r})\psi_v(\mathbf{r}) = V_I(\mathbf{r})\psi_v(\mathbf{r}) + V_P(\mathbf{r}, \mathbf{r}')\psi_v(\mathbf{r}'), \tag{2.45}$$

where we have defined the kernel of the $\hat{V}_P$ operator as

$$V_P(\mathbf{r}, \mathbf{r}') = \sum_c (\varepsilon_v - \varepsilon_c)\psi_c(\mathbf{r})\psi_c^*(\mathbf{r}'). \tag{2.46}$$

We can therefore rearrange (2.44) for the pseudo-valance states

$$(-\frac{1}{2}\nabla^2 + \hat{V}^{\mathrm{PS}})|\tilde{\psi}_v\rangle = \varepsilon_v |\tilde{\psi}_v\rangle . \tag{2.47}$$

The pseudopotential in (2.47) is much smoother in the core region than the bare nuclear potential, whereas far from the core, it can be construct to asymptotically match the Z/r tail of the Coulomb potential. By removing the singularity of the Coulomb potential, the pseudo-valence states are also smoother functions[113, 114] than the true valence states

and fewer basis functions will be needed to represent them, cf. Fig. 2.1.

A key parameter for a pseudopotential is the cut-off distance r_c. This parameter sets the separation between an inner and outer region. In the outer region, i.e. $r > r_c$, the true valence state and the pseudo-valence state are indistinguishable. In the inner region instead, the two functions differ largely. The true valence state is rapidly varying in the core region, while the pseudo-valence state is smooth. Tuning r_c enables to generate different pseudofunctions for different chemical environments, ultimately determining the transferability of the pseudopotential. Remarkably, $V^{\mathrm{PS}}(\mathbf{r}, \mathbf{r}')$ is not unique and different approaches have been suggested to generate smooth pseudopotentials while matching physical desiderata. In particular, two classes of pseudopotentials, known as norm-conserving[115–119] (NC-PP) and ultrasoft[120] (US-PP), are usually implemented in actual DFT codes. The latter allow plane-waves DFT calculations with lower kinetic energy cut-off than NC-PP, increasing the the speed of calculations. In this thesis we will make use in particular of NC-PP as developed by Rappe *et al.* in Ref. 118. Another approach based on the frozen-core approximation [121], known as projector-augmented wave method (PAW) allows for all-electron plane-waves calculations without the use of pseudopotentials. Being an all-electron method, PAW has in general greater accuracy than NC-PP and it is also more portable. Moreover, PAW make uses of US-PP, resulting in a lower cut-off energy. On the other side, in the PAW formalism different basis sets have to be used to describe the rapidly oscillating part (close to the nucleus) and the smooth part (far from the nucleus) of the atomic wave-function.

2.2.4 Kleinman-Bylander representation

In Section 2.2.3 we saw that, in order to accurately describe the effect of the core electrons, it is necessary to have a pseudopotential which is non-local. In particular, when considering atomic orbitals $|\psi_{nlm}\rangle$, where n, l and m are the usual quantum numbers, the pseudopotential must behave differently for different angular momenta l. In general, we may express the pseudopotential in a semi-local form, i.e. depending on different angular momenta l, but not on $\mathbf{r}$ and $\mathbf{r}'$ separately, as:

$$\hat{V}^{\mathrm{PS}} = \hat{V}^{\mathrm{loc}} + \sum_{l} \sum_{m=-l}^{l} |Y_{lm}\rangle \, \hat{V}_l \, \langle Y_{lm}| \,, \tag{2.48}$$

where, the local potential $\hat{V}^{\mathrm{loc}}$, although arbitrary in principle, is in practice chosen to compensate for the truncated sum on the r.h.s. in (2.48) (where one usually stops at $l = 2$). This form of the pseudopotential turns out to be computationally inefficient to use since the number of integrals $\langle g|\hat{V}_l|g'\rangle$ that needs to be computed scales quadratically with the

number of the basis functions $|g\rangle$, i.e. $O(n_g^2)$. Kleinman and Bylander [122] suggested the following representation, which overcomes this problem:

$$\hat{V}_{\mathrm{KB}} = \hat{V}_{\mathrm{loc}} + \sum_{l} \sum_{m=-l}^{l} \frac{|\hat{V}_l \chi_{lm}\rangle \langle \chi_{lm} \hat{V}_l|}{\langle \chi_{lm}|\hat{V}_l|\chi_{lm}\rangle}, \tag{2.49}$$

where $|\chi_{lm}\rangle$ is an eigenstate of the atomic pseudo-Hamiltonian

$$\chi_{lm}(\mathbf{r}) = R_{\mathrm{PS},l}(r) Y_{lm}(\theta, \phi). \tag{2.50}$$

This non-local form for the pseudopotential, though different from the original semi-local operator, acts in the same way on the reference state $|\chi_{lm}\rangle$ and, as such, is expected to maintain the same degree of transferability as the original representation. The advantage of the KB form is that matrix elements $\langle g|\hat{V}_{\mathrm{KB}}|g'\rangle$ are separable, i.e. they can be factorised into the sum of two integrals, each involving a single basis function $|g\rangle$, thence the calculation of the entire matrix requires only $O(n_g)$ integrals.

2.3 Bloch states and Wannier functions

Periodic systems, like crystals, are characterised by the highly-ordered arrangement of atoms in space. The group of atoms constituting the repeating pattern is called the basis. The way the basis is repeated in space gives the lattice. In three-dimensional space there exist 14 distinct ways to arrange a repeating unit, these are known as Bravais lattices[10]. A given lattice defines the discrete translational symmetry of the system and can be represented by three non-collinear lattice vectors $\mathbf{a}_1, \mathbf{a}_2, \mathbf{a}_3$, so that a translation

$$\boldsymbol{\tau}_n = n_1\mathbf{a}_1 + n_2\mathbf{a}_2 + n_3\mathbf{a}_3, \tag{2.51}$$

where $n_1, n_2, n_3 \in \mathbb{N}$, leaves the lattice invariant. A cell representing a Bravais lattice containing a single lattice point is called a primitive cell. To each Bravais lattice we can assign a reciprocal lattice $\{\mathbf{b}_i, i = 1, 2, 3\}$ (again a Bravais lattice) via the mapping

$$\exp[i\mathbf{a}_i \cdot \mathbf{b}_j] = 1 \quad \mapsto \quad \mathbf{a}_i \cdot \mathbf{b}_j = 2\pi\delta_{ij}. \tag{2.52}$$

By simple geometrical arguments and one can show that

$$\mathbf{b}_1 = 2\pi \frac{\mathbf{a}_2 \times \mathbf{a}_3}{|\mathbf{a}_1 \cdot (\mathbf{a}_2 \times \mathbf{a}_3)|} = 2\pi \frac{\mathbf{a}_2 \times \mathbf{a}_3}{V_{\mathrm{cell}}}, \tag{2.53}$$

where $\mathbf{b}_2$ and $\mathbf{b}_3$ are found by cyclic permutations. Analogously to (2.51) one can define a translation in the reciprocal lattice as

$$\mathbf{G}_m = m_1\mathbf{b}_1 + m_2\mathbf{b}_2 + m_3\mathbf{b}_3. \tag{2.54}$$

The first Brillouin zone is the Wigner-Seitz cell in the reciprocal lattice[10], whose volume is given by

$$\Omega_{\mathrm{BZ}} = \frac{(2\pi)^3}{V_{\mathrm{cell}}}. \tag{2.55}$$

For a periodic system, the Hamiltonian has the symmetry of the lattice, i.e.

$$\hat{H}(\mathbf{r} + \boldsymbol{\tau}_n) = \hat{T} + \hat{V}(\mathbf{r} + \boldsymbol{\tau}_n) = \hat{H}(\mathbf{r}).$$

This is also true for the potential and the density function. Bloch's theorem[8] states that the eigenstates of an infinitely periodic Hamiltonian are given by

$$\psi_{n,\mathbf{k}}(\mathbf{r}) = e^{i\mathbf{k}\cdot\mathbf{r}}u_{n,\mathbf{k}}(\mathbf{r}), \tag{2.56}$$

where $u_{n,\mathbf{k}}(\mathbf{r}+\boldsymbol{\tau}_r) = u_{n,\mathbf{k}}(\mathbf{r})$ and $\mathbf{k}$ is a vector in the reciprocal space. Therefore, the $\psi_{n,\mathbf{k}}(\mathbf{r})$ in an infinitely periodic system are given by a periodic function modulated by a plane wave[7], cf. Fig. 2.2. The energy eigenvalues are now labelled by two numbers: the band number n and $\mathbf{k}$, which when multiplied by $\hbar$ is defined as the crystal momentum.

A proof of the Bloch theorem starts by considering the properties of the translation operator $\hat{T}_r$

$$\hat{T}_r\psi_n(\mathbf{r}) = \psi_n(\mathbf{r} + \boldsymbol{\tau}_r). \tag{2.57}$$

The Hamiltonian operator and the translation operator obey to the following commutation relations

$$\begin{aligned}\left[\hat{T}_r, \hat{T}_s\right] &= 0\\ \left[\hat{T}_r, \hat{H}\right] &= 0,\end{aligned} \tag{2.58}$$

since the Hamiltonian is invariant to any of the translation $\boldsymbol{\tau}_r$. Therefore, they share the same set of eigenfunctions $\{\psi_n(\mathbf{r})\}$ and we can write

$$\hat{T}_r\psi_n(\mathbf{r}) = C_r\psi_n(\mathbf{r}). \tag{2.59}$$

[7] Or alternatively, the eigenfunctions of electrons in an infinitely periodic system are the same as free electrons modulated by a periodic function.

Obviously, the translation operator satisfies the group properties

$$\begin{aligned} \hat{T}_r \hat{T}_s &= \hat{T}_{r+s} \\ \hat{T}_r^* &= \hat{T}_{-r} = \hat{T}_r^{-1}, \end{aligned} \tag{2.60}$$

which imply

$$\hat{T}_r \hat{T}_s \psi_n(\mathbf{r}) = \hat{T}_r C_s \psi_n(\mathbf{r}) = C_r C_s \psi_n(\mathbf{r}) \tag{2.61}$$

$$\hat{T}_r \hat{T}_s \psi_n(\mathbf{r}) = \hat{T}_{r+s} \psi_n(\mathbf{r}) = C_{r+s} \psi_n(\mathbf{r}). \tag{2.62}$$

Equating (2.61) and (2.62) yields

$$C_r C_s = C_{r+s}. \tag{2.63}$$

Moreover, the coefficients C_r can be decomposed in the product of primitive translations as $C_r = [C_{\mathbf{a}_1}]^{r_1} [C_{\mathbf{a}_2}]^{r_2} [C_{\mathbf{a}_3}]^{r_3}$. The modulus of each of $[C_{\mathbf{a}_i}]^{r_i}$ must be unity by the symmetry of the system, thereby $[C_{\mathbf{a}_i}]^{r_i} = e^{i2\pi\nu_i}$. This is equivalent to write $C_r = e^{i\mathbf{k}\cdot\boldsymbol{\tau}_r}$, where $\mathbf{k} = x_1\mathbf{b}_1 + x_2\mathbf{b}_2 + x_3\mathbf{b}_3$, the $\{x_i\}$ being complex number in general. Finally, we can write

$$\psi_{n,\mathbf{k}}(\mathbf{r} + \boldsymbol{\tau}_r) = e^{i\mathbf{k}\cdot\boldsymbol{\tau}_r} \psi_{n,\mathbf{k}}(\mathbf{r}), \tag{2.64}$$

which states that the eigenfunctions $\psi_{n,\mathbf{k}}$ acquire a phase $e^{i\mathbf{k}\cdot\boldsymbol{\tau}_r}$ upon a lattice translation. From (2.64), (2.56) follows straightforwardly. To perform actual calculations within the KS-DFT framework, one models the idealised infinite periodic system as a finite volume consisting of $N = N_1 N_2 N_3$ cells and applying Born-von Kármán periodic boundary conditions

$$\psi(\mathbf{r} + N_i \mathbf{a}_i) = \psi(\mathbf{r}). \tag{2.65}$$

From (2.64) and (2.65) we obtain $\exp[iN_i\mathbf{k}\cdot\mathbf{a}_i] = 1$. This relation forces the coefficients $\{x_i\}$ to be real and equal to

$$\mathbf{k} = \frac{m_1}{N_1}\mathbf{b}_1 + \frac{m_2}{N_2}\mathbf{b}_2 + \frac{m_3}{N_3}\mathbf{b}_3. \tag{2.66}$$

In the limit of an infinite volume we have an infinite number of allowed $\mathbf{k}$ points (countably infinitely many). However, only the $\mathbf{k}$ within the Brillouin zone are required. In fact two points $\mathbf{k}$ and $\mathbf{k}'$ that differ by a $\mathbf{G}_m$ in (2.54) are equivalent. Moreover, by considering the set of all the point group symmetries, only the points belonging to a reduced zone, the irreducible Brilluoin zone (IBZ), are required.

The first attempt to develop a theory of electronic structure based on localised functions rather than extended Bloch states is due to Wannier[123] in the 1937. He proposed

to apply a unitary transformation to the Bloch states in order to find more localised states. The resulting functions are known as "Wannier functions" and are defined as

$$w_{n\boldsymbol{\tau}}(\mathbf{r}) = \frac{V_{\text{cell}}}{(2\pi)^3} \int_{1\text{BZ}} \mathrm{d}\mathbf{k}\ e^{-i\boldsymbol{\tau}\cdot\mathbf{k}} \psi_{n\mathbf{k}}(\mathbf{r}), \tag{2.67}$$

where $\boldsymbol{\tau}$ is a lattice vector. For long time it has been supposed that exponentially decaying Wannier functions could be obtained for insulators. However, the conditions for the existence of such functions in 2D and 3D insulators have only recently (2007) been found[124]. Hence, for insulators, the Wannier functions are localised in the cell defined by $\boldsymbol{\tau}$. Since the Bloch states are orthonormal and the Wannier transformation (2.67) is a unitary transformation, the orthonormality is preserved

$$\int \mathrm{d}\mathbf{r}\, w^*_{n\boldsymbol{\tau}}(\mathbf{r}) w_{m\boldsymbol{\tau}'}(\mathbf{r}) = \delta_{nm}\delta_{\boldsymbol{\tau}\boldsymbol{\tau}'}. \tag{2.68}$$

Both basis sets span the same band subspace of the Hilbert space, even though the Wannier functions are not eigenstates of the crystal Hamiltonian. It can be shown that the density matrix can be rewritten in terms of Wannier functions in the following manner

$$\rho(\mathbf{r}, \mathbf{r}') = \sum_{n,m} \sum_{\boldsymbol{\tau}\boldsymbol{\tau}'} w_{n\boldsymbol{\tau}}(\mathbf{r}) K_{nm}(\mathbf{r}' - \mathbf{r}) w^*_{m\boldsymbol{\tau}'}(\mathbf{r}'), \tag{2.69}$$

where we have introduced a density kernel $K_{nm}(\mathbf{r}' - \mathbf{r})$ given by

$$K_{nm}(\mathbf{r}' - \mathbf{r}) = \frac{V_{\text{cell}}}{(2\pi)^3} \int_{1\text{BZ}} \mathrm{d}\mathbf{k}\, e^{i\mathbf{k}\cdot(\mathbf{r}'-\mathbf{r})} f_{nm}\delta_{nm}, \tag{2.70}$$

which reduces to $\delta_{nm}\delta_{\boldsymbol{\tau}\mathbf{0}}$ for a set of fully occupied bands. In KS-DFT with periodic boundary conditions, the Bloch states are essentially the KS eigenstates. Consequently, KS eigenstates are not the best option as basis set, as they are generally delocalised over the all space due to the orthonormality requirements. It is well known, that orthogonality and localisation are competing requirements[125]. However, the theory of Wannier functions has an extra layer of complexity due to the presence of a "gauge freedom" that exists in the definition of the Bloch states. In fact, one may well write

$$|\tilde{u}_{n\mathbf{k}}\rangle = e^{i\varphi_n(\mathbf{k})} |u_{n\mathbf{k}}\rangle, \tag{2.71}$$

where $\varphi_n(\mathbf{k})$ is any real function that is periodic in reciprocal space, without changing the physical description of the system. In order to get well-localized Wannier functions, we need to enforce some degree of smoothness on the $|\tilde{u}_{n\mathbf{k}}\rangle$, e.g. by imposing $\nabla_{\mathbf{k}} |\tilde{u}_{n\mathbf{k}}\rangle$

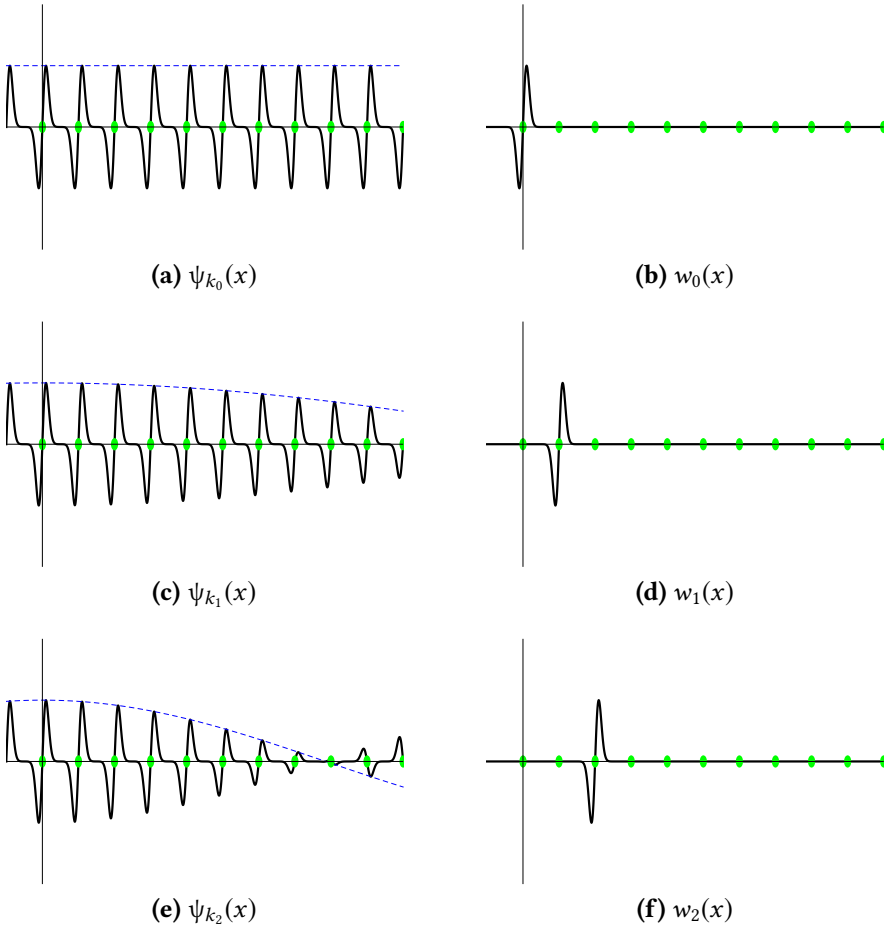

(a) $\psi_{k_0}(x)$ **(b)** $w_0(x)$ **(c)** $\psi_{k_1}(x)$ **(d)** $w_1(x)$ **(e)** $\psi_{k_2}(x)$ **(f)** $w_2(x)$

Figure 2.2: Left: Bloch functions associated with a single band in 1D, at three different values of wavevector k. Right: Wannier functions associated with the same 1D band, forming periodic images of one another. Green dots indicate atoms; blue dotted curves indicate envelopes e^{ikx} of the Bloch functions. Bloch and Wannier functions span the same Hilbert space.

being well-defined at all $\mathbf{k}$. This is typical of Fourier transforms: the smoother the reciprocal-space function, the more localized the real-space function, and vice versa.

Hence, depending on the choice of the gauge, one may obtain more or less localised Wannier functions. In this sense, the Wannier functions are more "non-unique" than the Bloch states, which only acquire a phase factor upon changing the gauge. Further complications arise when the band n is not isolated, but rather it is part of a so-called mixed band. In this case, we refer to a manifold of Q bands that remains separated in energy from other bands everywhere in the Brillouin zone. The generalisation of (2.71) to

the manifold of Q bands[125, 126] is

$$|\tilde{u}_{n\mathbf{k}}\rangle = \sum_{m=1}^{Q} U_{nm}^{\mathbf{k}} |u_{m\mathbf{k}}\rangle \,, \tag{2.72}$$

where $U_{nm}^{\mathbf{k}}$ is a unitary matrix of dimensions $Q \times Q$ periodic in $\mathbf{k}$. The corresponding Wannier function is given by

$$w_{n,\boldsymbol{\tau}}(\mathbf{r}) = \frac{V_{\text{cell}}}{(2\pi)^3} \int_{1\text{BZ}} \mathrm{d}\mathbf{k}\, e^{i\mathbf{k}\cdot\boldsymbol{\tau}} \sum_{m=1}^{Q} U_{nm}^{\mathbf{k}} u_{n,\mathbf{k}}(\mathbf{r}). \tag{2.73}$$

Several methods have been proposed to obtain localised Wannier functions, for a comprehensive review see Ref. 126. One popular method is to minimise a spread functional Ω with respect to the $U_{nm}^{\mathbf{k}}$

$$\Omega = \sum_{n} \left[\langle w_{n0}|r^2|w_{n0}\rangle - (\langle w_{n0}|\mathbf{r}|w_{n0}\rangle)^2 \right], \tag{2.74}$$

which is the solid-state equivalent of the Foster-Boys localisation scheme popular in computational chemistry[127, 128]. Once a representation in the reciprocal space for Ω is obtained, the minimisation procedure, subject to the constraints of orthonormalisation, returns the so-called maximally localised Wannier functions[126, 129].

2.4 Linear-scaling density functional theory

In Section 2.1 and Section 2.2, we introduced the general idea of DFT, together with the pseudopotential approach. The general formalism may be implemented in several "flavours", differing mainly in the choice of the basis set adopted to describe the KS states and the boundary conditions (PBC *vs.* OBC). The choice of basis set is crucial for the accuracy and performance of a given DFT algorithm, inasmuch as many DFT programs are defined by the type of basis set that they adopt. In general, different criteria contribute in making a given basis set successful for DFT calculations, such as systematic improvement of the degree of completeness. Basis sets formed by Gaussian-type orbitals (GTOs) [11, 58, 130] have the nice property that many operations like integrals and derivatives can be performed analytically. Nowadays, there exist extremely efficient algorithms for Gaussian based operations. Programs such as Gaussian[131] or NWChem[132] use multiple-Gaussian basis sets for accurate DFT calculations. GTOs together with Slater-type basis sets are usually used for calculations on molecules and finite systems, hence preferred by the computational chemistry community. Other successful approach can be

found in the BigDFT program [133], where Daubuchies wavelets are used with optimum results, and in FHI-aims [134] using numerical atom-centred orbitals. Plane-wave (PW) basis sets [14] on the other hand, are the natural choice for simulating periodic systems such as crystals, surfaces, rods and wires, thence preferred in the solid-state physics community. There is a long list of programs using PW basis sets, for instance ABINIT [135], castep [136], GPAW [137], quantum espresso [138], VASP [139, 140] to mention but a few. There are also hybrid methods that use a combination of Gaussians and PW, as in Quickstep [141].

The choice of plane-waves as basis set in PBC is supported by a number of reasons:

1. PWs form a complete orthonormal set;
2. The kinetic energy operator for a non interacting systems is diagonal in the PWs representation;
3. The Hartree potential and the local part of the pseudopotential $\hat{V}_{\text{loc}}$ have also a simple representation with PW basis set[142];
4. PWs naturally obey to PBC;
5. No no error due to superposition of basis functions (BSSE);
6. PWs do not depend on atomic position, hence no Pulay forces are needed. We can calculate forces directly from the Hellmann-Feynman theorem;
7. Accurate description in real space, through FFT;
8. The overall accuracy, is controlled by tuning a single parameter, namely the kinetic energy cut-off. The basis set is said to be *systematic*.

To see the last point, we can expand the periodic functions $|u_{n\mathbf{k}}\rangle(\mathbf{r})$ as a linear combination of infinite plane-waves. The Bloch states in the PWs basis become:

$$\psi_{n\mathbf{k}}(\mathbf{r}) = \sum_{\mathbf{G}} c_{n,\mathbf{k}+\mathbf{G}} e^{i(\mathbf{k}+\mathbf{G})\cdot\mathbf{r}}. \tag{2.75}$$

In practice, in plane-wave methods the sum over $\mathbf{G}$ is truncated according to a spherical cut-off in reciprocal space, denoted by $|\mathbf{G}_{\text{cut-off}}|$. In an equivalence to the expression of the kinetic energy of an electron (in atomic units), the plane-wave kinetic energy cut-off is defined as:

$$E_c = \frac{1}{2} |\mathbf{G}_{\text{cut-off}}|^2 . \tag{2.76}$$

The accuracy of the plane-wave basis set is hence well-controlled by a single parameter, namely $E_{\text{cut-off}}$. Larger values of $E_{\text{cut-off}}$ will automatically result in a more complete plane-wave basis set. PWs can also be used for non-periodic finite systems, such as clusters, slabs, surfaces etc.through the supercell approach. The idea is to have an enlarged simulation cell in real space, so to avoid all the interactions with the atoms in the periodic images (replicas). However, a cost has to be paid when increasing the volume of the simulation cell, since PWs extends over the entire volume. The first Brillouin zone becomes progressively smaller when the volume of the real space cell is increased, according to (2.55). Consequently, the system may be accurately described by only one $\mathbf{k}-$ point, namely the $\Gamma-$ point ($\mathbf{k} = \mathbf{0}$).

Despite the inherent non-locality in quantum mechanics, many important properties of interest may be found by using information that is only local (or semi-local). An equivalent approach to conventional KS-DFT, can be achieved by introducing the density matrix formalism, described in Section 1.3. From the N-body density matrix operator we can introduce the concept of reduced density matrix operators[59]. In fact, as shown in the previous sections, the KS Hamiltonian is the sum of "one-electron" and "two-electron" operators. This is also true for HF theory and for most theories in quantum chemistry. The first order density matrix, in position representation, is given by

$$\rho(\mathbf{r}, \mathbf{r}') = \langle \mathbf{r}|\rho|\mathbf{r}'\rangle = N \int \dots \int \mathrm{d}\mathbf{r}_2 \dots \mathrm{d}\mathbf{r}_N \, \Psi^*(\mathbf{r}, \mathbf{r}_2, \dots, \mathbf{r}_N)\Psi(\mathbf{r}', \mathbf{r}_2, \dots, \mathbf{r}_N). \tag{2.77}$$

The diagonal elements of $\rho(\mathbf{r}, \mathbf{r}')$ are thus related to the electronic density function by

$$n(\mathbf{r}) = 2\rho(\mathbf{r}, \mathbf{r}), \tag{2.78}$$

where the factor 2 accounts for spin degeneracy. Consequently, we have the following normalisation constraint

$$N = \int \mathrm{d}\mathbf{r}\, n(\mathbf{r}) = 2 \int \mathrm{d}\mathbf{r}\, \rho(\mathbf{r}, \mathbf{r}) = 2 \sum_i f_i = 2\,\mathrm{tr}[\rho], \tag{2.79}$$

where we have made used of (2.31) and (1.14).

For KS-like orbitals, the first order density matrix operator takes on the following form

$$\hat{\rho} = \sum_{i=1}^{N/2} |\psi_i\rangle\, f_i\, \langle\psi_i| \quad \Rightarrow \quad \rho(\mathbf{r}, \mathbf{r}') = \sum_{i=1}^{N/2} \psi_i(\mathbf{r}) f_i \psi_i^*(\mathbf{r}'), \tag{2.80}$$

where $\psi_i(\mathbf{r})$ are a set of (orthogonal) eigenstates[8] of the KS Hamiltonian operator (2.28).

[8]The occupation numbers f_i may also be seen as the probability of a given state being filled by one

Since the electronic density function can be derived from the first order density matrix, in virtue of the Kohn and Sham theorems, we can reformulate the KS equations in terms of $\rho(\mathbf{r}, \mathbf{r}')$. The kinetic energy for non-interacting particle in terms of the density matrix is given by

$$\begin{aligned} T[\rho] &= 2\sum_i f_i \int \mathrm{d}\mathbf{r}\, \psi_i^*(\mathbf{r}) \left(-\frac{1}{2}\nabla^2\right) \psi_i(\mathbf{r}) \\ &= \int \mathrm{d}\mathbf{r} \left[-\frac{1}{2}\nabla_{\mathbf{r}}^2 \rho(\mathbf{r}, \mathbf{r}')\right]_{\mathbf{r}=\mathbf{r}'} = 2\mathrm{tr}[\hat{T}\hat{\rho}]. \end{aligned} \tag{2.81}$$

The Hartree, external and exchange-correlation remain unchanged, except that the density is now given by (2.78). Thus, the KS equations can be reformulated in terms of the density matrix, and the total energy can be minimise with respect to the degrees of freedom in $\rho(\mathbf{r}, \mathbf{r}')$, subject to specific constraints, i.e. normalisation and idempotency. The normalisation constraint, being a linear constraint, may be enforced by performing an unconstrained minimisation on the following Lagrangian

$$\mathcal{L}[n] = E_{\mathrm{KS}}[n] - \mu\left(2\int \mathrm{d}\mathbf{r}\, \rho(\mathbf{r}, \mathbf{r}) - N\right). \tag{2.82}$$

Conversely, the idempotency constraint can not be enforced by adding an extra term in the Lagrangian 2.82. The idempotency constraints enforces the Pauli exclusion principle and together with energy minimisation satisfy the Aufbau principle. The non-linear nature of the idempotency constraints derives from the orthonormality constraints of the KS orbitals, which is the cause of the $O\left(N^3\right)$ scaling of conventional methods. An alternative to the direct approach, has been proposed by McWeeny[65]. This is a weaker condition to ensure idempotency, cf. Sec. 2.4. In materials that present a band gap in the energy spectrum between valence states and conduction states (insulators and semiconductors), the density matrix decays exponentially[143, 144]

$$\rho(\mathbf{r}, \mathbf{r}') \propto e^{-\gamma|\mathbf{r}-\mathbf{r}'|}, \tag{2.83}$$

where γ may be heuristically connected to the band gap, although the exact formula remains unknown[144–146]. The exponential law holds for metals at finite temperatures[147] as well, where γ, in this case, is related to the ratio between $\kappa_{\mathrm{B}}T$ and the Fermi velocity. Metals at $T = 0$ Kdo not show a band gap in the energy spectrum, and a power law, rather than an exponential one, is found instead. The property of the density matrix in (2.83) is sometimes referred to as "nearsightedness" of electronic matter,

electron. Hence $f_i \in [0, 1]$, and fractional values are allowed.

coined by Kohn[28]. The exponential decay of $\rho(\mathbf{r}, \mathbf{r}')$ can be exploited by setting to zero all the density matrix elements for which $|\mathbf{r} - \mathbf{r}'| > r_\rho$

$$\rho(\mathbf{r}, \mathbf{r}') = 0, \quad \text{for} \quad \left|\mathbf{r} - \mathbf{r}'\right| > r_\rho. \tag{2.84}$$

The exponential feature of the density matrix is strictly related to the existence of localised Wannier functions[125, 126, 143, 145]. This can be easily seen from (2.69). Recently, Brouder *et al.* have shown that the existence of well-localised Wannier functions in 2D and 3D systems is guaranteed by a zero Chern invariant, which in turn guarantees a globally smooth gauge[124]. In this situation, one can therefore imagine to use truncated Wannier-like orbitals and in doing so introducing only a small error in the electronic structure. After truncation, each Wannier-like function is strictly localised within a finite[9] region of space, which we will call localisation region. Glueing together all the localisation regions results in a wider molecular localisation region. Linear-scaling methods rely on density matrix truncation as a controlled approximation to reduce the computational cost of the calculations. In fact, only by exploiting the exponential property of the density matrix, we are able to design algorithms that require ON computations and memory allocations (sparse algebra). In this thesis we will mainly focus on system showing a finite band gap, i.e. insulators or large molecular systems. These systems allow us to perform zero-temperature linear-scaling KS-DFT calculations efficiently.

2.4.1 Tensor notation in linear-scaling density functional theory

As mentioned in the previous section, linear-scaling approaches are attainable only if one is able to exploit the nearsightedness of the electronic matter. However, as proved in Sec. 2.3 the electronic states of a periodic system are express in terms of Bloch states $\psi_{n\mathbf{k}}$, that are in general delocalised over the entire space. Nonetheless, we can still represent the density matrix using orthogonal localised functions, such as MLWFs. Over the last two decades, many works have emerged, proposing methods that scale linearly with the number of atoms by adopting localised orbitals[148–155]. For an excellent review on linear scaling methods the reader is referred to Ref. 143.

Localisation can be further improved by adopting a non-orthogonal basis[156, 157]. Nowadays, many codes make use of non-orthogonal localised functions in order to achieve linear scaling performance[158]. A simple strategy is to expand the localised functions in terms of a fixed basis set, such as pseudo-atomic orbitals (PAO) in CONQUEST [20] and

[9] Usually spherical

SIESTA [19, 159], numerical-atomic orbitals in FHI-AIMS [134], spherical waves [160] and gaussians [161]. This allows for a systematic way to increase the chemical accuracy, as one can easily generate multiple–ζ basis sets. However, the drawbacks of adopting such strategy lie in the lack of variational flexibility during the energy minimisation, which has to be compensated by using a large non-minimal basis set. A different strategy is to expand the localised functions in a underlying basis set and to optimise them *in situ*. This technique has been implemented with success in ONETEP [18] using periodic sinc functions as underlying basis set, in CONQUEST [20] using b-splines and OPENMX [162] using primitive PAOs. The advantage of this strategy lies in the possibility of attaining chemical accuracy with a minimal basis set, comparable in size with single–ζ basis sets. However, there is a caveat when adopting non-orthogonal functions: the mathematical framework required to deal with non-orthogonal objects is fairly more complicated, since one needs tensor algebra on curved manifolds. Here, we will only introduce the notation for non-orthogonal functions within the DFT formalism, but a general discussion can be found in Refs. 163–165. The notation presented here is common to all the methods cited above. We will then focus on the ONETEP specific approach to solve KS equations in the next section.

Let introduce a set of non-orthogonal supporting functions $\{\phi_\alpha(\mathbf{r})\}$, known as non-orthogonal generalised Wannier functions (NGWFs) in ONETEP (see Sec. 2.4.2), that are related to the KS eigenfunctions by a non-unitary transformation $\mathbf{M}$

$$|\psi_i\rangle = |\phi_\alpha\rangle M^\alpha{}_i. \tag{2.85}$$

where the KS states on the l.h.s. are orthogonal states, whereas the supporting functions are assumed to be (0,1)-tensors[163–166], i.e. covariant tensors. In (2.85), we have made use of Einstein's notation for repeated indices. Hereafter, Latin letters are used for labelling orthogonal objects, whereas Greek letters are used for non-orthogonal ones. It is worth noting that $\mathbf{M}$ does not have to be a square matrix. From the orthonormality relation of the KS states, we obtain

$$\langle\psi_l|\psi_k\rangle = (\mathbf{M}^\dagger)_l{}^\alpha \langle\phi_\alpha|\phi_\beta\rangle M^\beta{}_k = (\mathbf{M}^\dagger)_l{}^\alpha S_{\alpha\beta} M^\beta{}_k = \delta_{lk}, \tag{2.86}$$

where, we have implicitly defined a metric tensor $S_{\alpha\beta}$ for the space spanned by $\{\ |\phi_\alpha\rangle\}$, and it is represented by the overlap matrix $\mathbf{S}$

$$(\mathbf{S})_{\alpha\beta} = S_{\alpha\beta} = \langle\phi_\alpha|\phi_\beta\rangle = \int \mathrm{d}\mathbf{r}\, \phi^*_\alpha(\mathbf{r})\phi_\beta(\mathbf{r}). \tag{2.87}$$

We also introduce a set of (1,0)-tensors, also known as contravariant or dual functions,

$\{ \mid \phi^\alpha \rangle \}$, satisfying the following relations:

$$\langle \phi^\alpha | \phi_\beta \rangle = \langle \phi_\beta | \phi^\alpha \rangle = \delta^\alpha_\beta. \tag{2.88}$$

Analogously, we can define a metric tensor in the dual space, spanned by the dual functions, $S^{\alpha\beta} = \langle \phi^\alpha | \phi^\beta \rangle$, such that the two sets are related by

$$|\phi^\alpha\rangle = |\phi_\beta\rangle \left(\mathbf{S}^{-1}\right)^{\beta\alpha}. \tag{2.89}$$

It is straightforward to show that $S^{\alpha\beta} = \left(\mathbf{S}^{-1}\right)^{\alpha\beta}$. The density matrix operator of (2.77), can be cast in terms of a set WFs as in (2.69). The corresponding non-orthogonal case, in position representation, reads

$$\rho(\mathbf{r}, \mathbf{r'}) = \phi_\alpha(\mathbf{r}) K^{\alpha\beta} \phi^*_\beta(\mathbf{r'}), \tag{2.90}$$

where the density kernel of (2.69) for orthogonal functions, becomes $K^{\alpha\beta}$ in the non-orthogonal case

$$K^{\alpha\beta} = \langle \phi^\alpha | \hat{\rho} | \phi^\beta \rangle = \sum_i M^\alpha{}_i f_i \left(M^\dagger\right)^\beta_i. \tag{2.91}$$

Furthermore, the Hamiltonian matrix in the non-orthogonal basis is

$$H_{\alpha\beta} = \langle \phi_\alpha(\mathbf{r}) | \hat{H} | \phi_\beta(\mathbf{r}) \rangle. \tag{2.92}$$

This notation, where the Hamiltonian is a fully covariant tensor and the density kernel is a fully contravariant one is known as the covariant integral representation[164], which is the one adopted in this thesis. Another possibility, known as the *natural* representation, is given by representing all the kets as covariant tensors and all the bras as contravariant ones, so that the Hamiltonian matrix is written as $H^\alpha{}_\beta$. In this representation, all the equations would be isomorphic to the orthogonal case, greatly simplifying the notation. However, as we will see in the next section, when using localised functions with covariant indeces, the resulting contravariant functions are no longer localised in real space. Hence, the Hamiltonian matrix would no be less sparse in this representation.

Derivatives of scalars, (0,0)-tensors, with respect to covariant(contravariant) vectors generates contravariant(covariant) vectors, such as

$$\frac{\partial A}{\partial \varphi^\mu} = a_\mu, \tag{2.93}$$

where A is a scalar, φ^μ is a contravariant vector and a_μ a covariant vector. An analogous equation can readily be written for the derivative of A with respect to covariant vectors

φ_μ, resulting in contravariant vectors a^μ. Similarly, for rank 2 tensors we find

$$\frac{\partial A}{\partial P^{\mu\nu}} = a_{\mu\nu} \quad \frac{\partial A}{\partial P_\mu{}^\nu} = a^\mu{}_\nu \quad \frac{\partial A}{\partial P^\mu{}_\nu} = a_\mu{}^\nu \quad \frac{\partial A}{\partial P_{\mu\nu}} = a^{\mu\nu}. \tag{2.94}$$

It is worth mentioning that within linear-scaling methods one usually assumes that large simulation cells are employed and congruently only $\Gamma-$ point calculations are performed. This is the reason why the density kernel in (2.91) does not depend on lattice translation vectors. Another nice feature of $\Gamma-$ point only calculations is that the supporting function can always be chosen to be real functions. For $\rho(\mathbf{r}, \mathbf{r}')$ to be Hermitian, the matrix $K^{\alpha\beta}$ must be Hermitian. In our case, $K^{\alpha\beta}$ must be a real symmetric matrix.

2.4.2 The Onetep program

In Onetep, the supporting functions are known as Non-orthogonal generalised Wannier functions (NGWFs) [167]. They are atom-centred strictly localised functions. The localisation constraint is enforced by choosing a spherical region centred on atom I, say, for each $\phi_\alpha(\mathbf{r})$ $\mathrm{SR}_I(\phi_\alpha)$, outside of which the function vanishes. A single parameter, the cut-off radius r_c^α is used to specify the spherical volume for each NGWF[10]. Enforcing strict confinement on the NGWFs results in matrices such as the overlap $S_{\alpha\beta}$ and the Hamiltonian $H_{\alpha\beta}$ to be sparse. The density matrix cut-off of (2.84) can be strictly imposed by requiring that density matrix elements $K^{\alpha\beta}$, corresponding to NGWFs whose centres are separated by more than a chosen cut-off distance r_K, to be zero[11]. If the density kernel matrix $\mathbf{K}$ is truncated, the result is a sparse matrix.

However, for representing the NGWFs in real space, we need to expand them in a localised, ideally orthogonal, basis set $\{D_i(\mathbf{r})\}$. As mentioned at the end of the previous section, there are several options for this purpose, such as numerical orbitals, pseudoatomic orbitals, b-splines etc.. Remarkably, the performance of the linear-scaling code crucially depend on the properties of the underlying basis adopted. In Onetep, NGWFs are expanded in terms of periodic cardinal sine functions (psinc) [167, 168], sometimes

[10] This localisation criterion is conceptually equivalent to applying a spherical truncation operator

$$\Theta_I(\mathbf{r}) = \theta(r_c^\alpha - |\mathbf{R}_I - \mathbf{r}|)$$

onto $\phi_\alpha(\mathbf{r})$, where $\mathbf{R}_I$ is the position vector of atom I and $\theta(\mathbf{r})$ is the spherical Heaviside function.

[11] Obviously, $r_\mathrm{K} > 2(r_c^\alpha + r_c^\beta)$.

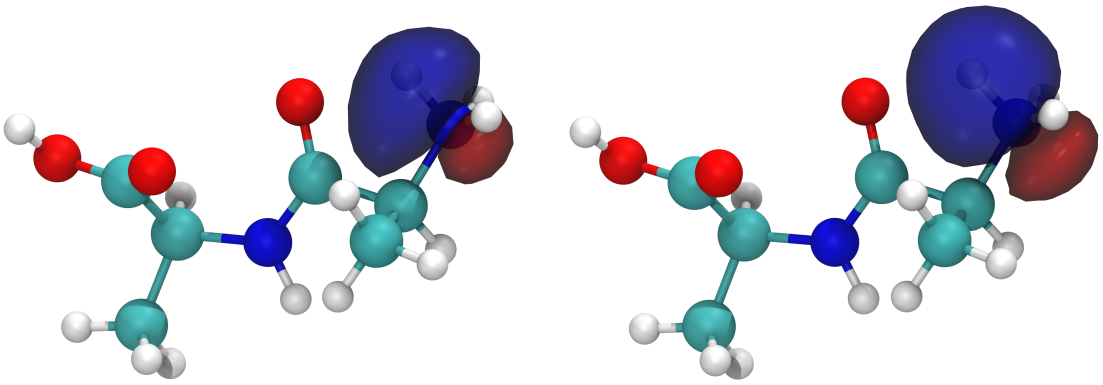

(a) NGWFs **(b)** MLWFs

Figure 2.3: Comparison of a single NGWFs and a single MLWFs on the terminal Nitrogen atom in 2-Ala+.

also referred as periodic[12], bandwidth limited Dirac delta functions

$$D_i(\mathbf{r}) = \frac{1}{N_1}\frac{1}{N_2}\frac{1}{N_3}\sum_r\sum_s\sum_t e^{ir\mathbf{b}_1+s\mathbf{b}_2+t\mathbf{b}_3}\cdot(\mathbf{r}-\mathbf{r}_i), \tag{2.95}$$

where the $\mathbf{b}_i$ are reciprocal lattice vectors and the sums run over all the grid points of the corresponding spatial dimension. There is a psinc function centred at each grid point in the simulation cell. Moreover, they are non-zero only at the grid point on which they are centred, cf. Fig. 2.4. This property of being non-zero only on one grid point, and zero on all others is known as *cardinality*. A unitary transformation relates the psincs functions to the plane-waves basis set that can be represented by the real space grid of the simulation cell. Hence, they span the same Hilbert space, and share many of the good properties listed in Sec. 2.4. For instance, psinc functions are orthogonal, naturally obey to periodic conditions, can be used very efficiently in combination with FFT techniques, they form a systematic set, such as completeness can be approached by tuning a single parameter: the kinetic energy cut-off (or equivalently the grid spacing of the simulation cell). It is worth mentioning that in order for the basis functions to be both real and orthogonal, we must impose an odd number of grid points N_i in each direction i of the simulation cell. Therefore any NGWF, may be expressed as

[12] With the period of the simulation cell.

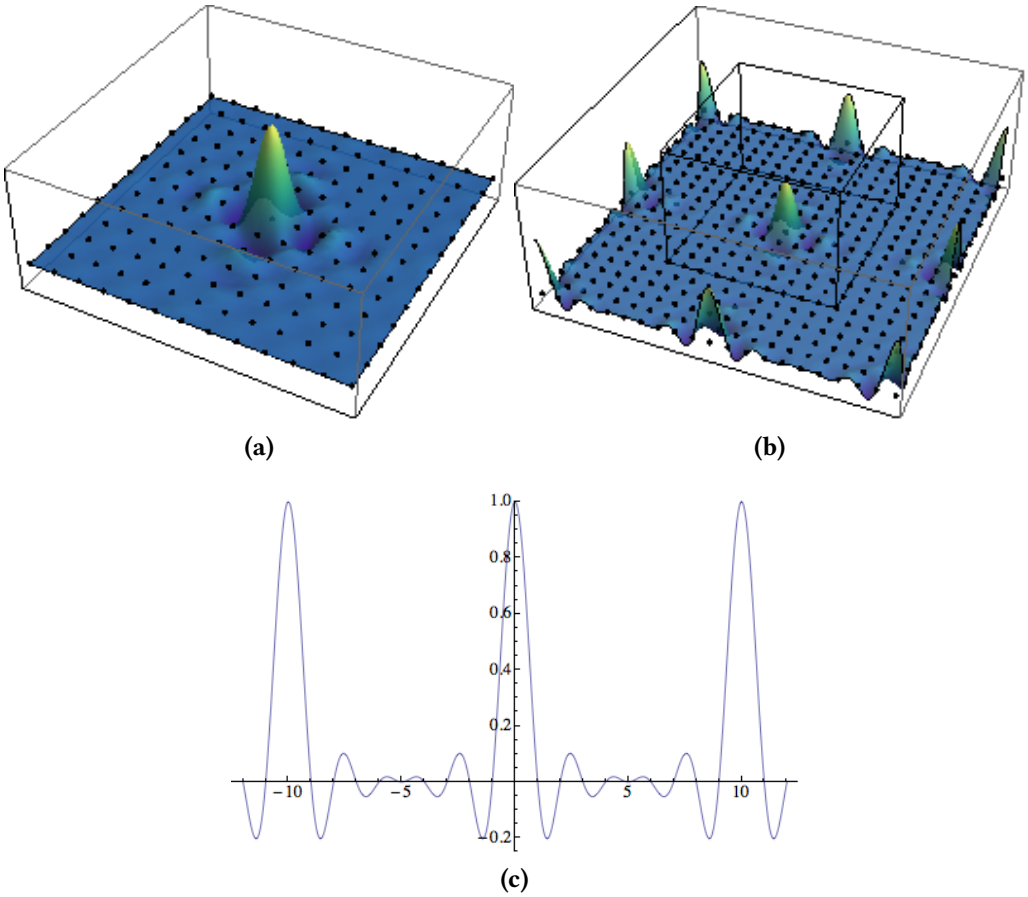

Figure 2.4: a) Periodic cardinal sinc function in 10x10 primitive cell with grid points (black dots) and grid unit grid spacing. b) Periodic cardinal sinc function in primitive cell and periodic images. c) Cross-section along a Cartesian axis (1D psinc function).

$$\phi_\alpha(\mathbf{r}) = \sum_i D_i(\mathbf{r}) d_{i\alpha}, \tag{2.96}$$

where, in principle, the sum runs over all the basis functions $D_i(\mathbf{r})$ in the simulation cell. In practice, the "FFT box" technique, developed by Skylaris *et al.* [169], is used instead. This technique reduces the cost to the ON regime by performing FFTs in a smaller box whose size is independent of the total number of atoms, and determined only by the NGWFs radii[13]. As a consequence, this formulation can take advantage of the locality of the density matrix in real space, and use sparse linear algebra in order to perform calculations that scale linearly with the system size.

In ONETEP a direct energy minimisation approach is employed to solve the electronic

[13]The FFT box is defined as the minimum box that contains any pair of NGWFs that exhibit a non-zero overlap.

problem. The total energy functional in ONETEP is given by (2.30)

$$E[\{K^{\alpha\beta}\},\{\phi_\alpha(\mathbf{r})\}] = \mathrm{tr}[\mathbf{KH}] - E_{\mathrm{DC}} + E_{\mathrm{Ewald}} = E_{\mathrm{BS}} - E_{\mathrm{DC}} + E_{\mathrm{Ewald}} \quad (2.97)$$

$$= T_{\mathrm{ind}} + E_{\mathrm{H}}[n] + E_{\mathrm{loc}}[n] + E_{\mathrm{nl}}[n] + E_{\mathrm{XC}}[n] + E_{\mathrm{Ewald}}, \quad (2.98)$$

where E_{DC} is the double counting correction, cf. (2.30). In the last row, $E_{\mathrm{loc}}[n]$ and $E_{\mathrm{nl}}[n]$ are the energy components from the local part and non-local part of the pseudopotential, respectively. The remaining two terms are the usual Hartree energy $E_{\mathrm{H}}[n]$ and kinetic energy for independent particles T_{ind}. Finally, Ewald summation[170] is adopted to compute the electrostatic interactions between nuclei E_{Ewald} within periodic boundary conditions. The Hamiltonian matrix elements $H_{\alpha\beta} = (\mathbf{H})_{\alpha\beta}$ in (2.98) are given by

$$H_{\alpha\beta} = \langle\phi_\alpha(\mathbf{r})| -\frac{1}{2}\nabla^2 + V_{\mathrm{loc}} + V_{\mathrm{nl}} + V_{\mathrm{H}} + V_{\mathrm{XC}}|\phi_\beta(\mathbf{r})\rangle\,. \quad (2.99)$$

In ONETEP, two minimisation regimes are available depending on the kind of NGWFs optimisation employed:

1. *in situ* NGWFs optimisation (minimal set): The electronic problem is solved self-consistently by optimising both the matrix elements of the density kernel $\{K^{\alpha\beta}\}$, and the expansion coefficients $d_{i\alpha}$ of the NGWFs[18, 171] in terms of an underlying psinc basis (2.96) (two nested loop regime):

$$E_0 = \min_{\{\phi_\alpha(\mathbf{r})\}} \min_{\{K^{\alpha\beta}\}} \mathcal{L}[\{\phi_\alpha(\mathbf{r})\},\{K^{\alpha\beta}\}], \quad (2.100)$$

   where $\mathcal{L}$ represents a modified energy functional accounting for the constraints on the density matrix.

2. fixed NGWFs (non-minimal set): The electronic problem is solved self-consistently by improving only the elements of the density kernel, for a set of fixed NGWFs that have been suitably initialised, e.g. to PAOs (single loop regime):

$$E_0 = \min_{\{K^{\alpha\beta}\}} \mathcal{L}'[\{\bar{\psi}_{nlm}(\mathbf{r})\},\{K^{\alpha\beta}\}]. \quad (2.101)$$

   The PAOs $\{\bar{\psi}_{nlm}(\mathbf{r})\}$ are obtained by solving the KS equations for the pseudoatom[172], within a sphere whose radius is equal to the radius of the spherical region of the corresponding NGWF. Given that the atomic pseudopotential has spherical symmetry, the pseudo atomic orbital solution can be cast as a product of a radial part and a (real) spherical harmonic $Z_{l,m}(\theta,\varphi)$. For the radial part we

choose the normalised[14] spherical Bessel functions $\tilde{j}_l(q_{l,\sigma}r), \sigma = 0, \ldots, n_j$, such as $q_{l,\sigma}r_c^\alpha$ are the zeros of the spherical Bessel functions associated with a given NGWF:

$$\tilde{\psi}_{nlm}(\mathbf{r}) = \sum_\sigma c_{n,\sigma}\tilde{j}_{l,\sigma}(q_{l,\sigma}r)Z_{l,m}(\theta,\varphi). \tag{2.102}$$

For both regime 1) and regime 2) a minimisation with respect to the degrees of freedom in the density kernel $\mathbf{K}$ has to be performed, hereafter named the inner loop minimisation. However, as anticipated in (2.100), the functional $\mathcal{L}[n]$ has to be different from $E[n]$ in (2.98) in order to satisfy the constraints on the density matrix. For insulators and semi-conductors, the occupation numbers f_i have to be either 0 or 1, the Fermi-Dirac becomes the Heaviside distribution and the density matrix is idempotent. Congruently, the density kernel has to satisfy the normalisation constraints and idempotency constraints during the minimisation. Li, Nunes and Vanderbilt (LNV) [173, 174], have proposed the following approach to satisfy the non-linear idempotency constraints, based on McWeeny purification[65]: an auxiliary density kernel $\mathbf{L}$ is introduced, which has the same localisation constraints as $\mathbf{K}$ and whose eigenvalues lie in the range $\left[\frac{1-\sqrt{5}}{2}, \frac{1+\sqrt{5}}{2}\right]$. A new "more idempotent" density kernel $\mathbf{K}$ is obtained by applying a McWeeny purification on $\mathbf{L}$

$$\mathbf{K} = 3\mathbf{LSL} - 2\mathbf{LSLSL}, \tag{2.103}$$

recursively applying (2.103) leads to a full idempotent $\mathbf{K}$[175], i.e. $\mathbf{KSK} = \mathbf{K}$. The LNV energy functional is therefore given by

$$E_{\text{LNV}}[\{L^{\alpha\beta}\}, \{\phi_\alpha(\mathbf{r})\}] = E[\{K^{\alpha\beta}\}, \{\phi_\alpha(\mathbf{r})\}], \tag{2.104}$$

where the energy functional on the r.h.s. is the same as (2.99). On the other hand, normalisation of the density matrix results in a linear constraint that can be easily addressed by defining a new functional $\mathcal{L}$ as

$$\mathcal{L}[\{\phi_\alpha(\mathbf{r})\}, \{K^{\alpha\beta}\}] = E_{\text{LNV}} - \mu\left(\text{tr}[\mathbf{KS}] - N_{\text{elec}}\right), \tag{2.105}$$

where μ is an undetermined Lagrange multiplier and N_{elec} is the number of electrons. Performing an unconstrained minimisation on $\mathcal{L}$ would automatically return a normalised density matrix, were μ known. However, the Lagrange multiplier is unknown during the minimisation. To solve the problem Li, Nunes and Vanderbilt proposed a slightly

[14] Normalised within the sphere of radius r_c^α, i.e. $\int_0^{r_c^\alpha} \mathrm{d}r \left|\tilde{j}_l(q_{l,\sigma}r)\right|^2 r^2 = 1$.

different definition for the density kernel:

$$\widetilde{\mathbf{K}} = \frac{N_{\text{elec}}}{\text{tr}[\mathbf{KS}]}\mathbf{K}, \tag{2.106}$$

such as $\text{tr}[\mathbf{K}'\mathbf{S}] = N_{\text{elec}}$ at all times by construction. A variant of the LNV algorithm has been put forward by Millam and Scuseria [176], where an estimate for the Lagrange multiplier is given by imposing conservation of the number of electrons to first order, making the density kernel rescaling unnecessary.

The minimisation process is carried out directly using either the conjugate gradient method or the steepest descent method. Both methods demand the evaluation of the functional derivative $\frac{\delta\mathcal{L}}{\delta L^{\alpha\beta}} = g_{\alpha\beta}$, which is a (0,2)-tensor, to generate the search direction $\mathbf{g}$ in the linear search step. The formula of the energy gradient $g_{\alpha\beta}$ for the corrected LNV energy functional it turns out to be

$$\frac{\delta E_{\text{LNV}}}{\delta L^{\mu\nu}} = \frac{\partial \widetilde{K}_{\iota\kappa}}{\partial L^{\mu\nu}} H_{\kappa\iota}, \tag{2.107}$$

which, ones the rescaled density kernel in (2.106) is used, yields

$$\frac{\delta E_{\text{LNV}}}{\delta L^{\mu\nu}} = \frac{N_{\text{elec}}}{\text{tr}[\mathbf{KS}]}\left[(3\mathbf{I} - 2\mathbf{SL})\mathbf{SLH} + \mathbf{HLS}(3\mathbf{I} - 2\mathbf{LS}) - \mathbf{SLHLS} - \mathbf{T}\right]_{\mu\nu}, \tag{2.108}$$

where $\mathbf{I}$ is the identity matrix and $\mathbf{T}$ is given by

$$6\frac{\text{tr}[\mathbf{KH}]}{N_{\text{elec}}}(\mathbf{LSL} - \mathbf{LSLSL}).$$

In deriving (2.108) we have used the definition in (2.103) and also the following property

$$\begin{aligned}\frac{\partial K^{\iota\kappa}}{\partial L^{\mu\nu}} &= 3\left(\delta^{\iota}{}_{\mu}S_{\nu\sigma}L^{\sigma\kappa} + L^{\iota\sigma}S_{\sigma\mu}\delta^{\kappa}{}_{\nu}\right) - 2\Big(\delta^{\iota}{}_{\mu}S_{\nu\sigma}L^{\sigma\tau}S_{\tau\zeta}L^{\zeta\kappa} + \\ &\quad L^{\iota\sigma}S_{\sigma\mu}S_{\nu\tau}L^{\tau\kappa} + L^{\iota\sigma}S_{\sigma\tau}L^{\tau\zeta}S_{\zeta\mu}\delta^{\kappa\nu}\Big).\end{aligned} \tag{2.109}$$

However, to maintain the correct tensor character of the auxiliary density kernel (a (2,0)-tensor), the search direction has to be transformed to a fully contravariant tensor. This is achieved by tensor contraction with the inverse overlap matrix

$$g^{\alpha\beta} = S^{\alpha\sigma}g_{\sigma\tau}S^{\tau\beta}.$$

Once the search direction exhibits the correct tensor character it can be used in the linear

search step:

$$\mathbf{L}_{\text{new}} = \mathbf{L}_{\text{old}} + \lambda \mathbf{g}, \tag{2.110}$$

where λ is usually found via a parabolic fit, although sometimes a cubic or quartic fit is required. Once a new $\mathbf{L}$ has been found a series of purification steps (2.103) are performed to generate an idempotent $\mathbf{K}$. At convergence of the inner loop, the Hamiltonian and the density matrix has to commute

$$[\mathbf{HKS} - \mathbf{SKH}] = 0. \tag{2.111}$$

In regime 1), once the density kernel has been optimised, one also need to consider an outer loop, where the energy is minimised with respect to the degrees of freedom in the NGWFs. As in the inner loop, we can use conjugate gradient or steepest descent to carry out the minimisation. Thus, we need to evaluate the functional derivative $\frac{\delta \mathcal{L}}{\delta \phi^*_\alpha(\mathbf{r})} = g^\alpha(\mathbf{r})$, which is a (1,0)-tensor. The search direction "vector" $g_\alpha(\mathbf{r})$ is expanded in the psinc basis and localisation constraints are applied, such as localisation of NGWFs is preserved along the minimisation. In the case of the corrected LNV functional it reads

$$\frac{\delta E_{\text{LNV}}}{\delta \phi^*_\alpha(\mathbf{r})} = \frac{N_{\text{elec}}}{\text{tr}[\mathbf{KS}]} \left[\hat{H}\phi_\beta(\mathbf{r})\widetilde{K}^{\beta\alpha} + \phi_\beta(\mathbf{r})Q^{\beta\alpha} - \phi_\beta(\mathbf{r})T^{\beta\alpha} \right], \tag{2.112}$$

where the matrix $\mathbf{Q}$ is given by

$$\mathbf{Q} = 3\mathbf{LHL} - 2\mathbf{LSLHL} - 2\mathbf{LHLSL}. \tag{2.113}$$

To recover the correct tensor character one needs to perform a tensor contraction with the metric tensor, i.e. the overlap $S_{\alpha\beta}$, as $g_\alpha(\mathbf{r}) = S_{\alpha\beta} g^\beta(\mathbf{r})$. The linear search step is given by

$$\phi^{\text{new}}_\alpha(\mathbf{r}) = \phi^{\text{old}}_\alpha(\mathbf{r}) + \lambda g_\alpha(\mathbf{r}). \tag{2.114}$$

After an update of the NGWFs, the density kernel no longer satisfies the condition of minimum (the Hamiltonian matrix changes as we change the NGWFs), therefore the whole procedure must be iterated to self-consistency. Convergence of the outer loop is achieved when the root-mean-square (RMS) of the energy gradient $g^\alpha(\mathbf{r})$ is below a predefined threshold.

For metals or systems with defects, one usually needs to introduce an electronic temperature, the Fermi-Dirac distribution 2.32 is no longer equal to the Heaviside distribution and fractional occupancies are allowed. A new functional, known as the Helmholtz free energy functional, which includes the entropic term S has to be considered instead of

2.98

$$A[T, \varepsilon_i, \{\psi_i\}] = \sum_i f_i(\varepsilon_i) \langle \psi_i | \hat{T}_{\text{ind}} | \psi_i \rangle + \int \mathbf{dr}\, V_{\text{ext}}(\mathbf{r}) n(\mathbf{r}) + E_{\text{H}}[n] + E_{\text{XC}}[n] - TS[\{f_i(\varepsilon_i)\}], \tag{2.115}$$

where the electronic entropy $S[\{f_i(\varepsilon_i)\}]$ is given by

$$S[\{f_i(\varepsilon_i)\}] = \sum_i f_i(\varepsilon_i) \ln f_i(\varepsilon_i) + [1 - f_i(\varepsilon_i)][\ln(1 - f_i(\varepsilon_i))] \tag{2.116}$$

and the occupation numbers $f_i(\varepsilon_i)$ are given by the FD distribution in 2.32.

A different strategy is therefore demanded for the inner loop minimisation. Three schemes have been implemented in ONETEP to this purpose: the ensemble DFT[177] (EDFT) method, the Fermi-operator expansion[178] method and density mixing. However, in this thesis we will not make use of methods for metals as we will deal with molecular systems through out. Our method of choice will be therefore the LNV method. For a more detailed discussion on how localised functions are expanded in terms of psinc functions, and how localisation constraints promote the use of sparse algebra, the Reader is referred to18, 41, 168.

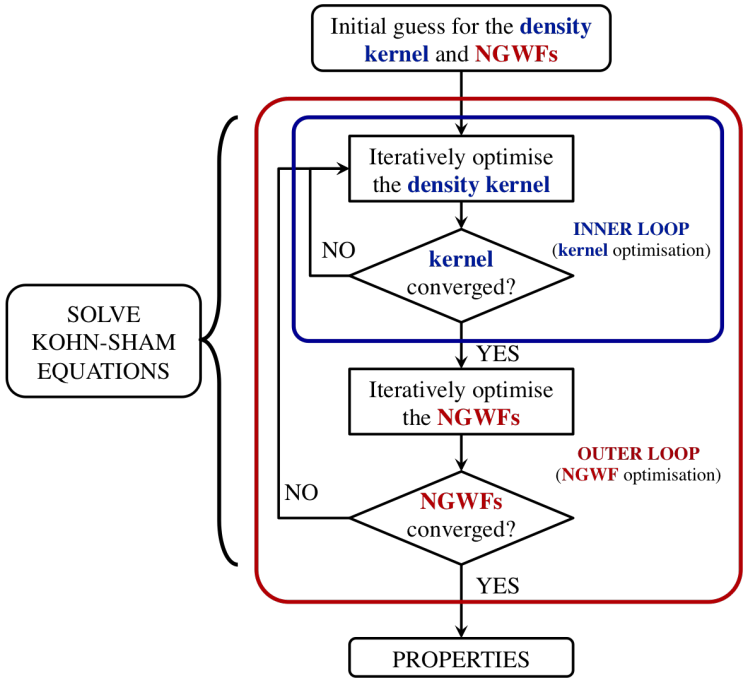

(a) *in situ* optimisation

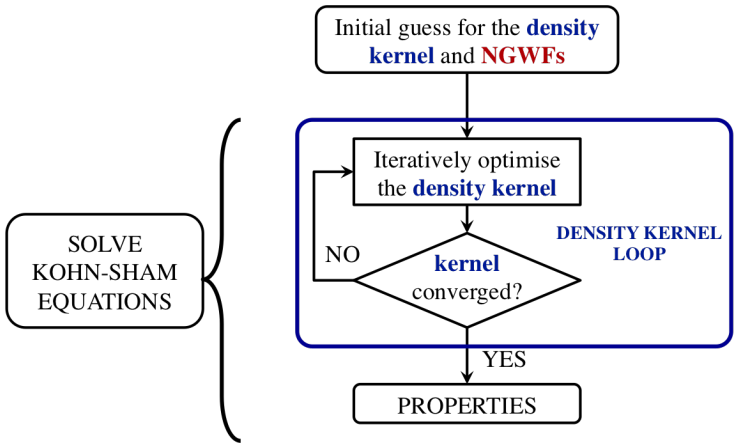

(b) No NGWF optimisation (PAOs)

Figure 2.5: Two regimes to achieve self-consistency to find the ground state density within the ONETEP approach. a) *In situ* optimisation of NGWFs and density kernel optimisation as given in 2.4.2. b) Fixed NGWFs (non-minimal basis) and density kernel optimisation only.

Chapter 3

Born-Oppenheimer Molecular Dynamics within linear-scaling DFT

> *λέγει που Ἡράκλειτος ὅτι ΄πάντα χωρεῖ καὶ οὐδὲν μένει΄*
> *Heraclitus says that 'everything changes and nothing remains still'*
> *καὶ ΄δὶς ἐς τὸν αὐτὸν ποταμὸν οὐκ ἂν ἐμβαίης΄*
> *and 'you cannot step twice into the same stream'*

Plato, Cratylus, *Paragraph 402 section a line 8*

Abstract

This chapter deals with *ab initio* molecular dynamics (MD), in particular Born-Oppenheimer molecular dynamics (BOMD), and the implementation of BOMD equations in the Onetep code. The first two sections describe how these equations can be elegantly derived from the time-dependent Schrödinger equation. In Section 3.3, I show how BOMD equations are discretised and solved numerically, using the well-known velocity Verlet integrator. When performing both classical MD and *ab initio* MD one is often interested in keeping the temperature of the system fixed to a certain value. This is achieved by coupling the system with a thermostat. Statistical ensembles and thermostats constitute the core material of Section 3.4, which also shows how several kinds of thermostats can be integrated in the velocity Verlet scheme. Finally, in Section 3.5 the different terms constituting the total ionic force within the Onetep framework are explained. The use of non-orthogonal strictly localised atom-centred functions compels us to consider additional (in the Hellmann-Feynman sense) terms in the forces, known as

Pulay terms. Interestingly, these terms are in general approximated (this is true for all the linear-scaling codes using non-orthogonal localised atom-centred functions, optimised *in situ*). The effect of these approximations on the quality of forces, and consequently on the energy conservation in long MD simulation, is discussed. This section ends with showing the effect of these approximations through some testcases. Some of the terminology and concepts introduced here will be later used in Chapter 4 and Chapter 5.

3.1 *Ab initio* molecular dynamics

In the previous two chapters, we dwelt on the electronic problem in QC and how to find approximate while accurate solutions. In particular, in chapter 2, we showed that KS-DFT is an effective route to accurately address the electronic problem for small-to-medium system size, due to the unfavourable $O\left(N^3\right)$ scaling. In Section 2.4 we presented the relevant concepts behind linear-scaling methods to overcome this obstacle, allowing for the study of large systems. The topic of this chapter is *ab initio* molecular dynamics (AIMD)[14, 29, 30, 179], and in particular Born-Oppenheimer molecular dynamics (BOMD) within the linear-scaling DFT framework.

Molecular dynamics simulations, together with Monte Carlo simulations, are undeniably one of the most successful tools to address the many-body problem. Since the first classical MD simulations in the late 1950s, a plethora of schemes employing a hierarchy of approximations for the description of inter-atomic interactions have emerged, ranging from classical fixed charge models to fully *ab initio* treatments. In classical MD simulations the inter-atomic potential is defined in terms of a parametrised force field, where parameters are obtained from experimental studies or from high-level quantum-mechanical calculations, although more sophisticated polarisable force fields exist, cf. Sec. 5.2. Conversely, AIMD simulations do not rely on any external parameter, and forces are computed "on-the-fly" directly from first principles electronic structure calculations. This endows AIMD simulations with a higher predictive power over classical MD simulations, especially when dealing with chemically complex processes, e.g. charge transfer, polarisation, the breaking and formation of chemical bonds etc. where the classical description is poor or in some force fields missing entirely. Most relevant is the fact that unforeseen phenomena, can simply emerge during the simulation. For these reasons, AIMD simulations have been successfully used to study either systems that are inherently dynamical, such as in conformational analysis of (bio)molecules at finite temperatures[2, 180, 181], chemical reaction paths in gas and condensed phase[182], surface (adsorption) processes[36], and solvation phenomena[37, 183, 184], or as an alternative method to energy minimisation techniques[14], for the search of equilibrium

structures of molecules, clusters, and surfaces at different pressure and temperature conditions[16, 39, 40]. Despite its advantages, there are some obstacles that arise when molecular dynamics is put on *ab initio* grounds. For example the correlation lengths and relaxation times that are accessible are much smaller than the ones reachable in classical molecular dynamics (from microseconds to tens of picoseconds). Nowadays, this drawback can be countered in part by the increasing power of parallel computing. Nonetheless, challenges remain in finding models and methods that are able to adequately describe complex environments and show a favourable accuracy-efficiency trade-off. In this regard, promising approaches include linear-scaling density functional theory[20, 143], cf. Sec. 2.4, classical polarisable force fields[185, 186], cf. Sec. 5.2, self-consistent field (SCF) tight-binding[187] and semi-empirical quantum mechanical (SQM) approaches[188].

There are four main ingredients required to perform a molecular dynamics simulation: 1) equations of motion, e.g. Hamilton's equations, Langevin equation, time-dependent Schrödinger equation, etc.; 2) a model to describe the interactions between the constituents; 3) an integrator and 4) a statistical ensemble. In Sec. 3.2 will derive the BOMD equations from the time-dependent Schrödinger equation. Properties of good integrators for MD simulations will be presented in Sec. 3.3, and we derive the velocity Verlet from the Liouville equation. In Sec. 3.4 we will consider the role of statistical ensembles and ergodicity in simulations. Finally, in Sec. 3.5 we will consider the importance of accurate forces to contain energy drift within the linear-scaling DFT approach.

3.2 Born-Oppenheimer molecular dynamics from TDSE

We have showed how the electronic problem can be separated from the nuclear one through the Born-Oppenheimer approximation, cf. Sec. 1.7. As a result of the BO ansatz one finds two coupled TISE-like equations (1.29) and (1.30). Inserting the BO ansatz (1.28) into the time-dependent Schrödinger equation (1.5), yields

$$\left(-\sum_I \frac{1}{2M_I}\nabla_I^2 + \epsilon_s(\{\mathbf{R}_I\})\right)\chi_s(\{\mathbf{R}_I\}) = i\hbar\partial_t\chi_s(\{\mathbf{R}_I\}), \tag{3.1}$$

where we have multiplied on the left by $\Phi_s^*(\{\mathbf{r}_i\};\{\mathbf{R}_I\})$ and integrated over all electronic coordinates. We have also neglected both the diagonal and off-diagonal coupling terms (1.38). Our goal is to approximate the nuclei as classical point charges. This can be attained through a well-known semi-classical approach. First, we rewrite the nuclear wave-function as

$$\chi_s(\{\mathbf{R}_I\},t) = A_s(\{\mathbf{R}_I\},t)\exp\left[iS_s(\{\mathbf{R}_I\},t)/\hbar\right], \tag{3.2}$$

where both the amplitude $A_s(\{\mathbf{R}_I\}, t)$ and the phase $S_s(\{\mathbf{R}_I\}, t)$ are real functions. Inserting (3.2) into (3.1) and separating the real and the imaginary part, yields

$$\frac{\partial S_s}{\partial t} + \sum_I \frac{1}{2M_I}(\nabla_I S_s)^2 + \epsilon_s = \hbar^2 \sum_I \frac{1}{2M_I}\frac{\nabla_I^2 A_s}{A_s} \tag{3.3}$$

$$\frac{\partial A_s}{\partial t} + \sum_I \frac{1}{M_I}(\nabla_I A_s)(\nabla_I S_s) + \sum_I \frac{1}{2M_I} A_s(\nabla_I^2 S_s) = 0. \tag{3.4}$$

The second of the above equations (3.4), can be recast into a continuity equation for the nuclear density $\rho_s = |\chi_s|^2 \equiv A_s^2$

$$\frac{\partial \rho_s}{\partial t} + \sum_I \nabla_I \mathbf{J}_{s,I} = 0, \tag{3.5}$$

where $\mathbf{J}_{s,I} = A_s^2(\nabla_I S_s)/M_I$ represents a current density. Equation (3.5) ensures the conservation of nuclear density in the presence of a flux and does not depends on $\hbar$, thereby is valid in the classical limit as well. The equation for the phase $S_s(\{\mathbf{R}_I\}, t)$ (3.3) contains a term proportional to $\hbar^2$. In the classical limit $\hbar \to 0$, we obtain

$$\frac{\partial S_s}{\partial t} + \sum_I \frac{1}{2M_I}(\nabla_I S_s)^2 + \epsilon_s = \frac{\partial S_s}{\partial t} + H_s(\{\mathbf{R}_I\}, \{\nabla_I S_s\}) = 0. \tag{3.6}$$

This equation is now in the form of a Hamilton-Jacobi equation of classical mechanics. Hence, the classical Hamiltonian can be recovered through

$$H_s(\{\mathbf{R}_I\}, \{\mathbf{P}_I\}) = T(\{\mathbf{P}_I\}) + V_s(\{\mathbf{R}_I\}) = H_s(\{\mathbf{R}_I\}, \{\nabla_I S_s\}), \tag{3.7}$$

with the substitution $\mathbf{P}_I \equiv \nabla_I S$, where we have dropped the subscript s, since we are now dealing with classical point charges with no multiple quantum states. This implies that the BO potential energy is given by $E^{\mathrm{BO}}(\{\mathbf{R}_I\}) = \epsilon(\{\mathbf{R}_I\})$ in (1.36). Therefore, in Born-Oppenheimer molecular dynamics BOMD, one simply solve the static electronic problem to find $\epsilon(\{\mathbf{R}_I\})$ at every MD step, with no real electron dynamics involved, since electrons are assumed to instantaneously adjust to the motion of the nuclei. As we have discussed in the previous chapter, many methods are available to the end of solving the static electronic problem, showing different accuracy and scaling, e.g. Hartree-Fock and DFT. Hence, at every MD step, an energy minimisation or a diagonalisation has to be performed. With the Hamiltonian in (3.7), Hamilton's equations for the classical nuclei

read

$$\frac{\mathrm{d}\mathbf{R}_I}{\mathrm{d}t} = \frac{\partial H(\{\mathbf{R}_I\},\{\mathbf{P}_I\})}{\mathbf{P}_I} = \frac{\mathbf{P}_I}{M_I}, \tag{3.8}$$

$$\frac{\mathrm{d}\mathbf{P}_I}{\mathrm{d}t} = -\frac{\partial H(\{\mathbf{R}_I\},\{\mathbf{P}_I\})}{\mathbf{R}_I} = \nabla_I H(\{\mathbf{R}_I\},\{\mathbf{P}_I\}) = -\nabla_I E^{\mathrm{BO}}(\{\mathbf{R}_I\}), \tag{3.9}$$

or equivalently

$$M_I \frac{\mathrm{d}^2\mathbf{R}_I}{\mathrm{d}t^2} = -\nabla_I E^{\mathrm{BO}}(\{\mathbf{R}_I\}). \tag{3.10}$$

Within LS-DFT framework, BOMD equations (3.9) assume the following form

$$M_I \frac{\mathrm{d}^2\mathbf{R}_I}{\mathrm{d}t^2} = -\nabla_I \left[\min_{\{\phi_\alpha(\mathbf{r})\}} \left[\min_{\{K^{\alpha\beta}\}} E[\{K^{\alpha\beta}\},\{\phi_\alpha(\mathbf{r})\};\{\mathbf{R}_I\}] \right] \right]. \tag{3.11}$$

To solve BOMD equations on a computer, one needs to introduce a finite time-step and use a discretised version of (3.9), cf. Sec. 3.3. Since no real electron dynamics is involved, the largest time-step achievable is limited only by the fast motion of light nuclei. For example, the period of an oscillation of a Hydrogen atom in H_2O at 300 K is circa 10 fs. Using 10 steps to sample this motion implies that a good time-step for the simulation is ~1 fs. One can use even a larger time-step if the light nuclei are constrained to rigidly move with the system, thus eliminating their fast rotovibrational motion from the picture.

BOMD represents one of the approaches to include the electronic structure in molecular dynamics simulations. However, other methods exist, notably Car-Parrinello MD[30] (CPMD), Ehrenfest MD[29] and Path integral MD (PIMD)[189–191], which differ from BOMD in the way the quantum electrons and the classical nuclei are coupled. Amongst these, CPMD is the most popular one. Within the CPMD framework, the electrons are treated as classical fields, with a fictitious mass μ, and a fictitious kinetic energy, thus restoring an electron dynamics. The starting point to derive the CPMD equations is the following class of extended Lagrangians[30]

$$\mathcal{L}(\{\mathbf{R}_I\},\{\dot{\mathbf{R}}_I\},\{\psi_i\},\{\dot{\psi}_i\}) = \frac{1}{2}\sum_I M_I \dot{\mathbf{R}}_I^2 - E[\{\psi_i\}] + \frac{\mu}{2}\sum_i |\dot{\psi}_i|^2 + constraints \tag{3.12}$$

where $E[\{\psi_i\}]$ is the expectation value of the electronic Hamiltonian in (1.31) in the $\{\psi_i\}$ basis and the constraints are usually imposed to maintain orthonormality of the ψ_i at each MD step. The true quantum electron dynamics is therefore replaced by a fictitious classical one. By appropriately choosing the value of the mass μ, the PES generated by the CP dynamics can be made to remain close to the BO PES at all times. The advantage of CPMD over BOMD is the possibility of by-passing the minimisation/diagonalisation step

altogether. In fact, at each MD step only an energy and force evaluation is needed, thereby significantly reducing the computational cost per MD step. However, the largest time-step that can be used is limited by the fast motion of the ψ_i, which in turn is determined by μ. In general the ratio between a CPMD time-step and the corresponding BOMD time-step is about 10^{-2}.

3.3 Velocity Verlet integrator

When integrating Hamilton's equations of motion (3.9) on a computer, one needs to introduce a finite time-step, and solve a discretised version of (3.9) at each step, i.e. using an integrator scheme. There are a number of properties that a good integrator has to satisfy. These properties are a direct consequence of the principles of classical Hamiltonian systems. In particular, for molecular dynamics simulations two properties are fundamental: stability and symplecticity.

In Onetep, the classical laws of motion are integrated using a finite scheme algorithm, namely the velocity Verlet[192, 193]. There exist a wide class of integrators, ranging from the leapfrog integrator to *nth* order Runge-Kutta integrator, but the velocity Verlet has the interesting properties that positions, velocities, and forces at time $t + \Delta t$ are obtained from information at time t. Therefore, we need $9N_I$ memory locations to save all the positions, velocities, and forces but we never need to have simultaneously stored these values at two different times for any one of these quantities. The velocity Verlet equations take on the following form:

$$\mathbf{R}(t + \Delta t) = \mathbf{R}(t) + \mathbf{V}(t)\Delta t + \frac{\mathbf{F}(\mathbf{R}(t))}{2M}\Delta t^2 \tag{3.13}$$

this equation is combined with the update for the velocities

$$\mathbf{V}(t + \Delta t) = \mathbf{V}(t) + \frac{\mathbf{F}(\mathbf{R}(t + \Delta t)) + \mathbf{F}(\mathbf{R}(t))}{2M}\Delta t^2 \tag{3.14}$$

The main idea is to compute the velocities at half step, i.e. at $t + \frac{1}{2}\Delta t$, and use this information together with the information of the positions at step t, to obtain positions, velocities, and forces at $t + \Delta t$. The velocity Verlet algorithm can be easily cast into a loop procedure.

Moreover, the error in a single time-step (local error) is proportional to $O(\Delta t^3)$, while the global error is quadratic in Δt [191]. The integrator is also symplectic. All these properties can be derived from a rearrangement of the classical Hamilton equations,

namely the classical Liouvulle equation:

$$\dot{\mathbf{x}}(t) = iL\mathbf{x}(t), \tag{3.15}$$

where $\mathbf{x} = (\{\mathbf{R}_I\}, \{\mathbf{P}_I\})$ is a $6N_I$ state vector, composed of all the positions and conjugate momenta, and L is the classical Liouville operator, given by

$$iL = \sum_I \frac{\partial H}{\partial \mathbf{P}_I}\frac{\partial}{\partial \mathbf{R}_I} - \frac{\partial H}{\partial \mathbf{R}_I}\frac{\partial}{\partial \mathbf{P}_I} = \{\cdot, H\}. \tag{3.16}$$

The solution to (3.15) is formally:

$$\mathbf{x}(t) = e^{iLt}\mathbf{x}(0). \tag{3.17}$$

If we knew how to express the effect of the time-evolution operator e^{iLt} on the state vector $\mathbf{x}$ we could analytically solve all the problem in classical mechanics. However, it turns out that an analytical solution to (3.17) is known only for few simple problems. Hence, in general an approximate solution to (3.17) is required. Now, we are going to assume that the Liouville operator can be cast as the sum of two terms, i.e. $iL = iL_1 + iL_2$, where

$$iL_1 = \sum_I \frac{\partial H}{\partial \mathbf{P}_I}\frac{\partial}{\partial \mathbf{R}_I}, \tag{3.18}$$

and

$$iL_2 = -\sum_I \frac{\partial H}{\partial \mathbf{R}_I}\frac{\partial}{\partial \mathbf{P}_I}. \tag{3.19}$$

However, since $[iL_1, iL_2] \neq 0$ in general, we cannot factorise the exponential in (3.17), i.e. $e^{i(L_1+L_2)t} \neq e^{iL_1 t}e^{iL_2 t}$. On the other hand, we can use the symmetric Trotter formula to write

$$e^{iLt} = e^{i(L_1+L_2)t} = \lim_{\Theta\to\infty}\left[e^{iL_2 t/2\Theta}e^{iL_1 t/\Theta}e^{iL_2 t/2\Theta}\right]^{\Theta}. \tag{3.20}$$

If we take a large but finite value of Θ (this is the approximation above mentioned), we can write $\Delta t = t/\Theta$ and (3.20) becomes

$$e^{i(L_1+L_2)t} \approx \left[e^{iL_2\Delta t/2}e^{iL_1\Delta t}e^{iL_2\Delta t/2}\right]^{\Theta} + O(\Delta t^2). \tag{3.21}$$

Hence, the global error when approximating (3.20) with the symmetric Trotter formula is quadratic in Δt. The local error can be found by simply taking the $1/\Theta$ power of both terms[191] in (3.21)

$$e^{i(L_1+L_2)\Delta t} = \left[e^{iL_2\Delta t/2}e^{iL_1\Delta t}e^{iL_2\Delta t/2}\right] + O(\Delta t^3) \tag{3.22}$$

Consequently, the action of the time-evolution operator (3.20) on the state-vector $\mathbf{x}(t) = (\{\mathbf{R}_I\}, \{\mathbf{P}_I\})$ can be approximated by the consecutive application of the operators in brakets on r.h.s. of (3.22). The application of the first operator $e^{iL_2\Delta t/2}$ gives

$$e^{iL_2\Delta t/2}\mathbf{x}(t) = e^{\Delta t/2\sum_J \mathbf{F}_J \frac{\partial}{\partial \mathbf{P}_J}} \begin{pmatrix} \{\mathbf{R}_I\} \\ \{\mathbf{P}_I\} \end{pmatrix} = \begin{pmatrix} \{\mathbf{R}_I\} \\ \{\mathbf{P}_I\} + \Delta t/2\{\mathbf{F}(\mathbf{R}_I)\} \end{pmatrix}, \tag{3.23}$$

where we have used the fact that coordinates and momenta are independent variables, and also the following property of exponential operators

$$e^{k\frac{\partial}{\partial s}} f(s) = \sum_{n=0} \frac{k^n}{n!} \frac{\partial^n f(s)}{\partial s^n} = f(s+k). \tag{3.24}$$

Now we can apply $e^{iL_1\Delta t}$ to the vector on the r.h.s. of (3.23)

$$e^{\Delta t\sum_J \frac{\mathbf{P}_J}{M_J}\frac{\partial}{\partial \mathbf{R}_I}} \begin{pmatrix} \{\mathbf{R}_I\} \\ \{\mathbf{P}_I\} + \Delta t/2\{\mathbf{F}(\mathbf{R}_I)\} \end{pmatrix} = \begin{pmatrix} \{\mathbf{R}_I\} + \Delta t/M_I\{\mathbf{P}_I\} \\ \{\mathbf{P}_I\} + \Delta t/2\{\mathbf{F}(\mathbf{R}_I + \Delta t\mathbf{P}_I/M_I)\} \end{pmatrix} \tag{3.25}$$

Finally, by applying the operator $e^{iL_2\Delta t/2}$ once more, yields

$$e^{\Delta t/2\sum_J \mathbf{F}_J \frac{\partial}{\partial \mathbf{P}_J}} \begin{pmatrix} \{\mathbf{R}_I\} + \Delta t\{\mathbf{P}_I/M_I\} \\ \{\mathbf{P}_I\} + \Delta t/2\{\mathbf{F}(\mathbf{R}_I + \Delta t\mathbf{P}_I/M_I)\} \end{pmatrix} =$$
$$\begin{pmatrix} \{\mathbf{R}_I\} + \Delta t\{\mathbf{P}_I/M_I\} + \Delta t^2/2\{\mathbf{F}(\mathbf{R}_I)/M_I\} \\ \{\mathbf{P}_I\} + \Delta t/2\{\mathbf{F}(\mathbf{R}_I)\} + \Delta t/2\{\mathbf{F}(\mathbf{R}_I + \Delta t\mathbf{P}_I/M_I + \Delta t^2/2\mathbf{F}(\mathbf{R}_I)/M_I)\} \end{pmatrix} \tag{3.26}$$

which is equivalent to the velocity Verlet equations (3.13) and (3.14), whem employing the substitution $\mathbf{P}_I/M_I = \mathbf{V}_I$.

3.4 Statistical ensembles and thermostats

For this section we will assume that the Reader is familiar with the basic notions of statistical thermodynamics, such as *statistical ensembles*, partition functions, and the thermodynamics laws. Hence, only a succinct and informal introduction is provided here. For a comprehensive review of these topics and how these are deeply related to molecular dynamics simulations the Reader is referred to Ref. 191

Very generally, the macroscopic description of a system in thermodynamic equilibrium is phenomenologically given in terms of few state variables, e.g. temperature, pressure

and chemical potential[1], and a so-called partition function.

When simulating a system consisting of a large number of interacting particles at thermodynamic equilibrium, one faces the problem of how to extract the state variables that macroscopically describe the system from the simulation. The thermodynamic limit, $\lim_{N\to\infty,V\to\infty} \frac{N}{V} = \text{const.}$, where N and V are the number of particles and the volume, respectively, is assumed to hold in actual simulations when employing periodic boundary conditions and large supercells. However, if the overall electric charge of the simulation cell is not zero, the thermodynamic limit does not exist, since the electric flux is ill-defined. In this case different strategies have been designed to overcome this problem, such as the cut-off Coulomb method[194], the Martyna-Tuckerman method[195] or the one based on solving the Poisson equation in open boundary conditions with a multigrid approach[196, 197].

The mathematical tool needed to bridge the description at the molecular level and the description at the macroscopic level is provided by statistical mechanics, and in particular by the concept of thermodynamic ensembles[198, 199]. A thermodynamic ensemble is the set of all the virtual copies of the system, whose microscopic state is compatible with the macroscopic thermodynamic state. In practice, it gives a distribution density $f(\mathbf{x})$ over all possible microstates that exhibit the given macroscopic state variables, e.g. the measured temperature and pressure. An observable Θ is computed by performing en ensemble average $\langle\theta(\mathbf{x})\rangle$, where $\theta(\mathbf{x})$ is the corresponding operator, as

$$\Theta = \langle\theta(\mathbf{x})\rangle = \int \mathrm{d}\mathbf{x}\, f(\mathbf{x})\theta(\mathbf{x}) \tag{3.27}$$

The most natural *ensemble* for MD simulations is the microcanonical or NVE *ensemble*[191, 200]. It is used to describe a closed (or isolated) system, where the number of particles (N), the volume (V), and the internal energy (E) are constants. There are no mass and energy exchange with the *external world*. The entropy of such a system can only increase, and the state of maximum entropy of the system corresponds to the thermodynamic equilibrium. Hence, one simply solves the Hamilton equations, for which the total energy is a constant of motion, with a fix number of particles in a simulation cell of a given volume and with PBC. Theoretically, since the energy of an isolated system is fixed, it can not fluctuate. Therefore, the system has access only to microstates corresponding to that fixed value of the energy E. The corresponding distribution density is simply

$$f(\mathbf{x}) = \frac{1}{Z}\delta(H(\mathbf{x}) - E), \tag{3.28}$$

[1]Some of which are *extensive*, like mass and energy, while others are *intensive*, like temperature and density.

where Z is the so-called partition function, and it represents a normalisation factor, which accounts for the number of all possible states

$$Z = \int \mathrm{d}\mathbf{x}\, \delta(H(\mathbf{x}) - E). \tag{3.29}$$

In actual simulations however, due to finite time steps and finite system sizes the internal energy fluctuates around an average value equal to E, with the magnitude of fluctuations proportional to $1/\sqrt{N}$.

Generally, the microcanonical *ensemble* is not the most suitable to reproduce experimental conditions. In fact, in real experiments it is easier to keep other thermodynamic variables fixed, such as temperature (T) rather than the energy. Hence, we need to modify our simple scheme used for the NVE *ensemble*, to accommodate energy exchange, in particular heat exchange. This can be done by employing thermostats in MD simulations[200]. From the theoretically point of view, we need different *ensembles* to relate the microscopic states to the macroscopic observables in the experimental setups.

This is the reason for the existence of several *ensembles*, for instance the canonical or NVT ensemble, where the temperature rather than the energy is kept fixed, the grand-canonical or μVT *ensemble*, where μ is the chemical potential, and isobaric-isothermal or NPT *ensemble*, to cite only the most relevant. To each *ensemble* is associate a distribution density. For example, the distribution density for the canonical ensemble is given by

$$f(\mathbf{x}) = \frac{1}{Z} e^{-\beta H(\mathbf{x})} = \frac{e^{-\beta H(\mathbf{x})}}{\int \mathrm{d}\mathbf{x}\, e^{-\beta H(\mathbf{x})}}, \tag{3.30}$$

where $\beta^{-1} = \kappa_{\mathrm{B}} T$, this is also known as the Boltzmann distribution. The choice of the *ensemble* affects the statistical averages of a given observable, although most of these differences disappear in the thermodynamic limit. However, the choice of *ensembles* does make a difference when computing the mean-squared value of fluctuations. Fortunately, techniques exist to relate fluctuations in different *ensembles*[191].

In ONETEP both NVE and NVT simulations can be performed. In the latter case, we need to introduce a mechanism through which the system can exchange energy with an external bath, i.e. a thermostat.

3.4.1 THERMOSTATS

For equilibration purposes or to extract thermodynamic averages, it is often desirable to sample the canonical ensemble rather than the microcanonical one. Several thermostats, Andersen [201], Langevin [200], Bussi [202], Nosé-Hoover chains [203, 204]

and Berendsen [205] are available in ONETEP. The first three use stochastic approaches to keep the temperature constant during the simulation. The Nosé-Hoover chain employs an extended-system approach, whereas the Berendsen thermostat is derived by introducing a weak coupling with an external bath.

ANDERSEN THERMOSTAT One of the simplest constant temperature algorithm has been proposed by Andersen [201]. The system is thermally coupled with a bath of fictitious particles at temperature T. In practice, the coupling acts by replacing the momentum of some atoms with a new momentum drawn from the appropriate Boltzmann distribution. The strength of the coupling can be tuned through the characteristic time (τ) at which the momentum rescaling occurs and the magnitude (γ) of the rescaling. Eventually, the probability that collision occurs during a time step Δt is given by,

$$p_{\text{col}} = 1 - e^{-\Delta t/\tau} \tag{3.31}$$

and the collision on atom I as the following effect on its momentum $\mathbf{P}_I$

$$\mathbf{P}_I^{\text{new}} = \sqrt{(1-\gamma^2)}\,\mathbf{P}_I + \gamma \mathbf{P}_I^{\text{boltzmann}}, \tag{3.32}$$

where $\mathbf{P}_I^{\text{new}}$ is the rescaled momentum, and $\mathbf{P}_I^{\text{boltzmann}}$ is a stochastic variable with appropriate Boltzmann distribution.

LANGEVIN THERMOSTAT The Langevin thermostat accounts for the motion of the atoms in the presence of a fictitious viscous solvent [206] (continuum). The fictitious solvent creates a friction force damping the momentum of the atoms. Besides the friction force, random perturbations of the ionic forces, arising from the collisions between the atoms and the fictitious particles, are also taken into account. The Langevin equations of motion

Table 3.1: Most popular *ensembles* and their independent and dependent variables. N is the number of particles in the system, T is the temperature, V the volume, E the total energy, P the pressure, μ the chemical potential and H the enthalpy.

Ensemble	Independent variables	Dependent variables
Microcanonical	NVE	μPT
Macrocanonical	NVT	μPE
Grandcanonical	μVT	NPH
Isothermal-isobaric	NPT	μVH

have therefore two extra terms

$$\dot{\mathbf{P}}_I = \mathbf{F}_I - \gamma \frac{\mathbf{P}_I}{M_I} + \Xi_I \tag{3.33}$$

where $\mathbf{F}_I$ is the conservative force acting on the nucleus I, γ is the damping factor associated with the solvent viscosity and Ξ_I is the random force accounting for the collisions. In order to guarantee that the momenta satisfy the canonical distribution, the random forces and the damping factor are selected such as they satisfy the fluctuation-dissipation theorem. The update of the momenta $\mathbf{P}_I$ and forces $\mathbf{F}_I$ is given by,

$$\mathbf{P}_I^{\text{new}} = \mathbf{P}_I e^{-\gamma \Delta t} \tag{3.34}$$

$$\mathbf{F}_I^{\text{new}} = \mathbf{F}_I \frac{1}{\gamma}(1 - e^{-\gamma \Delta t}) + \Xi_I \tag{3.35}$$

$$\Xi_I = \sqrt{\frac{M_I \kappa_B T (1 - e^{-2\gamma \Delta t})}{\Delta t^2}} \mathbf{\Gamma}_I \tag{3.36}$$

where $\{\mathbf{\Gamma}_I\}$ is a set of mutually uncorrelated random Gaussian variables with a zero mean and unit variance $\langle \mathbf{\Gamma} \rangle = 0$, $\left\langle (\mathbf{\Gamma} - \langle \mathbf{\Gamma} \rangle)^2 \right\rangle = 1$. Langevin equations of motion are smooth, stochastic and time-irreversible.

Nosé-Hoover thermostat and Nosé-Hoover chains In the Andersen and Langevin approaches, the constant temperature is achieved by stochastic collisions with fictitious particles. Nosé method addresses the problem in deterministic terms, by introducing an extended-Lagrangian [203]. In fact, to generate isotherm MD simulations, an additional coordinate s, with an associated mass $Q > 0$ and a velocity $\dot{s}$, is introduced in the original NVE Lagrangian ruling the dynamics of the nuclei [191]. This new variable plays the same role of a time-scaling parameter or a Maxwell daemon[191]. From the Lagrangian, one can obtain an extended Hamiltonian (in terms of the conjugate momentum $t = \frac{\partial \mathcal{L}}{\partial \dot{s}}$) as

$$H(\{\mathbf{R}_I\}, \{\mathbf{P}_I\}, s, t) = \sum_I \frac{\mathbf{P}_I^2}{2 M_I s^2} + E[n; \{\mathbf{R}_I\}] + \frac{t^2}{2Q} - g \kappa_B T^* \ln s \tag{3.37}$$

where $E[n; \{\mathbf{R}_I\}]$ is the potential energy from the electronic structure calculation, T^* is the target temperature and g is a factor that takes care of the degrees of freedom. In particular, the value of g has to be chosen such as the microcanonical distribution of the extended $6N + 2$-dimensional phase space of H yields a canonical distributions for the $6N$-dimensional real phase space. It can be shown that g has to be equal to $3N + 1$ [191]. A formulation in terms of real variables instead of extended variables was given by Hoover [204]. In this alternative formulation, g is equal to $3N$ instead. The resulting

set of equations form a non-Hamiltonian system. One of the drawbacks of the original Nosé-Hoover formulation is that if more than one conservation law is obeyed by the system, the Nosé-Hoover thermostat does not lead to a canonical distribution of positions and momenta, this can be shown when using simple systems, such as a single free particle or a 1D harmonic oscillator. To solve this deficiency, more phase space dimensions are added by introducing extra variables, as each conservation law reduces the accessible phase space of one dimension. In order to ensure that the Boltzmann distribution is preserved the extra variables are also coupled to Nosé-Hoover thermostats, which gives the so called Nosé-Hoover chains. In ONETEP, the effective mass of the extended variable (Q) is chosen following the prescription of Martyna and Tuckerman [207]

$$Q^1 = 3N\frac{\kappa_B T}{\omega^2} \tag{3.38}$$

$$Q^n = \frac{\kappa_B T}{\omega^2}, \tag{3.39}$$

where $\omega = 2\pi/\tau$ is the characteristic frequency of the thermostats. That parameter τ has to be chosen so as to guarantee a good coupling with the atomic system, e.g. for water molecules, a value of 9.4 fs is appropriate as it corresponds to the first asymmetric stretching mode of O-H bonds.The resulting equations are smooth, deterministic and time-reversible.

BERENDSEN THERMOSTAT In the Berendsen thermostat, the equations of motion are combined with a first order equation for the kinetic energy,

$$dK = \frac{K^* - K}{\tau}dt, \tag{3.40}$$

where K^* stands for the target kinetic energy. The weak coupling of the system with the heat bath is controlled by the time constant τ. This thermostat does not generate a canonical ensemble but is vary efficient for thermalisation of large systems. This is the reason why we used the Berendsen thermostat in our investigations, cf. Chapter 5.

BUSSI THERMOSTAT OR CANONICAL VELOCITY SCALING To recover the canonical distribution of the kinetic energy from the Berendsen approach, Bussi *et al.* [202] have proposed a stochastic method such as the instantaneous kinetic energy is propagated using an auxiliary stochastic dynamics. The equation of motion for the kinetic energy becomes

$$dK = \frac{K^* - K}{\tau}dt + 2\sqrt{\frac{KK^*}{3N\tau}}dW, \tag{3.41}$$

where dW is a Wiener noise[208]. In the same way as for the Berendsen thermostat, the coupling of the system with the heat bath is controlled by the characteristic time τ.

3.4.2 Ergodicity

The ergodic hypothesis, although formulated towards the end of the 19th century, still remains an active and open research topic, particularly in the field of pure mathematics. We will not go through the mathematical intricacies of theory, but we will adopt a more operational approach, that will enable us to calculate relevant average properties from MD simulations[200].

As mentioned above, the average behaviour of a many-body system is described in terms of *ensemble* averages. However, this is not the way we usually think about the average behaviour of a system. In most experiments we perform a series of measurements during a certain time interval and then we calculate the average of these measurements. This is also the information accessible in a MD simulation. In an ensemble average however, one considers many virtual copies of the system, where the microscopic states are compatible with the values of the independent state variables. One then performs measurements on all the virtual copies and computes the average of these measurements according to the statistics of the ensemble. The ergodic hypothesis states that, given an infinitely long time, the ensemble averages and the time averages become the same

$$\overline{A(\mathbf{R})} = \lim_{T\to\infty} \frac{1}{T} \int_T^0 \mathrm{d}t\, A(\mathbf{R}, t) = \langle A(\mathbf{R}, t)\rangle_{\text{ensemble}} = A \tag{3.42}$$

It is worthy to note that (3.42) does not hold in general. Dynamical systems that are known to depart from ergodicity are spin glasses or systems that undergoes to a spontaneous symmetry breaking. Also, systems whose potential energy posses high barriers. However, in what follows, we will assume that ergodicity holds to all systems under investigation, such as MD simulations can be employed. As a result, we will be able to evaluate ensemble averages via (discrete) time averages.

3.5 Ionic forces in Onetep

The forces acting on a ion must be evaluated very efficiently in order to attain an accurate BO-PES, and consequently accurate trajectories. The force on a given atom I is defined as the negative total derivative of the energy with respect to the nuclear

coordinates. Within the ONETEP framework the force on atom I is given by

$$\mathbf{F}_I = -\underbrace{\frac{\mathrm{d}E_{\mathrm{LNV}}}{\mathrm{d}\mathbf{R}_I}}_{\text{Total force}} = -\underbrace{\frac{\partial E_{\mathrm{LNV}}}{\partial \mathbf{R}_I}}_{\text{HF force}} - \underbrace{\frac{\partial E_{\mathrm{LNV}}}{\partial K^{\alpha\beta}}\frac{\mathrm{d}K^{\alpha\beta}}{\mathrm{d}\mathbf{R}_I}}_{\text{kernel Pulay force}} - \underbrace{\int \mathrm{d}\mathbf{r}\, \frac{\delta E_{\mathrm{LNV}}}{\delta \phi_\alpha(\mathbf{r})}\frac{\mathrm{d}\phi_\alpha(\mathbf{r})}{\mathrm{d}\mathbf{R}_I}}_{\text{NGWF Pulay force}}, \tag{3.43}$$

where we have considered the explicit and implicit dependence of the total energy function with respect to the nuclear coordinates [172]. As the total energy is variational with respect to both the degrees of freedom in the density kernel and in the NGWFs, once full self-consistency is reached, we should have

$$\frac{\partial E_{\mathrm{LNV}}}{\partial K^{\alpha\beta}} = 0, \quad \forall \alpha, \beta, \tag{3.44}$$

$$\frac{\partial E_{\mathrm{LNV}}}{\partial \phi_\alpha(\mathbf{r})} = 0, \quad \forall \alpha \quad \Rightarrow \quad \frac{\partial E}{\partial d_{i\alpha}} = 0, \quad \forall i, \alpha, \tag{3.45}$$

where the second equation in (3.45) derives from the fact that the NGWFs are represented in terms of psinc functions, cf. Section 2.4.2. Thus, at self-consistency, we obtain the simple expression for the force

$$\mathbf{F}_I = -\frac{\partial E_{\mathrm{LNV}}}{\partial \mathbf{R}_I} = \mathbf{F}_I^{\mathrm{HF}}. \tag{3.46}$$

This result corresponds to direct application of the Hellmann-Feynman theorem, cf. Section 1.5, after successful SCF energy minimisation, with vanishing Pulay forces. With the LNV energy functional the HF force on nucleus I reads

$$\mathbf{F}_I^{\mathrm{HF}} = \mathbf{F}_I^{\mathrm{loc}} + \mathbf{F}_I^{\mathrm{nl}} + \mathbf{F}_I^{\mathrm{Ewald}} (+\mathbf{F}_I^{\mathrm{NLCC}}), \tag{3.47}$$

where kinetic, XC and Hartree terms do not contribute to HF forces. The last term $\mathbf{F}_I^{\mathrm{NLCC}}$ is computed only when non-linear core correction terms are applicable [41, 172].

In practical calculations, the density kernel can be (and is) optimised to a very tight threshold in the inner loop, making the kernel Pulay force negligible. Conversely, obtaining a tight convergence in the outer loop, can be challenging at times. This is mainly due to the competition between the kinetic energy operator in the KS Hamiltonian, which tends to delocalise the NGWFs over all the FFTbox, and the strict localisation constraint [167]. The additional NGWF Pulay term on the r.h.s. in (3.43) is therefore non-negligible in general, and needs to be evaluated[172]. ONETEP can also operate with a fixed basis set (PAOs), where NGWFs are not optimised *in situ*. In this scenario, the functional derivative $\frac{\delta E_{\mathrm{LNV}}}{\delta \phi_\alpha(\mathbf{r})}$ is not approaching to zero and the NGWF Pulay force becomes the dominant contribution to the total force (3.43). Clearly, the inclusion of the

NGWF Pulay forces is crucial for improving the accuracy in both regimes, as shown in Ref. 41. This is in contrast to the expectation for Pulay forces to vanish in approaches employing basis sets that do not depend on atomic positions, such as plane waves or psincs.

The NGWF Pulay forces in ONETEP are computed as

$$\mathbf{F}_I^{\text{Pulay}} = -\int \mathrm{d}\mathbf{r}\, \frac{\delta E_{\text{LNV}}}{\delta \phi_\alpha(\mathbf{r})} \frac{\partial \phi_\alpha(\mathbf{r})}{\partial \mathbf{R}_I}, \tag{3.48}$$

which invokes the following approximations, namely:

(a) The total derivative $\frac{\mathrm{d}\phi_\alpha(\mathbf{r})}{\mathrm{d}\mathbf{R}_I}$ is approximated with the partial derivative, i.e. gradient: $\frac{\partial \phi_\alpha(\mathbf{r})}{\partial \mathbf{R}_I} = \nabla_{\mathbf{R}_I} \phi_\alpha(\mathbf{r})$.

(b) Subsequently, the gradient $\nabla_{\mathbf{R}_I} \phi_\alpha(\mathbf{r})$ is compute in reciprocal space [172], using the FFTbox technique, as

$$\nabla_I \phi_\alpha(\mathbf{r}) = \nabla_{\mathbf{r}} \phi_\alpha(\mathbf{r}) \delta_{\alpha,I} = \frac{1}{N_{\mathbf{G}}} \sum_{\mathbf{G}}^{\mathbf{G}_{\max}} i\mathbf{G} e^{i\mathbf{G}\cdot(\mathbf{r}-\mathbf{R}_{I_\alpha})} \widetilde{\phi}_\alpha(\mathbf{G}), \tag{3.49}$$

where the $\mathbf{G}$ vectors belong to the FFTbox, and only the NGWFs centred on atom I are affected.

(c) Applying strict localisation to both $\frac{\delta E_{\text{LNV}}}{\delta \phi_\alpha(\mathbf{r})}$ and $\frac{\partial \phi_\alpha(\mathbf{r})}{\partial \mathbf{R}_I}$ during the minimisation, ignoring the fact that these quantities tend to delocalise when computed in reciprocal space.

(d) Numerical integration on a real-space grid with finite spacing. Owing to the cardinality of the psincs (cf. Sec. 2.4.2), the integral in (3.47) is numerical exact provided the functions are bandwidth-limited. This is "almost" the case due to exchange and correlation contributions in E_{LNV}.

Amongst these four approximations, (b) has been verified to be harmless [168, 169] and (d) is assumed to have little or no effect (to numerical precision). On the other hand, approximations (a) and (c) can become rather crude in some situations. In fact, by replacing the *total* derivative of an NGWF with respect to the position of a nucleus with a *partial* derivative[2], one is ignoring the deformation of the NGWF due to the new electronic environment. This neglected deformation involves a change in the psinc coefficients of the expansions and possibly requires a larger psinc set to be described

[2]Which only takes into account the displacement of the NGWF centre across the simulation cell, i.e. is a mere phase factor due to the displacement of the nucleus [41].

accurately. We note here that when working with fixed NGWFs (a) is no longer an approximation, since the psinc expansion coefficients remain constant in this regime.

3.5.1 Accuracy of forces and energy drifts

In the scenario where NGWFs are optimised *in situ* the Pulay force is usually small (typically less than 10% of the total force), since $\frac{\delta E}{\delta \phi_\alpha(\mathbf{r})} \approx 0$. However, due to the approximation (a), discussed in the previous section, the Pulay force term can be inaccurate. In Fig. 3.1 we show the cross-section along the x-axis of the gradient of the valence NGWF on the Hydrogen (H_1) atom in the following formaldehyde-water system

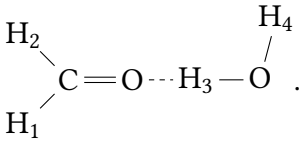

The reference value is computed with a 4^{th} finite difference scheme

$$\frac{\mathrm{d}\phi_{H_1}(X)}{\mathrm{d}X} \approx \frac{-\phi_{H_1}(X+2h) + 8\phi_{H_1}(X+h) - 8\phi_{H_1}(X-h) + \phi_{H_1}(X-2h)}{12h}, \tag{3.50}$$

where h has to be chosen small enough to give an accurate representation of the derivative, but no too small to incur into numerical noise. From convergence tests we opted for $h = 0.01\ a_0$. At each displacement we fully optimise the NGWFs, hence taking into account the deformation as well as the shift factor.

Fig. 3.1 shows that also in simple situations, e.g. 1s-like orbital, the (numerical evaluated) total derivative may slightly differ from the analytic gradient of the NGWF computed as (3.49). It is worth stressing that this approximation in the Pulay forces is a common feature of all the linear-scaling codes that perform *in situ* optimisation of the support functions. Improvements in the accuracy of the Pulay forces with respect to the NGWF can be seen from Fig. 3.2. Here, we show that the total force on the H_1, with a kinetic energy cutoff of 800 eV, in the extended regime differs from the CASTEP[3] result (which has no Pulay correction by construction) by less than $1E-4$ Ha/ a_0. This is a sign of the improved accuracy in the Pulay forces, since from numerical experiments all the contributions in the force expression, but the local term $\mathbf{F}_I^{\mathrm{loc}}$, match the CASTEP counterpart to sub milli Ha/ a_0.

A good descriptor for the accuracy of the forces is given by the magnitude of the

[3]In our tests, all the parameters in the CASTEP simulation, e.g. cell size, energy cutoff, Γ-only, psudopotentials, etc., are chosen to be the same of the corresponding ONETEP ones.

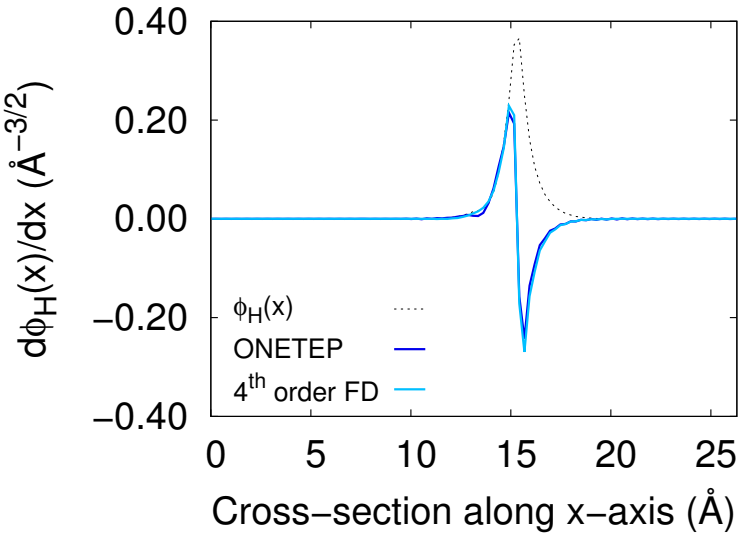

Figure 3.1: Cross-section along the x-axis of the gradient of the NGWF $\frac{\partial \phi_{H_1}(\mathbf{r})}{\partial x}$ on the Hydrogen atom H_1 in the formaldehyde-water system. Solid blue line represent the ONETEP result, whereas the solid light blue line represent the result obtained thorough a fourth-order finite difference scheme. For completeness, the cross-section of the 1*s*-like orbital is also shown (dotted line).

zero-correction force term, also known as residual force, that has to be added to the total nuclear forces in order to satisfy $\sum_I \mathbf{F}_I = 0$

$$\mathbf{F}_I^{\text{mass-corr}} = \frac{M_I}{M_{\text{tot}}} \sum_K \mathbf{F}_K, \tag{3.51}$$

such as $\mathbf{F}_I^{\text{new}} = \mathbf{F}_I^{\text{old}} - \mathbf{F}_I^{\text{mass-corr}}$. In MD calculations this non-zero net force, when uncorrected for, will lead to spurious translational motion of the system. Correcting the non-zero net force (by subtracting the mass averaged net force from the force acting on each atom) will prevent the spurious motion from appearing[209]. The error in the forces can be mitigated by using tighter inner loop convergence thresholds and by increasing the NGWFs localisation regions. Using extended (non-localised) NGWFs alleviates the problem entirely, as it reduces the magnitude of the Pulay force by 3-4 orders of magnitude. This can be seen in Fig. 3.3 panel b), which shows a geometry relaxation on the formaldehyde-water system, using the well-known pseudo Newton- Raphson method of Broyden, Fletcher, Goldfarb and Shanno (BFGS) [210], with three different descriptions: 1) Strictly localised NGWFs ($r_c^\alpha = 8.0\ a_0, \forall \alpha$) and no Pulay correction; 2) Strictly localised NGWFs with Pulay correction; 3) Extended localised NGWFs, for which

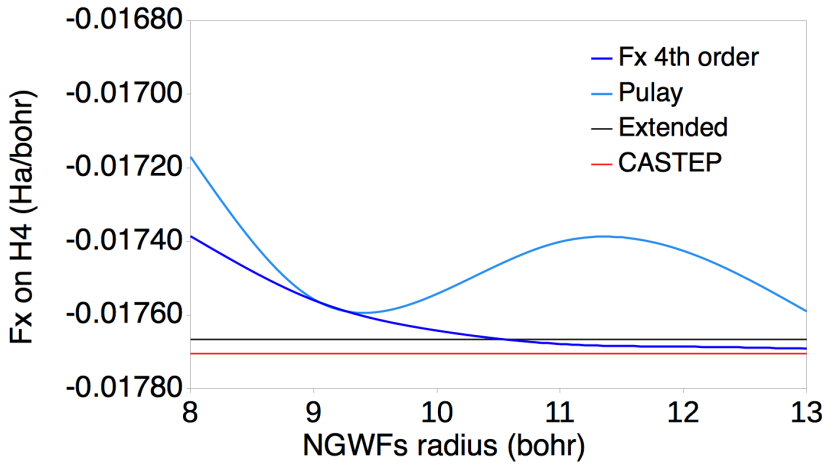

Figure 3.2: X component of the total force F_x acting on the Hydrogen atom H_1 in the formaldehyde-water system with respect to the NGWF radius. ONETEP result in the extended NGWFs regime (solid black). ONETEP result with localised NGWFs and Pulay corrections (solid light blue). CASTEP result (solid red). ONETEP result with a fourth-order finite difference scheme, where the force is considered as the total derivative of the total energy (solid dark blue).

Pulay corrections are immaterial. At each BFGS relaxation step, the extended NGWFs regime always gives the lowest value for the correction term. Also, when considering the maximum component of the total forces $|\mathbf{F}|_{\max}$, differences arise, especially in the first few iterations, between the extended NGWFs regime and the other regimes. However, as discussed in the previous chapter, adopting extended basis is not practical due to the associated overload in computer time and memory. Effectively, using extended NGWFs results in performing unoptimised $O\left(N^3\right)$ simulations.

Interestingly, Mohr *et al.* [211] have shown that introducing a confining potential in the Hamiltonian, which is adaptively turned off during the simulation, results in a greater accuracy in the forces, up to the point that Pulay corrections become negligible. In their implementation of a linear-scaling DFT code, known as BigDFT [212], Daubechies wavelets are employed as opposed to psincs. Beside the differences in the underlying basis, the two implementations, ONETEP and BigDFT, share the same theoretical framework, and it is likely that some level of confinement could be beneficial in ONETEP as well. Effects of strictly localisation on NGWFs, also known as "shaving", on the outer loop convergence have been reported in Ref. 213, where a new method is proposed to impose localisation constraints within a variational approach. We have performed preliminary tests on forces in ONETEP, employing the same test systems described above, to study the effect of the addition of a confining potential to the total potential. However, we did not perform a systematic study with different confining potentials, each coming with

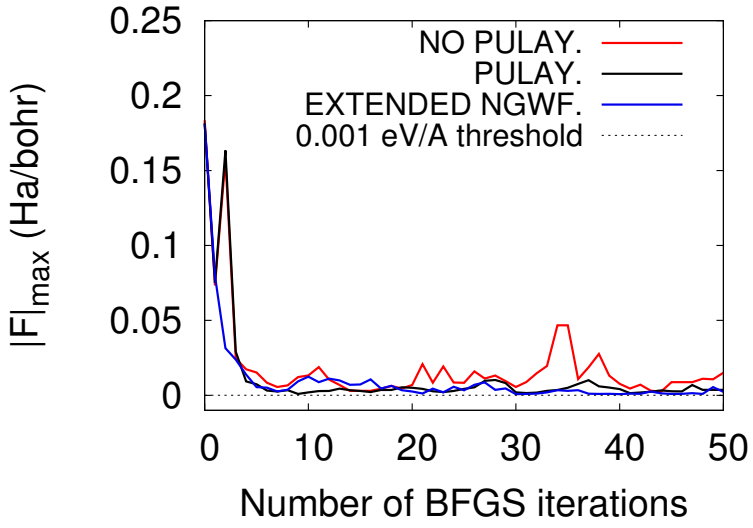

(a)

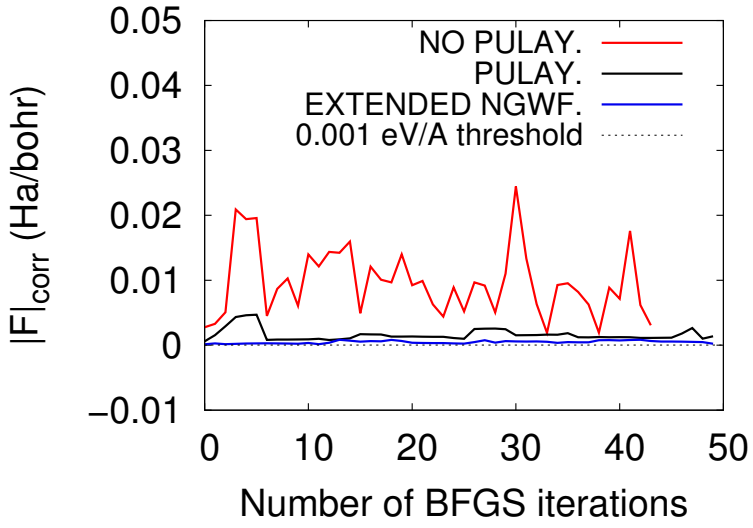

(b)

Figure 3.3: Geometry optimisation of the formaldehyde-water system with the BFGS method. a) Profile of the modulus of the maximum force, used as a converge criterion, for three different regimes: 1) Strictly localised NGWFs with no Pulay correction. 2) Strictly localised NGWFs with Pulay correction. 3) Extended NGWFs. b) Profile of the modulus of the zero-correction force (3.51) for the same three regimes of the a) panel.

a different set of parameters to optimise. Hence, although some improvements on the quality of the forces were obtained, more investigations are needed to fully support such a claim, which we leave as a possible project for the future.

When NGWFs are fixed, Pulay forces do not suffer from approximation (a), and their contribution is rather accurate. However, since the energy gradient $\frac{\delta E}{\delta \phi_\alpha(\mathbf{r})}$ is not

approaching zero, the magnitude of the Pulay forces is vastly increased (typically by a factor of 10-20 compared to when NGWFs are optimised, with the actual value ultimately depending on the quality of the fixed basis). As a result, they become the dominant term in the force expression (3.47). The accuracy improvement due to the disappearance of approximation (a) is consistent, as evidenced by the zero-net force correction diminishing by 2-3 orders of magnitude. Other sources of inaccuracies remain, most likely approximation (c). Also, the approximation of neglecting a kernel Pulay term, which may become more pronounced, as more LNV iterations are required to converge the density when NGWFs are kept unoptimised. However, in MD simulations we have found that there is little sensibility to the energy drift to the LNV convergence, so this term alone cannot be blamed. In this scenario, we have found that in NVE MD the instantaneous total energy oscillations are small ($\Delta E/E \approx 1 \times 10^{-7}$), but the long-term energy drift, although improved respect to the *in situ* optimisation regime, is still severe - corresponding to a loss/gain in temperature of $\approx 2-5$ K/ps. For comparison in CASTEP, the corresponding drift is ≈ 0.08 K/ps. A comparison of energy drifts expressed in K/ps between several methods, from naïve classical fixed point charge models, to more sophisticated LS-DFT is presented in Tab. 3.2. We used a representative system of 64 H_2O to perform our analysis.

Table 3.2: Energy drifts calculated for a representative system of 64 H_2O, expressed as temperature loss/gain rate per picosecond, using a velocity Verlet integrator, with $\Delta t = 0.5$ fs.

Energy drift [K/ps]	Method	Parameters
2×10^{-6}	Classical MD fixed point charge (FFs)	
8×10^{-6}	Classical MD polarisable force field	polar-eps=10^{-6}D
8×10^{-2}	CASTEP BOMD	$E_c = 1000$ eV
6×10^{0}	ONETEP BOMD	PAOs 2ZP basis, $r_c^\alpha = 8\ a_0$, $E_c = 900$ eV, $5E-7$ LNV threshold
8×10^{0}	ONETEP BOMD	PAOs 2ZP basis, $r_c^\alpha = 8\ a_0$, $E_c = 900$ eV, $1E-4$ LNV threshold
1.4×10^{2}	ONETEP BOMD	optimised NGWFs, $r_c^\alpha = 8\ a_0$, $E_c = 900$ eV, $5E-7$ LNV threshold

3.6 Summary

In this chapter I have introduced the fundamental ideas of *ab initio* molecular dynamics (AIMD), in particular Born-Oppenheimer molecular dynamics (BOMD), and I have showed how the corresponding equations are solved within the Onetep framework. For completeness, I have presented a section on statistical ensembles and thermostats (Sec. 3.3), which will be relevant for the next two chapters. Furthermore, in the last section, I have showed how additional terms, known as Pulay terms, arise in the expression for the ionic forces when using optimised *in situ* non-orthogonal localised atom-centred functions, e.g. NGWFs. I have also shown how these terms are addressed within the Onetep code. In particular, I have lingered on the approximations made for the Pulay terms and their effect on the quality of ionic forces and on the energy conservation. Possible developments to improve the accuracy of the forces have been proposed, although these have not been thoroughly tested and further studies are needed. This chapter serves also to introduce the terminology and the concepts developed in the next two chapters, particularly in Chapter 5, where a novel algorithm for accelerating the BOMD is presented.

Chapter 4

Vibrational anharmonicity and temperature effects through *ab initio* molecular dynamics

Abstract

In this chapter I show how BOMD and linear-scaling DFT can be coupled to the Fourier time-correlation function formalism to compute accurate vibrational and infrared spectra of large systems. In general, the advantage of using AIMD to compute such spectra lies in the fact that both temperature effects and anharmonicity of the potential energy surface (PES) are inherently taken into account. These are particularly important for the study of "floppy" molecules, e.g. peptides, which undergo to conformational changes at room temperature. Furthermore, AIMD simulations are able to provide a huge amount of information, that can be coupled with data from experiments to better understand complex molecular systems, where the interpretation of the spectral line-shapes is not straightforward. AIMD can provide a valuable tool for the interpretation of IR signatures of biological systems in both the gas- and in the aqueous-phase. In the latter case, we need a way of partitioning the electron density (a non-unique operation) to include in the computation of the dipole moment only the contribution from the solute, whereas the effect of the solvent enters only indirectly. Two methods have been implemented in Onetep, which fully exploit the locality of the NGWFs to perform the electron density partitioning: 1) Density kernel partitioning and 2) Distributed multipole analysis. Furthermore, I have implemented all the routines necessary to compute the infrared spectra through the Fourier transform of the auto-correlation function of the dipole moment. After a first introductory section on infrared spectroscopy, two self-

contained theory sections (Sec. 4.2 and Sec. 4.3) on the time-correlation function formalism are presented. Section 4.4 deals with the computation of the dipole moment in ONETEP. In Section 4.5 the two methods for partitioning the electron density are presented. Finally, Section 4.6 and Section 4.7 show the performance of these methods on a variety of small molecules in vacuum and aqueous phase. The chapter ends with a section on the results and comparisons with similar methods in the literature.

4.1 INTRODUCTION

Experimental spectroscopic techniques are amongst the foremost employed in chemistry to unveil the dynamical and structural properties of molecular systems[214]. This is achieved by exploiting a broad range of physical phenomena in the realm of matter light interaction.

In this chapter we will focus mainly on vibrational and infrared spectroscopy. For example, infra-red (IR) spectroscopy exploits the ability of molecules to absorb photons with specific frequencies ω ($\simeq 4000 - 500$ cm^{-1}), whose effect is to excite definite vibrational (and rotational) modes. Notably, only the vibrational modes that generate a net change in dipole moment are active to IR. The peaks and the bands in the frequency region $4000 - 1500$ cm^{-1}of the resulting absorption spectra can be in general interpreted and assigned to vibrational modes of characteristic functional groups, e.g. the stretching of O-H and C=O bonds. On the other hand, the region between 1500 and 500 cm^{-1}, known as the fingerprint region, shows in general a very intricate pattern, providing little contribution for the identification of bonds in unknown compounds. However, the pattern in this region is unique for a given molecule and can be used to differentiate between known compounds with similar type of bonds, e.g. propan-1-ol and propan-2-ol. Nonetheless, even in the "clear" region, a direct assignment of the peaks is at times infeasible, particularly for large and complex systems. In fact, many factors can contribute in making a spectrum hard to interpret for these systems, e.g. overlap of overtones modes with fundamentals, effects due to solvation and temperature.

From the computational point of view there are two main routes to obtain vibrational spectra. The first approach is based on static calculations at 0 K. The potential energy surface (PES) is assumed to be a quadratic function of the nuclear displacements near the equilibrium geometry (harmonic approximation). Then one expresses the potential energy in terms of mass-weighted Cartesian coordinates and evaluates the Hessian matrix[1] either analytically or numerically and diagonalise it to find the normal modes. In order to take into account the anharmonicity of the PES one needs to go beyond the harmonic

[1]The matrix of second derivatives of the potential with respect to the nuclear displacements

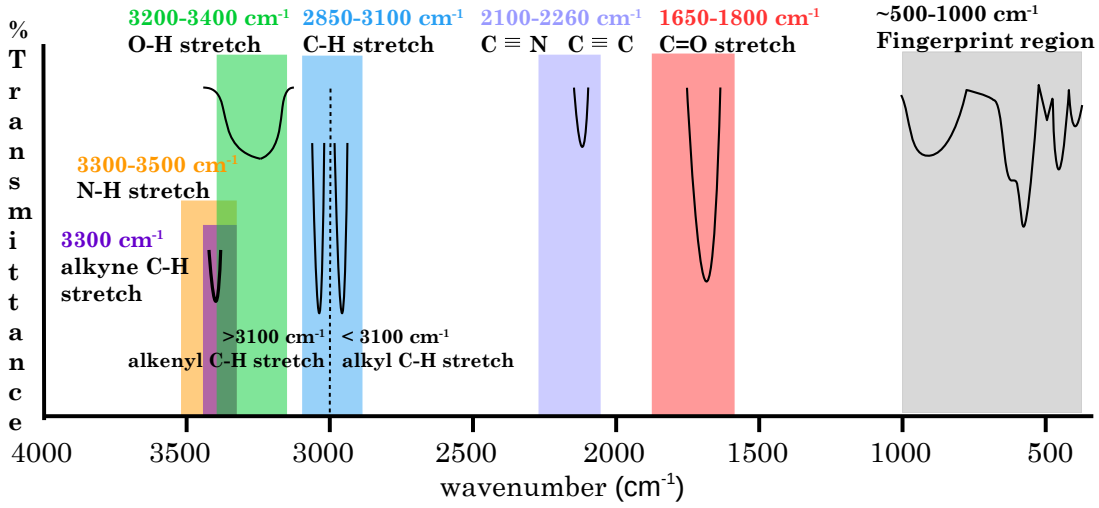

Figure 4.1: Sketch graph representing the frequency ranges of the most important chemical functional groups with distinct features.

approximation by adding higher-order derivatives in the potential[215, 216]. Although very accurate computational methods can be employed, the disadvantage is that large basis sets are required and in general the analytical expressions of high-order derivatives are unknown or very costly to compute numerically. Moreover, only normal modes frequencies are obtainable from these calculations and effects due to a finite temperature are missing. On the other hand, molecular dynamics simulations allow for a direct computation of time-correlation functions (TCFs)[217, 218], from which several kinds of spectra, such as vibrational, (mid)infra-red and Raman can be obtained. Remarkably, anharmonic and temperature effects are inherently taken into account. Intensities are recovered, as they are proportional to the time spent by the system in the corresponding vibrational mode. Particularly, AIMD provides the basis for developing very accurate techniques for computational molecular spectroscopy. Considering also the huge amount of information provided by AIMD simulations, we can use them jointly with experimental techniques to better understand complex molecular systems, where the interpretation of the spectral line-shapes is not straightforward.

Identifying the structure of biomolecules is extremely important as it is widely accepted that their function is deeply related to the three-dimensional domains[219]. How-

ever, for many years experimental difficulties have limited the use of spectroscopic techniques, such as IR, on "floppy" biological molecules[2]. Advances towards sufficiently accurate experimental results for these systems have only recently emerged. Especially worth mentioning are jet-expansion based techniques[220, 221] and superfluid helium droplets[222]. AIMD can provide a valuable tool for the interpretation of IR signatures of biological systems in both the gas- and in the condensed-phase.

4.2 Time-correlation function formalism

Line-shape computation of vibrational, infra-red, and Raman spectra relies on the assumption that the system and the external field used to probe it are weakly coupled. For a system in thermal equilibrium, i.e. obeying to the detailed balance condition, the energy dissipated in the interaction with the field is of the same magnitude of the energy of thermal fluctuations, also known as fluctuation-dissipation theorem. Under this assumption, it is legitimate to use the results of the linear response theory and time correlation functions of observables of the unperturbed system. The aim of the next two sections is to briefly gather known results[191, 217] and present them in a concise but self-contained fashion.

Let $\hat{H}_0$ be the unperturbed time-independent Hamiltonian of the ground state, for an N-body system, i.e. $\hat{H}_0 |s\rangle = \varepsilon_s |s\rangle$. If the system now interacts weakly with an external electric field of frequency ω, excitations from an initial states $|k\rangle$ to other quantum states $|\ell\rangle$ will occur if the frequency of the radiation is close to $(\varepsilon_\ell - \varepsilon_k)/\hbar$. For a monochromatic field, we can write

$$\mathbf{E}(t) = E_0 \cos(\omega t)\mathbf{e}, \tag{4.1}$$

where $\mathbf{e}$ is the unit vector that defines the direction of the incident radiation. Assuming a uniform field or a field with a wavelength λ much larger than molecular dimensions ($\lambda \mapsto \infty$), also known as dipole approximation, the interaction between the field and the system can be written as

$$\hat{H}_1(t) = -\hat{\boldsymbol{\mu}} \cdot \mathbf{E}(t), \tag{4.2}$$

where $\hat{\boldsymbol{\mu}}$ is the dipole moment operator. Hence, the new Hamiltonian can be written as $\hat{H}(t) = \hat{H}_0 + \hat{H}_1(t)$, where the explicit time dependence is due to the oscillatory external field, and not to the operator itself (Schrödinger picture). Fermi's Golden Rule[223, 224] is used to find the probability per unit time $\Omega_{k\to\ell}(\omega)$, of a transition from state $|k\rangle$ to state

[2]Here with the term floppy molecules we are referring to the property of such molecules to show several conformers with near-degenerate energies. Small energy barriers imply that at room temperature floppy molecules can explore several conformers and go through several conformational changes.

$|\ell\rangle$, in the first order in the perturbation $\hat{H}_1(t)$:

$$\Omega_{k\to\ell}(\omega) = \frac{\pi E_0^2}{2\hbar^2} |\langle \ell | \mathbf{e}\cdot\hat{\boldsymbol{\mu}} | k\rangle|^2 [\delta(\omega_{\ell k}+\omega) + \delta(\omega_{\ell k}-\omega)], \tag{4.3}$$

where $\omega_{\ell k} = \omega_\ell - \omega_k = (\varepsilon_\ell - \varepsilon_k)/\hbar$, and $\delta(x)$ is the Dirac delta function.

The rule states that the transition rate depends solely on the square of the matrix elements of the operator $\hat{\boldsymbol{\mu}}$. Energy conservation is ensured by the two delta functions. Without loss of generality, we assume $\omega_{\ell k} > 0$. For an absorption process, $\omega > 0$ and the argument of the first δ in (4.3) is always non-zero and it can be dropped. The transition rate for the ensemble is given by the ensemble average of $\Omega_{k\to\ell}(\omega)$ over initial states consistent with the macroscopic observables. For the canonical ensemble it reads

$$\Omega(\omega) = \langle \Omega_{k\to\ell}(\omega)\rangle = \frac{\pi E_0^2}{2\hbar^2} \sum_{k,\ell} \rho_k |\langle \ell | \mathbf{e}\cdot\hat{\boldsymbol{\mu}} | k\rangle|^2 \delta(\omega_{\ell k}-\omega), \tag{4.4}$$

where we have to sum over all the final states $|\ell\rangle$ that are connected to the initial states $|k\rangle$ by energy conservation.

So far we have implicitly used the Schrödinger picture. An equivalent but handier formula can be derived if one uses the interaction picture instead, cf. Appendix A

$$\Omega(\omega) = \frac{1}{3}\frac{E_0^2}{4\hbar^2} \int \mathrm{d}t\, e^{-i\omega t} \langle \hat{\boldsymbol{\mu}}(0)\hat{\boldsymbol{\mu}}(t)\rangle\,, \tag{4.5}$$

where the factor 1/3 is due to the assumption of an isotropic system, for which any response is independent from the direction of the incident radiation $\mathbf{e}$, and $\langle \hat{\boldsymbol{\mu}}(0)\hat{\boldsymbol{\mu}}(t)\rangle = C^{\mathrm{rs}}(t)$ is the right-sided quantum autocorrelation function of the dipole moment operator.

We point out here that the operators $\hat{\boldsymbol{\mu}}(0)$ and $\hat{\boldsymbol{\mu}}(t)$ are individually Hermitian, but since they do not commute in general, the autocorrelation function $C^{\mathrm{rs}}(t)$ is an expectation value of a non-Hermitian operator. As a consequence, $C^{\mathrm{rs}}(t)$ is a complex function. This fact creates a breach between the quantum and classical formulation, and in fact the imaginary part of the autocorrelation function can be used as a measure of quantum effects.

A connection with the classical formulation can be recovered through a complete analysis of the transition rate function in the frequency spectrum, i.e. considering the case of $\omega < 0$ as well. In this case, the argument of the second δ in (4.3) is always non-zero and it can be dropped. This is equivalent to substituting $-\omega$ for ω in (4.4), which corresponds to an emission process. By interchanging the indices k and ℓ in (4.4) and

using the relation for ρ_ℓ for a system in thermal equilibrium :

$$\rho_\ell = \frac{e^{-\beta\varepsilon_\ell}}{\mathrm{Tr}(e^{-\beta\hat{H}_0})} = \frac{e^{-\beta(\varepsilon_k+\hbar\omega)}}{\mathrm{Tr}(e^{-\beta\hat{H}_0})} = \rho_k e^{-\beta\hbar\omega}, \tag{4.6}$$

the ensemble transition rate for the emission process becomes

$$\begin{aligned}\Omega(-\omega) &= \frac{\pi E_0^2}{2\hbar^2} e^{-\beta\hbar\omega} \sum_{k,\ell} \rho_k |\langle k|\mathbf{e}\cdot\hat{\boldsymbol{\mu}}|\ell\rangle|^2 \delta(\omega_{\ell k}-\omega) \\ &= e^{-\beta\hbar\omega}\Omega(\omega). \end{aligned} \tag{4.7}$$

The relation in (4.7) represents the well-known detailed balance condition for a system in thermal equilibrium. The ensemble averaged absorption and emission rates, $\Omega(\omega)$ and $\Omega(-\omega)$ respectively, do not obey the microscopic reversibility condition.

If we carry out the same analysis that led us from (4.4) to (4.5) for the transition rate $\Omega(-\omega)$, the result is

$$\Omega(-\omega) = \frac{E_0^2}{12\hbar^2}\int \mathrm{d}t\, e^{-i\omega t}\langle\hat{\boldsymbol{\mu}}(t)\hat{\boldsymbol{\mu}}(0)\rangle\,, \tag{4.8}$$

and since $\Omega(-\omega) \neq \Omega(\omega)$, the two correlation functions $\langle\hat{\boldsymbol{\mu}}(t)\hat{\boldsymbol{\mu}}(0)\rangle$ and $\langle\hat{\boldsymbol{\mu}}(0)\hat{\boldsymbol{\mu}}(t)\rangle$ are not the same function.

The net absorption energy per unit time at frequency ω is given by

$$\Pi(\omega) = [\Omega(\omega)-\Omega(-\omega)]\,\hbar\omega = \hbar\omega\Omega(\omega)(1-e^{-\beta\hbar\omega}). \tag{4.9}$$

However, from the detailed balance condition we can obtain the following relation

$$\Omega(\omega)+\Omega(-\omega) = (1+e^{-\beta\hbar\omega})\Omega(\omega). \tag{4.10}$$

Since taking an ensemble average is a linear operation, we can rewrite $\Omega(\omega)+\Omega(-\omega)$ as

$$\frac{E_0^2}{12\hbar^2}\int \mathrm{d}t\, e^{-i\omega t}\langle\hat{\boldsymbol{\mu}}(0)\hat{\boldsymbol{\mu}}(t)+\hat{\boldsymbol{\mu}}(t)\hat{\boldsymbol{\mu}}(0)\rangle = \frac{E_0^2}{12\hbar^2}\int \mathrm{d}t\, e^{-i\omega t}\langle\{\hat{\boldsymbol{\mu}}(0),\hat{\boldsymbol{\mu}}(t)\}\rangle\,, \tag{4.11}$$

where $\{\hat{A},\hat{B}\} = \hat{A}\hat{B}+\hat{B}\hat{A}$ is the anticommutator of $\hat{A}$ and $\hat{B}$. Finally, we can recast the formula for the net energy absorption spectrum in (4.9) as

$$\Pi(\omega) = \frac{2\omega E_0^2}{12\hbar}\tanh\left[\frac{\beta\hbar\omega}{2}\right]\int \mathrm{d}t\, e^{-i\omega t}\left\langle\frac{1}{2}\{\hat{\boldsymbol{\mu}}(0),\hat{\boldsymbol{\mu}}(t)\}\right\rangle, \tag{4.12}$$

where now $\left\langle\frac{1}{2}\{\hat{\boldsymbol{\mu}}(0),\hat{\boldsymbol{\mu}}(t)\}\right\rangle = C^{\mathrm{sym}}(t)$, is the symmetrised autocorrelation function. Unlike

the function in (4.5), $C^{\mathrm{sym}}(t)$ is a real function. We have found a quantum analogue candidate for the absorption spectrum in terms of the autocorrelation function of a Hermitian operator.

We can define an absorption cross-section $\alpha(\omega)$ as the ratio between the net energy density $\Pi(\omega)/V$, where V is the volume of the system, and the magnitude of the incident energy flux density of the radiation $\|\mathbf{S}\|$, i.e. the Poynting vector. The product of $\alpha(\omega)$ and the refractive index $n(\omega)$ can be put in direct relationship with $\Pi(\omega)$. Different formulas for $\alpha(\omega)$ are possible, depending on which autocorrelation function is adopted. It is also useful to define an absorption lineshape $I(\omega)$, as

$$I(\omega) \equiv \frac{1}{2\pi} \int \mathrm{d}t \, e^{-i\omega t} C(t), \tag{4.13}$$

where $C(t)$ is the generic autocorrelation function, such that the cross-section function can be more generally written as

$$\alpha(\omega) = \frac{4\pi^2 \omega}{3\hbar V c n(\omega)} (1 - \exp[-\beta\hbar\omega]) \zeta(\omega) I^{\zeta}(\omega), \tag{4.14}$$

where c is the speed of light, and $\zeta(\omega)$ is a function implicitly defined by the autocorrelation function $C(t)$. In the next section we will show that many physically equivalent quantum autocorrelation function can be defined. The formula in (4.14) represents the main result of our derivation, that is that the cross-section function $\alpha(\omega)$ can be expressed in terms of the Fourier transform of a given dipole moment autocorrelation function $C(t)$ of the quantum system in the absence of any external field.

4.3 Detailed balance condition and quantum correction factor

The formulas in (4.13)-(4.14) are derived directly from first principles, with the assumption of a weak coupling between the system and the external field. Under this assumption, the linear response theory [217] can be used to predict many dynamical properties of the system.

However, in BOMD the trajectories of nuclei are generated by integrating the classical laws of motion, with the forces computed "on-the-fly" from electronic structure calculations. Consequently, the observables that depend on the classical degrees of freedom, such as the total dipole moment, must be considered as classical quantities. Obviously, the BOMD approach does not satisfy the assumptions made in the previous section.

Nonetheless, we can formally maintain the formulas in (4.12) and take the limit $\hbar \mapsto 0$. In this limit, the quantum operators become classical vectors $\hat{\boldsymbol{\mu}}(t) \mapsto \boldsymbol{\mu}(t)$. Moreover, there exists only one autocorrelation function, $C^{\mathrm{cl}}(t) = \langle \boldsymbol{\mu}(0) \cdot \boldsymbol{\mu}(t) \rangle$, where $\langle\, \rangle$ have now the meaning of classical ensemble average. Hence, the classical $\Pi(\omega)$ is given by

$$\Pi(\omega) = \frac{\beta\omega^2 E_0^2}{12} \int \mathrm{d}t\, e^{-i\omega t} C^{\mathrm{cl}}(t), \tag{4.15}$$

where we have used $\tanh[\hbar\beta\omega/2]/\hbar = \beta\omega/2$ for $\hbar \mapsto 0$. Analogously, we can define a classical lineshape and a classical cross-section.

However, the classical and the quantum lineshapes have different symmetry. In fact, $I^{\mathrm{cl}}(\omega)$ is an even function of ω and does not satisfy the more complicated relation $I(-\omega) = \exp[-\beta\hbar\omega] I(\omega)$ required by the quantum counterpart (which is essentially a restatement of the detailed balance condition in the frequency domain). This breaks the symmetry of the cross-section function $\alpha(\omega) = \alpha(-\omega)$. The failure of the classical approach in fulfilling the detailed balance condition is at the heart of the problem. A standard procedure to force $I^{\mathrm{cl}}(\omega)$ to satisfy the detailed balance condition is to introduce a frequency-dependent quantum correction factor, such that the symmetry enclosed in (4.14) is restored. Alternatively, more sophisticated and direct approaches could be used, such as PIMD.

In addition to $C^{\mathrm{rs}}(t)$ and $C^{\mathrm{sym}}(t)$ defined in the previous section, we can define other quantum autocorrelation functions[3], such as the symmetric $C^{\mathrm{asym}}(t)$, the shifted $C^{\mathrm{shift}}(t)$ and the Kubo autocorrelation functions $C^{\mathrm{kubo}}(t)$[226].

The physical information embodied into the different autocorrelation functions is the same, since their Fourier transforms are interrelated by simple expressions [226], cf. Appendix B. Amongst the possible correlation functions, of particular importance is the Kubo autocorrelation function :

$$\begin{aligned} C^{\mathrm{kubo}}(t) &= \left\langle \frac{1}{\beta} \int_0^\beta d\lambda\, \hat{\boldsymbol{\mu}}(0) \hat{\boldsymbol{\mu}}(t + i\hbar\lambda) \right\rangle \\ &= \left\langle \widetilde{\hat{\boldsymbol{\mu}}}(0) \hat{\boldsymbol{\mu}}(t) \right\rangle, \end{aligned} \tag{4.16}$$

which in the frequency domain is related to the right-sided lineshape through

$$I^{\mathrm{rs}}(\omega) = \frac{\beta\hbar\omega}{1 - \exp[-\beta\hbar\omega]} I^{\mathrm{kubo}}(\omega). \tag{4.17}$$

In fact, it can be shown that $C^{\mathrm{kubo}}(t)$ is a real and even function of time, as is $C^{\mathrm{cl}}(t)$, and

[3] The only difference between $C^{\mathrm{rs}}(t)$ and the other correlation functions appears in the quantum limit, $\beta \mapsto \infty$, where there is a loss of dynamical information, as pointed out in Ref. 225.

since the Fourier transform conserves parity, it follows straightforwardly that $I^{\text{kubo}}(\omega) = I^{\text{kubo}}(-\omega)$.
Moreover, in the classical limit, $\beta \mapsto 0$, the prefactor in (4.17) approaches to unity, which implies $I^{\text{rs}}(\omega) = I^{\text{kubo}}(\omega)$, which in turn implies the equality of the respective autocorrelation functions. This suggests $C^{\text{cl}}(t)$ be replaced with the Kubo autocorrelation function, and to use the corresponding prefactor to restore the symmetry in (4.14). The lineshape function with the correct symmetry can be written as

$$I(\omega) = Q^{\text{QC}}(\omega) I^{\text{cl}}(\omega). \tag{4.18}$$

In the literature, the Kubo correction factor is also known as the harmonic correction factor and is widely used to correct classical molecular dynamics results for detailed balance, as it systematically gives results in better agreement with experimental works for the mid-infrared range compared to other correction factors[34]. By testing the different prefactors we arrived at the same conclusions, therefore this is the only prefactor used in our results.

4.4 Electronic dipole moment with periodic boundary conditions

For finite system, such as molecules in vacuum, the electronic dipole moment, in atomic units, is given by the expectation value of the position operator[227]

$$\begin{aligned}
\boldsymbol{\mu}_{\text{el}}(\mathbf{r}) &= -\langle \Psi_0 | \hat{\mathbf{r}} | \Psi_0 \rangle \\
&= \int \mathrm{d}\mathbf{r}_1 \mathrm{d}\mathbf{r}_2 \ldots \mathrm{d}\mathbf{r}_N \, \Psi_0^*(\mathrm{d}\mathbf{r}_1 \mathrm{d}\mathbf{r}_2 \ldots \mathrm{d}\mathbf{r}_N) \times \\
&\quad \left(-\sum_i \mathbf{r} \delta(\mathbf{r} - \mathbf{r}_i) \right) \Psi_0(\mathrm{d}\mathbf{r}_1 \mathrm{d}\mathbf{r}_2 \ldots \mathrm{d}\mathbf{r}_{\text{N}}) \\
&= \int \mathrm{d}\mathbf{r} \, \mathbf{r} n(\mathbf{r}) \\
&= \text{Tr}(\hat{\rho}\hat{\mathbf{r}}).
\end{aligned} \tag{4.19}$$

The integral on the r.h.s. on the second and third line in (4.19) converges as long as the wave-function belongs to the space of square-integrable functions. This is always the case for finite systems within open boundary conditions (OBC), as the wave-function is assumed to decay to zero at infinity. Conversely, when treating crystalline systems, one usually considers periodic boundary conditions (PBE), in particular Born-von Kàrman

boundary conditions, to avoid surface effects. Generally, PBC are justified in the thermodynamic limit. However, the expectation value of the position operator is ill-defined under PBC and the integral in (4.19) does not converge [10, 57]. When using PBC, the knowledge of the periodic electron density cannot, even in principle, be used to define the electronic polarization in the bulk of dielectrics[56]. A new view emerged only in the early 1990s pursued by Resta, Vanderbilt, and others. This paradigm shift is now known as the "modern theory of polarisation"[56, 228]. According to this new quantum theory of microscopic polarisation (or dipole moment density), what is actually measurable in experiments are *differences* in polarisation $\Delta\mathbf{P}$ (an integrated current), rather than the absolute value of $\mathbf{P}$ itself, which is a multivalued function in systems subjected to PBC. The difference $\Delta\mathbf{P}$ is between two states that can be connected through an adiabatic process. Along the path between the two points the system has to remain an insulator, no band gap closure. This implies a shift from a formulation based on charges to one based on currents, which also explains the appearance of phases of wave-functions in the theory.

The difference in polarisation can be represented as a "Berry phase"[55, 229], a gauge-invariant geometrical phase of a closed manifold (the Brillouin zone) on which a set of vectors (orbitals) are defined

$$\mathbf{P}_{\text{el}} = \frac{\boldsymbol{\mu}_{\text{el}}}{V_{\text{cell}}} = -\frac{i}{(2\pi)^3}\sum_n \int \mathrm{d}\mathbf{k}\, \langle u_{n,\mathbf{k}} | \nabla_{\mathbf{k}} u_{n,\mathbf{k}} \rangle \,. \tag{4.20}$$

It turns out that an equivalent and more intuitive description of the dipole moment for periodic systems can be given in terms of Wannier functions. In fact, after the wannierisation of the KS orbitals, that is a unitary transformation, the electronic dipole moment is given by the sum of the centres of the Wannier functions, since the expectation value of the centre of the kth Wannier function can be expressed as

$$\langle \mathbf{r}_k^{WF} \rangle = -\frac{L}{2\pi}\mathrm{Im}\ln \mathbf{z}_k, \tag{4.21}$$

and the dipole moment can be approximated as

$$\boldsymbol{\mu}_{\text{el}} = -2e\sum_k \langle \mathbf{r}_k^{\text{WF}} \rangle \,. \tag{4.22}$$

The problem is that WFs are not unique, i.e. starting from the same set of KS orbitals, several but equivalent sets of WFs can be generated. Formally, this is due to a gauge-dependency (dependence on the extra degree of freedom) of the unitary transformation of the KS orbitals. To fix this degree of freedom, Marzari *et al.* have developed a clever

strategy to get maximally localised WFs (MLWFs)[125, 126], resolving the gauge problem by imposing an extra constraint on the WFs: the minimisation of the spread functional

$$\Omega = \sum_{n}^{N} \left[\langle r^2 \rangle_n - |\langle \mathbf{r}_n \rangle|^2 \right].$$

Hence, with this algorithm they find the set of MLWFs amongst equivalent WFs sets (implemented in WANNIER90[129]).

MLWFs are orthogonal functions and their centres tend to be located close to atoms or bond centres and therefore can be uniquely attributed to a given molecule. They also have a more direct chemical interpretation than NGWFs, in terms of *s,p,d* and hybrid orbitals. However, the non-orthogonality of the NGWFs is their extra gear, as they are suitable for linear-scaling codes, and they usually are more localised than MLWFs. The locality of both MLWFs and NGWFs, is a key feature for the partitioning of the dipole moment. In fact, if we consider a system consisting of two interacting but separate molecules A and B, using the MLWFs we find a natural way to partition the density and it can be shown that[29]

$$\boldsymbol{\mu}_{\text{el}}^{\text{AB}} = \boldsymbol{\mu}_{\text{el}}^{\text{A}} + \boldsymbol{\mu}_{\text{el}}^{\text{B}} = \sum_{I \in A} -e \langle \boldsymbol{r}_I \rangle + \sum_{J \in B} -e \langle \boldsymbol{r}_J \rangle , \tag{4.23}$$

neglecting the cross-interaction terms.

4.5 Dipole moment in linear-scaling DFT

In the LS-DFT framework, equation (4.19) reads

$$\boldsymbol{\mu}_{\text{el}}(\mathbf{r}) = -2K^{\alpha\beta}\mathbf{R}_{\beta\alpha}, \tag{4.24}$$

where the factor 2 accounts for spin degeneracy, and

$$\mathbf{R}_{\alpha\beta} = \{\langle \phi_\alpha(\mathbf{r})|x|\phi_\beta(\mathbf{r})\rangle , \langle \phi_\alpha(\mathbf{r})|y|\phi_\beta(\mathbf{r})\rangle , \langle \phi_\alpha(\mathbf{r})|z|\phi_\beta(\mathbf{r})\rangle\}$$

is the expectation value of the position operator in the NGWFs basis. The total dipole moment is given by the sum of nuclear and electronic components

$$\boldsymbol{\mu}_{\text{tot}}(\mathbf{r}) = \sum_{I} Z_I \mathbf{R}_I - 2K^{\alpha\beta}\mathbf{R}_{\beta\alpha}. \tag{4.25}$$

A comparison between NGWFs and MLWFs has been presented in Ref. 230, showing

the accuracy of our approach in computing electric dipole polarisabilities comparable to MLWF methods, with the advantage that NGWFs are computed "on-the-fly", obviating the need for post-processing, see also Sec. 4.6.

For the electronic dipole moment of a non-isolated system A within a larger system $A' = A + B$, a density partitioning scheme is required. Different methods for partitioning the density matrix into atomic/pointwise[231, 232], or fragment[233] contributions are known. Partitioning methods based on other criteria are possible. Notably, Bader's theory "atom in molecule" based on the topology of the electron density [234] and Voronoi dipole moments [235]. The plurality of methods is a result of the non-uniqueness of density partitioning.

Thanks to the orthogonality and localisation constraints, MLWF approaches offer a very natural way to partition the electron density[126]: the density matrix ρ_A corresponding to system A can be built from MLWFs whose centre can be easily assigned to A only, and the number of electrons in A is correctly given by $N_A^{\text{elec}} = \text{Tr}(\rho_A)$. Ambiguities remain in bonded systems.

In the ONETEP framework, on one hand, NGWFs are more easily assigned to a given system, as they are centred on atoms, while MLWFs are not. On the other hand, non-orthogonality of NGWFs plays an important role: the density matrix ρ_A can not be built from NGWFs centred exclusively on atoms belonging to A, and in what follows we outline two approaches to overcome this obstacle: the density kernel partitioning and the distributed multipole analysis. Both methods have been implemented in ONETEP and they are now part of its Academic distribution.

4.5.1 Density partitioning by kernel partitioning

The density kernel partitioning (DKP) method we present, computes the dipole moment of a subsystem A directly from the matrix elements of $\mathbf{K}$ and $\mathbf{R}$ of the total system A'.

To properly describe the electronic dipole of A, contributions originating from the NGWFs centred on atoms in B whose overlap S_{BA} with NGWFs centred on atoms in A is non-zero, have to be included. In our method we consider $\mathbf{K}$ and $\mathbf{X}, \mathbf{Y}, \mathbf{Z}$ of the entire system A', which are real and symmetric matrices by construction. They can be rearranged into block matrices: two square, diagonal blocks AA and BB, whose elements originate from NGWFs centred only on atoms in A or B, respectively, and two rectangular, off-diagonal blocks AB and BA, where $AB = BA^T$, with the obvious meaning of symbols. The double tensor contraction in (4.24), represents a matrix multiplication $\mathbf{M} = \mathbf{K} \cdot \mathbf{R}$ followed by taking the trace of the resulting matrix.The block structure is preserved under matrix multiplication. Therefore the trace of the block AA in $\mathbf{M}$, gives the electronic

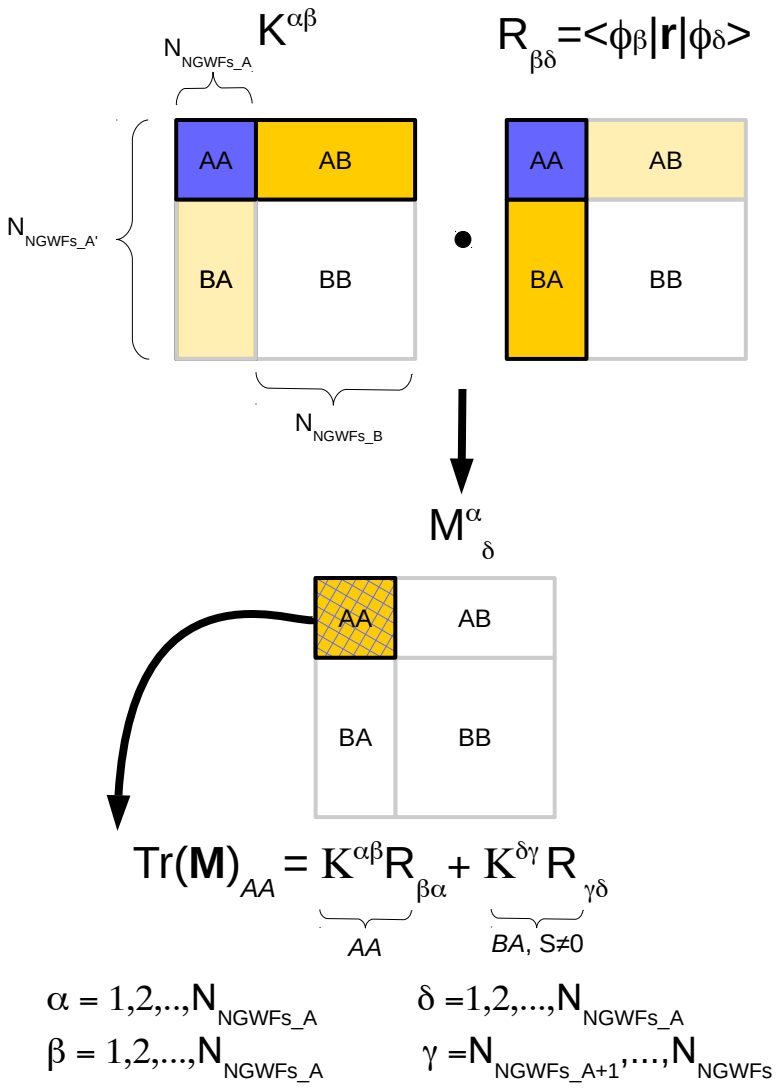

Figure 4.2: Schematic representation of the DKP method for the partitioning of the dipole moment.

dipole of the subsystem *A*, see Fig. 4.1. This is equivalent to adding the trace of the matrices obtained from the multiplication of the *AA* blocks in **K** and **R**s and the trace of the matrices obtained from the multiplication of the *BA* block in **K** and *AB* block in **R**s (or the transpose of the *BA* block since **R**s are symmetric), which is half of the total

contribution from off-diagonal blocks:

$$\begin{aligned} \boldsymbol{\mu}_{\mathrm{el}}^{A} &= 2\left[\mathrm{Tr}(\mathbf{KR})_{AA} + \mathrm{Tr}(\mathbf{KR})_{BA}\right] \\ &= 2\left[\sum_{\alpha,\beta\in AA} K^{\alpha\beta}R_{\beta\alpha} + \sum_{\gamma,\delta\in BA} K^{\delta\gamma}R_{\gamma\delta}\right]. \end{aligned} \tag{4.26}$$

We end this section by stressing that the density kernel partitioning does not retain the exact number of electrons for the subsystems. However, in numerical tests we performed the electronic charge of the subsystem $\mathrm{Tr}(\mathbf{M}_{AA})$, was within 0.05% of the expected number of valence electron.

4.5.2 Density partitioning by distributed multipole analysis

Another approach to partitioning the density between the two subsystems relies on distributed multipole analysis (DMA). Here the charge distribution of the entire system is represented in terms of a multipole expansion. Atomic centres are usually, although not universally, used as the centres for the multipoles. The DMA approach, first proposed by Rein [236], has been pioneered and popularised by Stone [231] and Alderton [232]. Distributed multipole analysis is typically performed in a Gaussian basis set [237, 238]; below we outline how electronic densities represented in a localised (NGWF) basis can be similarly expanded.

We begin by decomposing the total electronic density $n(\mathbf{r})$ into on-site and off-site contributions:

$$n(\mathbf{r}) = \sum_{I}\sum_{i_1,i_2\in I} \phi_{i_1}(\mathbf{r})K^{i_1 i_2}\phi_{i_2}(\mathbf{r}) + \sum_{I}\sum_{J\neq I}\sum_{i\in I}\sum_{j\in J} \phi_i(\mathbf{r})K^{ij}\phi_j(\mathbf{r}) \tag{4.27}$$

$$= \sum_{I} n_{II}(\mathbf{r}) + \sum_{I}\sum_{\substack{J\neq I \\ S_{IJ}\neq 0}} n_{IJ}(\mathbf{r}). \tag{4.28}$$

In (4.28) we have explicitly separated density contributions from NGWFs on the same atomic centre I and those on different atomic centres I and J with non-zero overlap S_{IJ}. By construction, NGWFs which do not overlap do not contribute to density. We denote with i or $i_1, i_2, \ldots$ (and correspondingly with $j, j_1, j_2, \ldots$) the NGWFs belonging to the atom I (J).

Our next goal is to approximate each of the off-site contributions to density as a sum

of on-site contributions, represented in an auxiliary basis set, i.e.:

$$\tilde{n}_{IJ}(\mathbf{r}) = \sum_{s}^{N_\ell} f_s(\mathbf{r})\, c_{IJ}^s, \tag{4.29}$$

where c_{IJ}^s are the sought coefficients in the expansion, and $\{f_s(\mathbf{r})\}_{s=1}^{N_\ell}$ are the functions comprising our auxiliary basis set, $N_\ell/2$ of which originate on centre I, and the remaining $N_\ell/2$ on centre J.

We subsequently define an electrostatic metric V :

$$V_{st} = (f_s|f_t)\,, \tag{4.30}$$

where, for the sake of brevity, we introduced the notation

$$(g|h) = \int\int \mathrm{d}\mathbf{r}\,\mathrm{d}\mathbf{r}'\, g^*(\mathbf{r})\frac{1}{|\mathbf{r}-\mathbf{r}'|}h(\mathbf{r}'). \tag{4.31}$$

Minimization of the electrostatic self-energy of the difference between the exact and approximate (interpolated) density, i.e. of the quantity

$$\frac{1}{2}\Big(\big[n_{IJ}-\tilde{n}_{IJ}\big]\Big|\big[n_{IJ}-\tilde{n}_{IJ}\big]\Big) \tag{4.32}$$

yields the expansion coefficients as

$$c_{IJ}^s = \sum_{t}^{N_\ell} \big(n_{IJ}|f_t\big)\, V^{ts}, \tag{4.33}$$

where t similarly indexes auxiliary basis functions originating on centres I and J, and V^{ts} are elements of the inverse electrostatic metric matrix. The electrostatic overlaps $\big(n_{IJ}|f_t\big)$ are equivalent to standard overlaps $\langle n_{IJ}|u_t\rangle$, where the auxiliary basis function f_t has been replaced by its Coulomb potential u_t, i.e.

$$u_t(\mathbf{r}) = \int \mathrm{d}\mathbf{r}'\,\frac{f_t(\mathbf{r}')}{|\mathbf{r}-\mathbf{r}'|}. \tag{4.34}$$

In practice the overlaps are evaluated numerically on a Cartesian grid, and the auxiliary basis functions are chosen such that their potential can be obtained analytically. For a detailed description of the procedure, with a discussion of the practicality of using truncated spherical waves as the auxiliary basis set, the Reader is referred to Ref. 239.

We note that the above expressions retain validity for the case of $I = J$, which lets us

use the same formalism to expand on-site products for consistency[4].

We have now decomposed the electronic density of the system into a sum of atom-centred contributions, with each contribution being a linear combination of auxiliary basis functions. As each atomic centre I participates in the expansion of a number of pairs (I, J), the total number $n(I)$ of coefficients associated with each centre I is $n(I) = \frac{1}{2}\sum_{J,S_{IJ}\neq 0} N_\ell$, while the number of auxiliary basis functions on each centre is $N_\ell/2$.

For the sake of concreteness, in the text that follows, we explicitly assume the auxiliary basis functions to be truncated spherical waves (SWs) [239–241], i.e.:

$$f_s(\mathbf{r}) \equiv f_{lmq}(\mathbf{r}) = \begin{cases} j_l(r/b_{lq}) Z_{lm}(\hat{\mathbf{r}}) & r < a, \\ 0 & r \geq a \end{cases}, \tag{4.35}$$

where $j_l(r/b_{lq})$ is a spherical Bessel function and $Z_{lm}(\hat{\mathbf{r}})$ is a real spherical harmonic, cf. Fig. 4.3. Values of b_{lq} are chosen so that the $j_l(r/b_{lq})$ has exactly q zeros and does not introduce a discontinuity, i.e. $j_l(a/b_{ql}) = 0$. The radii of localisation of the SWs (a) and of the NGWFs coincide. For the purpose of calculating dipole moments we limit the values of the angular momentum quantum number to $l \leq 1$ (although the approach is general), the magnetic quantum number $m \in [-l, l]$, and the number of distinct values of q in the auxiliary basis set (typically about 10) depends on the psinc kinetic energy cutoff used in the calculations.

We now turn to the calculation of the dipole moment. The multipoles associated with an atomic centre I can be calculated as

$$\mathcal{M}_{lm}(I) = \sum_{\substack{J \\ S_{IJ}\neq 0}} \sum_{s_I}^{N_\ell/2} c_{IJ}^{s_I} \int_{\mathcal{S}_{I,a}} \mathrm{d}\mathbf{r}\, |\mathbf{r}|^l C_{lm}(\hat{\mathbf{r}}) f_{s_I}(\mathbf{r}), \tag{4.36}$$

where the subscript I applied to s reminds the Reader that only the SWs originating on atom I participate in the second sum. Owing to the localisation of truncated spherical waves, the integral only runs over a spherical volume $\mathcal{S}_{I,a}$ of radius a centred at $\mathbf{R}_I$. C_{lm} are spherical harmonics with Racah normalisation, i.e.:

$$C_{lm}(\hat{\mathbf{r}}) = \sqrt{\frac{4\pi}{2l+1}} Y_{lm}(\hat{\mathbf{r}}), \tag{4.37}$$

where Y_{lm} denote complex spherical harmonics.

For the sake of facilitating subsequent discussion we will now switch to explicitly

[4]When on-site densities are expanded, only one centre is used, and the number of functions N_ℓ in the auxiliary basis set is halved accordingly.

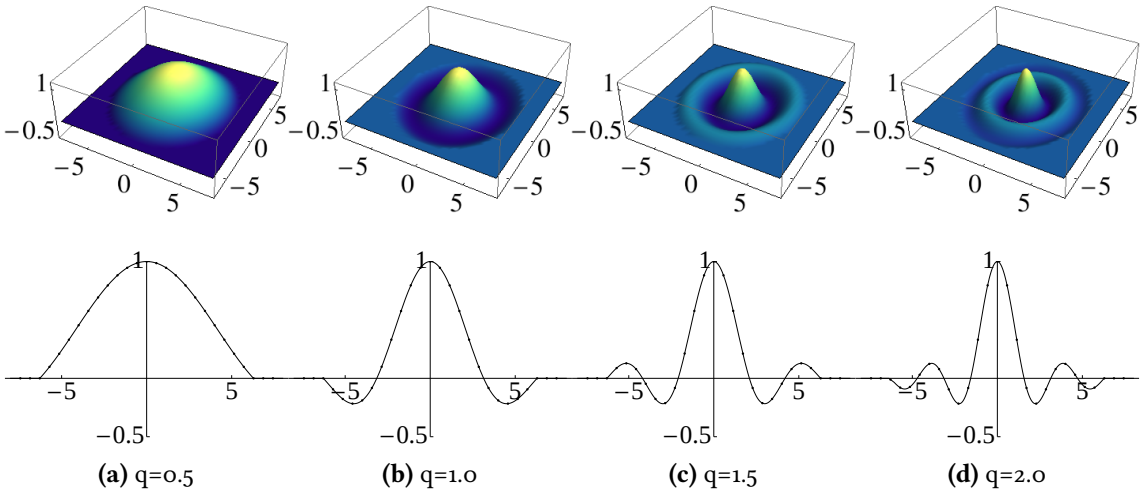

(a) q=0.5 **(b)** q=1.0 **(c)** q=1.5 **(d)** q=2.0

Figure 4.3: First four real spherical waves $f_{lmq}(\mathbf{r})$ with $l = 0, m = 0$. The value of a is set to $2\pi a_0$.

labelling the SWs with the indices $l(s_I)$, $m(s_I)$ and $q(s_I)$, i.e.:

$$f_{l(s_I)m(s_I)q(s_I)}(\mathbf{r}) \equiv f_{s_I}(\mathbf{r}). \tag{4.38}$$

We separate the angular and radial parts in the integrals in (4.36), and employ the properties of spherical harmonics, obtaining

$$\int_{\mathcal{S}_{I,a}} \mathrm{d}\mathbf{r}\, |\mathbf{r}|^l C_{lm}(\hat{\mathbf{r}}) f_{l(s_I)m(s_I)q(s_I)}(\mathbf{r}) = \delta_{ll(s_I)}\delta_{mm(s_I)} J_{l(s_I)q(s_I)}, \tag{4.39}$$

where

$$J_{lq} = \int_0^a \mathrm{d}r\, r^{l+2} j_l(r/b_{lq}) \tag{4.40}$$

is a radial integral that can be computed analytically.

The atom-centred multipoles obtained from (4.36) are already suitably normalised; and atom-centred, Cartesian dipoles are obtained as

$$\boldsymbol{\mu}_{\mathrm{el}}(I) = [\mathcal{M}_{11}(I), \mathcal{M}_{1-1}(I), \mathcal{M}_{10}(I)]. \tag{4.41}$$

The total electronic dipole moment of subsystem A with respect to a chosen origin $\mathbf{O}$ is computed by vector addition of atom-centred multipoles (see Fig. 4.4), following a suitable change of frame of reference:

$$\boldsymbol{\mu}^A_{\mathrm{el}}(\mathbf{O}) = \sum_{I\in A} \boldsymbol{\mu}_{\mathrm{el}}(I) - (\mathbf{O} - \mathbf{R}_I)\, \mathcal{M}_{00}(I). \tag{4.42}$$

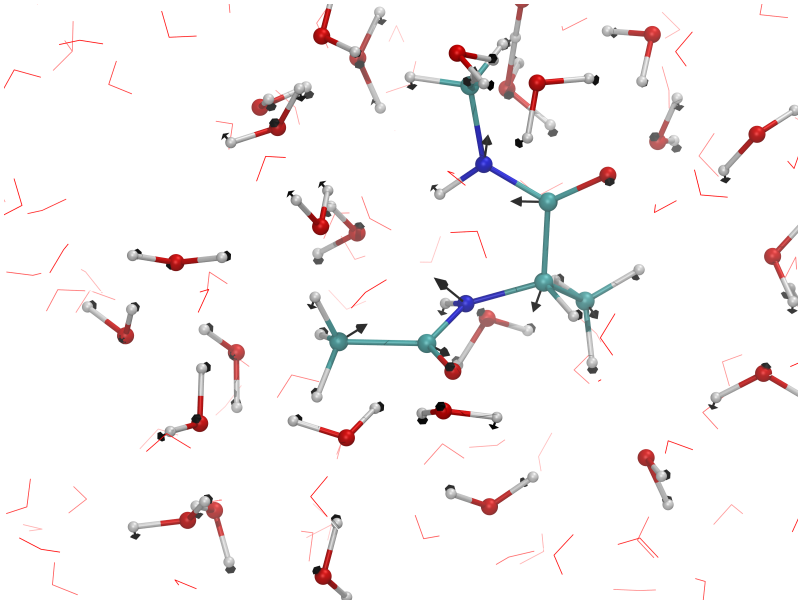

Figure 4.4: Example of atom centred dipoles $\boldsymbol{\mu}$ in (4.41) (black arrows) on 2-Ala and QM water molecules (balls and sticks). The remaining water molecules are treated as embedded classical charges (thin red sticks), see Sec. 4.7.

We note that the procedure described above minimises the quantity (4.32), with no constraint on the total charge of the entire system $\sum_I \mathcal{M}_{00}(I)$, let alone any of its subsystems. In the numerical tests we performed the total monopole obtained from the expansion was within 0.05% of the expected number of valence electrons for reasonable qualities of the auxiliary basis set.

4.6 Preliminary tests

In this section we report preliminary tests to compare the performance of both DKP and DMA approaches in computing the dipole moment of molecule in solution with respect to dipole moments obtained from MLWFs in Wannier90[126]. quantum espresso[138] was used as the plane-wave code to generate the extended KS states. The system we have chosen is a reduced version of the one we studied in production calculations[193], cf. Sec. 4.7. It consists of a alanine dipeptide 2-Ala in 43 H_2O molecules, see paragraph 4.7.2 . For this test system a kinetic energy cutoff of 800 eV was set, and we employed PBE exchange-correlation functional, both in Onetep and in quantum espresso. A cell volume of 15373.42 $Å^3$ was used. The initial configuration was obtained with AMBER12, as explained in the next section. The set of MLWFs chosen to compute the dipole moment of the 2-Ala only were obtained by visual inspection of the MLWFs centres.

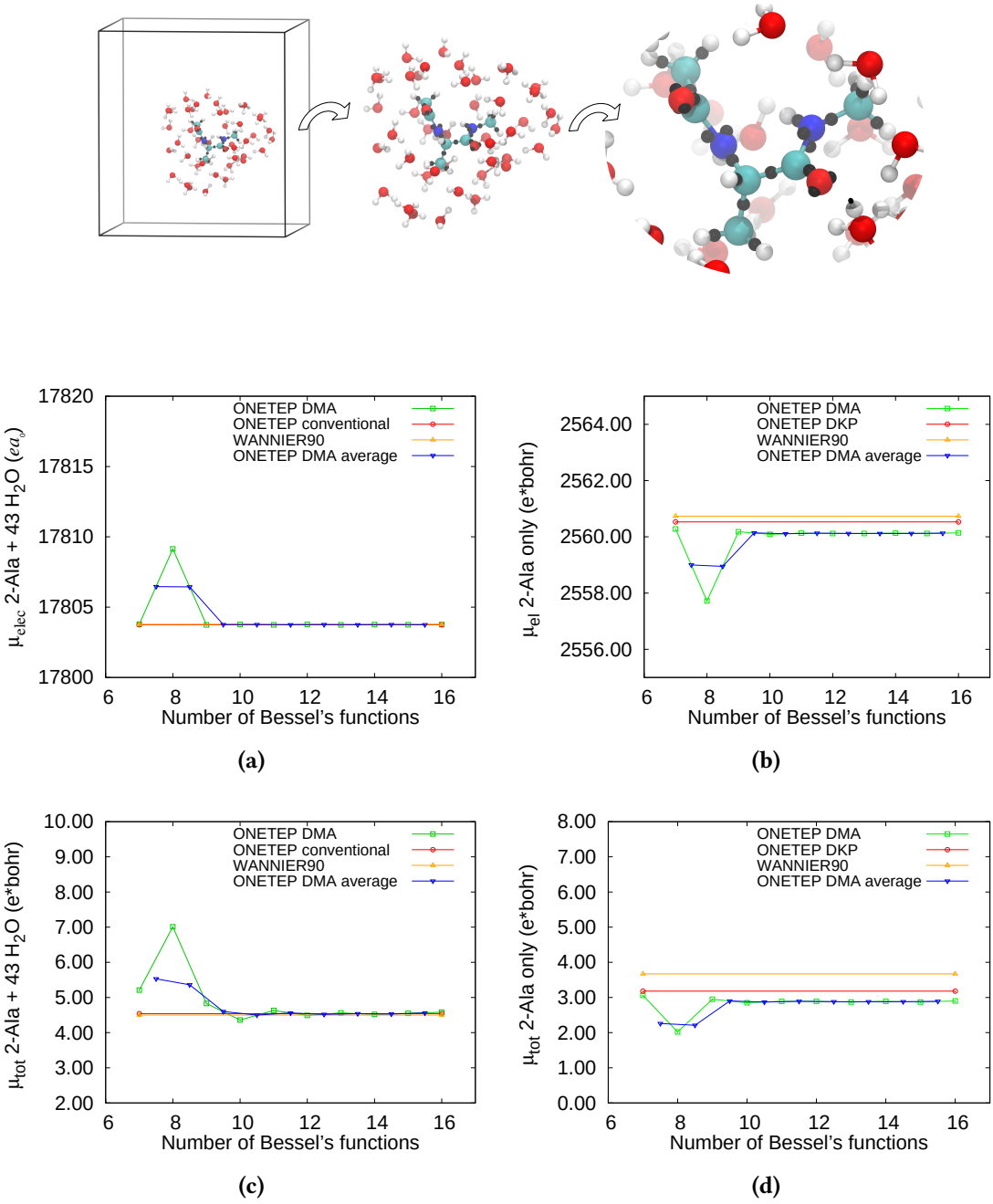

Figure 4.5: Three levels of magnification of the 2-Ala in 43 H_2O molecules system, with MLWFs centres for 2-Ala in black (top). Dipole moment convergence tests for the 2-Ala in 43 H_2O molecules system. Electronic dipole moment for the entire system a) and 2-Ala only b). Total (electronic + nuclear) dipole moment for the entire system c) and 2-Ala only d). DMA convergence tests with respect to the number of Bessel functions (Bessel functions with different values for q) are shown in green. For the DMA method the averages between two consecutive points are shown in blue. WANNIER90 results are shown in orange and ONETEP results, both for conventional calculations panels a) and c) and DKP panels b) and d), are shown in red.

When considering the dipole moment of the entire system, an excellent agreement between DMA in ONETEP and QUANTUM ESPRESSO-WANNIER90 is found, particularly when using 9 Bessel's functions or more in the expansion (4.35), cf. Fig. 4.5 panel a) and c). The error increase when computing the total dipole moment of the solute only. In this case, there is a $\sim$ 20% discrepancy between ONETEP and QUANTUM ESPRESSO-WANNIER90, due to the different ways of partitioning the density. However, DMA and DKP methods differ by less than 10%, Fig. 4.5 panel d).

4.7 VALIDATION TESTS

All the BOMD calculations and post-processing were carried out in ONETEP, whereas the classical MD trajectories were generated with the AMBER12 MD engine SANDER[242]. In the ONETEP BOMD engine, Newtonian equations of motion for the nuclei are integrated by adopting the well-known velocity Verlet scheme, where forces are generated "on-the-fly" from the ground state electronic configuration. Hybrid parallelism [243] and extrapolation schemes were exploited to minimise the wall-time per MD step.

For all the *ab initio* calculations we ran microcanonical BOMD with periodic boundary conditions. A time step of 0.5 fs was used, this value is a compromise between energy conservation, minimisation of error due to time discretisation, and computational cost. We employed a kinetic energy cutoff of 800 eV, with the PBE exchange-correlation functional and the D2 Grimme dispersion correction[244, 245]. The radius for the NGWFs localisation regions has been set to 8.0 a_0 . For the valence states we required 4 NGWFs for all the atoms but hydrogens, where only 1 NGWF was sufficient; norm-conserving pseudopotentials were adopted for dealing with core states. The total energy was minimised self-consistently through the LNV scheme[171, 173, 176]. At every time step, the starting set of NGWFs and density kernel fed to the LNV minimisation scheme were obtained from a linear combination of the previous MD steps NGWFs/density kernels

$$\chi_k^{\text{init}} = 2\chi_{i-1}^{\text{scf}} - \chi_{i-2}^{\text{scf}},$$

where χ^{scf} represents a converged NGWF/density kernel. The equations in (4.24) and (4.26) were used to compute the dipole moment of single molecules in the gas phase, and the dipole moment of the solute when considering a molecule in solution, respectively. Unless stated otherwise, the parameters summarised in Tab. 4.1 were used in all BOMD simulations.

In all the classical calculations we used the general AMBER force field (GAFF). A

Table 4.1: Parameters common to all BOMD simulations.

Parameter	Value
Time step	0.5 fs
Temperature	300 K
Kinetic energy cutoff	800 eV
NGWF radius	8.0 a_0
Outer loop RMS threshold	10^{-9} Ha $a_0^{-3/2}$
Inner loop RMS threshold	10^{-6} Ha $a_0^{-3/2}$
Thermostat	None
XC functional	PBE
NGWF extrap. scheme	Linear
Density kernel extrap. scheme	Linear

time-step of 0.5 fs was chosen for consistency with BOMD calculations. The parameter file and the initial coordinates were generated with the LEAP graphical user interface xLEaP. We followed this protocol: we performed a geometry relaxation calculation for 2500 steps, where in the first 1500 steps we used steepest-descents for minimising the energy, and in the remaining 1000 steps the conjugate gradient method. The bonds containing hydrogen atoms were kept fixed throughout using the SHAKE algorithm[191]. After the geometry relaxation, we performed a heating calculation, where we let the temperature increase from 0 to 300 K, using Langevin dynamics with the collision frequency coefficient $\gamma = 2.0$ ps^{-1} for 10 ps with a cutoff for the electrostatic interactions of 10.0 Å. A further equilibration calculation was performed at a fixed temperature of 300 K for 10.0 ps, with the other parameters unchanged. After this equilibration phase, a production run was performed, where the SHAKE constraints and the thermostat were removed, and the total simulation length was set to 20.0 ps.

The IR spectra were then computed through (4.14), where the dipole moments are simply given by

$$\boldsymbol{\mu}(t) = \sum_I \nu_I \mathbf{R}_I(t), \tag{4.43}$$

where ν_I are the total classical charges on each atom I, obtained from the force field parameters, and $\mathbf{R}_I$ are the atomic positions. The parameters in Tab. 4.2 were used in all the classical calculations.

Following Gaigeot[34], we applied a Gaussian filter window in the time domain, such that each term of the correlation function $C(t_k)$ was multiplied by a Gaussian function $\exp(-0.5\sigma(t_k/\tau)^2)$, where τ is the length of the simulation, and σ is 10 for the gas phase,

Table 4.2: Parameters common to all classical simulations.

Parameter	Value
Time-step	0.5 fs
Temperature	300 K
Frequency coefficient γ	2.0 ps^{-1}
Electrostatic interaction cutoff	10.0 Å
Pressure relaxation time τ	2.0 ps
Force field	GAFF
Thermostat	Langevin

and 40 for the aqueous phase.

4.7.1 Gas phase

Water For water in the gas phase we used a cubic cell with a length of $a = 15.0$ Å. The water molecule was originally placed at the centre of the cell. The initial geometry was obtained from a geometry optimisation calculation. The initial velocities were extracted from a Maxwell-Boltzmann distribution at the imposed temperature of 300 K. The total time was 8.0 ps. We let the system equilibrate for 1.0 ps, and then performed a production run of 7.0 ps. To calculate the normal modes we used the built-in phonon module in Onetep. In order to compute the normal modes, the forces on the nuclei and their derivatives must be evaluated with high accuracy, as the normal modes are obtained from the diagonalisation of the Hessian matrix of the total energy. Thus, a geometry optimisation calculation with a well-converged density is required. The procedure requires $3N$ energy and forces calculations and one Hessian diagonalisation.

Carbon dioxide For carbon dioxide we used a cubic cell with a length of $a = 12.0$ Å. As for the water molecule, we placed the CO_2 molecule at the centre of the cell. The simulation time was 8.0 ps, where we equilibrated the system over the initial 1.0 ps. The initial velocities were extracted from a Maxwell-Boltzmann distribution at the imposed temperature of 300 K.

Ethanol For the ethanol molecule in the gas phase, we adopted the same procedure described above. We used a cubic cell with a length of $a = 18.0$ Å. The temperature was fixed at 296.15 K for consistency with the experimental data. The simulation length was 5.5 ps, and a time-step of 0.75 fshas been used. This slightly larger time-step allowed to

speed up the simulations while still ensuring a good conservation of total energy. As a consequence, we performed NVE -BOMD for $\approx$ 7300 steps. The systems was equilibrated for 1.5 ps, and the length of the production run was 4.0 ps.

2-Ala In order to test the accuracy of the DKP and the DMA methods of sections 2.5 and 2.6 in generating IR spectra of systems in the condensed phase, we considered a well-known system referred in the literature as alanine dipeptide (2-Ala). 2-Ala is the alanine amino-acid equipped with minimal peptide bonds and with the C-terminal and N-terminal capped with methyl groups, and constitutes one of the simplest system with a peptide motif. This system has been extensively studied by Gaigeot *et al.* [2, 3, 34, 246], both in the gas and the aqueous phase. The study of 2-Ala in the gas phase is crucial for the understanding of the effects of the solvent in the aqueous phase. However, addressing the issue of the preferred conformations of 2-Ala in water is not the object of this work.

For 2-Ala in the gas phase, we used a cubic box with a length of $a = 20.0$ Å. We ran a 2600-step NVE -BOMD simulation (1.3 ps). The initial momenta were generated from a Maxwell-Boltzmann distribution, in order to obtain an initial temperature of 300 K. Prior to the MD, the initial geometry[5] was relaxed, by performing a geometry optimisation in Onetep.

4.7.2 Aqueous phase

The 2-Ala-water system is not interesting *per se*, but it is a prototype of larger and more complex peptides. Moreover, since 2-Ala represents a floppy molecule of minimal size, it is a perfect candidate for testing our methods within the BOMD approach. Studying 2-Ala conformational changes in a polar solvent like water can help shed light on the complex dynamics of larger biomolecules *in vivo*.

2-Ala in AMBER For 2-Ala in the aqueous phase we used periodic boundary conditions. We solvated the system with 500 water molecules through the SOLVATEBOX command in the xLEaP interface, using the TIP3P model for the water molecules. Subsequently, the system was relaxed by first relaxing the solvent for 1500 steps while keeping the solute's atomic positions fixed, and then relaxing the entire system for a further 3500 steps. We then carried on with heating the system from 0 to 300 K, followed by a constant pressure calculation at $p_{\text{ext}} = 1$ atm for 10.0 ps to let the entire system expand and to obtain a density of 0.9847 g cm^{-3}. We used an isotropic position scaling barostat and a pressure

[5]The initial geometry was taken from the xLeap coordinate file.

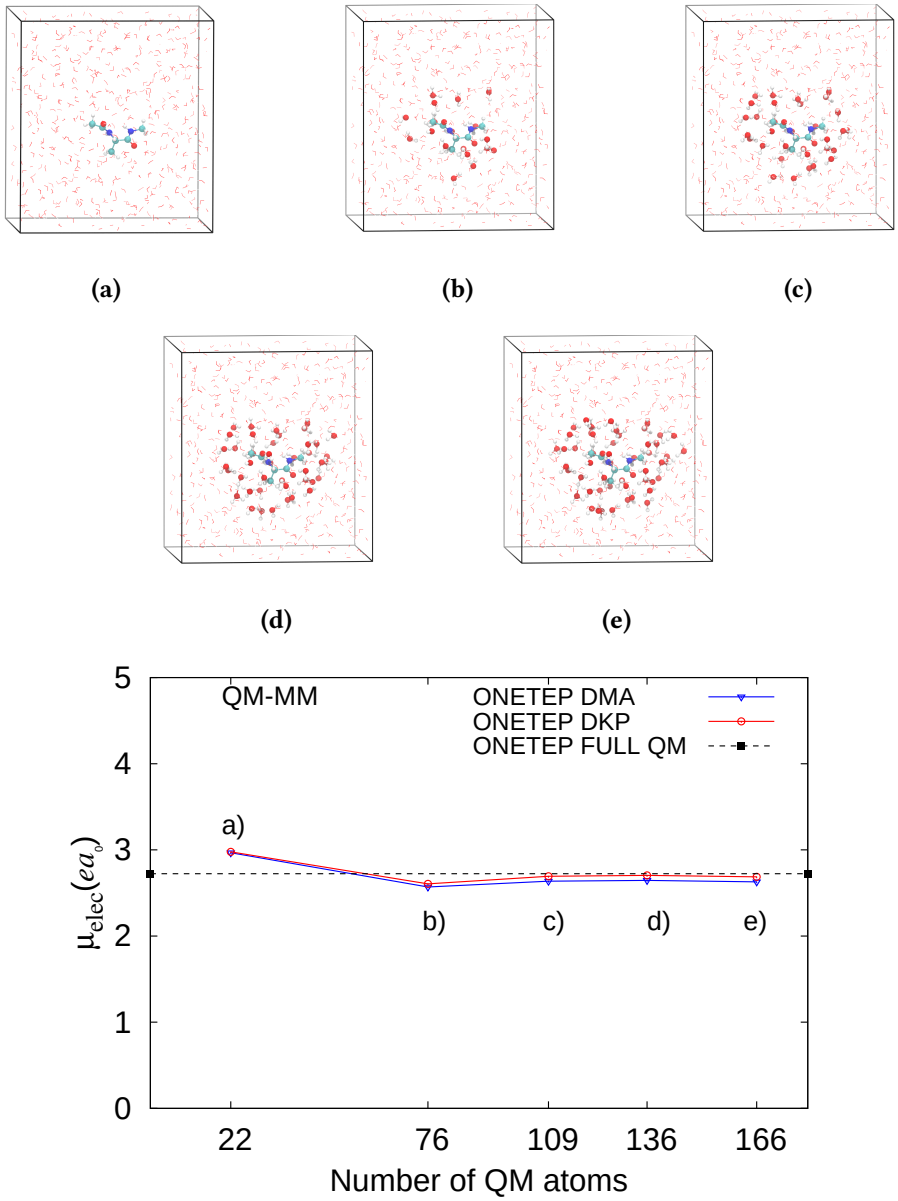

Figure 4.6: Convergence tests for the electronic dipole moment of 2-Ala in H_2O box with respect to the number of QM atoms in the simulation cell. 2-Ala only a) 2-Ala plus closest 18 H_2O molecules b) 2-Ala plus closest 29 H_2O molecules c) 2-Ala plus closest 38 H_2O molecules d) and 2-Ala plus closest 48 H_2O molecules. For DMA results we have use the average between $q = 10$ and $q = 11$ (solid blue with empty triangles). DKP results are computed from the NGWFs centred on the QM molecules only according to (4.26) (solid red with empty circles).

relaxation time τ of 2.0 ps. The final cell volume was $V_{\text{fin}} = 15373.4$ Å^3. Finally, we performed an NVE production run for 40.0 ps, where all the SHAKE constraints were removed.

2-Ala in ONETEP Both the DKP and DMA methods are linear scaling and they can be performed "on the fly". However, the DMA method at this stage of the implementation is not able to treat systems where the NGWFs span the boundary of the simulation cell, i.e. when periodic images of NGWFs re-enter the original cell. Moreover, the DMA method requires the computation of the electrostatic metric V of (4.30) at every MD step, which although it can be very efficiently parallelised, is still very costly for large systems.

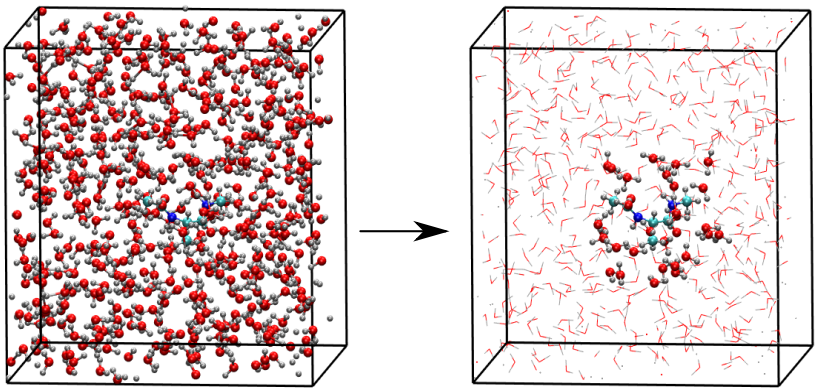

Figure 4.7: Reduction of the system size. Left: the original cell with all QM atoms. Right the reduced-size system with 109 QM atoms and the remaining 1413 atoms represented as embedded classical charges. This transformation was applied to all the BOMD steps.

Consequently, at every MD step we extracted from the full system of 1522 atoms, a smaller system containing the 2-Ala molecule and the closest 29 water molecules whose NGWFs were all fully contained inside the original simulation cell. The remaining water molecules of the full system were transformed into embedding classical charges. For every MD step we therefore considered 109 quantum atoms and 1413 embedding classical charges, see Fig. 4.7. Convergence tests were performed to ensure that the size of the reduced quantum system was sufficient to obtain well-converged values for the Cartesian components of the solute dipole moment, see Fig. 4.6. The partial charges on classical hydrogen and oxygen atoms were obtained from the TIP3P model as explained in Ref. 247. Specifically, the partial charge on classical oxygen atoms was $-0.834e$, and for classical hydrogen atoms was $0.417e$. The effect of embedding classical charges is to yield a smoother profile for the 2-Ala electronic dipole moment with respect to the system size and therefore to reach the converged full quantum system value faster.

The initial atomic coordinates and velocities and the simulation cell for the full quantum system were obtained from the classical calculations described above, after the equilibration procedure. We ran a 2080-step NVE -BOMD simulation with 1522 atoms using 2256 CPU cores to obtain a $\approx$ 1.0 ps-long trajectory.

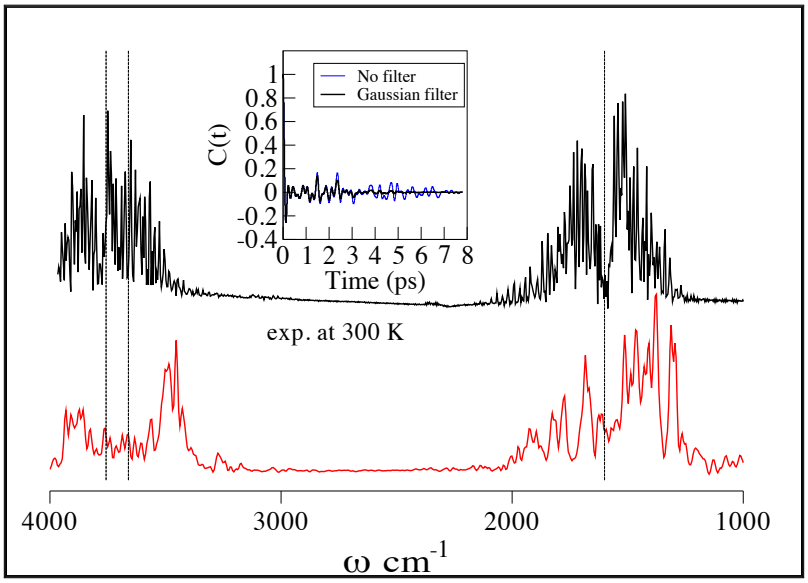

Figure 4.8: IR spectrum of water in the gas phase at 300 K calculated in ONETEP through *NVE* -BOMD simulations, using the Kubo quantum correction factor (solid red). Experimental IR spectrum of water in the gas phase at 300 K from Ref. 1 (solid black). Frequencies from normal mode analysis obtained with ONETEP (dotted black). Autocorrelation function of the total dipole moment of water in vacuum, with and without Gaussian convolution (inset).

4.8 Results and discussion

The results from the BOMD and classical simulations were post-processed to obtain the autocorrelation functions and the IR spectra.

The water molecule in the gas phase vibrates in several ways involving combinations of the symmetric (exp. at 3657.1 cm^{-1}), and asymmetric (exp. at 3755.9 cm^{-1}) stretching, and bending of the covalent bonds (exp. at 1594.7 cm^{-1})[248]. The results for the entire simulation and the final spectra with the Kubo quantum correction factor are shown in Fig. 4.8. As we can see from Fig. 4.8, we found a good agreement with the experimental spectrum, where both the positions and the intensities of the different bands are very well reproduced. The breadth of the symmetric and asymmetric stretch bands is due to the rotational fine structure of these bands.

The results for the carbon dioxide are shown in Fig. 4.9. As we can see, the intensities and positions of the asymmetric C=O stretch mode (exp. at 2249 cm^{-1}) and the two degenerate O=C=O bending modes (exp. at $\approx$ 660 cm^{-1}) are very well reproduced. As expected, the symmetric C=O stretch mode (exp. at 1338 cm^{-1}) is not IR-active as the molecular dipole moment does not change under this vibrational mode, and therefore is absent in the spectrum. More interestingly, the combination bands at $\approx$ 3600 cm^{-1} and

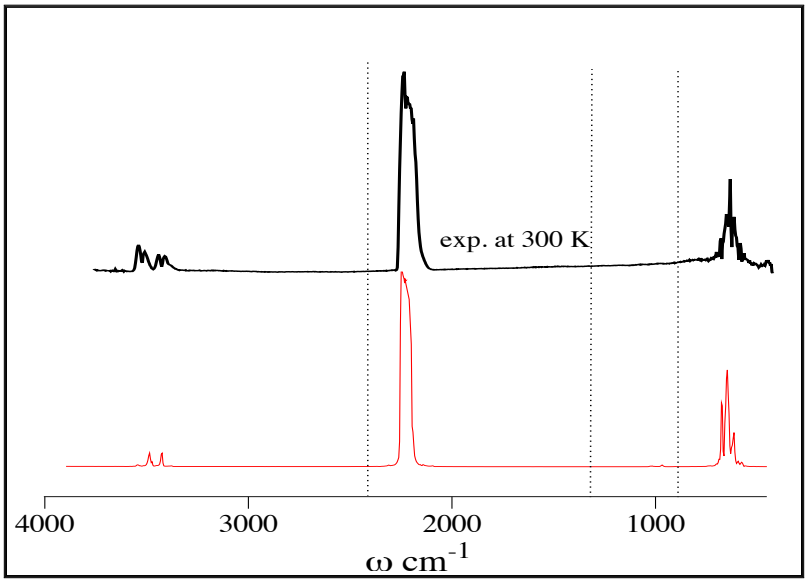

Figure 4.9: IR spectrum of carbon dioxide in the gas phase at 300 K computed through *NVE* -BOMD simulations in ONETEP, using the Kubo quantum correction factor (solid red). Experimental IR spectrum of CO_2 in the gas phase at 300 K from Ref. 1 (black line). Frequencies from normal mode analysis obtained with ONETEP (dotted black).

3700 cm^{-1}, which originate purely from anharmonic effects, are also recovered.

As we can see from Fig. 4.10, also in the case of ethanol in the gas phase we obtain a good overall agreement with the experimental spectrum. Shapes, intensities and the relative positions of the different bands are well reproduced. The two strong peaks at $\approx$ 1100 cm^{-1} correspond to stretches of the C-O bond, while the double bond C=O signature corresponds to the bands in the region around 1600 cm^{-1}. The broad band in the region 2800 – 3100 cm^{-1} is known to be characteristic of C-H bond stretching. Since ethanol has five C-H bonds, no more than five bands should present in the harmonic approximation results. Nonetheless, the experimental spectrum as well as the anharmonic one, can show more than five bands due to conformational changes (*trans*- and *gauche*-conformers) and Fermi resonance effects[249]. However, the correct assignment of fine vibrational structure is outside the purpose of this work. It is worthy to mention that in the IR spectrum obtained from the BOMD calculation, the position of the O-H stretch mode is at ω = 3500 cm^{-1}, whereas in the experimental spectrum it is at $\approx$ 3645 cm^{-1}. Intensity and broadness are also reduced. This is possibly a consequence of using a larger time-step, which affects more the high-frequency modes. Interestingly, this band is completely missing in the spectrum computed from the AMBER calculation with the GAFF force field with all SHAKE constraints removed, Fig. 4.10. This reinforces our statement that spectra computed at finite temperatures from an accurate molecular dynamics trajectory yield a better description of the absorption bands compared to classical simulations or

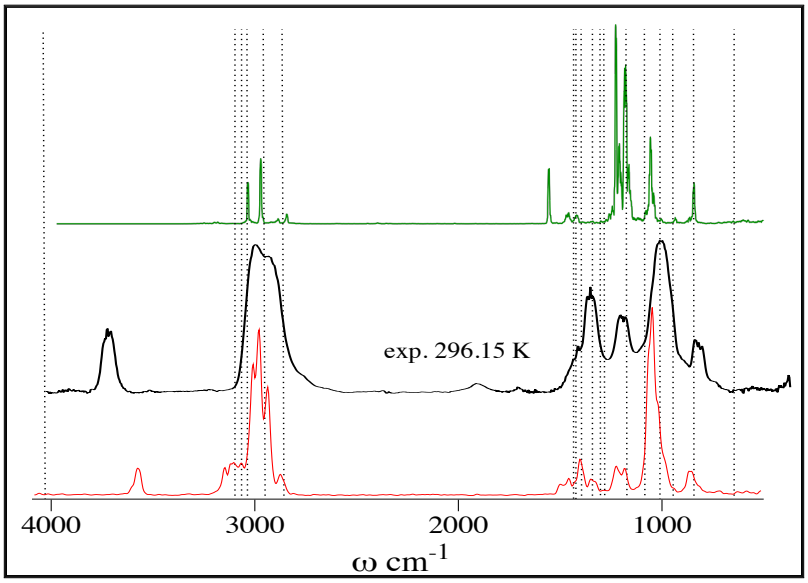

Figure 4.10: IR spectrum of ethanol in the gas phase at 296.15 K obtained from *NVE* -BOMD simulations in ONETEP, using the Kubo quantum correction factor (solid red). Experimental absorption IR spectrum of ethanol in the gas phase at 296.15 K from Ref. 1 (solid black). Frequencies from normal mode analysis generated in ONETEP (dotted black). AMBER-generated IR spectrum for ethanol in gas phase at 296.15 K (solid green).

calculation with the harmonic approximation.

Due to the short length of the BOMD simulation, we are only able to sample the fast vibrational modes of 2-Ala. In fact, we are not able to properly compute a spectrum in the near infrared. We focused instead on the range 1000-2000 cm^{-1} of the infrared spectrum, as it shows the contribution of Amide I-III bands and it is the domain typically used to assess the structural properties of peptides. In Fig. 4.11, we show the IR spectra calculated from the BOMD simulation in ONETEP and from classical MD in AMBER in vacuum. The three bands appearing in the spectrum obtained from BOMD, relative to Amide I at $\approx$ 1675 cm^{-1}, Amide II at $\approx$ 1515 cm^{-1}, and Amide III at $\approx$ 1263 cm^{-1} are in good agreement with the bands reported in Refs. 34 and 2, which are at $\approx$ 1670 – 1680 cm^{-1}, $\approx$ 1257 cm^{-1}, and $\approx$ 1210 cm^{-1} respectively, even for the shorter simulation length employed here. Interestingly, the IR spectra in Ref. 34 were computed using Car-Parrinello MD, with the need of a fictitious electronic mass and consequent shifting of the final spectra. As explained in Refs. 34 and 2, of these three bands, shape and position of Amide I band appears to be a good candidate as vibrational signature for 2-Ala at 300 K when compared to larger and more complex alanine peptide chains.

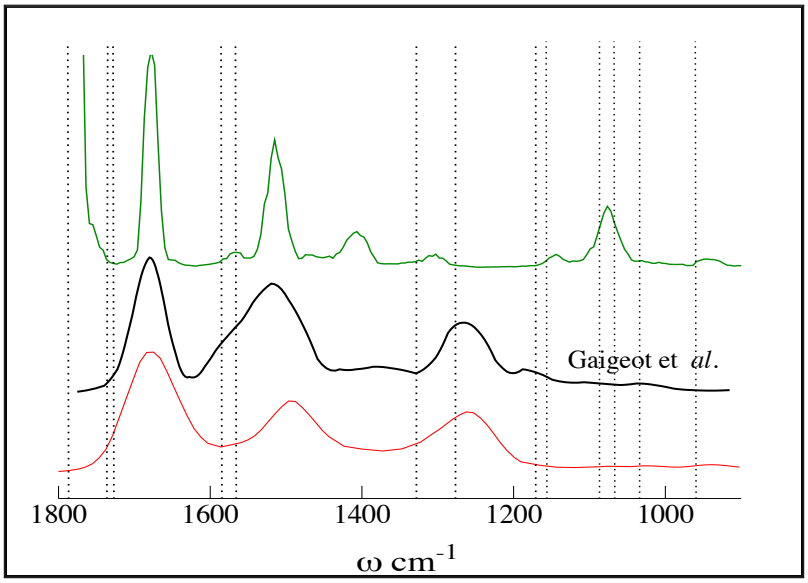

Figure 4.11: IR spectrum of 2-Ala in the gas phase at 300 K computed from *NVE* -BOMD simulations in ONETEP (solid red). The computed IR spectrum of 2-Ala in the gas phase at 300 K from classical MD simulation in AMBER (solid green). Frequencies from normal mode analysis as obtained from ONETEP (dotted black). IR spectrum of 2-Ala in the gas phase from CPMD simulations, results from Ref. 2 (solid black).

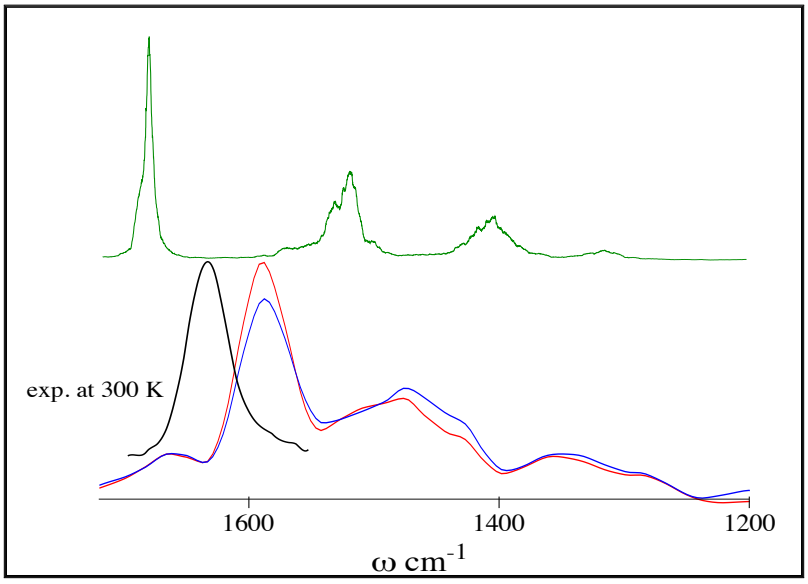

Figure 4.12: IR spectrum of 2-Ala in the aqueous phase at 300 K, obtained from *NVE* -BOMD simulations in ONETEP with the DKP method (solid red) and DMA method (solid blue). IR spectrum of 2-Ala in AMBER (solid green). Experimental spectrum at 300 K of 2-Ala in deuterated water (D_2O) from Ref. 3.

4.8.1 2-Ala in the aqueous phase (1522 atoms)

The spectra computed with the DKP and DMA methods for 2-Ala in water are shown in Fig. 4.13. The spectrum from classical simulation is also shown for reference. DKP and DMA methods are in good agreement, especially in the range $1200 - 1400$ cm^{-1}. In the region between $1400 - 1700$ cm^{-1} the shape and position of the bands is the same but not the intensities. This is likely to be due to the different way the density is partitioned in the two methods. In our simulation, the 2-Ala explores mostly the unfolded β and P_{II} conformations (see Fig. 4.13), since the folded α_R shows a slightly higher free energy (about 1 Kcal mol^{-1}) at room temperature, leading to a preference for P_{II}/β population. Consequently, a single peak in the region $\approx 1590 - 1600$ cm^{-1} is found. This is in good agreement with what found by Gaigeot et *al.* in Ref. 246. The Amide II band is blue-shifted and merged into one broader Amide I-II band. This property of folded 2-Ala in water makes the Amide I-II band featureless[246]. These does not mean that the α_R conformation is absent, since this view could be altered by longer statistics.

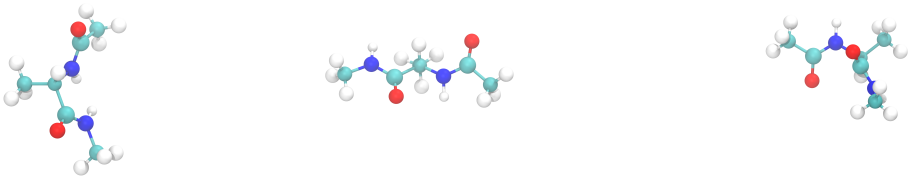

(a) α_R **(b)** β **(c)** P_{II}

Figure 4.13: Three conformers of 2-Ala in aqueous phase. a) α_R folded configuration. b) β unfolded configuration and c) P_{II} unfolded configuration.

The experimental spectrum also shows a single peak at $\approx$ 1635 cm^{-1}. However, the solvent used in the experiment is D_2O to avoid vibrational mixing between H_2O bending modes with Amide I bands. In fact, mixing between Amide I and II modes and the bending modes of H_2O will broaden the Amide bands. The difference between the computed spectra and the experimental one can be potentially explained by the difference in solvents used. In addition, the combination of trajectories from folded and unfolded configurations will also improve the Amide I-II band position and shape[246]. The strong hydrogen bonds formed between 2-Ala and its surroundings yield to a red-shift of the position of Amide I band of about 80.0 cm^{-1} with respect to 2-Ala in the gas phase. On the other hand, the Amide II band is blue-shifted by $\approx$ 50 cm^{-1}. The merging of the Amide I and Amide II into one single peak is a clear effect of conformational changes and couplings with the solvent, which strongly affect the final spectrum.

4.9 Summary

We have presented two methods to compute the dipole moment of selected molecules in a larger environment, such as the solvent. Our methods are based on density kernel partitioning (DKP) and distributed multipole analysis (DMA), respectively. Both methods have been implemented in Onetep. Combining our methods with the Fourier transform time-correlation function (FTTCF) formalism and Born-Oppenheimer molecular dynamics we are able to compute fully anharmonic infrared spectra of molecules in the gas phase and in solution at finite temperature. With this approach, conformational dynamics and anharmonic effects (anharmonicity of the potential energy surface) are naturally taken into account within the molecular dynamics simulation without the need of any *a posteriori* correction. Moreover, for systems in solution, only the spectrum of the solute is computed while retaining the effect of the vibrational coupling of the modes of the solute with the surroundings. This feature allows the rigorous study of molecules in solution, providing a formidable tool for the understanding and the assignment of bands from experimental spectra.

The theory for the FTTCF formalism is derived from first-order time-dependent quantum perturbation theory. We stress the point that the only approximation made here, from a theoretical point of view, consists in treating the nuclei classically. This approximation leads to the detailed balance condition symmetry problem that is partially recovered by introducing a theoretically-derived quantum correction factor.

A number of NVE -BOMD simulations at finite temperature on benchmark molecules in the gas phase have been performed. For all the systems very good agreement was found; when compared with the corresponding experimental spectra positions, shapes and intensities of the bands were accurately reproduced. It is worth noting that even for small molecules the role played by the anharmonicity of the PESs at finite temperature is important. This is evident in the case of CO_2, where combination bands naturally emerge in our spectrum, whereas they are completely absent in the harmonic approximation. In general, we found that spectra computed with our method are in much better agreement with experiments than the ones computed through normal mode analysis or a classical force field.

Finally, we performed an NVE -BOMD simulation to validate the DKP and DMA methods on the 2-Ala peptide in 500 water molecules, i.e. 1522 atoms. The spectrum for 2-Ala was compared to similar calculations from Gaigeot *et al.*, obtained by performing CPMD with MLWFs for the calculation of the dipole[2, 34], and good agreement was found with these methods and with experiment.

Schemes for speeding-up BOMD in Onetep, such as extended-Lagrangian

schemes [42], are the topic of the next chapter. These schemes are promising for extending the time-scale of the dynamics, by reducing the number of self-consistency cycles while retaining time reversibility and energy conservation. By exploiting fast BOMD and linear scaling, computational spectroscopy based on DFT-MD can be made viable even for large systems.

Chapter 5

Extended Lagrangian schemes in classical polarisable force field and linear-scaling density functional theory

Abstract

This chapter deals with two novel integration schemes, based on extended-Lagrangian techniques, for accelerating molecular dynamics simulations which relies on self-consistence loops for the computation of energy and forces, e.g. classical polarisable force field molecular dynamics and DFT-BOMD. Self-consistence loops have crucial consequences for energy conservation and computational time in these approaches. Hence, being able to improve the performance of these approaches, by reducing the number of steps required to achieve self-consistency, while maintaining the same level of accuracy, is crucial for the exploration of new phenomena at larger scales (i.e. larger system sizes and longer simulation times). These integrators are explicitly designed to retain energy conservation to high orders, despite using information from previous steps in the self-consistence loop. After a general introduction dedicated to the importance of fast and accurate molecular dynamics simulations, I continue with describing the general ideas behind these integration schemes and how they are related to extended-Lagrangian techniques. Then I comment on issues specific to classical polarisable force field MD as implemented in TINKER, by T. Head-Gordon and her collaborators. After this detour, I present how I implemented both integrators within the ONETEP code and what modifications were necessary to make them compatible with the ONETEP framework.

Finally, a detailed study of the performance of these schemes is proposed, showing how these schemes consistently enable significant, and usually similar, boost in performance over simulations not employing them, both for classical polarisable force field MD and linear-scaling DFT BOMD. Most importantly, in the ONETEP case, both schemes were capable of decreasing the calculation time per MD step of a factor of 2. Thus, these novel algorithms constitute significant improvements that extend the timescales accessible to classical and linear-scaling DFT BOMD simulations alike.

5.1 Introduction

Starting from the first classical molecular dynamics (MD) simulations in the late 1950s, myriad schemes employing a hierarchy of approximations for the description of inter-atomic interactions have appeared, ranging from *ab initio* methods, some of which have been described in Chapter 2, to classical fixed charge models.

The last two decades have witnessed substantial developments in the sophistication of classical force fields[250, 251], driven by the need of overcoming the weaknesses present in old fixed point charge models. The dynamic response of a molecular system to a given environment, e.g. an organic solvent or metallic ions in solution, becomes difficult to capture when an explicit treatment of polarisation is absent[186]. Moreover, when the physical and chemical conditions are far from the ones used to parametrise the potential and charges, fixed point charge models can perform poorly[251]. Usually, severe inaccuracies are found at extreme pressures or temperatures, or at interfaces. Hence, the inclusion of polarisation effects is essential for obtaining an adequate description of complex systems, and improving the transferability of classical models. This has led to a gamut of polarisation models, employing: Drude oscillators [252, 253] fluctuating charges[254, 255] and induced point dipoles [256–262] or higher multipoles[263]. From the computational point of view, in general polarisation effects involve a relatively costly variational self-consistent determination of the induction response, although alternate schemes have recently been proposed[264, 265]. See Refs. 251,186 and185 for a review.

Self-consistent loops are a common feature of both classical MD calculations with polarisable force fields and BOMD calculations, with crucial consequences for energy conservation and computational time in these approaches. Energy conservation is known to be sensitive to the degree of convergence of the self-consistency loop. In polarisable MD with induced dipoles this is a consequence of a force term proportional to the energy gradient residual $\frac{\partial U}{\partial \boldsymbol{\mu}}$[265]. This term vanishes in schemes where induced dipoles are not determined self-consistently (e.g. iAMOEBA[264]), whereas in self-consistent schemes it can only be neglected if the iterative dipole equations are tightly converged.

In KS-DFT the error in the forces on the nuclei is first order with respect to the error in the incompletely converged density, even though the error in the energy is second order[14]. This means it is significantly harder to compute accurate forces than it is to calculate energies. Additionally, the numerical machinery of KS-DFT, which typically involves FFTs on grids with finite spacing and finite extents, numerical integrations on a variety of grids, the use of moment approximations, etc. results in an increase in the inaccuracy of the forces compared to the classical case, where closed analytical expressions are often readily at hand. Furthermore, many DFT approaches have to contend with additional – beyond Hellmann-Feynman – contributions to the forces, known as Pulay forces[266], that arise as a result of the dependence of the basis set on nuclear positions, cf. Sec. 3.5. Although the magnitude of the Pulay forces is, in principle, independent of how close the electronic configuration is to the ground state[14], errors in *approximate* treatments of Pulay forces can be larger when the system is insufficiently converged[172]. More precisely, this is relevant only for *in situ* optimised localised orbitals, whereas for fixed localised orbitals the Pulay forces can be computed exactly. Finally, in LS-DFT approaches additional difficulties arise due to the use of strictly localised orbitals[267], where further non-Hellmann-Feynman contributions to the forces can be expected to arise as a consequence of localisation constraints[211] or of the incomplete convergence of localised orbitals[172, 211].

For polarisable classical MD and BOMD calculations alike, tight SCF convergence is thus a necessary requirement for maintaining adequate energy conservation. The large number of SCF steps demanded to achieve a tight convergence leads to an undesired increase of calculation walltimes. It is tempting to speed up the process to re-use, at each new MD step, the converged solutions obtained at previous steps. Although the pitfalls of such intuitive extrapolation schemes have been known since the early nineties[268, 269], adequate ways around the problem have been proposed only recently[42, 270, 271]. The self-consistent solution does not depend on the initial guess only when the SCF optimisation is fully converged. In practice, the SCF optimisation is always incomplete, leading to memory effects and the breaking of time-reversal symmetry[42], which gives rise to systematic errors in energy gradients that manifest as a drift in microcanonical energy[271]. Such undesired memory effects can be elegantly addressed through extended Lagrangian BOMD (XL-BOMD) formulations, where the initial guesses are not extrapolated, but rather *propagated* as extended degrees of freedom, allowing time-reversibility to be recovered.

Self-consistency has also a major impact on the computational cost, since evaluation of energies and forces is in general the most demanding part in MD simulations. Schemes able to by-pass the SCF loop, e.g. Car-Parrinello MD or fixed charge force fields, are

inherently faster in terms of wall-time per MD step.

In this chapter we focus our attention on two integration schemes proposed recently – a *dissipative* formulation by Niklasson *et al.* [42] and an *inertial* formulation by Albaugh *et al.*[272]. These improvements to the original scheme by Niklasson *et al.*[273] use different strategies to mitigate the problem of error accumulation that causes two extended potential energy surfaces – that of the real degrees of freedom, and that of the initial guesses – to diverge. In this chapter we study the performance of the two schemes in MD simulations of liquid water, which are carried out in two different regimes – using the polarisable, classical force field AMOEBA, and using the ONETEP LS-DFT formulation. Both the implementation and the calculations concerning polarisable classical force field were performed by people in Teresa Head-Gordon group at Berkeley University in California (USA). In particular, some of the results shown in what follows had already appeared in the paper by Albaugh *et al.*[272]. A thorough analysis of the performance of both schemes in the classical regime and in the quantum regime, made in collaboration with the authors of the schemes, has been accepted for publication[274]. Our analysis employs similar systems, but tests how the schemes operate under distinct conditions, namely long simulation times with inherently accurate forces and classical potential energy surfaces *vs.* short simulation times with inherently more noisy forces and quantum-mechanical potential energy surfaces. This allows us to highlight the differences between the two schemes, and their strengths and weaknesses in each of the two regimes.

We begin with a short presentation of the classical approaches used in our study (Section 5.2), quantum approaches were reviewed in Chapter 2, followed by a presentation of the original extended Lagrangian scheme (Section 5.3), and the dissipative (Section 5.4) and inertial (Section 5.5) integration scheme variants, pausing briefly to comment on issues specific to linear-scaling BOMD and its non-orthogonal orbital variants in particular. Sections 5.6.1, 5.6.2 and 5.6.3 describe the computational set-ups and the results obtained in the simulations, respectively. We finish with a summary (Section 5.7), where we outline our observations and lay out directions for promising future research.

5.2 Classical polarisable force-field molecular dynamics

For our analysis of classical molecular dynamics, we have adopted the polarisable force field AMOEBA[260, 275], as implemented in the TINKER[258] program. AMOEBA is part of a new generation of force fields that go beyond the time-honoured fixed point charges model. In AMOEBA, electrostatic interactions are modelled as interactions be-

tween point multipoles, where each nuclear site I is host to a set of permanent multipoles, $\mathbf{M}_I = \{q_I, \boldsymbol{\mu}_I, \mathbf{Q}_I\}$, representing a charge, dipole and quadrupole respectively. Permanent multipoles are parametrised from *ab initio* calculations[276–278]. Alongside permanent multipoles, an inducible dipole $\boldsymbol{\mu}_I^{\text{ind}}$ is also placed at each nuclear site, allowing polarisation effects to be explicitly captured. Scaling of electrostatic interactions based on inter-atomic connectivity[259], and Thole damping[279] are used to ensure a smooth transition between the electrostatic and bonded descriptions of interactions and to avoid the polarisation catastrophe. The following criteria are adopted in the actual implementation: 1) Polarisation groups are introduced alongside with molecules, defined through connectivity information[259]. 2) Permanent multipoles interact with other permanent multipoles both within and between polarisation groups, but in the latter case a scaling factor is usually applied. 3) Permanent multipoles polarise inducible dipoles only between polarisation groups, regardless of whether the groups are on the same molecule or on different molecules. Moreover, permanent multipoles interact with other permanent multipoles both within and between molecules. However, within molecules they are scaled depending on the neighbourhood, regardless of polarisation groups. For 1-2 and 1-3 neighbours they are scaled to zero, for 1-4 neighbours to 0.4, for 1-5 neighbours to 0.8, and no scaling is applied for further neighbours. 4) Permanent-permanent interactions are not Thole-damped, whereas induced-induced interactions and permanent-induced interactions are. In the latter case, they are zeroed for 1-2 and 1-3 neighbours.

The inducible dipoles, $\boldsymbol{\mu}_I^{\text{ind}}$, on the nuclear site, are formally obtained by the product of the site-specific isotropic polarisability α_I and the total external electric field exerted:

$$\boldsymbol{\mu}_I^{\text{ind}} = \alpha_I(\mathbf{E}_I + \mathbf{E}'_I), \tag{5.1}$$

where $\mathbf{E}_I$ is the electric field due to the permanent multipoles belonging to polarisation groups different from the one nucleus I belongs, and $\mathbf{E}'_I$ is the field generated by the induced dipoles on all the other nuclear sites:

$$\mathbf{E}_I = \sum_J \mathbf{T}_{IJ}\mathbf{M}_J^{(\text{d})} \tag{5.2}$$

$$\mathbf{E}'_I = \sum_{J \neq I} \mathbf{T}'_{IJ}\boldsymbol{\mu}_J^{\text{ind}}, \tag{5.3}$$

where $\mathbf{T}'_{IJ}$ now refers to appropriate powers of $1/r_{IJ}$ according to the dipole induction, whereas the superscript (d) refers to special scaling factors for electrostatic interactions employed in AMOEBA[258]. Since both the l.h.s. and the r.h.s. of (5.1) rely on the induced dipoles, a procedure for guaranteeing self-consistency is required. This is usually

achieved through iterative techniques, such as successive over-relaxation (SOR)[258, 280] or the more recent use of a precondition conjugate gradient self-consistent field (CG-SCF) approach[281]. Once convergence of induced dipoles $\{\boldsymbol{\mu}_I^{\text{ind}}\}$ has been achieved, the polarisation energy is given by

$$U_{\text{ele}}^{\text{ind}} = -\frac{1}{2}\sum_I \boldsymbol{\mu}_I^{\text{ind}} \cdot \mathbf{E}_I, \tag{5.4}$$

where the factor $-1/2$ accounts for the energy cost spent to polarise the dipoles, cf. appendix in Ref. 282.

A detailed discussion of the AMOEBA electrostatics model is beyond the scope of this thesis, even more so given the author is not an expert of the field and comprehensive reviews exist[257, 258, 275]. For a more in-depth discussion, and for a description of bonded and van der Waals interactions used in the AMOEBA model, the Reader is referred to Ref. 282.

5.3 Extended Lagrangian formalism

Extended Lagrangian methods were originally introduced to perform MD simulations in statistical ensembles other than the microcanonical[201, 203, 283]. For example, the effect of a thermostat (barostat) can be described through the interaction of the system with a heat bath (piston), representing the extra variables. By postulating operational expressions for the kinetic and potential energy of the extra dynamical variables one can write down an extended Lagrangian that describes the dynamics of the total system, original plus extended. Similarly, CPMD defines the electronic states as extended classical dynamical variables (classical fields), with a fictitious kinetic energy and a fictitious mass, with the purpose of by-passing the expensive electronic self-consistency procedure altogether. Recently, several authors have proposed schemes based on the CP Lagrangian, using the density matrix (DM) elements as the extra degrees of freedom[284, 285], where the orthonormality constraints are replaced with idempotency constraints of the DM.

Starting from the broken time-reversal symmetry problem in BOMD[270], Niklasson and his collaborators[286] introduced a time-reversible extrapolation scheme for the electronic degrees of freedom. It is now recognised, that the original scheme can be derived from an extended Lagrangian[273, 287], in which an additional set of degrees of freedom is propagated alongside the nuclei with the purpose of generating good quality time-reversal guesses for the SCF loop. Since the extra degrees of freedom are only a computational device to reduce the number of iterations in the SCF step, we will refer to them as *auxiliary* degrees of freedom hereafter. In its most recent refinement it has been

shown it can be formulated to completely avoid the SCF problem[287].

Quite generally, a system of classical interacting nuclei moving in an external potential field U, which contains a SCF-derived component, has the following Lagrangian:

$$\mathcal{L}^{\text{SCF}}(\{\mathbf{R}_I\}, \{\mathbf{V}_I\}) = \frac{1}{2}\sum_I M_I V_I^2 - U(\{\mathbf{R}_I\}, \{\chi_{\text{SCF},\mathbf{s}}\}), \tag{5.5}$$

where $\{\mathbf{R}_I\}$ and $\{\mathbf{V}_I\}$ represent the sets of the nuclear positions and nuclear velocities respectively, M_I is the mass of atom I, and $\{\chi_{\text{SCF},\mathbf{s}}\}$ is the set of converged degrees of freedom that generate the SCF-derived part of the potential energy. The subscript $\mathbf{s}$ represents a generic collection of indices, which can account for atomic-centred quantities, such as atomic dipoles in classical polarisable force field, as well as global (atom-independent) quantities, such as the density matrix elements in DFT. The detailed form of the potential energy U depends on the model employed, but in general can be cast as a sum of an SCF-independent part, such as permanent electrostatics or dispersion interactions, and a potential energy component obtained through an SCF procedure, for example, solution of inducible dipoles in the case of a classical polarisable force fields.

Following Niklasson[273], we can introduce generalised auxiliary degrees of freedom $\{\zeta_\mathbf{s}\}$ into the Lagrangian (5.5), provided we have a definition for their kinetic and potential energies. The goal is to force the $\{\zeta_\mathbf{s}\}$ to closely follow the dynamics of $\{\chi_{\text{SCF},\mathbf{s}}\}$, so that they can serve as initial guesses for the $\{\chi_\mathbf{s}\}$ in the SCF loop. To keep the energy expression simple, a harmonic potential centred around the converged solution $\{\chi_{\text{SCF},\mathbf{s}}\}$ can be employed, with a single parameter $k = m\omega^2$ to control the steepness of the harmonic well, which yields:

$$\mathcal{L}^{\text{ext}} = \mathcal{L}^{\text{SCF}} + \frac{1}{2}m\sum_\mathbf{s}\dot{\zeta}_\mathbf{s}^2 - \sum_\mathbf{s}\frac{k}{2}(\chi_{\text{SCF},\mathbf{s}} - \zeta_\mathbf{s})^2, \tag{5.6}$$

where $\dot{\zeta}_\mathbf{s}$ represent the generalised velocities of the auxiliary degrees of freedom and m represents their mass. The extended Lagrangian (5.6) can now be used to derive a new set of equations of motion (Euler-Lagrange equations):

$$M_I\ddot{\mathbf{R}}_I = -\frac{\partial U}{\partial \mathbf{R}_I} + k(\chi_{\text{SCF},\mathbf{s}} - \zeta_\mathbf{s})\frac{\partial \zeta_\mathbf{s}}{\partial \mathbf{R}_I} \tag{5.7}$$

$$m\ddot{\zeta}_\mathbf{s} = k(\chi_{\text{SCF},\mathbf{s}} - \zeta_\mathbf{s}). \tag{5.8}$$

In the limit $m \to 0$ ($k \to 0, k/m \to \omega^2$) we obtain:

$$M_I \ddot{\mathbf{R}}_I = -\frac{\partial U}{\partial \mathbf{R}_I} \tag{5.9}$$

$$\ddot{\zeta}_{\mathbf{s}} = \omega^2(\chi_{\mathrm{SCF},\mathbf{s}} - \zeta_{\mathbf{s}}). \tag{5.10}$$

It is worth pointing out that (5.9) is exactly the same equation we would have obtained if no auxiliary variables were introduced, i.e. when using (5.5) instead of (5.6). This is a consequence of taking the limit $m \to 0$ only after having derived the Euler-Lagrange equations (5.10). In doing so, we recover the correct potential energy surface, provided the SCF procedure converges exactly. Integrating the (5.10) gives the $\{\zeta_{\mathbf{s}}(t)\}$, which in turn provide the initial guesses for the SCF loop.

5.3.1 Adaptation to classical polarisable force-field methods

In order to extend Niklasson's extended Lagrangian methods to classical polarisation methods, we introduce a set of auxiliary atomic dipoles as extra variables[272, 274]. More specifically, the real self-consistent induced dipoles $\{\boldsymbol{\mu}_{\mathrm{SCF},I}\}$ take the role of $\{\chi_{\mathrm{SCF},\mathbf{s}}\}$, and the auxiliary dipoles $\{\boldsymbol{\mu}_I\}$ replace $\{\zeta_{\mathbf{s}}\}$ in (5.6). The nuclear centres $\mathbf{R}_I$ are propagated in the usual way, i.e. according to (5.11), while the real self-consistent induced dipoles are solved for using an SCF solver initiated by an initial guess that is propagated through the auxiliary dipoles according to (5.12):

$$M_I \ddot{\mathbf{R}}_I = -\left.\frac{\partial U\left(\{\mathbf{R}_I\}, \{\boldsymbol{\mu}_{\mathrm{SCF},I}\}\right)}{\partial \mathbf{R}_I}\right|_{\{\boldsymbol{\mu}_I\}} \tag{5.11}$$

$$\ddot{\boldsymbol{\mu}}_I = \omega^2 \left(\boldsymbol{\mu}_{\mathrm{SCF},I} - \boldsymbol{\mu}_I\right), \tag{5.12}$$

where $U\left(\{\mathbf{R}_I\}, \{\boldsymbol{\mu}_{\mathrm{SCF},I}\}\right)$ is the total potential energy from the AMOEBA force field.

5.3.2 Adaptation to linear-scaling DFT

In the case of linear-scaling DFT the density matrix elements $K^{\alpha\beta}$ would take the role of the real degrees of freedom $\chi_{\mathbf{s}}$ in (5.6). Analogously to the classical case, we would proceed by introducing matrix elements of an auxiliary matrix $X^{\alpha\beta}$ as the auxiliary degrees of freedom $\zeta_{\mathbf{s}}$. However, simply substituting quantities in (5.10) leads to equations that are geometrically inconsistent due to the tensorial nature of $\mathbf{K}$ and $\mathbf{X}$ and the fact that the underlying metric also changes with time. It is worth stressing here that the metric tensor $\mathbf{S}$ is not propagated (as the NGWFs are not treated as dynamical variables), but rather it is generated at every MD step from the current NGWFs. Arita *et al.* have

proposed an alternative scheme[288] based on propagating the matrix elements $(\mathbf{KS})^{\alpha}{}_{\beta}$ as dynamical variables in (5.6), with associated $X^{\alpha}{}_{\beta}$ as auxiliary degrees of freedom. This approach has the advantage of propagating a representation of the density matrix which maintains the correct metric. At a given MD step n, the initial guess $\mathbf{K}^{\text{init}}$ for the SCF procedure is computed from the auxiliary matrix $\mathbf{X}$ as

$$\mathbf{K}^{\text{init}} = \mathbf{X}\mathbf{S}^{-1}, \tag{5.13}$$

where $\mathbf{S}^{-1}$ is the inverse overlap matrix at step n, approximated through an iterative Hotelling algorithm[289] (to maintain a linear scaling behaviour).

The disadvantage of the above approach is that it does not preserve the symmetry of the density kernel matrix, i.e.$\mathbf{K}^{\dagger} \neq \mathbf{K}$, since at a given step $\mathbf{X}$ and $\mathbf{S}^{-1}$ do not commute in general. One possible solution is to instead employ the symmetrised version of (5.13). In our experience this quickly leads to instabilities for larger systems, particularly with a velocity Verlet integrator (to be outlined in Section 5.5).

Here, we propose a different approach, based on a different, orthogonal representation of the density kernel matrix $\mathbf{K}^{\perp} = \mathbf{S}^{\frac{1}{2}}\mathbf{K}\mathbf{S}^{\frac{1}{2}}$, where $\mathbf{S}^{\frac{1}{2}}$ is computed through a modified Newton-Schulz linear-scaling algorithm[290]. This procedure can be performed to a desired level of accuracy, and can be made numerically exact, thus not introducing time-irreversibility, or, strictly speaking, it does not introduce any more time-irreversibility than other operations performed with finite-precision floating-point arithmetic, such as matrix multiplications or inversions. The initial guess for the SCF procedure at a given step n is given by

$$\mathbf{K}^{\text{init}} = \mathbf{S}^{-\frac{1}{2}}\mathbf{X}\mathbf{S}^{-\frac{1}{2}}, \tag{5.14}$$

which ensures $\mathbf{K}$ is symmetric at all times. The Euler-Lagrange equations in our framework read

$$M_I\ddot{\mathbf{R}}_I = -\frac{\partial E[\mathbf{K}_{\text{SCF}}, \{\phi_{\text{SCF}}\}; \{\mathbf{R}_I\}]}{\partial \mathbf{R}_I}\bigg|_{\mathbf{K},\{\phi\}} \tag{5.15}$$

$$\ddot{\mathbf{X}} = \omega^2[\mathbf{K}^{\perp}_{\text{SCF}} - \mathbf{X}], \tag{5.16}$$

where $E[\mathbf{K}_{\text{SCF}}, \{\phi_{\text{SCF}}\}; \{\mathbf{R}_I\}]$ is the potential energy in ONETEP

$$E[\mathbf{K}_{\text{SCF}}, \{\phi_{\text{SCF}}\}; \{\mathbf{R}_I\}] = E_{\text{elec}}[\mathbf{K}_{\text{SCF}}, \{\phi_{\text{SCF}}\}; \{\mathbf{R}_I\}] + E_{\text{Ewald}}(\{\mathbf{R}_I\}) + E_{\text{disp}}(\{\mathbf{R}_I\}) \tag{5.17}$$

given by a sum of three terms: 1) the electronic potential energy E_{elec}; 2) the Ewald Coulombic interaction energy of the atomic cores; 3) an empirical dispersion energy correction for dealing with a well-known deficiency of generalised gradient approximation

(GGA) functionals in describing dispersion interactions[245].

Within KS theory the potential energy E_{elec} can be cast as a functional of the single-particle density matrix, hence the dependence on $\mathbf{K}$ and $\{\phi_\alpha(\mathbf{r})\}$, as

$$E_{\text{elec}}[\mathbf{K}_{\text{SCF}}, \{\phi_{\text{SCF}}\}; \{\mathbf{R}_I\}] = -\frac{1}{2}\int \mathrm{d}\mathbf{r}\left[\nabla^2_{\mathbf{r}'}\rho(\mathbf{r},\mathbf{r}')\right]_{\mathbf{r}'=\mathbf{r}} + \frac{1}{2}\iint \mathrm{d}\mathbf{r}\mathrm{d}\mathbf{r}'\,\frac{n(\mathbf{r})n(\mathbf{r}')}{|\mathbf{r}-\mathbf{r}'|} + \int \mathrm{d}\mathbf{r}\, v_{\text{ext}}(\{\mathbf{R}_I\})n(\mathbf{r}) + E_{\text{XC}}[n(\mathbf{r})] \tag{5.18}$$

where the terms on the RHS represent, respectively, the kinetic energy of the non-interacting KS states, the classical interaction between charged densities, the potential interaction energy of electrons and clamped nuclei, and the exchange-correlation energy. Equations (5.15)-(5.16) are the AIMD counterparts to the classical equations (5.11)-(5.12).

5.4 Extended Lagrangian with dissipative Verlet integrator (dXL)

It is now recognised[272–274] that the above simple formulation suffers from numerical instabilities in the evolution of the auxiliary degrees of freedom. In fact, the velocities of the auxiliary degrees of freedom increase in an unbounded fashion, ultimately resulting in initial guesses that are unacceptably far from the converged values, negating the efficiency gains of the scheme[274]. The origin of this phenomenon lies in the fact that exact convergence is never achieved in practical calculations, which couples (5.9) and (5.10) through a "memory effect"[42] or kinetic resonances[272]. Energy can therefore flow from the real degrees of freedom to the (massless) auxiliary ones, producing a runaway increase in the velocities of the latter. This is demonstrated in Fig. 5.1, which displays the runaway in the velocities for a 64 H_2O-molecule AIMD simulation, with an LNV convergence threshold of 10^{-5} Ha $a_0^{-3/2}$. The temperature of the auxiliary degrees of freedom was computed as $\text{Tr}[\dot{\mathbf{X}}^2]/N$ and the temperature associated with the real degrees of freedom was calculated as $\text{Tr}[\dot{\mathbf{K}}^2]/N$ (cf. comment following (5.26)). The arrow at 0.27 ps indicates the point where the initial guesses obtained from propagation become worse than the default initialisation, negating the efficiency gains of the scheme. The arrow at 0.53 ps indicates the point where the guesses become so far from the converged values as to make the QM calculation unstable.

Recognising this issue, Niklasson *et al.* proposed a modified Verlet integrator[42], which breaks the time-reversal symmetry of the equations of motion of the auxiliary variables to a small degree through the addition of a dissipative-like term in the integration. Since this effect is introduced through the integration, rather than a physical term in

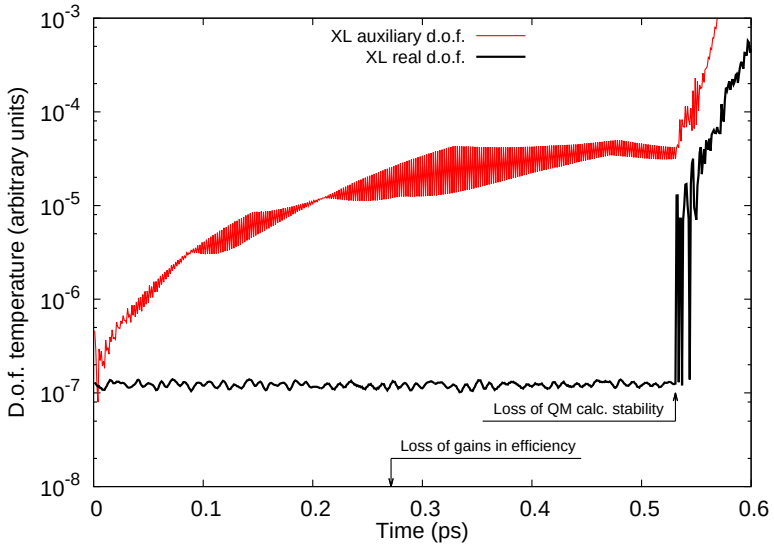

Figure 5.1: Illustration of the runaway accumulation of kinetic energy in the auxiliary degrees of freedom in the original XL scheme. See text in Sec. (5.4).

the Lagrangian, it does not yield new equations of motion for the auxiliary degrees of freedom. Instead, the approach can be thought as being similar to Langevin-like dynamics for the degrees of freedom $\{\chi_s\}$ with internal numerical error fluctuations and external, approximately energy conserving, dissipative forces f^{diss}.

In order to minimise the breaking of time-reversal symmetry, dissipative forces proportional to $\dot{\zeta}^{\text{diss}}$ are avoided so that the time-reversal symmetry can be maintained to a chosen higher order. Hence, the modified Verlet algorithm to integrate (5.10) for the dXL scheme is given by

$$\zeta_{\mathbf{s}}^{n+1} = 2\zeta_{\mathbf{s}}^{n} - \zeta_{\mathbf{s}}^{n-1} + \kappa(\chi_{\text{SCF},\mathbf{s}} - \zeta_{\mathbf{s}})^{n} + \gamma \sum_{l=0}^{L} c_l \zeta_{\mathbf{s}}^{n-l}, \tag{5.19}$$

where we δt is the time-step chosen to integrate the equations of motion and $\kappa = \delta t^2 \omega^2$. The coefficients γ and c_l are obtained in such a way that for a given L all the odd-order terms in δt cancel out[42] up to order δt^{2L-3}. Fig. 5.2 illustrates the behaviour of the dXL scheme, for a 64 H_2O-molecule AIMD simulation, with the same approach for the calculation of temperatures as explained above for Fig. 5.1. The auxiliary degrees of freedom closely follow their real counterparts and the instability is removed.

Equation (5.19) is readily adapted to the classical framework with the usual substitution

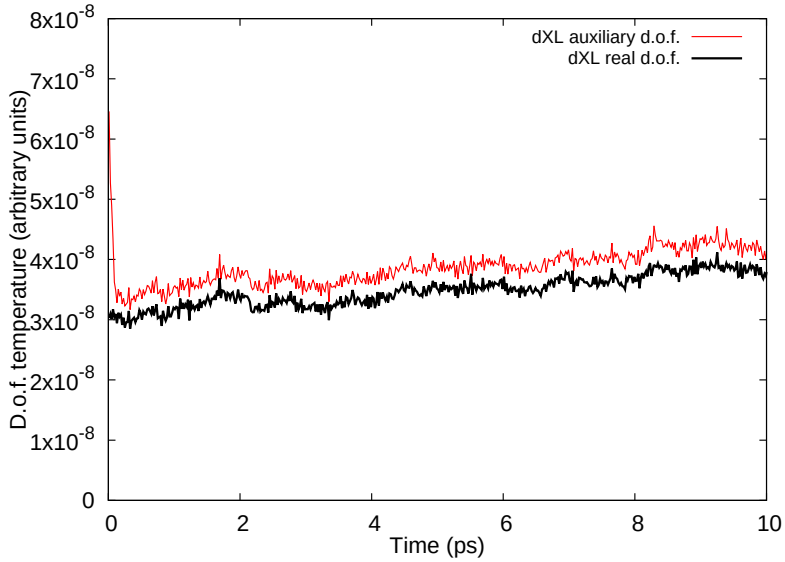

Figure 5.2: Illustration of the stability of the dXL ($L = 7$) scheme. In the interest of clarity, averages over 10 fs are shown.

$\zeta_s \rightarrow \boldsymbol{\mu}_I$:

$$\boldsymbol{\mu}_I^{n+1} = 2\boldsymbol{\mu}_I^n - \boldsymbol{\mu}_I^{n-1} + \kappa(\boldsymbol{\mu}_{\mathrm{SCF},I} - \boldsymbol{\mu}_I)^n + \gamma \sum_{l=0}^{L} c_l \boldsymbol{\mu}_I^{n-l}. \tag{5.20}$$

Here the dissipative force is given as a linear combination of previous values of the auxiliary dipoles up to some order L, with the optimal expansion coefficients c_l, and overall scaling parameter γ given in Ref. 42.

The dXL can be analogously introduced for the linear-scaling DFT framework through a linear combination of previous auxiliary degrees of freedom:

$$\mathbf{X}^{n+1} = 2\mathbf{X}^n - \mathbf{X}^{n-1} + \kappa(\mathbf{K}_{\mathrm{SCF}}^{\perp} - \mathbf{X})^n + \gamma \sum_{l=0}^{L} c_l \mathbf{X}^{n-l}, \tag{5.21}$$

where the coefficients γ and c_l are the same as the ones used for the classical approach [42].

5.5 Extended Lagrangian with thermostat-control (iXL)

The success of the dissipative scheme for a number of QM models has been reported in the literature[42, 273]. Since the role of the dissipation is to counteract the numeri-

cal instabilities generated by the propagation scheme, for short timescales a *bona fide* microcanonical dynamics can be generated. On the other hand, the main drawback of the scheme lies in the fact that it breaks time-reversibility (though to a high order), and therefore introduces a small, but measurable drift in the total energy. This can be ameliorated by carefully optimising the coefficients of the expansion, but it cannot be removed completely. For long time scales, the steady drift of total energy is unavoidable, as first demonstrated in Ref. 272, which is consistent with our results obtained with classical polarisable force-field MD (Section 5.6.2).

An alternative approach for overcoming the problem of breaking time-reversal symmetry has been proposed by Albaugh *et al.* [272] The main idea is to apply a simple thermostat to the velocities of the auxiliary variables, resulting in an *inertial* extended Lagrangian SCF formulation (iXL) *in lieu* of dissipation. Here the scheme will be illustrated using a general thermostat, γ, applied to the time-reversible velocity Verlet integrator (5.10):

$$\dot{\zeta}_{\mathbf{s}}^{n+\frac{1}{2}} = \dot{\zeta}_{\mathbf{s}}^{n} + \frac{1}{2}\delta t\omega^2\ddot{\zeta}_{\mathbf{s}}^{n} \tag{5.22}$$

$$\zeta_{\mathbf{s}}^{n+1} = \zeta_{\mathbf{s}}^{n} + \delta t\dot{\zeta}_{\mathbf{s}}^{n+\frac{1}{2}} \tag{5.23}$$

$$\{\zeta_{\mathbf{s}}\}^{n+1} \rightarrow \text{SCF} \rightarrow \{\chi_{\text{SCF},\mathbf{s}}\}^{n+1} \rightarrow \text{ENERGY AND FORCES}$$

$$\dot{\tilde{\zeta}}_{\mathbf{s}}^{n+1} = \dot{\zeta}_{\mathbf{s}}^{n+\frac{1}{2}} + \frac{1}{2}\delta t\omega^2\ddot{\zeta}_{\mathbf{s}}^{n+1} \tag{5.24}$$

$$\dot{\zeta}_{\mathbf{s}}^{n+1} = \gamma^{n+1}\dot{\tilde{\zeta}}_{\mathbf{s}}^{n+1}, \tag{5.25}$$

where γ^{n+1} is the velocity scaling factor generated by a general thermostatting procedure at full time-step update. For example, in the case of Berendsen velocity rescaling, γ^{n+1} is given by

$$\gamma^{n+1} = \sqrt{1 + \frac{\delta t}{\tau}\left(\frac{T^*}{T^{n+1}} - 1\right)}, \tag{5.26}$$

where T^{n+1} is the temperature of the auxiliary degrees of freedom at MD step $n+1$, T^* is the target (desired) value of this temperature, and τ is the characteristic time of the thermostat. T^* and τ are parameters of the scheme.

Although strictly speaking in the limit $m \rightarrow 0$ one can no longer define a kinetic energy, and therefore a temperature, for the auxiliary degrees of freedom $\zeta_{\mathbf{s}}$, Albaugh *et al.*[272] have suggested the ensemble average of the squared auxiliary velocities, i.e. $T = \langle\dot{\zeta}_{\mathbf{s}}^2\rangle$ as an operational definition for the pseudo-temperature T. In this paper we follow this convention, referring to the quantity in question simply as "temperature". The characteristic time τ is chosen similarly as in typical applications of thermostats – on the one hand we want the decay rate of the temperature towards T^* to be much shorter than

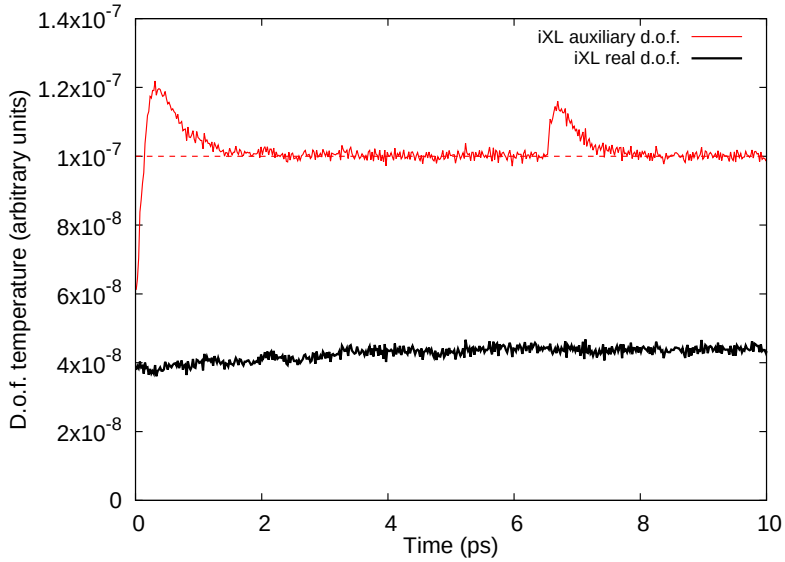

Figure 5.3: Illustration of the behaviour of the iXL scheme – the temperature of the auxiliary degrees of freedom quickly decays to the pre-set desired temperature T^* (shown as a dashed line). The two peaks correspond to instants where the number of SCF steps briefly flipped from 7 to 6, causing a temporary increase in the auxiliary temperature. Here $T^* = 10^{-7}$ and $\tau = 30$ fs. Testcase and the approach to calculation of temperatures: as in Fig. 5.1. In the interest of clarity, averages over 10 fs are shown.

the length of the simulation t_{sim}: $\tau \ll t_{\text{sim}}$; on the other hand we want to avoid a strong damping of instantaneous jumps in the temperature, and so $\tau \gg \delta t$. Provided τ satisfies the above constraints, the exact choice is expected to be inconsequential to the dynamics.

The desired auxiliary temperature T^* is chosen to approximately conform to the equipartition of energy consistent with a classical harmonic oscillator[272]. One possible way of obtaining T^* is by approximating the auxiliary velocity with the maximum displacement of the distribution of the real degrees of freedom[272]. One can also run a brief dXL calculation beforehand, and subsequently set T^* to the time average of T^n obtained from that run. Another option is to simply compute the temperature of the real degrees of freedom, i.e. $\langle \dot{\chi}_{\text{SCF},\mathbf{s}} \rangle$ over a brief initialisation period, and use a value slightly larger than that (since the real degrees of freedom are the minimum around which auxiliary degrees of freedom are meant to harmonically oscillate). A typical behaviour of the iXL scheme is illustrated in Fig. 5.3.

The equations for the iXL approach for a polarisable force field are obtained from (5.22)-(5.25), with the substitutions $\boldsymbol{\mu} \to \zeta$ and $\dot{\boldsymbol{\mu}} \to \dot{\zeta}$. The coupling constant γ^n is given by

$$\gamma^n = \sqrt{1 + \frac{\delta t}{\tau}\left(\frac{T^*}{\langle \dot{\boldsymbol{\mu}}_I^2 \rangle^n} - 1\right)}. \tag{5.27}$$

For the sake of clarity, a simple Berendsen thermostat has been used to illustrate the iXL approach. However, any other (more efficient) thermostat can be used in principle, since the scope of a thermostat in this scheme, is only to remove heat (numerical noise) from the auxiliary degrees of freedom. In fact, in all results reported later we use 4th order Nosé-Hoover chains for thermostatting the auxiliary velocities, which we found to be marginally better than the Berendsen thermostat.

Analogously, for a linear-scaling DFT approach, we apply the following substitutions in (5.22)-(5.25): $K^{\perp\alpha\beta} \rightarrow \zeta$ and $\dot{K}^{\perp\alpha\beta} \rightarrow \dot{\zeta}$. The coupling constant is given by

$$\gamma^n = \sqrt{1 + \frac{\delta t}{\tau}\left(\frac{T^*}{\mathrm{Tr}[\dot{\mathbf{X}}^2]^n} - 1\right)}. \tag{5.28}$$

5.6 Validation tests on water boxes

5.6.1 Computational set-up

We studied the three extended Lagrangian schemes described in Secs. 5.3-5.5 – the original extended Lagrangian scheme (extended Lagrangian), and its dissipative (dXL) and inertial (iXL) variants. Calculations not employing any propagation (starting the SCF procedure from scratch at every MD iteration) were used as baseline comparisons. We tested the extended Lagrangian schemes in two regimes – in classical MD calculations with the AMOEBA polarisable force field, and in AIMD calculations with linear-scaling DFT. The former calculations were carried out using the TINKER[258] program, and the latter – using ONETEP[18, 291].

As test systems we chose pure water-box systems with increasing numbers of water molecules: 16, 32, 64, 128 (and 512 with classical calculations), although all methods described should be generalisable to any molecular system. Liquid water is ubiquitous in biological systems and, as it is well-known, is a prototypical system for hydrogen bonding that influences its anomalous behaviour throughout its phase diagram. Standard DFT GGA models struggle to correctly describe the structure and dynamics of water, with the non-locality of dispersion interactions, deficiencies of local and semi-local exchange, presence of self-interaction error, and the neglect of quantum nuclear effects often cited as culprits[292–294]. At the same time, many successes and failures of both classical and quantum approaches for bulk water systems have been reported[258, 264, 292–297]. Consequently, bulk water systems provide an appropriate and stringent test for the extended Lagrangian methods where many-body effects are paramount.

For all classical polarisable force-field simulations we used the water parameters of

the AMOEBA14 water model[297]. The equations of motion for the nuclear degrees of freedom were integrated using the velocity Verlet integrator[298] with a time step of $\delta t = 1.0$ fs. Each system started with the water molecules arranged on a lattice in an equilibrium geometry with a cubic cell, whose volume corresponded to the reported density for the force field $\rho = 1.0003$ g cm^{-3}. The Particle-mesh Ewald method[299, 300] with a 9 Å real-space cutoff for long-range electrostatics was employed. Equilibration simulations were carried out in the NVT ensemble at 298 K for 0.5 ns, with temperature controlled using a Nosé-Hoover thermostat[204] with a fourth-order chain and a characteristic time of $\tau = 0.1$ ps.

Following equilibration, we ran NVE production calculations for 1 ns with each of the above extended Lagrangian schemes, along with a baseline calculation where initial guesses were not propagated using the default conjugate gradient (CG) SCF method in TINKER, with a threshold of 10^{-6}D . For production calculations, we integrated the equation of motion (5.12) using the time-reversible velocity Verlet integration for the original extended Lagrangian scheme and iXL, whereas a modified Verlet scheme was used for dXL, as described in section (5.4). For the original extended Lagrangian scheme and for the iXL scheme we set $\omega = \sqrt{2}/\delta t$ according to the criterion in Ref. 273. The target temperature T^* for the auxiliary degrees of freedom in the iXL scheme was estimated by approximating the square of the auxiliary dipole velocity $\langle \dot{\boldsymbol{\mu}}_I^2 \rangle$ with the maximum displacement of the distribution of the real dipoles[272]. For these systems this gave a value of $T^* \approx 10^5\ e^2\text{Å}^2/\text{ps}^2$, which is the value used in this work. The Nosé-Hoover thermostat[204] with a fourth-order chain and a characteristic time of $\tau = 0.1$ ps was used for the auxiliary degrees of freedom. For all the extended Lagrangian schemes and for all the system sizes N, we ran our simulations with three different thresholds for the SCF optimisation: 10^{-1} D (loose), 10^{-4} D (moderate) and 10^{-6} D (tight).

For linear-scaling DFT calculations we used the pre-equilibrated systems obtained from the classical calculation to avoid lengthy equilibration in AIMD. These were subsequently further equilibrated with ONETEP for 1 ps with conventional BOMD (i.e. in the absence of a propagation scheme) in order for the systems to adjust to the switch from a classical to an *ab initio* Hamiltonian. The NVT ensemble was used, with temperature controlled via a Nosé-Hoover chain thermostat. No adjustments were made to the densities of the systems. The LNV convergence threshold was set to an RMS gradient of 10^{-6} Ha $a_0^{-3/2}$, which generally required 19-20 SCF steps to converge.

For both equilibration and production calculations, we used the BLYP exchange-correlation functional[301, 302] with Grimme D2 dispersion correction[244] in order to improve the DFT description of water[293]. The kinetic energy cutoff was set to 900 eV, and norm-conserving pseudopotentials were employed. We used 8 a_0 as the

localisation radii of the NGWFs throughout, except for the 16 H_2O system, where the small size of the periodic box (14.78 a_0) forced us to use a slightly smaller localisation radius of 7.35 a_0. Since we used fixed (non-*in situ*-optimised) localised orbitals, we chose a non-minimal double-zeta with polarisation (DZ+P) basis set to improve the description. No density kernel truncation was applied, due to the systems' sizes being too small for the truncation to show any benefit. A velocity Verlet scheme was employed, with a timestep of $\delta t = 0.5$ fs to integrate the nuclear degrees of freedom.

Production calculations were carried out with all of the extended Lagrangian schemes, and calculations with no propagation as baseline, using a selection of LNV convergence thresholds: 10^{-4} Ha $a_0^{-3/2}$ (loose), 10^{-5} Ha $a_0^{-3/2}$ (moderate) and 10^{-6} Ha $a_0^{-3/2}$ (tight). These sampled the NVE ensemble and were carried out for 10 ps. While a longer sampling would certainly be desired, the large computational cost of AIMD simulations precluded that. Analogously to the classical calculations, we employed a velocity Verlet scheme for the auxiliary degrees of freedom both for the original extended Lagrangian scheme and the iXL scheme, with a timestep of 0.5 fs. For the dissipative dXL scheme we used a modified Verlet scheme as explained in Sec. (5.4). The target temperature T^* for the iXL was set by running a brief dXL calculation, taking the time average of the auxiliary temperature, and using a slightly larger (more conservative) value for iXL, as otherwise the scheme's thermostat struggled to keep the desired temperature, leading to excessive drift. This more heuristic approach has the advantage of avoiding a long simulation to compute the distribution of the displacements of real electronic degrees of freedom, which can be quite computationally demanding for AIMD. The value we settled for was $T^* = 10^{-7}\ e^2/\text{fs}^2$ for all thresholds, except for the 128 H_2O system at the loose threshold, where a larger value of $T^* = 10^{-6}\ e^2/\text{fs}^2$ was necessary to maintain stability. Due to the short time scale of our AIMD simulations, we set $\tau = 0.03$ ps for the thermostat characteristic time, forcing the thermostat to work six times faster than its classical counterpart.

5.6.2 Results for polarisable force fields

We will use the largest (512 H_2O) system as the main testcase for classical calculations, and all results will refer to this system, unless indicated otherwise. We begin by confirming the problems of the original extended Lagrangian scheme due to its quickly deteriorating quality of the propagated guesses. We laid out the origin of this undesired behaviour in Sec. 5.3. Fig. 5.4 shows how the number of SCF iterations increases over time, regardless of the assumed convergence threshold. Given sufficient time, the quality of the propagated guesses becomes worse than in the absence of propagation, negating the efficiency gains of the scheme, even if, in principle, this formulation is expected not to introduce a drift

Table 5.1: Comparison of the energy drift (K/ps) between calculations with no propagation, and calculations using the dXL ($L = 6$) and iXL schemes – for four different system sizes (16, 32, 64 and 128 H_2O molecules) and three different CG-SCF convergence thresholds. $\overline{N}_{\text{SCF}}$ is the average number of SCF steps for a combination of method and threshold (detailed breakdown in Tab. 5.2).

CG-SCF threshold [D]	Propagation scheme	System size: 16 H_2O drift [K/ps ($\times 10^{-4}$)]			32 H_2O drift [K/ps ($\times 10^{-4}$)]			64 H_2O drift [K/ps ($\times 10^{-4}$)]			128 H_2O drift [K/ps ($\times 10^{-4}$)]			$\overline{N}_{\text{SCF}}$
10^{-1}	no prop.	48752.2	±	5969.3	49642.4	±	8490.7	40048.8	±	5110.5	38739.4	±	3827.8	1.0
	dXL	2395.9	±	685.2	−3371.2	±	663.7	−6003.1	±	3986.1	−5613.2	±	4632.9	1.0
(loose)	iXL	−7.9	±	154.9	158.4	±	104.7	84.8	±	93.8	74.9	±	18.7	3.0
10^{-4}	no prop.	5.0	±	7.4	−6.7	±	9.4	−3.7	±	1.7	1.6	±	2.1	5.6
	dXL	−20.8	±	9.2	−23.4	±	4.6	−20.0	±	1.7	−22.9	±	3.2	3.7
(moderate)	iXL	−0.9	±	8.0	0.4	±	2.6	−0.8	±	1.0	−0.5	±	29.6	6.9
10^{-6}	no prop.	5.9	±	7.9	−0.8	±	2.7	−0.4	±	1.5	−0.6	±	1.7	8.7
	dXL	1.4	±	5.3	0.3	±	4.0	0.0	±	1.8	−0.6	±	1.4	6.9
(tight)	iXL	3.5	±	6.8	2.3	±	2.1	0.8	±	5.0	−0.7	±	1.5	9.1

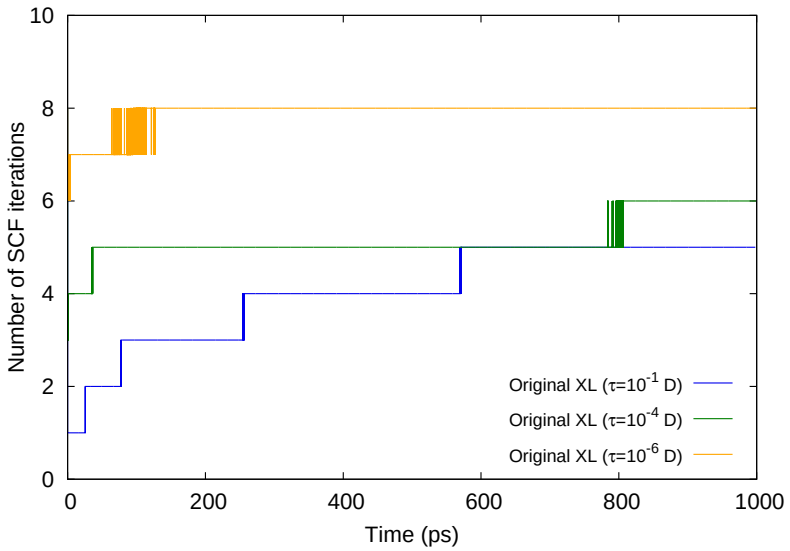

Figure 5.4: Decaying quality of the initial guesses propagated through the original extended Lagrangian scheme, evidenced by the number of SCF steps needed to converge the induced dipoles (solid lines).

in the energy.

The dissipative scheme addresses the deficiency of the original formulation, at the price of weaker (finite-order) time-reversibility as outlined in Sec. 5.4. We will now estimate the typical energy drift that manifests as a consequence. Fig. 5.5 shows the change in energy per atom in an *NVE* simulation with the dXL scheme, for several

Table 5.2: A comparison of the number of CG-SCF iterations between calculations with no propagation, and calculations using the dXL and iXL schemes – for four different system sizes (16, 32, 64 and 128 H_2O molecules) and three different CG-SCF thresholds.

CG-SCF threshold [D]	Propagation scheme	System size			
		16	32	64	128
10^{-1}	no prop.	1.00	1.00	1.00	1.00
	dXL	1.00	1.00	1.00	1.00
(loose)	iXL	3.00	3.00	3.00	3.00
10^{-4}	no prop.	5.42	5.51	5.65	5.77
	dXL	3.62	3.65	3.83	3.79
(moderate)	iXL	6.89	6.72	6.84	6.99
10^{-6}	no prop.	8.38	8.70	8.92	8.99
	dXL	6.68	6.85	6.96	6.99
(tight)	iXL	9.02	9.07	9.17	9.16

selected values of the order parameter L (cf. (5.19)) and for calculations with a loose, moderate and tight SCF threshold. For all three SCF convergence thresholds the drift is substantial, with the loose threshold being the most severe case, corresponding to a drift rate of $\sim 2 \times 10^{-1}$ K/ps. While the energy drift rate gets smaller as the SCF tolerance increases, the drift is systematic and will become non-negligible in calculations spanning hundreds of nanoseconds.

The iXL scheme adopts yet another approach to overcome the issues of the original extended Lagrangian scheme. A thermostat is introduced to control the temperature of the auxiliary dipoles in order to avoid the accumulation of noise in the propagation, as described in Sec. 5.5. Fig. 5.6 shows the change in energy per atom in a NVE simulation for this case. Energy conservation is maintained even at loose thresholds, with a drift rate of $\sim 3 \times 10^{-3}$ K/ps and requiring only three SCF iterations at the 10^{-1} D threshold (see inset in Fig. 5.6), making this scheme very competitive and suitable for performing long (μs-scale) NVE simulations. A modest price to pay for the iXL method, apart from the need to choose suitable parameters T^* and τ (cf. Sec. 5.5), is its dependence on a definition of "pseudo-temperature" through the kinetic energy of the system, which may become less valid as the number of degrees of freedom in the system decreases. It is thus prudent to examine the behaviour of the method for smaller systems to assess its transferability to other systems.

Table 5.1 and Table 5.2 summarise our findings for the smaller systems. In particular, in Tab. 5.1 we compare the drift in the total energy for the unpropagated (conventional SCF-MD) scheme, which serves as reference, the dXL scheme and the iXL scheme for four system sizes each with three SCF-CG thresholds.

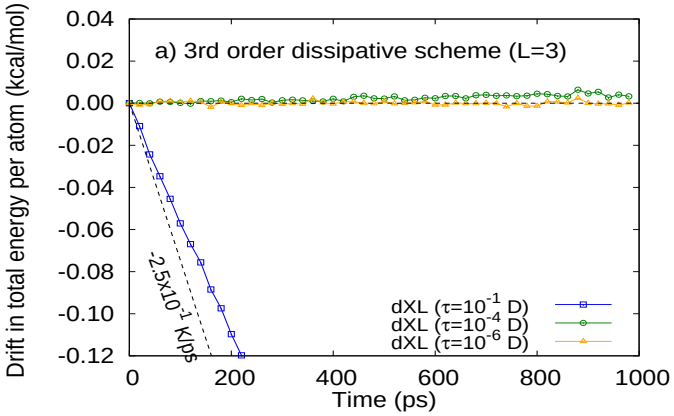

(a) L=3

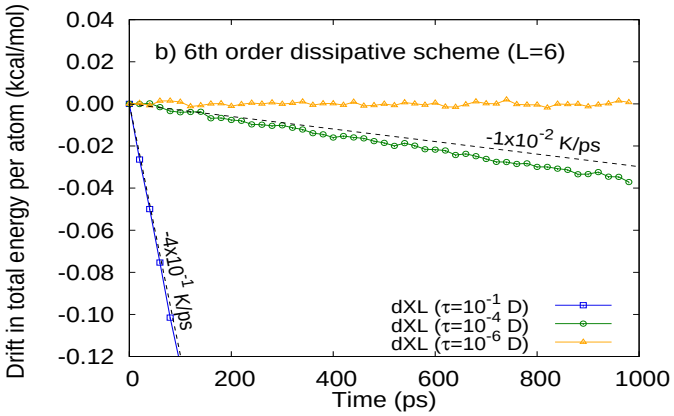

(b) L=6

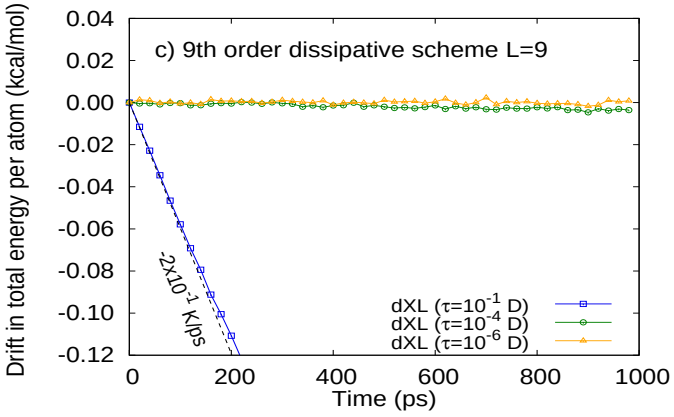

(c) L=9

Figure 5.5: Total energy conservation of dXL for different dissipation orders: L=3 (panel a), L=6 (panel b), and L=9 (panel c). Different curves within each panel correspond to different SCF thresholds: loose ($\tau = 10^{-1}$D), moderate ($\tau = 10^{-4}$D) and tight ($\tau = 10^{-6}$D). The dashed lines are meant as a guide to the eye and correspond to energy drifts expressed as system cooling/heating rates in K/ps. In the interest of clarity, only points 20 ps apart are shown.

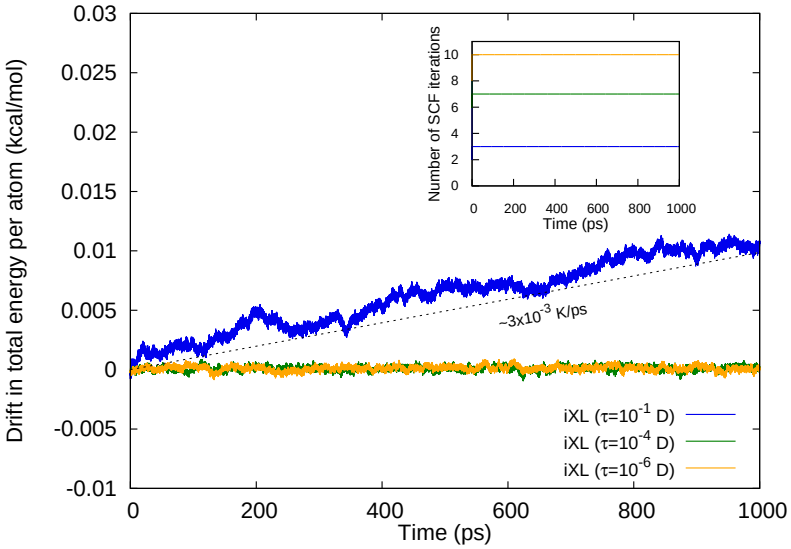

Figure 5.6: Total energy conservation of iXL for different convergence thresholds (solid lines): loose ($\tau = 10^{-1}$D), moderate ($\tau = 10^{-4}$D), and tight ($\tau = 10^{-6}$D). The dashed line is meant as a guide to the eye and corresponds to energy drift expressed as system heating rates in K/ps. In the interest of clarity, averages over 10 fs are shown.

The reasons for large uncertainties in the drifts, even given a long simulation time, are as follows: for the loose threshold, the drift is so severe that over 1000 ps the system heats up (cools down) so much that the drift is no longer linear due to the massive increase (decrease) in kinetic energy. For the moderate and tight thresholds, the large uncertainty reflects the difficulty of accurately estimating extremely small (sub-mK/ps) drifts. The drifts and their uncertainties were calculated by assuming the drifts to be approximately linear. In a simulation with a length of t ($t = 1000$ ps), we can use a subset of data, viz. the interval $[0, t_0]$ to evaluate the linear coefficient in the drift, $a(t_0)$, over this interval. The final drift estimate is $a(t)$. The uncertainty is taken as the largest difference between $a(t_0)$ and $a(t)$ calculated over $t_0 \geq t/2$.

Tab. 5.2 presents an analogous analysis to Tab. 5.1, with the number of CG-SCF iterations replacing the energy drift. Tab. 5.1 and Fig. 5.7 demonstrate that for loose and moderate CG-SCF thresholds the iXL scheme outperforms all orders of the dXL scheme in terms of energy conservation, even for very small system sizes. In the tight threshold regime the two schemes are equivalent. However, as shown in Tab. 5.2, the trend is inverted when considering the average number of CG-SCF iterations. In fact, $\overline{N}_{\text{SCF}}$ for iXL is always larger than the corresponding $\overline{N}_{\text{SCF}}$ for dXL, regardless of the CG-SCF threshold. Notably, at moderate convergence thresholds the dXL scheme shows energy drifts of the same order of magnitude (10^{-3} K/ps) as iXL with a loose threshold, and also a comparable average number of CG-SCF iterations ($\overline{N}_{\text{SCF}} = 3.7$). Therefore, dXL and

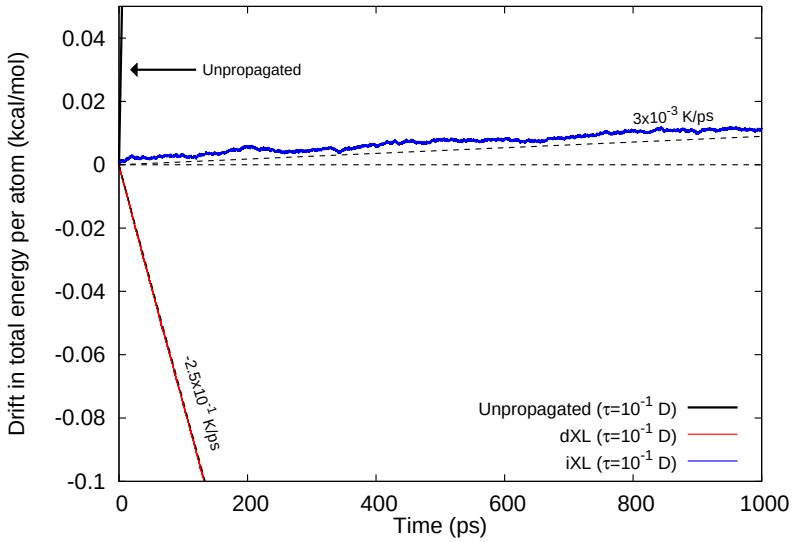

Figure 5.7: Comparison of drifts in total energy between calculations with no propagation, dXL and iXL. SCF convergence was set to 10^{-1} D (loose) for all integration schemes. In the interest of clarity, averages over 10 fs are shown.

iXL display similar performance but in different SCF threshold windows: moderate for dXL and loose for iXL.

To assess how these integration schemes affect the actual dynamics, the oxygen-oxygen pair correlation function $g_{OO}(r)$ has been computed, see Fig. 5.8. Clearly, the blue curve and red curve in Fig. 5.8, corresponding to dXL with a moderate threshold and iXL with a loose threshold respectively, lie on top of each other and they are indistinguishable from the reference curve (solid black). The latter has been obtained with the conventional (unpropagated) scheme and a tight threshold to provide a robust baseline. No artefacts are hence introduced in the dynamics by these two integration schemes, and they essentially provide the "correct" result as obtained from the reference calculation.

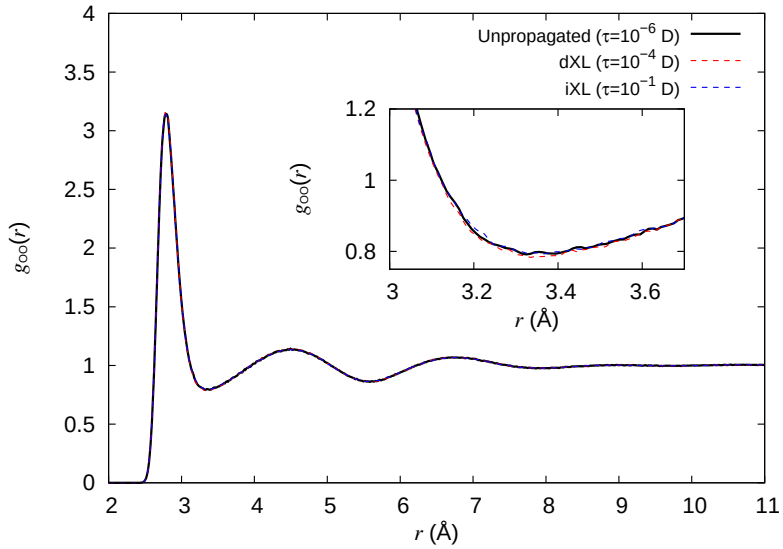

Figure 5.8: Oxygen-oxygen pair correlation function $g_{OO}(r)$ obtained in the absence of a propagation scheme, and with the dXL and iXL schemes with different thresholds. Test-case: 512 H_2O molecule system. The reference unpropagated calculation uses a tight RMS threshold of 10^{-6} D. The SCF convergence threshold was set to RMS 10^{-1} D (loose) for the iXL scheme (solid red). The SCF convergence threshold was set to RMS 10^{-4} D (moderate) for the dXL scheme (solid blue). The differences between the predictions obtained with dXL and iXL and in the absence of propagation are seen to be minor, as also highlighted in the inset.

5.6.3 Results for LS-DFT

As the main testcase for linear-scaling DFT calculations we will use the 64 H_2O system, unless indicated otherwise. As we have done for the classical calculations, we begin by confirming the impracticality of the original extended Lagrangian scheme. Fig. 5.9 shows that for linear-scaling DFT calculations the quality of the propagated guesses decays even more rapidly than for the classical calculations. Indeed, for the loose SCF convergence threshold the original extended Lagrangian scheme becomes less efficient than the unpropagated scheme as early as after 0.04 ps (80 MD steps), probably reflecting the good quality of Onetep's (unpropagated) initial guesses for the simpler scenario of fixed NGWFs.

A significant difference between classical polarisable force field MD calculations and their linear-scaling DFT counterparts is the much higher "noise floor" of *ab initio*-derived forces. This is a consequence of more intricate numerical machinery involved in DFT calculations (commonplace use of grid-based operations, such as Fast Fourier Transforms (FFTs), numerical integration of quantities on a variety of grids with up- and downsampling between grids, inexact translational and rotational invariance ("egg-box effect"),

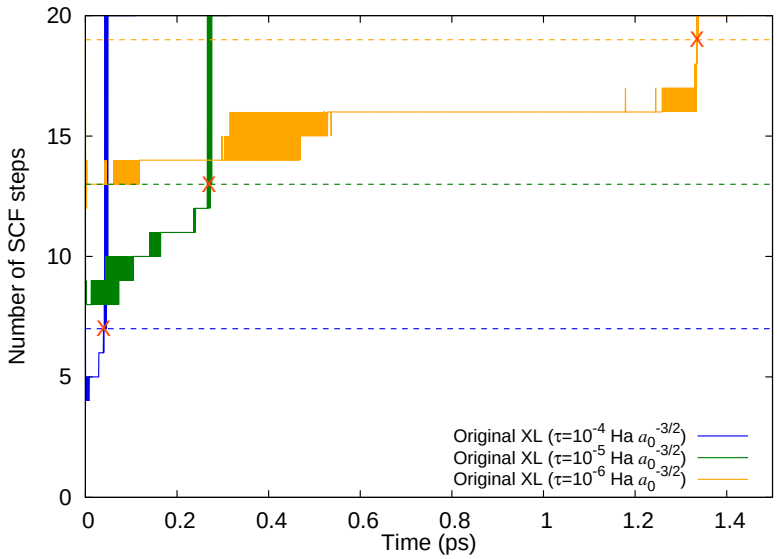

Figure 5.9: Decaying quality of the initial guesses propagated through the original extended Lagrangian scheme, evidenced by the number of SCF steps needed to converge the induced dipoles (solid lines). Dashed lines denote corresponding number of SCF steps in the absence of propagation. Crosses at 0.04 ps, 0.27 ps and 1.33 ps denote points where the efficiency gain of extended Lagrangian over the unpropagated scheme is lost.

use of polynomial interpolations in the handling of pseudopotentials, etc.), and the fact that the error in Kohn-Sham DFT forces is first order with respect to the error in the incompletely converged wave-function, even though the error in the energy is second order[14]. While tighter SCF convergence can be imposed for dynamical calculations, this can quickly become impractical, as to reach those stricter convergence thresholds grids must be made finer, and other approximations need to be well-controlled. In practice, the resultant noise in DFT forces, even though perfectly acceptable e.g. for geometry optimisation, leads to energy drifts in the order of 10^{-1} K/ps, while in classical MD, even when iterative schemes are involved, drifts are not expected to exceed 10^{-3} K/ps (cf. Tab. 5.1).

Linear-scaling formulations of DFT necessarily add further approximations to conventional DFT, even if in robust approaches these approximations are controllable. For example, the use of finite-box FFTs leads to a slight delocalisation of gradients beyond the localisation regions of local orbitals, exchange-correlation energy is typically evaluated on a finite Cartesian grid, and Pulay-like corrections to forces are often not numerically exact for reasons of efficiency. Some of these approximations are common to all LS-DFT formulations, whereas others are specific to the different implementations. A consequence of these approximations is a further increase in the inaccuracy of forces, with residual errors in ONETEP typically in the order of 0.1% – this can be estimated from the

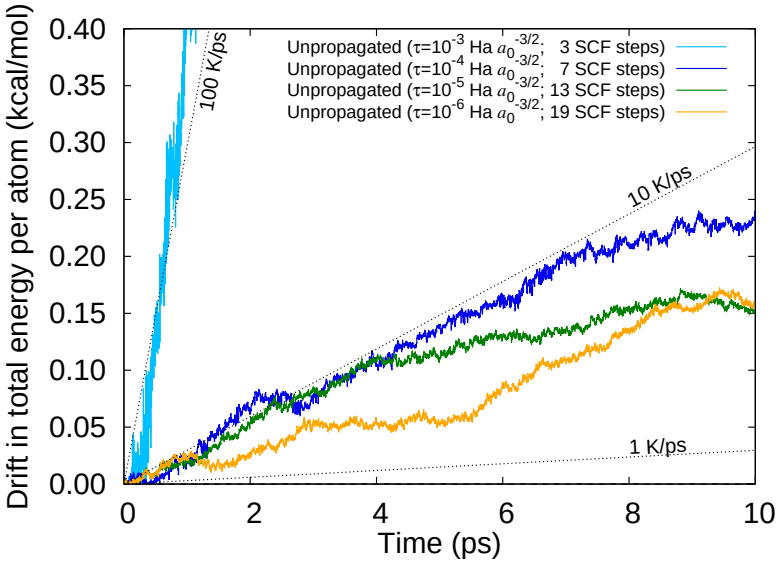

Figure 5.10: Drift in the total energy for linear-scaling DFT for unpropagated BOMD (testcase: 64 H_2O molecules), for a selection of SCF convergence thresholds. Excessively loose thresholds ($\tau = 10^{-3}$ Ha $a_0^{-3/2}$) lead to extreme drift, but inherent drift at $\sim$ 5 K/ps is apparent regardless of how tight SCF convergence is. The dashed lines are meant as a guide to the eye and correspond to energy drifts expressed as system cooling/heating rates in K/ps.

magnitude of the net force, which, in the absence of noise, should be zero by Newton's 3rd law of motion. While approaches for correcting some of these approximations have recently been proposed[172, 211], the current state of the art necessitates using mild thermostatting to control for energy drifts in LS-DFT, as these typically result in temperature increase/decrease rates of several K/ps.

To wit, in Fig. 5.10 we show drifts obtained for the 64 H_2O system in the absence of any propagation scheme. For consistency, we adopt the same criterion to initialise the NGWFs as outlined in Sec. 5.6.1. While the drift in excess of 100 K/ps obtained for the LNV convergence threshold of 10^{-3} Ha $a_0^{-3/2}$ is clearly due to an excessively loose threshold, there is little improvement when the threshold is tightened from 10^{-4} Ha $a_0^{-3/2}$ to 10^{-5} Ha $a_0^{-3/2}$, and no further gain whatsoever with 10^{-6} Ha $a_0^{-3/2}$, which indicates the presence of an inherent drift that cannot be mitigated by improving the degree of SCF convergence. The magnitude of this drift is in the order of 5 K/ps, which leads us to expect that the drift due to time-reversal symmetry breaking in dXL (estimated between 10^{-3} and 10^{-4} K/ps in the classical case, cf. Tab. 5.1, for moderate and tight thresholds) will be entirely obscured by the intrinsic drift due to forces.

Fig. 5.11 compares the energy drift of the unpropagated calculation, and the two extended Lagrangian approaches for a loose SCF threshold (10^{-4} Ha $a_0^{-3/2}$). The drift in

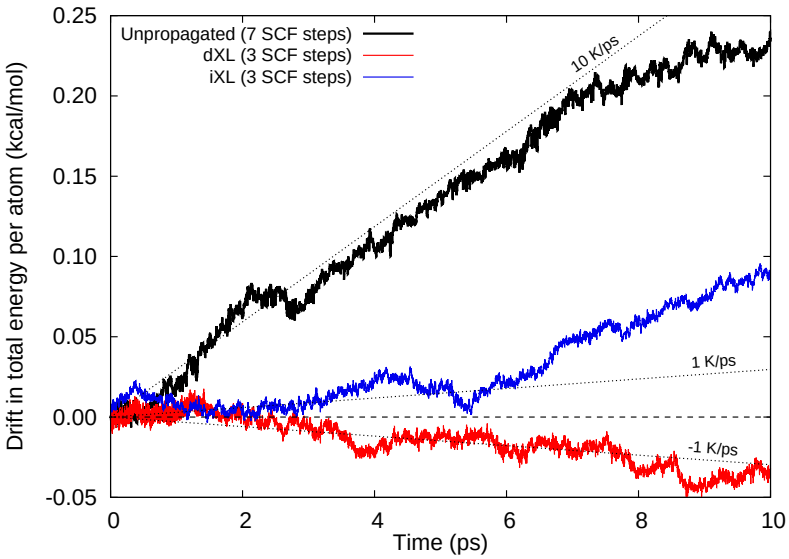

Figure 5.11: Comparison of drifts in total energy between calculations with no propagation and dXL and iXL (testcase: 64 H_2O molecules). SCF convergence threshold was set to 10^{-4} Ha $a_0^{-3/2}$ (loose), as this is what would be used in practical simulations. The dashed lines are meant as a guide to the eye and correspond to energy drifts expressed as system cooling/heating rates in K/ps.

the absence of propagation is 8.5 ± 0.9 K/ps, with dXL and iXL performing better: at −1.5 ± 0.3 K/ps and 2.8 ± 2.1 K/ps, respectively. The fact that the drifts are comparable between dXL and iXL is in line with our expectations – the drift that makes dXL less desirable for long classical MD simulations does not play an appreciable role in LS-DFT MD, since it is dwarfed by inherent drift due to the noise in LS-DFT forces.

To add more weight to this argument, we examine the drifts for the remaining systems and for tighter SCF thresholds. The results are summarised in Tab. 5.3. For all system sizes, regardless of how and if the initial guesses are propagated, we observe drifts of several K/ps[1]. No correlation is apparent between the magnitude of the drift and the SCF convergence threshold, which indicates that the threshold is not excessively loose, and that no accuracy gains can be achieved by using tighter thresholds. Neither of the extended Lagrangian methods is seen to discernibly outperform the other, and the drifts are comparable to the case with no propagation. This confirms that the observed drifts are a result of inherent noise in LS-DFT forces, and are hardly affected by the properties of an extended Lagrangian scheme.

Of course, the use of an extended Lagrangian approach is expected to yield a perfor-

[1]The drifts and their uncertainties were calculated as follows. We assume the drift to be approximately linear. In a simulation with a length of t (t = 10 ps), we can use a subset of data, viz. the interval $[0, t_0]$ to evaluate the linear coefficient in the drift, $a(t_0)$, over this interval. The final drift estimate is $a(t)$. The uncertainty is taken as the largest difference between $a(t_0)$ and $a(t)$ calculated over $t_0 \geq t/2$.

Table 5.3: Comparison of the energy drift (K/ps) between calculations with no propagation, and calculations using the dXL and iXL schemes – for four different system sizes (16, 32, 64 and 128 H_2O molecules) and three different SCF(LNV) convergence thresholds. Large uncertainties of computed drifts reflect necessarily short simulation times. $\overline{N}_{\text{SCF}}$ is the average number of SCF steps for a combination of method and threshold (detailed breakdown in Tab. 5.4).

SCF threshold $[\text{Ha}\, a_0^{-3/2}]$	Propagation scheme	System size: 16 H_2O	32 H_2O	64 H_2O	128 H_2O	$\overline{N}_{\text{SCF}}$
		drift (K/ps $[\times 10^0]$)				
10^{-4}	no prop.	4.8 ± 0.4	4.2 ± 1.9	8.5 ± 0.9	3.3 ± 1.1	7.8
	dXL	3.5 ± 1.8	6.6 ± 0.5	-1.5 ± 0.3	0.2 ± 0.2	3.3
(loose)	iXL	1.5 ± 0.8	-3.9 ± 2.1	2.8 ± 2.1	-2.4 ± 0.4	4.0
10^{-5}	no prop.	3.8 ± 5.3	2.3 ± 2.1	5.6 ± 3.2	3.0 ± 0.5	13.5
	dXL	2.9 ± 0.8	0.2 ± 3.0	1.9 ± 2.9	3.4 ± 0.2	5.7
(moderate)	iXL	4.8 ± 0.7	3.8 ± 1.5	0.9 ± 0.8	2.6 ± 0.3	7.7
10^{-6}	no prop.	3.2 ± 2.7	5.7 ± 1.6	5.8 ± 2.2	2.5 ± 0.9	19.3
	dXL	2.2 ± 1.4	4.6 ± 1.9	1.5 ± 0.4	3.1 ± 0.7	10.2
(tight)	iXL	2.8 ± 2.5	7.1 ± 1.5	5.4 ± 0.7	2.8 ± 0.4	13.5

Table 5.4: A comparison of the number of SCF iterations between calculations with no propagation, and calculations using the dXL and iXL schemes – for four different system sizes (16, 32, 64 and 128 H_2O molecules) and three different SCF thresholds.

SCF threshold $[\mathrm{Ha}\, a_0^{-3/2}]$	Propagation scheme	System size 16	32	64	128
10^{-4}	no prop.	9.0	8.0	7.1	7.0
	dXL	3.8	3.4	3.1	3.0
(loose)	iXL	4.0	4.0	3.0	5.0
10^{-5}	no prop.	14.0	14.0	13.0	13.0
	dXL	6.3	6.0	5.5	5.0
(moderate)	iXL	9.0	8.0	7.0	7.0
10^{-6}	no prop.	20.0	20.0	19.1	18.0
	dXL	11.0	10.8	10.0	9.0
(tight)	iXL	14.4	13.9	13.7	12.0

mance improvement by reducing the number of SCF steps needed to converge to a given threshold. We report that number in Table 5.4 for all systems and methods under study. Both dXL and iXL offer a performance gain of 30%–60%, depending on the convergence thresholds, with looser thresholds offering larger gains. Except for an isolated case (64 H_2O molecules, loose convergence threshold), the use of the dissipative scheme leads to slightly faster convergence compared to the inertial scheme. This is a consequence of manually setting the auxiliary temperature for iXL to a slightly more conservative value than the exact average auxiliary temperature of dXL (cf. Sec. 5.6.1). With more aggressive settings we would expect the performance of iXL to be indistinguishable from that of dXL, but with the caveat that iXL immediately starts to drift appreciably when T^* is set to an excessively low value, necessitating care in the choice of this parameter. The drift in this case is a consequence of the thermostat's persistent scaling of velocities, with the time average of γ^n (eq. 5.28) being excessively lower than 1.

Apart from not impairing energy conservation and improving performance, a natural requirement for a propagation scheme is for it not to visibly affect the calculated properties of the system. In this study we examine the basic structural characteristic of water, the oxygen-oxygen pair correlation function $g_{OO}(r)$, shown in Fig. 5.12. The reference (unpropagated) calculation was run with a tight threshold, to provide a robust baseline that we assume is the correct result. The calculations with dXL and iXL were performed with a loose threshold, as this is what would be used in practice. The differences between the predictions of the two integration schemes are minuscule, and the differences between

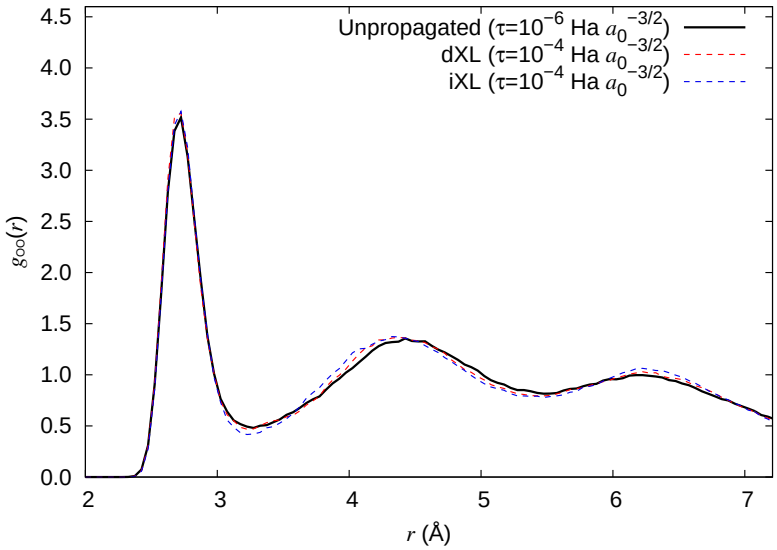

Figure 5.12: Oxygen-oxygen pair correlation function $g_{\mathrm{OO}}(r)$ obtained in the absence of a propagation scheme, and with the dXL and iXL schemes. Testcase: 64 H_2O molecule system. For calculations with propagation, the SCF convergence threshold was set to 10^{-4} Ha $a_0^{-3/2}$ (loose), as this is what would be used in practical simulations. The reference (unpropagated) calculation uses a tight threshold (10^{-6} Ha $a_0^{-3/2}$). The differences between the predictions obtained with dXL and iXL and in the absence of propagation are seen to be minor.

the propagated calculations and the reference are also very modest – the first peak is described practically identically, and for larger distances the introduction of propagation (in particular with the iXL scheme) appears to introduce a very slight over-structuring, which we find perfectly acceptable given the timescale of the simulations. We do not include experimental results in the comparison, knowing full well that the DFT model of water significantly over-structures for reasons that we do not expect the propagation schemes to compensate for. The same over-structuring exacerbates the problem (the system takes longer to fully equilibrate). We thus attribute the small differences to the noise stemming from the limited timescale.

5.7 Summary

In this chapter we assessed the performance of two integrators for the extended Lagrangian introduced by Niklasson *et al.*[42] – a dissipative formulation (dXL)[42], and an inertial formulation (iXL)[272], in two distinct regimes, by employing them in classical polarisable force field and in LS-DFT *NVE* MD calculations on condensed water systems[274]. The well-known necessity of counteracting the unbounded increase in the

kinetic energy of the auxiliary degrees of freedom through some form of energy leaching was assessed.

In the classical polarisable force field regime we reproduced the observations of Albaugh *et al.* [272], showing that over long (~ns) timescales, for maximally loose SCF thresholds, where an unpropagated scheme drifts catastrophically, iXL offers better energy conservation compared to dXL. This advantage is a consequence of a different approach to "energy leaching" taken by the iXL method, which strictly preserves time reversibility[274]. However, at this loose SCF threshold dXL has the advantage of needing substantially fewer SCF steps (1 *vs.* 3) to converge, and thus offers an efficiency gain over iXL. As the SCF threshold is made progressively tighter, the performance of the two schemes begins to converge, with the drift of dXL improving considerably, and the almost constant absolute efficiency advantage of 2-3 SCF steps that dXL maintains over iXL becoming relatively less important.

In the LS-DFT MD regime the picture is substantially different due to the high intrinsic noise of LS-DFT forces, which leads to energy drifts that are much larger than the additional drift due to energy leaching from the extended Lagrangian approach[274]. As such the dXL and iXL propagation schemes can be used with the loosest of LNV-SCF threshold investigated (10^{-4} Ha $a_0^{-3/2}$), beyond which an additional drift of an extended Lagrangian scheme starts to become apparent. Although there is no discernible difference in practice between the dXL and iXL schemes at the loose convergence threshold, the dXL would currently be the mildly preferred choice for LS-DFT MD calculations due to its parameter-free nature.

As it is now, we believe that in practical and sufficiently long (many-ps) LS-DFT MD calculations a gentle thermostatting would currently be necessary to counteract the excessive increase/decrease in temperature that is a consequence of intrinsic drift, and which is as large as several K/ps. Further work is desirable in the area of linear-scaling DFT to improve the accuracy of forces in the presence of artefacts that result from localisation constraints and the approximate treatment of Pulay-like terms in the forces. We feel obliged to point out that the energy drifts in LS-DFT would likely change noticeably if the localised orbitals were to be optimised (not studied in this work). This is because on the one hand the *in situ* optimisation significantly reduces the magnitude of Pulay-like terms, while on the other hand it introduces a further approximation into their calculation. It is possible that the change that the optimisation of localised orbitals would introduce to the "noise background" of LS-DFT forces, and the ensuing change in intrinsic energy drift, would uncover differences in the behaviour of the two extended Lagrangian integration schemes that are currently obscured in AIMD. We intend to study this behaviour in the future.

We highlighted the non-triviality of correctly evolving the auxiliary degrees of freedom over a curved manifold in *ab initio* calculations, a fact that is not always appreciated in the literature. We presented and tested a viable scheme for propagating the density kernel in this scenario, using a fixed, non-orthogonal generalised Wannier function basis. Further work is necessary to develop a scheme where the localised orbitals could be similarly propagated.

Finally, we showed that both dXL and iXL consistently enable significant, and usually similar, increases in performance over calculations not employing propagation, both for classical polarisable force field MD and LS-DFT MD. Thus, both of these schemes constitute important algorithmic improvements that markedly extend the timescales accessible to classical and LS-DFT MD simulations alike.

Conclusions

The work presented in this thesis focuses on the development of new algorithms for molecular dynamics simulations of large molecules and assessment of their performance within the linear-scaling DFT (LS-DFT) framework. All our developments were implemented in the ONETEP program, but they can be readily transferred to other linear-scaling codes. We are therefore confident that our research can reach a broad audience and be employed by a wide class of researchers.

LS-DFT is a relatively young and very active research field whose theoretical pillars are the density functional theory and the property of locality of the electronic matter. Locality in the electronic structure of materials manifests itself in the form of an exponential decay of the single-particle reduced density matrix in real space. The rate of the exponential decay is proportional to the band gap in the energy spectrum between the highest occupied band (valence) and the lowest unoccupied band (conduction). Insulating and semi-conducting materials intrinsically present a well-defined separation of states at the Fermi level, whereas metals show no such gap. Remarkably, it has been suggested that also for metals at finite electronic temperatures, some degree of localisation in the electronic structure is observed. In this case the rate of decay is proportional to the ratio between the Fermi velocity and thermal energy $\kappa_B T$. However, for metals at 0 K only a polynomial decay of the density matrix is found.

Linear-scaling approaches exploit the exponential form of the density matrix to generate sparse matrices and thence using sparse algebra. In doing so, only $\approx N$ elements need to be stored. Moreover, by employing localised orbitals the cost of building the Hamiltonian and the overlap matrix, as well as other computational demanding calculations, can also be made to scale with the first power of the system size[2]. The aim of our research was to combine molecular dynamics simulations, within the Born-Oppenheimer approximation (BOMD), with LS-DFT methods.

In particular, we have implemented new algorithms that exploit locality of the electronic structure to compute the IR spectra of molecules in a larger environment, such as

[2]Only the operations requiring FFTs scale as $O(N \log N)$. Generally, these represent a small fraction of CPU time.

a solvent. Our methods are based on density kernel partitioning (DKP) and distributed multipole analysis (DMA), respectively. In particular, by combining our methods with BOMD we were able to compute fully anharmonic infrared spectra of molecules in the gas phase and in solution at finite temperature. With this approach, conformational dynamics and anharmonic effects (anharmonicity of the potential energy surface) are naturally taken into account within the molecular dynamics simulation without the need of any *a posteriori* correction. We performed several NVE -BOMD simulations at finite temperature on benchmark molecules in vacuum. We found very good agreement with the experimental spectra for all the benchmark systems. Subsequently, we performed an NVE -BOMD simulation to validate the DKP and DMA methods on the 2-Ala peptide in 500 water molecules, i.e. 1522 atoms. Although the accuracy of the spectrum was not our main goal for this study, we found a relatively good agreement between our spectrum and the one from a similar calculations by Gaigeot *et al.*, obtained by performing CPMD with MLWFs for the calculation of the dipoles[2, 34], and with experiments.

We have also implemented two different integrators for the extended Lagrangian scheme introduced by Niklasson *et al.* [42]. These schemes are employed for speeding-up molecular dynamics simulations within which self-consistent field (SCF) calculations are required. We have assessed their performance in two different frameworks: LS-DFT BOMD, and classical polarisable force field. In the classical polarisable force field case we reproduced the findings of Albaugh *et al.* [272], showing that over long timescales (~ns), iXL offers better energy conservation compared to dXL, since the dissipative term breaks time-reversibility even if at high orders. However, at loose SCF thresholds dXL has the advantage of needing substantially fewer SCF steps (1 *vs.* 3) to converge, and thus offers an efficiency gain over iXL. In the LS-DFT MD regime, we found a significantly different picture due to the high intrinsic noise in LS-DFT forces, which leads to energy drifts much larger than the small additional drift due to the extended Lagrangian approach[274]. Consequently, the two integration schemes can be used with the loosest of LNV-SCF threshold investigated (10^{-4} Ha $a_0^{-3/2}$). Although there is no discernible difference in practice between the dXL and iXL schemes at the loose convergence threshold, the dXL would currently be the preferred option for LS-DFT MD calculations since it is parameter-free in nature, i.e. no target temperature is required to obtain a stable integration. As it stands now, we believe that in sufficiently long (many-ps) LS-DFT MD calculations a gentle thermostatting of the real degrees of freedom, would currently be necessary to counteract the excessive increase/decrease in temperature that is a consequence of intrinsic drift, and which can be as large as several K/ps. Finally, we showed that both dXL and iXL consistently enable significant, and usually similar, increases in performance over standard calculations, both for classical polarisable force field MD and LS-DFT MD.

Thus, both these schemes constitute important algorithmic improvements that markedly extend the timescales accessible to classical and LS-DFT MD simulations alike.

Future research works and perspectives

Further work is desirable in the area of linear-scaling DFT to improve the accuracy of forces when optimised support functions and strict localisation constraints are employed. In this case, artefacts that result from localisation constraints and the approximate treatment of Pulay-like terms in the forces arise. *in situ* optimisation significantly reduces the magnitude of Pulay-like terms, while on the other hand it introduces a further approximation into their calculation. It is also possible that the change that the optimisation of localised orbitals would introduce to the "noise background" of LS-DFT forces, would uncover differences in the behaviour of the two extended Lagrangian integration schemes that are currently obscured in AIMD. In the future, we intend to study in more detail the effects of strict localisation constraints on the quality of the forces and also the beneficial (if any) effects of a gentle confinement on the support functions.

Appendix A

Derivation of the transition rate in the interaction picture

The state vectors $|k\rangle$ and $|\ell\rangle$ are eigenstates of the unperturbed Hamiltonian $\hat{H}_0$. Accordingly, in the Schrödinger picture, the time dependence of these states is given by (1.6). One can pass to the so-called interaction picture by introducing the Fourier transform of the Dirac delta function

$$\delta(\omega_{\ell k} - \omega) = \frac{1}{2\pi} \int \mathrm{d}t \, \exp\left[\left(\frac{\varepsilon_\ell - \varepsilon_k}{\hbar} - \omega\right) it\right]. \tag{A.1}$$

By substituting (A.1) into (4.4) and redistributing the exponentials as[1]

$$\begin{aligned} \langle \ell | \mathbf{e} \cdot \hat{\boldsymbol{\mu}} | k \rangle \, e^{\left(\frac{\varepsilon_\ell - \varepsilon_k}{\hbar}\right) it} &= \langle \ell | e^{\frac{i\varepsilon_\ell t}{\hbar}} \mathbf{e} \cdot \hat{\boldsymbol{\mu}} e^{\frac{-i\varepsilon_k t}{\hbar}} | k \rangle \\ &= \langle \ell | \mathbf{e} \cdot e^{i\hat{H}_0 t/\hbar} \hat{\boldsymbol{\mu}} e^{-i\hat{H}_0 t/\hbar} | k \rangle \\ &= \langle \ell | \mathbf{e} \cdot \hat{\boldsymbol{\mu}}(t) | k \rangle \,, \end{aligned} \tag{A.2}$$

the ensemble average of the transition rates becomes

$$\Omega(\omega) = \frac{E_0^2}{4\hbar^2} \int \mathrm{d}t \, e^{-i\omega t} \sum_{k,\ell} \rho_k \, \langle k | \mathbf{e} \cdot \hat{\boldsymbol{\mu}}(0) | \ell \rangle \, \langle \ell | \mathbf{e} \cdot \hat{\boldsymbol{\mu}}(t) | k \rangle \,. \tag{A.3}$$

Since the $|\ell\rangle$ are eigenstates of the unperturbed Hamiltonian, they form a complete basis of the Hilbert space, and therefore the closure relation $\sum_\ell |\ell\rangle \langle \ell| = 1$ holds. Substituting

[1] In deriving (A.2) we have used the symmetry of the inner product in complex vector space, and the Hermicity of the operator $\hat{\boldsymbol{\mu}}$.

this relation into (A.3), we find

$$\Omega(\omega) = \frac{E_0^2}{4\hbar^2} \int \mathrm{d}t \, e^{-i\omega t} \sum_k \rho_k \langle k|\mathbf{e} \cdot \hat{\boldsymbol{\mu}}(0)\mathbf{e} \cdot \hat{\boldsymbol{\mu}}(t)|k\rangle \,. \tag{A.4}$$

Finally, multiplying by ρ_k and summing over all the initial states, we obtain the equilibrium ensemble average in (4.5)

Appendix B

Quantum correction factors

This also implies that $C^{\text{sym}}(t)$ and $C^{\text{asym}}(t)$ are not independent functions, which is a consequence of the Kramers-Kronig relation. In addition to $C^{\text{rs}}(t)$ and $C^{\text{asym}}(t)$ defined in section 3.1, we can define other quantum autocorrelation functions as

$$\begin{aligned} iC^{\text{asym}}(t) &= C^{\text{rs}}(t) - C^{\text{sym}}(t) \\ &= \left\langle \frac{1}{2}[\hat{\boldsymbol{\mu}}(0), \hat{\boldsymbol{\mu}}(t)] \right\rangle \qquad \text{(B.1)} \\ C^{\text{shift}}(t) &= C^{\text{rs}}(t + i\beta\hbar/2) \qquad \text{(B.2)} \\ C^{\text{kubo}}(t) &= \left\langle \frac{1}{\beta} \int_0^\beta d\lambda \, \hat{\boldsymbol{\mu}}(0)\hat{\boldsymbol{\mu}}(t + i\hbar\lambda) \right\rangle \\ &= \left\langle \widetilde{\hat{\boldsymbol{\mu}}}(0)\hat{\boldsymbol{\mu}}(t) \right\rangle \qquad \text{(B.3)} \end{aligned}$$

Where $C^{\text{asym}}(t)$ is the imaginary part of the right-sided [1] autocorrelation function $C^{\text{rs}}(t)$ and $[\cdot, \cdot]$ is the commutator. $C^{\text{shift}}(t)$ is the time-shifted correlation function, and $C^{\text{kubo}}(t)$ is the Kubo-transformed correlation function.

As forementioned, the physical information carried by all the autocorrelation functions is the same, in the sense that if any of these quantum functions is known, we can easily derive the others, since their Fourier transform are interrelated by simple expressions [226]. This also implies that $C^{\text{sym}}(t)$ and $C^{\text{asym}}(t)$ are not independent functions, which

[1] Right-sided because the time dependence is given to the second operator. A left-sided correlation function would be $\widetilde{C}(t) = \langle \hat{\boldsymbol{\mu}}(t) \cdot \hat{\boldsymbol{\mu}} \rangle$.

stems from the Kramers-Kronig relations. In the frequency domain we have

$$
\begin{aligned}
I^{\mathrm{rs}}(\omega) &= I^{\mathrm{sym}}(\omega) + iI^{\mathrm{asym}}(\omega). \\
&= \frac{2}{1+\exp[-\beta\hbar\omega]} I^{\mathrm{sym}}(\omega) && \text{(B.4)} \\
&= \frac{2}{1-\exp[-\beta\hbar\omega]} I^{\mathrm{asym}}(\omega) && \text{(B.5)} \\
&= \exp\left[\frac{\beta\hbar\omega}{2}\right] I^{\mathrm{shift}}(\omega) && \text{(B.6)} \\
&= \frac{\beta\hbar\omega}{2}\left(\coth\frac{\beta\hbar\omega}{2}+1\right) I^{\mathrm{kubo}}(\omega) \\
&= \frac{\beta\hbar\omega}{1-\exp[-\beta\hbar\omega]} I^{\mathrm{kubo}}(\omega), && \text{(B.7)}
\end{aligned}
$$

where $I^{\mathrm{rs}}(\omega) = \frac{1}{2\pi}\int dt\, e^{-i\omega t} C^{\mathrm{rs}}(t)$ and likewise for the other functions.
The fact that $I^{\mathrm{rs}}(\omega)$ can be expressed in terms of other lineshapes, is a crucial point if we want to use the classical lineshape to calculate the cross-section function. It can be shown that $C^{\mathrm{sym}}(t)$, $C^{\mathrm{shift}}(t)$, and $C^{\mathrm{kubo}}(t)$ are real and even functions of time, as $C^{\mathrm{cl}}(t)$, while $C^{\mathrm{asym}}(t)$ is a real and odd function of time, and since the Fourier transform preserves the parity, it follows immediately $I^{\mathrm{sym}}(\omega) = I^{\mathrm{sym}}(-\omega)$, $I^{\mathrm{asym}}(\omega) = -I^{\mathrm{asym}}(-\omega)$, $I^{\mathrm{shift}}(\omega) = I^{\mathrm{shift}}(-\omega)$, and $I^{\mathrm{kubo}}(\omega) = I^{\mathrm{kubo}}(-\omega)$.
Moreover, in the classic limit, $\beta \to 0$, the prefactors in (B.4),(B.6), and (B.7) approach to unity, which implies $I^{\mathrm{rs}}(\omega) = I^{\mathrm{sym}}(\omega) = I^{\mathrm{shift}}(\omega) = I^{\mathrm{kubo}}(\omega)$, that in turn implies the equality of the respective autocorrelation functions. This suggests to replace one of these autocorrelation functions with $C^{\mathrm{cl}}(t)$ and to use the corresponding prefactor to restore the symmetry in (4.14)). Popular correction factors found in literature are[2]

$$
\begin{aligned}
Q^{\mathrm{sym}}(\omega) &= \frac{2}{1+\exp[-\beta\hbar\omega]} && \text{(B.8)} \\
Q^{\mathrm{kubo}}(\omega) &= \frac{\beta\hbar\omega}{1-\exp[\beta\hbar\omega]} && \text{(B.9)} \\
Q^{\mathrm{shift}}(\omega) &= \exp\left[\frac{\beta\hbar\omega}{2}\right], && \text{(B.10)}
\end{aligned}
$$

[2] We follow here the nomenclature in [226]

Appendix C

Stability of velocity Verlet with weak coupling

In Section 5.3, we have derived the equations of motion for the auxiliary degrees of freedom $\{\zeta\}$, starting from the extended Lagrangian (5.6) and coupling the $\{\zeta\}$ to an external bath:

$$\dot{\zeta}^{n+\frac{1}{2}} = \dot{\zeta}^{n} + \frac{\Delta t}{2}\ddot{\zeta}^{n} = \dot{\zeta}^{n} + \frac{\omega^2 \Delta t}{2}[\chi^{n}_{\mathrm{SCF}} - \zeta^{n}] \tag{C.1}$$

$$\zeta^{n+1} = \zeta^{n} + \dot{\zeta}^{n+\frac{1}{2}}\Delta t \tag{C.2}$$

$$\mathrm{SCF} \rightarrow \mathrm{ENERGY\ AND\ FORCES}$$

$$\tilde{\dot{\zeta}}^{n+1} = \dot{\zeta}^{n+\frac{1}{2}} + \frac{\Delta t}{2}\ddot{\zeta}^{n+1} = \dot{\zeta}^{n+\frac{1}{2}} + \frac{\omega^2 \Delta t}{2}[\chi^{n+1}_{\mathrm{SCF}} - \zeta^{n+1}] \tag{C.3}$$

$$\dot{\zeta}^{n+1} = \alpha^{n+1}\tilde{\dot{\zeta}}^{n+1}, \tag{C.4}$$

where $\zeta, \dot{\zeta}$ and $\ddot{\zeta}$ represent the auxiliary generalized coordinates, velocities and accelerations, respectively, whereas χ_{SCF} is the converged SCF solution (real degrees of freedom). The coupling strength with the external bath is given by α. In deriving (C.1)-(C.4) we have adopted the velocity Verlet integrator with a timestep Δt. A possible choice for α is given by the Berendsen thermostat:

$$\alpha^{n} = \sqrt{1.0 + \frac{\Delta t}{\tau}\left(\frac{T^*}{T^n} - 1.0\right)}, \tag{C.5}$$

where τ represents the characteristic time scale of the thermostat. T^* is the target temperature. The instantaneous temperature T^n is generally a quadratic function of the

auxiliary generalized velocities

$$T \propto f(\dot{\zeta}^2). \tag{C.6}$$

The discretized equations of motion (C.1)-(C.4) can be cast in matrix form as

$$\begin{bmatrix} \zeta^{n+1} \\ \dot{\zeta}^{n+1} \end{bmatrix} = \mathbf{T}(\alpha, \chi_{\text{SCF}}, \Delta t) \begin{bmatrix} \zeta^{n} \\ \dot{\zeta}^{n} \end{bmatrix}. \tag{C.7}$$

Following a change of variable $\dot{\zeta}\Delta t \to \dot{\zeta}$, the propagation matrix $\mathbf{T}$ takes the form

$$\begin{aligned} \mathbf{T} &= \begin{bmatrix} 1 & 0 \\ \frac{\alpha\omega^2\Delta t^2}{2}[\chi_{\text{SCF}}^{n+1}\left(\zeta^{-1}\right)^{n+1} - 1] & \alpha \end{bmatrix} \times \begin{bmatrix} 1 + \frac{\omega^2\Delta t^2}{2}[\chi_{\text{SCF}}^{n}\left(\zeta^{-1}\right)^{n} - 1] & 1 \\ 0 & 1 \end{bmatrix} + \\ &\quad \begin{bmatrix} 0 & 0 \\ \frac{\alpha\omega^2\Delta t^2}{2}[\chi_{\text{SCF}}^{n}\left(\zeta^{-1}\right)^{n} - 1] & 0 \end{bmatrix} \\ &= \begin{bmatrix} 1 + \frac{\omega^2\Delta t^2}{2}Q^n & 1 \\ \frac{\alpha\omega^2\Delta t^2}{2}Q^{n+1} + \frac{\alpha\omega^4\Delta t^4}{4}Q^{n+1}Q^n + \frac{\alpha\omega^2\Delta t^2}{2}Q^n & \frac{\alpha\omega^2\Delta t^2}{2}Q^{n+1} + \alpha \end{bmatrix} \\ &= \begin{bmatrix} 1 + \kappa Q^n & 1 \\ \alpha\kappa\{Q^{n+1} + Q^n + \kappa Q^{n+1}Q^n\} & \alpha(\kappa Q^{n+1} + 1) \end{bmatrix}, \end{aligned} \tag{C.8}$$

where in the last two steps we have set $Q = \chi_{\text{SCF}}\zeta^{-1} - 1$ and we have grouped together all scalar parameters, but α, into $\kappa = \omega^2\Delta t^2/2$. Following the analysis in Ref. 303, we can study the stability of the propagation by linearizing the SCF optimization around an exact ground state χ_*:

$$\chi_{\text{SCF}} = \text{SCF}[\zeta] \approx \chi_* + \Gamma(\zeta - \chi_*), \tag{C.9}$$

where the linearized SCF optimization kernel is represented by Γ. Now we look at the homogeneous equation, i.e. $\chi_* \equiv 0$, and replace Γ with its largest eigenvalue γ, and insert this equation into the propagation matrix $\mathbf{T}$, which reads

$$\mathbf{T} = \begin{bmatrix} 1 + \kappa(\gamma^n - 1) & 1 \\ \alpha\kappa\{(\gamma^{n+1} - 1) + (\gamma^n - 1) + \kappa(\gamma^{n+1} - 1)(\gamma^n - 1)\} & \alpha[\kappa(\gamma^{n+1} - 1) + 1] \end{bmatrix}, \tag{C.10}$$

where we want to ensure the propagation to be stable for the entire range of convergence, $\gamma \in [-1, 1]$.

The stability of the integrator is determined by the largest eigenvalue $|\lambda_{\text{max}}|$ of the propagation matrix in (C.10), which is a measure of the loss of energy conservation. To

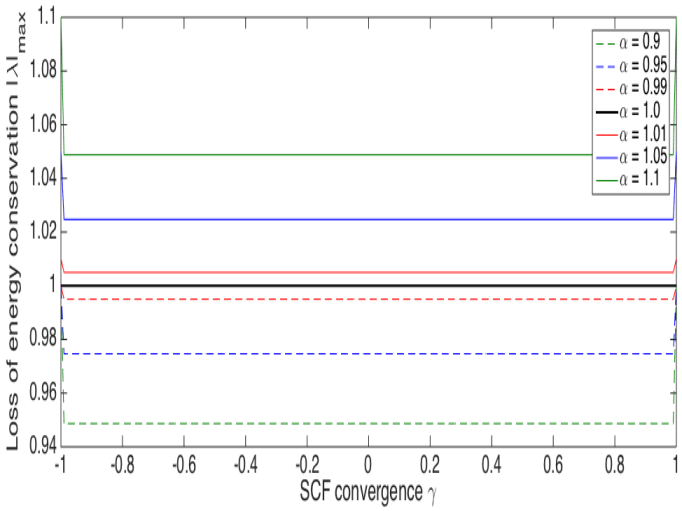

Figure C.1: Stability measured by the largest eigenvalue $|\lambda|_{\max}$ of (C.10) as a function of the degree of SCF convergence measured by $\gamma \in [-1, 1]$ for selected values of α for the velocity Verlet scheme.

Table C.1: Different values for the α parameter and the corresponding optimal values for κ and maximal dissipation.

Method/coefficients	α	κ_{opt}	$\lvert\lambda\rvert_{\max}$
velocity Verlet	1.0	1.0	1.0
	0.99	1.0	0.995
	0.95	1.0	0.975
	0.9	1.0	0.949
	1.01	1.0	1.005
	1.05	1.0	1.025
	1.1	1.0	1.049

simplify the discussion, we can look at:

$$\gamma^{n+1} \approx \gamma^n = \widetilde{\gamma},$$

which is achieved when two subsequent SCF steps converge with the same accuracy. In this case, the propagation matrix $\mathbf{T}$ simplifies to

$$\mathbf{T} = \begin{bmatrix} 1 + \kappa(\widetilde{\gamma} - 1) & 1 \\ \alpha\kappa[2(\widetilde{\gamma} - 1) + \kappa(\widetilde{\gamma} - 1)^2] & \alpha[\kappa(\widetilde{\gamma} - 1) + 1] \end{bmatrix}. \tag{C.11}$$

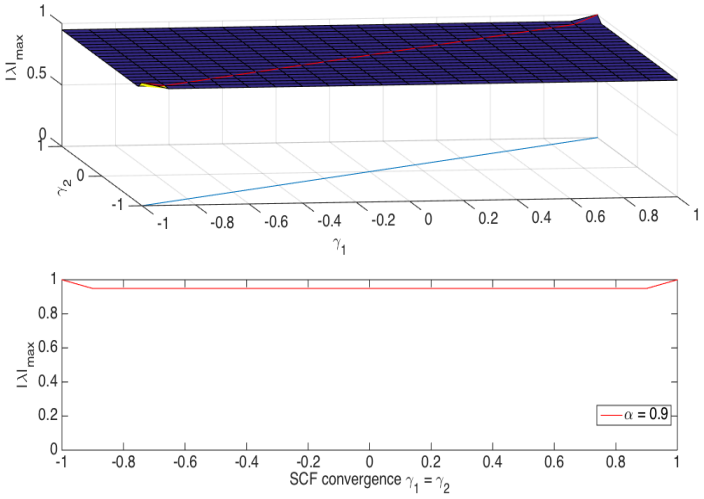

(a) $\alpha = 0.9$

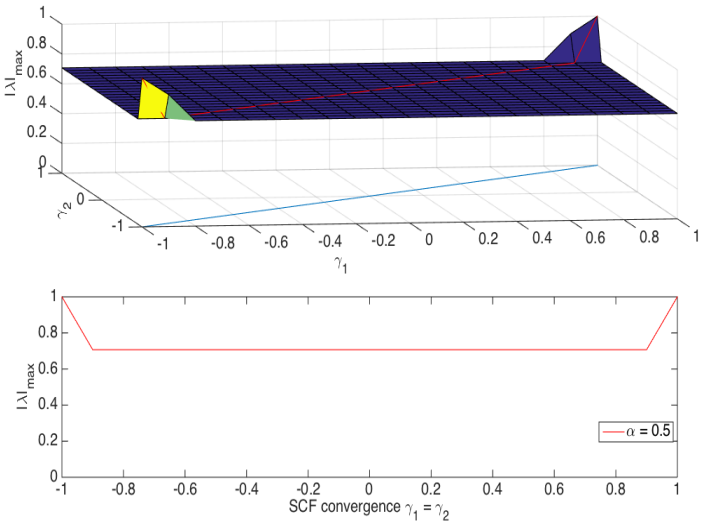

(b) $\alpha = 0.5$

Figure C.2: Stability measured by the largest eigenvalue $|\lambda|_{\max}$ of (C.11) as a function of the degree of SCF convergence when $\gamma^{n+1} \neq \gamma^n$ and they are independently allowed to vary in the range $[-1, 1]$ for $\alpha = 0.9$ panel a), and $\alpha = 0.5$ panel b) for the velocity Verlet scheme.

This simplification captures most of the results for the stability as demonstrated by comparing Fig. C.1 with Fig. C.2a-C.2b, where we let both γ^n and γ^{n+1} to independently vary in the range $[-1, 1]$, with no significant impact on the stability. This implies that the stability of the integrator is mainly determined by the coupling parameter α. In fact, the propagation matrix in (C.11) shows the important symplectic property

$$\mathbf{T}^{\mathrm{T}}\mathbf{J}\mathbf{T} = \alpha\mathbf{J}, \tag{C.12}$$

where $\mathbf{J}$ is the symplectic structure matrix

$$\mathbf{J} = \begin{bmatrix} 0 & 1 \\ -1 & 0 \end{bmatrix}. \tag{C.13}$$

This is simply a re-statement of the fact that when $\alpha = 1$ we recover the canonical velocity Verlet scheme, which is of course symplectic. Our analysis is in line, at least qualitatively, with the results obtained by Albaugh *et al.* for the simpler Verlet scheme[272]. We also find that any $\kappa \neq 1$ results in a suboptimal regime, cf. Tab. C.1, which means that the optimal choice for ω ought to be $\sqrt{2}/\Delta t$.

PhD data directory tree graphs

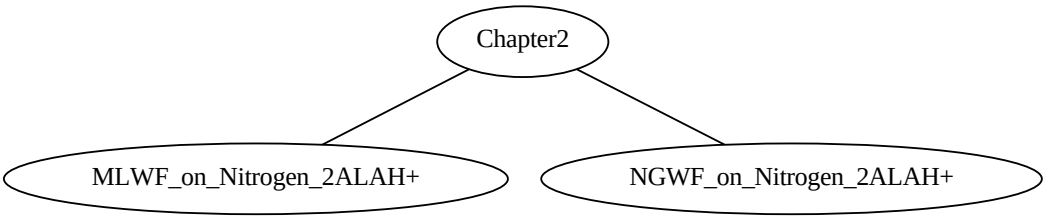

Chapter4
FILES_FOR_FIG4.10_ETHANOL
AIMD
AMBER
HARMONIC_VIBRATIONAL_MODES
STAGE_1
STAGE_2
STAGE_3
Geometry_optimisation
FILES_FOR_FIG4.4
FILES_FOR_FIG4.8_WATER
AIMD
AMBER
Equilibration
Minimisation
Parameters
HARMONIC_VIBRATIONAL_MODES
FILES_FOR_FIG4.11_2ALA_VACUUM
AIMD
AMBER
HARMONIC_VIBRATIONAL_MODES
FILES_FOR_FIG4.5
Fig_a_b_c_d
TOP
FILES_FOR_FIG4.9_CO2
AIMD
AMBER
HARMONIC_VIBRATIONAL_MODES

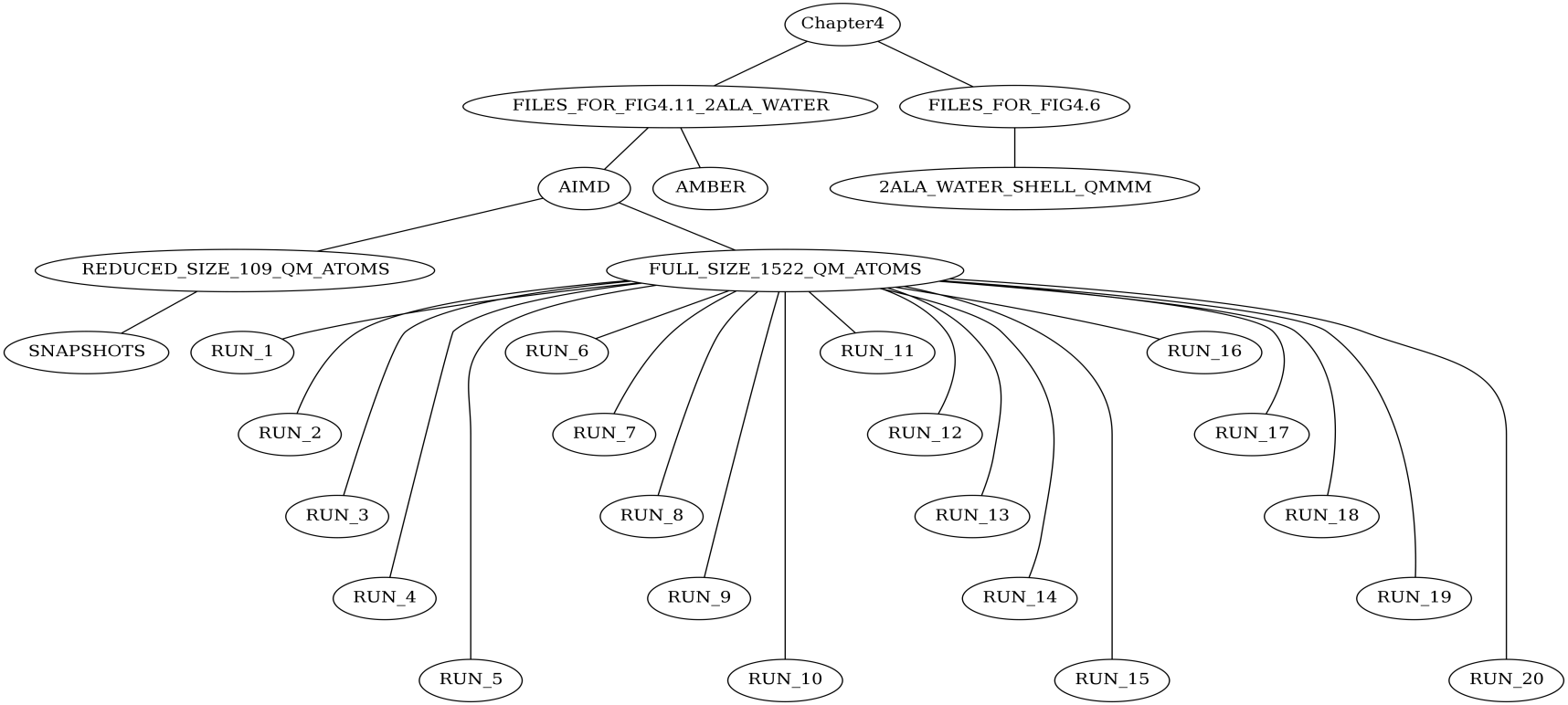
Chapter4
FILES_FOR_FIG4.11_2ALA_WATER
FILES_FOR_FIG4.6
AIMD
AMBER
2ALA_WATER_SHELL_QMMM
REDUCED_SIZE_109_QM_ATOMS
FULL_SIZE_1522_QM_ATOMS
SNAPSHOTS
RUN_1
RUN_2
RUN_3
RUN_4
RUN_5
RUN_6
RUN_7
RUN_8
RUN_9
RUN_10
RUN_11
RUN_12
RUN_13
RUN_14
RUN_15
RUN_16
RUN_17
RUN_18
RUN_19
RUN_20

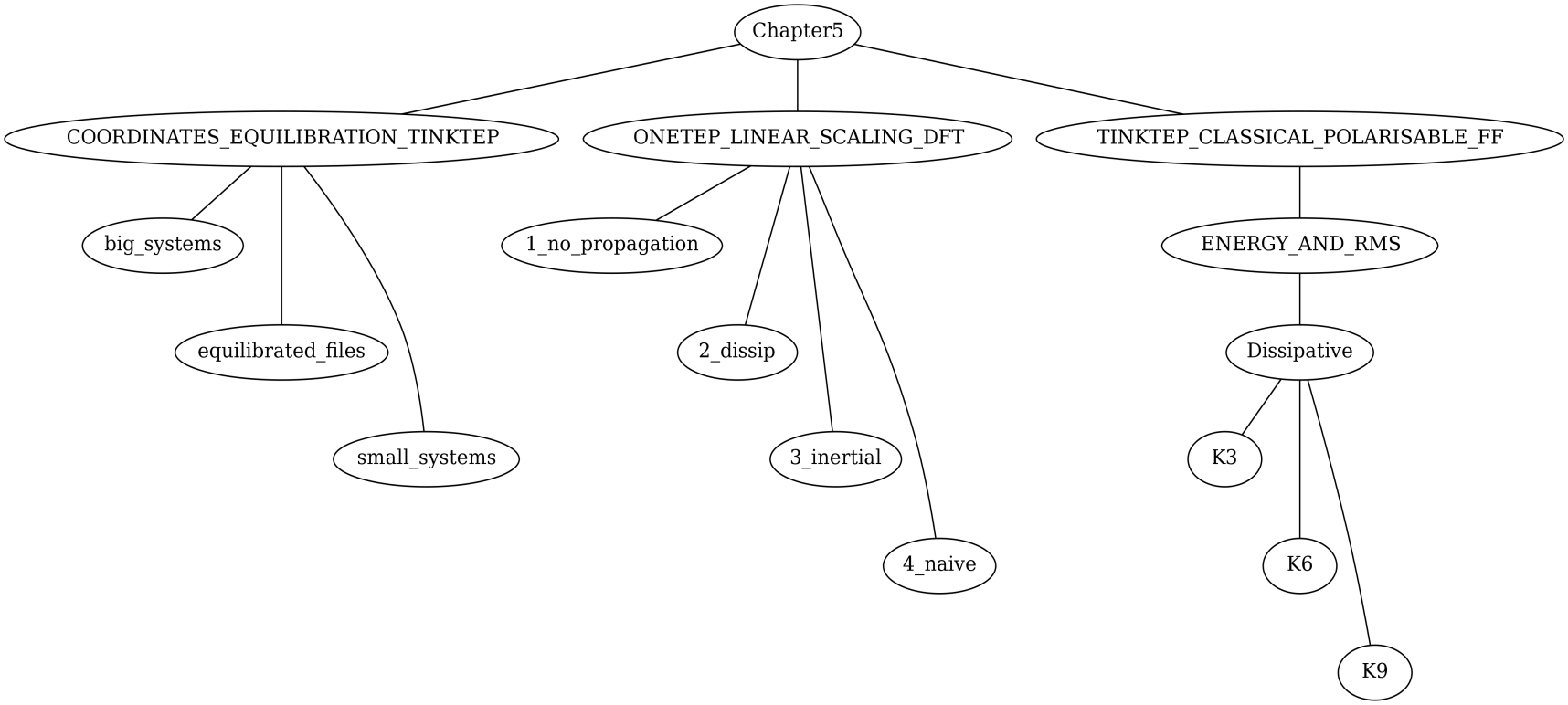
Chapter5
COORDINATES_EQUILIBRATION_TINKTEP
ONETEP_LINEAR_SCALING_DFT
TINKTEP_CLASSICAL_POLARISABLE_FF
big_systems
equilibrated_files
small_systems
1_no_propagation
2_dissip
3_inertial
4_naive
ENERGY_AND_RMS
Dissipative
K3
K6
K9

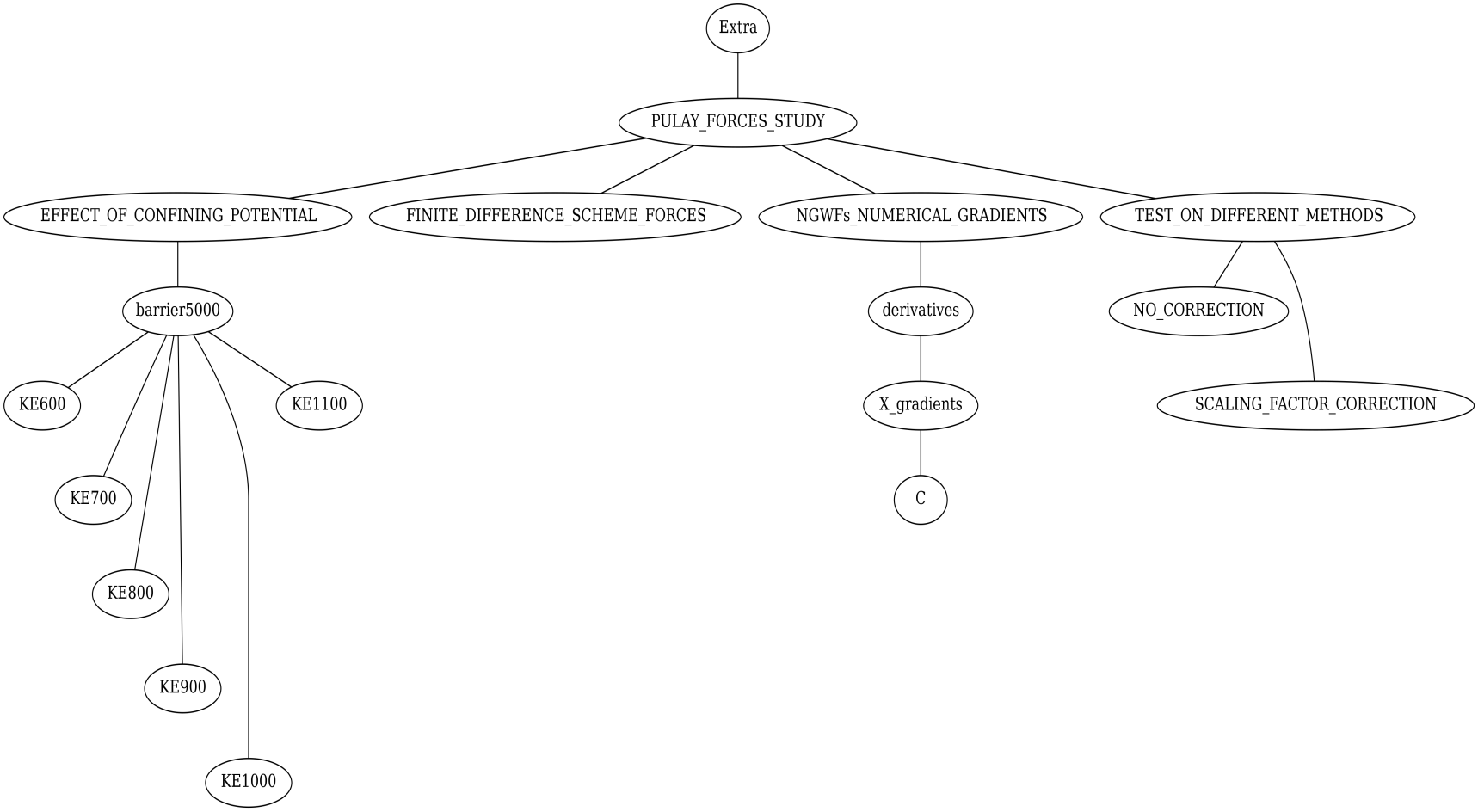
Extra
PULAY_FORCES_STUDY
EFFECT_OF_CONFINING_POTENTIAL
FINITE_DIFFERENCE_SCHEME_FORCES
NGWFs_NUMERICAL_GRADIENTS
TEST_ON_DIFFERENT_METHODS
barrier5000
derivatives
NO_CORRECTION
KE600
KE1100
X_gradients
SCALING_FACTOR_CORRECTION
KE700
C
KE800
KE900
KE1000

Bibliography

[1] P. Linstrom and W. Mallard, *NIST Chemistry WebBook, NIST Standard Reference Database Number 69*, National Institute of Standards and Technology, Gaithersburg MD, 20899. xi, 106, 107, 108

[2] M.-P. Gaigeot, The Journal of Physical Chemistry A **112**, 13507 (2008). xi, 60, 103, 108, 109, 111, 146

[3] K. Kwac, K.-K. Lee, J. B. Han, K.-I. Oh, and M. Cho, The Journal of Chemical Physics **128**, 105106 (2008). xii, 103, 109

[4] E. Schrödinger, Annalen der Physik **384**, 361 (1926). 1, 6, 10

[5] E. Schrödinger, Annalen der Physik **384**, 489 (1926). 1, 6, 10

[6] W. Heisenberg, Zeitschrift für Physik **33**, 879 (1925). 1, 6

[7] P. A. M. Dirac, Proceedings of the Royal Society of London A: Mathematical, Physical and Engineering Sciences **117**, 610 (1928). 1

[8] F. Bloch, Zeitschrift für Physik **52**, 555 (1929). 1, 39

[9] A. Messiah, *Quantum Mechanics*, Dover books on physics, Dover Publications, 1961. 1

[10] R. Martin, *Electronic Structure: Basic Theory and Practical Methods*, Cambridge University Press, 2004. 1, 12, 38, 39, 90

[11] T. Helgaker, P. Jorgensen, and J. Olsen, *Molecular Electronic-Structure Theory*, Wiley, 2014. 1, 43

[12] P. Hohenberg and W. Kohn, Phys. Rev. **136**, B864 (1964). 2, 23

[13] W. Kohn and L. J. Sham, Phys. Rev. **140**, A1133 (1965). 2, 23, 28

[14] M. C. Payne, M. P. Teter, D. C. Allan, T. A. Arias, and J. D. Joannopoulos, Rev. Mod. Phys. **64**, 1045 (1992). 2, 44, 60, 115, 137

[15] M. T. Green, J. H. Dawson, and H. B. Gray, Science **304**, 1653 (2004). 2

[16] D. Alfé, M. J. Gillan, and G. D. Price, Nature **401**, 462 (1999). 2, 61

[17] J. Javier and G. Philippe, Nature **422**, 506 (2003). 2

[18] C.-K. Skylaris, P. D. Haynes, A. A. Mostofi, and M. C. Payne, The Journal of Chemical Physics **122**, 084119 (2005). 2, 3, 24, 48, 53, 57, 127

[19] J. M. Soler et al., Journal of Physics: Condensed Matter **14**, 2745 (2002). 2, 24, 48

[20] M. Gillan, D. Bowler, A. Torralba, and T. Miyazaki, Computer Physics Communications **177**, 14 (2007), Proceedings of the Conference on Computational Physics 2006CCP 2006Conference on Computational Physics 2006. 2, 24, 47, 48, 61

[21] S. Mohr et al., The Journal of Chemical Physics **140**, 204110 (2014). 2, 24

[22] N. Todorova, L. Yeung, A. Hung, and I. Yarovsky, PLOS ONE **8**, 1 (2013). 2

[23] N. Todorova, A. J. Makarucha, N. D. M. Hine, A. A. Mostofi, and I. Yarovsky, PLOS Computational Biology **9**, 1 (2013). 2

[24] M. V. Escárcega-Bobadilla et al., Nature Communications **4**, 2648 (2013). 2

[25] R. A. Bell, M. C. Payne, and A. A. Mostofi, Phys. Rev. B **89**, 245426 (2014). 2

[26] L. G. Verga et al., Phys. Chem. Chem. Phys. **18**, 32713 (2016). 2

[27] W. Kohn, Phys. Rev. Lett. **76**, 3168 (1996). 2

[28] E. Prodan and W. Kohn, Proceedings of the National Academy of Sciences of the United States of America **102**, 11635 (2005). 2, 47

[29] D. Marx and J. Hutter, *Ab Initio Molecular Dynamics: Basic Theory and Advanced Methods*, Cambridge University Press, 2009. 2, 60, 63, 91

[30] R. Car and M. Parrinello, Phys. Rev. Lett. **55**, 2471 (1985). 2, 60, 63

[31] M. Born and R. Oppenheimer, Annalen der Physik **389**, 457 (1927). 2, 17

[32] M. Born and K. Huang, *Dynamical Theory of Crystal Lattices*, International series of monographs on physics, Clarendon P, 1954. 2

[33] D. C. Marinica et al., The Journal of Physical Chemistry A **110**, 8802 (2006). 2

[34] M.-P. Gaigeot, Phys. Chem. Chem. Phys. **12**, 3336 (2010). 2, 89, 101, 103, 108, 111, 146

[35] Y. Kanai, A. Tilocca, A. Selloni, and R. Car, The Journal of Chemical Physics **121**, 3359 (2004). 2

[36] W. Qin, X. Li, W.-W. Bian, X.-J. Fan, and J.-Y. Qi, Biomaterials **31**, 1007 (2010). 2, 60

[37] F. A. Momany, J. Willett, and U. Schnupf, Journal of Molecular Structure: THEOCHEM **953**, 61 (2010). 2, 60

[38] R. C. Remsing, M. D. Baer, G. K. Schenter, C. J. Mundy, and J. D. Weeks, The Journal of Physical Chemistry Letters **5**, 2767 (2014). 2

[39] C. Lee, D. Vanderbilt, K. Laasonen, R. Car, and M. Parrinello, Phys. Rev. Lett. **69**, 462 (1992). 2, 61

[40] M. A. Morales, C. Pierleoni, E. Schwegler, and D. M. Ceperley, Proceedings of the National Academy of Sciences **107**, 12799 (2010). 2, 61

[41] N. D. M. Hine et al., Phys. Rev. B **83**, 195102 (2011). 3, 57, 73, 74

[42] A. M. N. Niklasson et al., The Journal of Chemical Physics **130**, 214109 (2009). 4, 112, 115, 116, 122, 123, 124, 142, 146

[43] W. Heisenberg, *Physics and Philosophy: The Revolution in Modern Science*, Penguin Classics, 1958. 5

[44] P. Dirac, *The Principles of Quantum Mechanics*, International series of monographs on physics (Oxford, England), Clarendon Press, 1958. 5, 6, 8, 9, 10, 12

[45] R. P. Feynman, Rev. Mod. Phys. **20**, 367 (1948). 5, 6

[46] H. Everett, Rev. Mod. Phys. **29**, 454 (1957). 5

[47] M. Jammer, *The philosophy of quantum mechanics: the interpretations of quantum mechanics in historical perspective*, Wiley Interscience publication, Wiley, 1974. 5

[48] M. Jammer, *The conceptual development of quantum mechanics*, International series in pure and applied physics, McGraw-Hill, 1966. 5

[49] M. Planck, Annalen der Physik **309**, 553 (1901). 6

[50] N. Bohr, Nature **92**, 231 (1913). 6

[51] N. Bohr, Nature **107**, 104 (1921). 6

[52] M. Born and P. Jordan, Zeitschrift für Physik **34**, 858 (1925). 6

[53] J. VonNeumann, *Mathematische Grundlagen der Quantenmechanik*, Springer, 1932. 6

[54] J. Sakurai and J. Napolitano, *Modern Quantum Mechanics*, Pearson new international edition, Pearson, 2013. 6

[55] R. Resta, Rev. Mod. Phys. **66**, 899 (1994). 7, 90

[56] R. Resta and D. Vanderbilt, *Theory of Polarization: A Modern Approach*, pages 31–68, Springer Berlin Heidelberg, Berlin, Heidelberg, 2007. 7, 90

[57] R. Resta, Phys. Rev. Lett. **80**, 1800 (1998). 7, 90

[58] A. Szabo and N. Ostlund, *Modern Quantum Chemistry: Introduction to Advanced Electronic Structure Theory*, Dover Books on Chemistry, Dover Publications, 1989. 8, 21, 43

[59] P. R.G and Y. W., *Density-Functional Theory of Atoms and Molecules*, International Series of Monographs on Chemistry, Oxford University Press, 1994. 8, 14, 45

[60] E. Fermi, Rendiconti lincei **3**, 145 (1926). 9

[61] P. A. M. Dirac, Proceedings of the Royal Society of London A: Mathematical, Physical and Engineering Sciences **112**, 661 (1926). 9

[62] U. Fano, Rev. Mod. Phys. **29**, 74 (1957). 12

[63] J. v. Neumann, Nachrichten von der Gesellschaft der Wissenschaften zu Göttingen, Mathematisch-Physikalische Klasse **1927**, 245 (1927). 12

[64] L. Landau, Zeitschrift für Physik **45**, 430 (1927). 12

[65] R. McWeeny, Rev. Mod. Phys. **32**, 335 (1960). 12, 46, 54

[66] I. Mayer, *Simple Theorems, Proofs, and Derivations in Quantum Chemistry*, Mathematical and Computational Chemistry, Springer, 2003. 14

[67] H. Hellmann, *Einführung in die Quantenchemie*, Franz Deuticke, 1937. 15

[68] R. P. Feynman, Phys. Rev. **56**, 340 (1939). 15

[69] J. Esteve, F. Falceto, and C. G. Canal, Physics Letters A **374**, 819 (2010). 15

[70] D. R. Hartree, Mathematical Proceedings of the Cambridge Philosophical Society **24**, 89–110 (1928). 20

[71] V. Fock, Zeitschrift für Physik **61** (1930). 20

[72] J. C. Slater, Phys. Rev. **35**, 210 (1930). 20

[73] J. C. Slater, Phys. Rev. **81**, 385 (1951). 20

[74] C. Møller and M. S. Plesset, Phys. Rev. **46**, 618 (1934). 21

[75] J. Ĉížek, The Journal of Chemical Physics **45**, 4256 (1966). 21

[76] B. Roos, Chemical Physics Letters **15**, 153 (1972). 21

[77] B. r. O. Roos, P. R. Taylor, and P. E. Siegbahn, Chemical Physics **48**, 157 (1980). 22

[78] P. Siegbahn, A. Heiberg, B. Roos, and B. Levy, Physica Scripta **21**, 323 (1980). 22

[79] L. H. Thomas, Mathematical Proceedings of the Cambridge Philosophical Society **23**, 542 (1927), http://dx.doi.org/10.1017/S0305004100011683. 23

[80] E. Fermi, Rend. Accad. Naz. Lincei **6**, 1253 (1927). 23

[81] P. A. M. Dirac, Mathematical Proceedings of the Cambridge Philosophical Society **26**, 376 (1930). 23

[82] E. H. Lieb, Rev. Mod. Phys. **53**, 603 (1981). 23

[83] V. L. Lignéres and E. A. Carter, *An Introduction to Orbital-Free Density Functional Theory*, pages 137–148, Springer Netherlands, 2005. 23

[84] W. Kohn, A. D. Becke, and R. G. Parr, The Journal of Physical Chemistry **100**, 12974 (1996). 24

[85] N. D. Mermin, Phys. Rev. **137**, A1441 (1965). 27

[86] M. Levy, Proc. Nat. Acad. Sci USA **76**, 6062 (1979). 27

[87] M. Levy, Phys. Rev. A **26**, 1200 (1982). 27

[88] E. H. Lieb, International Journal of Quantum Chemistry **24**, 243 (1983). 27

[89] T. L. Gilbert, Phys. Rev. B **12**, 2111 (1975). 28

[90] J. F. Janak, Phys. Rev. B **18**, 7165 (1978). 31

[91] T. Tsuneda, J.-W. Song, S. Suzuki, and K. Hirao, The Journal of Chemical Physics **133**, 174101 (2010). 31

[92] M. Aldegunde, J. R. Kermode, and N. Zabaras, Journal of Computational Physics **311**, 173 (2016). 32

[93] P. A. M. Dirac, Mathematical Proceedings of the Cambridge Philosophical Society **26**, 376–385 (1930). 32

[94] J. P. Perdew and A. Zunger, Phys. Rev. B **23**, 5048 (1981). 32

[95] D. M. Ceperley and B. J. Alder, Phys. Rev. Lett. **45**, 566 (1980). 32

[96] M. Gell-Mann and K. A. Brueckner, Phys. Rev. **106**, 364 (1957). 32

[97] O. Gunnarsson, M. Jonson, and B. I. Lundqvist, Phys. Rev. B **20**, 3136 (1979). 32

[98] J. Harris, Phys. Rev. A **29**, 1648 (1984). 32

[99] J. P. Perdew and Y. Wang, Phys. Rev. B **45**, 13244 (1992). 33

[100] J. P. Perdew, K. Burke, and M. Ernzerhof, Phys. Rev. Lett. **78**, 1396 (1997). 33

[101] A. D. Becke, Phys. Rev. A **38**, 3098 (1988). 33, 34

[102] C. Lee, W. Yang, and R. G. Parr, Phys. Rev. B **37**, 785 (1988). 33, 34

[103] D. C. Langreth and M. J. Mehl, Phys. Rev. B **28**, 1809 (1983). 33

[104] J. P. Perdew et al., Phys. Rev. B **46**, 6671 (1992). 33

[105] J. Tao, J. P. Perdew, V. N. Staroverov, and G. E. Scuseria, Phys. Rev. Lett. **91**, 146401 (2003). 33, 34

[106] P. J. Stephens, F. J. Devlin, C. F. Chabalowski, and M. J. Frisch, The Journal of Physical Chemistry **98**, 11623 (1994). 34

[107] S. H. Vosko, L. Wilk, and M. Nusair, Canadian Journal of Physics **58**, 1200 (1980). 34

[108] R. Peverati and D. G. Truhlar, Philosophical Transactions of the Royal Society of London A: Mathematical, Physical and Engineering Sciences **372** (2014). 34

[109] J. P. Perdew and K. Schmidt, AIP Conference Proceedings **577**, 1 (2001). 34

[110] R. Car, Nat Chem **8**, 820 (2016). 34

[111] V. Heine, Solid State Physics **24**, 1 (1970). 35

[112] W. E. Pickett, Computer Physics Reports **9**, 115 (1989). 35

[113] C. Herring and A. G. Hill, Phys. Rev. **58**, 132 (1940). 36

[114] J. C. Phillips and L. Kleinman, Phys. Rev. **116**, 287 (1959). 36

[115] D. R. Hamann, M. Schlüter, and C. Chiang, Phys. Rev. Lett. **43**, 1494 (1979). 37

[116] G. B. Bachelet, D. R. Hamann, and M. Schlüter, Phys. Rev. B **26**, 4199 (1982). 37

[117] D. R. Hamann, Phys. Rev. B **40**, 2980 (1989). 37

[118] A. M. Rappe, K. M. Rabe, E. Kaxiras, and J. D. Joannopoulos, Phys. Rev. B **41**, 1227 (1990). 37

[119] N. Troullier and J. L. Martins, Phys. Rev. B **43**, 1993 (1991). 37

[120] D. Vanderbilt, Phys. Rev. B **41**, 7892 (1990). 37

[121] P. E. Blöchl, Phys. Rev. B **50**, 17953 (1994). 37

[122] L. Kleinman and D. M. Bylander, Phys. Rev. Lett. **48**, 1425 (1982), `http://link.aps.org/doi/10.1103/PhysRevLett.48.1425`. 38

[123] G. H. Wannier, Phys. Rev. **52**, 191 (1937). 40

[124] C. Brouder, G. Panati, M. Calandra, C. Mourougane, and N. Marzari, Phys. Rev. Lett. **98**, 046402 (2007). 41, 47

[125] N. Marzari and D. Vanderbilt, Phys. Rev. B **56**, 12847 (1997). 41, 43, 47, 91

[126] N. Marzari, A. A. Mostofi, J. R. Yates, I. Souza, and D. Vanderbilt, Rev. Mod. Phys. **84**, 1419 (2012). 43, 47, 91, 92, 98

[127] S. F. Boys, Rev. Mod. Phys. **32**, 296 (1960). 43

[128] J. M. Foster and S. F. Boys, Rev. Mod. Phys. **32**, 300 (1960). 43

[129] A. A. Mostofi et al., Computer Physics Communications **178**, 685 (2008). 43, 91

[130] J. G. Hill, International Journal of Quantum Chemistry **113**, 21 (2013). 43

[131] F. M. J. et al., Gaussian~09, Gaussian Inc. Wallingford CT 2016. 43

[132] M. Valiev et al., Computer Physics Communications **181**, 1477 (2010). 43

[133] L. Genovese et al., The Journal of Chemical Physics **129**, 014109 (2008). 44

[134] X. Ren et al., New Journal of Physics **14**, 053020 (2012). 44, 48

[135] X. Gonze et al., Computer Physics Communications **180**, 2582 (2009). 44

[136] C. Stewart J. et al., Zeitschrift für Kristallographie - Crystalline Materials **220** (2005). 44

[137] J. Enkovaara et al., Journal of Physics: Condensed Matter **22**, 253202 (2010). 44

[138] P. Giannozzi et al., Journal of Physics: Condensed Matter **21**, 395502 (2009). 44, 98

[139] G. Kresse and J. Furthmüller, Phys. Rev. B **54**, 11169 (1996). 44

[140] G. Kresse and J. Furthmüller, Computational Materials Science **6**, 15 (1996). 44

[141] G. Lippert, J. Hutter, and M. Parrinello, Molecular Physics **92**, 477 (1997). 44

[142] J. Ihm, A. Zunger, and M. L. Cohen, Journal of Physics C: Solid State Physics **12**, 4409 (1979). 44

[143] S. Goedecker, Rev. Mod. Phys. **71**, 1085 (1999). 46, 47, 61

[144] S. N. Taraskin, D. A. Drabold, and S. R. Elliott, Phys. Rev. Lett. **88**, 196405 (2002). 46

[145] J. D. Cloizeaux, Phys. Rev. **135**, A698 (1964). 46, 47

[146] S. Ismail-Beigi and T. A. Arias, Phys. Rev. Lett. **82**, 2127 (1999). 46

[147] S. Goedecker, Phys. Rev. B **58**, 3501 (1998). 46

[148] F. Mauri, G. Galli, and R. Car, Phys. Rev. B **47**, 9973 (1993). 47

[149] P. Ordejón, D. A. Drabold, M. P. Grumbach, and R. M. Martin, Phys. Rev. B **48**, 14646 (1993). 47

[150] F. Mauri and G. Galli, Phys. Rev. B **50**, 4316 (1994). 47

[151] J. Kim, F. Mauri, and G. Galli, Phys. Rev. B **52**, 1640 (1995). 47

[152] P. Ordejón, D. A. Drabold, R. M. Martin, and M. P. Grumbach, Phys. Rev. B **51**, 1456 (1995). 47

[153] E. Hernández and M. J. Gillan, Phys. Rev. B **51**, 10157 (1995). 47

[154] E. Hernández, M. J. Gillan, and C. M. Goringe, Phys. Rev. B **53**, 7147 (1996). 47

[155] E. Hernández, M. J. Gillan, and C. M. Goringe, Phys. Rev. B **55**, 13485 (1997). 47

[156] P. W. Anderson, Phys. Rev. Lett. **21**, 13 (1968). 47

[157] L. He and D. Vanderbilt, Phys. Rev. Lett. **86**, 5341 (2001). 47

[158] D. R. Bowler and T. Miyazaki, Reports on Progress in Physics **75**, 036503 (2012). 47

[159] E. Anglada, J. M. Soler, J. Junquera, and E. Artacho, Phys. Rev. B **66**, 205101 (2002). 48

[160] P. Haynes and M. Payne, Computer Physics Communications **102**, 17 (1997). 48

[161] G. E. Scuseria, The Journal of Physical Chemistry A **103**, 4782 (1999). 48

[162] T. Ozaki and H. Kino, Phys. Rev. B **72**, 045121 (2005). 48

[163] E. Artacho and L. Miláns del Bosch, Phys. Rev. A **43**, 5770 (1991). 48

[164] M. Head-gordon et al., Tensors in electronic structure theory: Basic concepts and applications to electron correlation models, 2009. 48, 49

[165] E. Artacho and D. D. O'Regan, Phys. Rev. B **95**, 115155 (2017). 48

[166] M. Head-Gordon, P. E. Maslen, and C. A. White, The Journal of Chemical Physics **108**, 616 (1998). 48

[167] C.-K. Skylaris, A. A. Mostofi, P. D. Haynes, O. Diéguez, and M. C. Payne, Phys. Rev. B **66**, 035119 (2002). 50, 73

[168] A. A. Mostofi, C.-K. Skylaris, P. D. Haynes, and M. C. Payne, Computer Physics Communications **147**, 788 (2002). 50, 57, 74

[169] C.-K. Skylaris, A. A. Mostofi, P. D. Haynes, C. J. Pickard, and M. C. Payne, Computer Physics Communications **140**, 315 (2001). 52, 74

[170] P. P. Ewald, Annalen der Physik **369**, 253 (1921). 53

[171] P. D. Haynes, C.-K. Skylaris, A. A. Mostofi, and M. C. Payne, Journal of Physics: Condensed Matter **20**, 294207 (2008). 53, 100

[172] A. Ruiz-Serrano, N. D. M. Hine, and C.-K. Skylaris, The Journal of Chemical Physics **136**, 234101 (2012). 53, 73, 74, 115, 138

[173] X.-P. Li, R. W. Nunes, and D. Vanderbilt, Phys. Rev. B **47**, 10891 (1993). 54, 100

[174] R. W. Nunes and D. Vanderbilt, Phys. Rev. B **50**, 17611 (1994). 54

[175] A. H. R. Palser and D. E. Manolopoulos, Phys. Rev. B **58**, 12704 (1998). 54

[176] J. M. Millam and G. E. Scuseria, The Journal of Chemical Physics **106**, 5569 (1997). 55, 100

[177] A. Ruiz-Serrano and C.-K. Skylaris, The Journal of Chemical Physics **139**, 054107 (2013). 57

[178] J. Aarons, M. Sarwar, D. Thompsett, and C.-K. Skylaris, The Journal of Chemical Physics **145**, 220901 (2016). 57

[179] N. Bernstein, J. R. Kermode, and G. Csányi, Reports on Progress in Physics **72**, 026501 (2009). 60

[180] M. Karplus and J. A. McCammon, Nat Struct Mol Biol **9**, 646 (2002). 60

[181] M. Thomas, M. Brehm, R. Fligg, P. Vohringer, and B. Kirchner, Phys. Chem. Chem. Phys. **15**, 6608 (2013). 60

[182] M. Iannuzzi, A. Laio, and M. Parrinello, Phys. Rev. Lett. **90**, 238302 (2003). 60

[183] M. Tuckerman, K. Laasonen, M. Sprik, and M. Parrinello, The Journal of Chemical Physics **103**, 150 (1995). 60

[184] C. J. Cramer and D. G. Truhlar, Chemical Reviews **99**, 2161 (1999). 60

[185] S. W. Rick and S. J. Stuart, *Potentials and Algorithms for Incorporating Polarizability in Computer Simulations*, pages 89–146, John Wiley and Sons, Inc., 2003. 61, 114

[186] P. Cieplak, F.-Y. Dupradeau, Y. Duan, and J. Wang, Journal of Physics: Condensed Matter **21**, 333102 (2009). 61, 114

[187] M. Elstner and G. Seifert, Philosophical Transactions of the Royal Society of London A: Mathematical, Physical and Engineering Sciences **372** (2014). 61

[188] N. D. Yilmazer and M. Korth, Computational and Structural Biotechnology Journal **13**, 169 (2015). 61

[189] D. Marx and M. Parrinello, The Journal of Chemical Physics **104**, 4077 (1996). 63

[190] M. E. Tuckerman, D. Marx, M. L. Klein, and M. Parrinello, The Journal of Chemical Physics **104**, 5579 (1996). 63

[191] M. Tuckerman, *Statistical Mechanics: Theory and Molecular Simulation*, Oxford Graduate Texts, OUP Oxford, 2010. 63, 64, 65, 66, 67, 68, 70, 84, 101

[192] L. Verlet, Phys. Rev. **159**, 98 (1967). 64

[193] V. Vitale, J. Dziedzic, S. M.-M. Dubois, H. Fangohr, and C.-K. Skylaris, Journal of Chemical Theory and Computation **11**, 3321 (2015). 64, 98

[194] M. R. Jarvis, I. D. White, R. W. Godby, and M. C. Payne, Phys. Rev. B **56**, 14972 (1997). 67

[195] G. J. Martyna and M. E. Tuckerman, The Journal of Chemical Physics **110**, 2810 (1999). 67

[196] L. Genovese, T. Deutsch, A. Neelov, S. Goedecker, and G. Beylkin, The Journal of Chemical Physics **125**, 074105 (2006). 67

[197] L. Genovese, T. Deutsch, and S. Goedecker, The Journal of Chemical Physics **127**, 054704 (2007). 67

[198] J. Gibbs, *Elementary Principles in Statistical Mechanics: Developed with Especial Reference to the Rational Foundations of Thermodynamics*, Elementary Principles in Statistical Mechanics: Developed with Especial Reference to the Rational Foundation of Thermodynamics, C. Scribner's sons, 1902. 67

[199] T. Hill, *An Introduction to Statistical Thermodynamics*, Addison-Wesley series in chemistry, Dover Publications, 1960. 67

[200] D. Frenkel and B. Smit, *Understanding Molecular Simulation: From Algorithms to Applications*, Computational science series, Elsevier Science, 2001. 67, 68, 72

[201] H. C. Andersen, The Journal of Chemical Physics **72**, 2384 (1980). 68, 69, 118

[202] G. Bussi, D. Donadio, and M. Parrinello, The Journal of Chemical Physics **126**, 014101 (2007). 68, 71

[203] S. Nosé, Molecular Physics **100**, 191 (2002). 68, 70, 118

[204] W. G. Hoover, Phys. Rev. A **31**, 1695 (1985). 68, 70, 128

[205] H. J. C. Berendsen, J. P. M. Postma, W. F. van Gunsteren, A. DiNola, and J. R. Haak, The Journal of Chemical Physics **81**, 3684 (1984). 69

[206] G. S. Grest and K. Kremer, Phys. Rev. A **33**, 3628 (1986). 69

[207] G. J. Martyna, M. E. Tuckerman, D. J. Tobias, and M. L. Klein, Molecular Physics **87**, 1117 (1996). 71

[208] N. Wiener, *Extrapolation, interpolation, and smoothing of stationary time series: with engineering applications*, Technology press books in science and engineering, Technology Press of the Massachusetts Institute of Technology, 1964. 72

[209] Journal of Computational Physics **225**, 1 (2007). 76

[210] B. G. Pfrommer, M. Côté, S. G. Louie, and M. L. Cohen, Journal of Computational Physics **131**, 233 (1997). 76

[211] S. Mohr et al., The Journal of Chemical Physics **140**, 204110 (2014). 77, 115, 138

[212] L. Genovese et al., The Journal of Chemical Physics **129**, 014109 (2008). 77

[213] Álvaro Ruiz-Serrano and C.-K. Skylaris, The Journal of Chemical Physics **139**, 164110 (2013). 77

[214] J. Ingle and S. Crouch, *Spectrochemical Analysis*, Prentice Hall, 1988. 82

[215] *Molecular Spectroscopy*, Pearson Education, 2008. 83

[216] J. Grunenberg, *Computational Spectroscopy: Methods, Experiments and Applications*, Wiley, 2011. 83

[217] D. McQuarrie, *Statistical Mechanics*, University science books, 2000. 83, 84, 87

[218] R. Zwanzig, Annual Review of Physical Chemistry **16**, 67 (1965). 83

[219] P. M. Kim, L. J. Lu, Y. Xia, and M. B. Gerstein, Science **314**, 1938 (2006). 83

[220] P. Butz, R. T. Kroemer, N. A. Macleod, and J. P. Simons, The Journal of Physical Chemistry A **105**, 544 (2001). 84

[221] L. C. Snoek, R. T. Kroemer, and J. P. Simons, Phys.Chem.Chem.Phys. **4**, 2130 (2002). 84

[222] F. Huisken, O. Werhahn, A. Y. Ivanov, and S. A. Krasnokutski, The Journal of Chemical Physics **111**, 2978 (1999). 84

[223] P. A. M. Dirac, **114**, 243 (1927). 84

[224] E. Fermi, *Nuclear Physics*, University of Chicago Press, 1967. 84

[225] L. Hernandez de la Peña, Molecular Physics **0**, 1 (0). 88

[226] R. Ramírez, T. López-Ciudad, P. Kumar P, and D. Marx, The Journal of Chemical Physics **121**, 3973 (2004). 88, 151, 152

[227] L. Landau and E. Lifshítsˇ, *Quantum Mechanics: Non-relativistic Theory*, Butterworth-Heinemann, Butterworth-Heinemann, 1977. 89

[228] R. Resta, Journal of Physics: Condensed Matter **22**, 123201 (2010). 90

[229] R. D. King-Smith and D. Vanderbilt, Phys. Rev. B **47**, 1651 (1993). 90

[230] D. D. O'Regan, M. C. Payne, and A. A. Mostofi, Phys. Rev. B **85**, 193101 (2012). 91

[231] A. Stone, Chemical Physics Letters **83**, 233 (1981). 92, 94

[232] A. Stone and M. Alderton, Molecular Physics **56**, 1047 (1985). 92, 94

[233] M. H. Cohen and A. Wasserman, The Journal of Physical Chemistry A **111**, 2229 (2007). 92

[234] R. F. W. Bader, Chemical Reviews **91**, 893 (1991). 92

[235] M. Thomas, M. Brehm, and B. Kirchner, Phys. Chem. Chem. Phys. **17**, 3207 (2015). 92

[236] R. Rein, On physical properties and interactions of polyatomic molecules: With application to molecular recognition in biology, volume 7 of *Advances in Quantum Chemistry*, pages 335 – 396, Academic Press, 1973. 94

[237] A. J. Stone, Gdma: distributed multipoles from gaussian98 wavefunctions, Technical report, University of Cambridge, 1998. 94

[238] A. J. Stone, Journal of Chemical Theory and Computation **1**, 1128 (2005). 94

[239] J. Dziedzic, Q. Hill, and C.-K. Skylaris, The Journal of Chemical Physics **139**, 214103 (2013). 95, 96

[240] Q. Hill, *Development of more accurate computational methods within linear-scaling density functional theory*, PhD thesis, University of Southampton, Southampton, United Kingdom, 2010. 96

[241] P. D. Haynes and M. C. I, cpc **102**, 17 (1997). 96

[242] D. A. Case et al., Amber 12, 2012. 100

[243] K. A. Wilkinson, N. D. M. Hine, and C.-K. Skylaris, Journal of Chemical Theory and Computation **10**, 4782 (2014). 100

[244] S. Grimme, Journal of Computational Chemistry **27**, 1787 (2006). 100, 128

[245] Q. Hill and C.-K. Skylaris, Proceedings of the Royal Society of London A: Mathematical, Physical and Engineering Sciences **465**, 669 (2009). 100, 122

[246] M.-P. Gaigeot, Phys. Chem. Chem. Phys. **12**, 10198 (2010). 103, 110

[247] S. J. Fox et al., The Journal of Physical Chemistry B **117**, 9478 (2013). 105

[248] R. Lemus, Journal of Molecular Spectroscopy **225**, 73 (2004). 106

[249] Y. Yu et al., The Journal of Physical Chemistry C **111**, 8971 (2007). 107

[250] W. L. Jorgensen, Journal of Chemical Theory and Computation **3**, 1877 (2007). 114

[251] O. Demerdash, E.-H. Yap, and T. Head-Gordon, Annual Review of Physical Chemistry **65**, 149 (2014). 114

[252] G. Lamoureux, A. D. MacKerell, and B. Roux, The Journal of Chemical Physics **119**, 5185 (2003). 114

[253] D. P. Geerke and W. F. van Gunsteren, The Journal of Physical Chemistry B **111**, 6425 (2007). 114

[254] A. C. T. van Duin, S. Dasgupta, F. Lorant, and W. A. Goddard, The Journal of Physical Chemistry A **105**, 9396 (2001). 114

[255] D.-X. Zhao et al., Journal of Chemical Theory and Computation **6**, 795 (2010). 114

[256] G. A. Kaminski et al., Journal of Computational Chemistry **23**, 1515 (2002). 114

[257] P. Ren and J. W. Ponder, Journal of Computational Chemistry **23**, 1497 (2002). 114, 118

[258] P. Ren and J. W. Ponder, The Journal of Physical Chemistry B **107**, 5933 (2003). 114, 116, 117, 118, 127

[259] P. Ren, C. Wu, and J. W. Ponder, Journal of Chemical Theory and Computation **7**, 3143 (2011). 114, 117

[260] J. W. Ponder et al., The Journal of Physical Chemistry B **114**, 2549 (2010). 114, 116

[261] P. Cieplak, J. Caldwell, and P. Kollman, Journal of Computational Chemistry **22**, 1048 (2001). 114

[262] P. N. Day et al., The Journal of Chemical Physics **105**, 1968 (1996). 114

[263] A. Holt, J. Boström, G. Karlström, and R. Lindh, Journal of Computational Chemistry **31**, 1583 (2010). 114

[264] L.-P. Wang et al., The Journal of Physical Chemistry B **117**, 9956 (2013). 114, 127

[265] A. C. Simmonett, F. C. Pickard, Y. Shao, T. E. Cheatham, and B. R. Brooks, The Journal of Chemical Physics **143** (2015). 114

[266] P. Pulay, Molecular Physics **17**, 197 (1969). 115

[267] M. V. Fernández-Serra and E. Artacho, The Journal of Chemical Physics **121**, 11136 (2004). 115

[268] T. A. Arias, M. C. Payne, and J. D. Joannopoulos, Phys. Rev. Lett. **69**, 1077 (1992). 115

[269] D. K. Remler and P. A. Madden, Mol. Phys. **70**, 921 (1990). 115

[270] P. Pulay and G. Fogarasi, Chemical Physics Letters **386**, 272 (2004). 115, 118

[271] J. M. Herbert and M. Head-Gordon, Phys. Chem. Chem. Phys. **7**, 3269 (2005). 115

[272] A. Albaugh, O. Demerdash, and T. Head-Gordon, The Journal of Chemical Physics **143**, 174104 (2015). 116, 120, 122, 125, 126, 128, 142, 143, 146, 157

[273] A. M. N. Niklasson, Phys. Rev. Lett. **100**, 123004 (2008). 116, 118, 119, 122, 124, 128

[274] V. Vitale et al., J. Chem. Phys. **146** (2017). 116, 120, 122, 142, 143, 146

[275] Y. Shi et al., Journal of Chemical Theory and Computation **9**, 4046 (2013). 116, 118

[276] R. T. Bradshaw and J. W. Essex, Journal of Chemical Theory and Computation **12**, 3871 (2016). 117

[277] L.-P. Wang, J. Chen, and T. Van Voorhis, Journal of Chemical Theory and Computation **9**, 452 (2013). 117

[278] L.-P. Wang, T. J. Martinez, and V. S. Pande, The Journal of Physical Chemistry Letters **5**, 1885 (2014). 117

[279] P. T. van Duijnen and M. Swart, The Journal of Physical Chemistry A **102**, 2399 (1998). 117

[280] D. M. Young, editor, *Iterative Solution of Large Linear Systems*, Academic Press, 1971. 118

[281] W. Wang and R. D. Skeel, The Journal of Chemical Physics **123**, 164107 (2005). 118

[282] J. Dziedzic et al., The Journal of Chemical Physics **145**, 124106 (2016). 118

[283] M. Parrinello and A. Rahman, Journal of Applied Physics **52**, 7182 (1981). 118

[284] H. B. Schlegel et al., The Journal of Chemical Physics **114**, 9758 (2001). 118

[285] J. M. Herbert and M. Head-Gordon, The Journal of Chemical Physics **121**, 11542 (2004). 118

[286] A. M. N. Niklasson, C. J. Tymczak, and M. Challacombe, Phys. Rev. Lett. **97**, 123001 (2006). 118

[287] A. M. N. Niklasson and M. J. Cawkwell, The Journal of Chemical Physics **141**, 164123 (2014). 118, 119

[288] M. Arita, D. R. Bowler, and T. Miyazaki, Journal of Chemical Theory and Computation **10**, 5419 (2014). 121

[289] T. Ozaki, Phys. Rev. B **64**, 195110 (2001). 121

[290] B. Jansík, S. Høst, P. Jørgensen, J. Olsen, and T. Helgaker, The Journal of Chemical Physics **126**, 124104 (2007). 121

[291] P. D. Haynes, A. A. Mostofi, C.-K. Skylaris, and M. C. Payne, Journal of Physics: Conference Series **26**, 143 (2006). 127

[292] M. J. Gillan, D. Alfé, and A. Michaelides, The Journal of Chemical Physics **144**, 130901 (2016). 127

[293] I.-C. Lin, A. P. Seitsonen, I. Tavernelli, and U. Rothlisberger, Journal of Chemical Theory and Computation **8**, 3902 (2012). 127, 128

[294] R. A. DiStasio, B. Santra, Z. Li, X. Wu, and R. Car, The Journal of Chemical Physics **141**, 084502 (2014). 127

[295] C. J. Burnham and S. S. Xantheas, The Journal of Chemical Physics **116**, 5115 (2002). 127

[296] B. Santra, R. A. D. Jr., F. Martelli, and R. Car, Molecular Physics **113**, 2829 (2015). 127

[297] M. L. Laury, L.-P. Wang, V. S. Pande, T. Head-Gordon, and J. W. Ponder, The Journal of Physical Chemistry B **119**, 9423 (2015). 127, 128

[298] G. J. Martyna, M. E. Tuckerman, D. J. Tobias, and M. L. Klein, Molecular Physics **87**, 1117 (1996). 128

[299] J. Kolafa and J. W. Perram, Molecular Simulation **9**, 351 (1992). 128

[300] T. Darden, L. Perera, L. Li, and L. Pedersen, Structure **7**, R55 (1999). 128

[301] A. D. Becke, Phys. Rev. A **38**, 3098 (1988). 128

[302] C. Lee, W. Yang, and R. G. Parr, Phys. Rev. B **37**, 785 (1988). 128

[303] A. Odell, A. Delin, B. Johansson, M. J. Cawkwell, and A. M. N. Niklasson, The Journal of Chemical Physics **135**, 224105 (2011). 154